



University
of Glasgow

<https://theses.gla.ac.uk/>

Theses Digitisation:

<https://www.gla.ac.uk/myglasgow/research/enlighten/theses/digitisation/>

This is a digitised version of the original print thesis.

Copyright and moral rights for this work are retained by the author

A copy can be downloaded for personal non-commercial research or study, without prior permission or charge

This work cannot be reproduced or quoted extensively from without first obtaining permission in writing from the author

The content must not be changed in any way or sold commercially in any format or medium without the formal permission of the author

When referring to this work, full bibliographic details including the author, title, awarding institution and date of the thesis must be given

Enlighten: Theses

<https://theses.gla.ac.uk/>
research-enlighten@glasgow.ac.uk

Free-Flyer Path Planning in the Proximity to Large Space Structures

Alexander B. Roger B.Eng

Thesis submitted to the Faculty of Engineering, University of Glasgow,
for the degree of Doctor of Philosophy. All aspects of the work
presented herein are original in concept except where indicated.

The research was conducted between October 1997 and October 2000
at the Department of Aerospace Engineering, University of Glasgow,
and completed externally between October 2000 and October 2003.

Alexander B. Roger, October 2003

ProQuest Number: 10391094

All rights reserved

INFORMATION TO ALL USERS

The quality of this reproduction is dependent upon the quality of the copy submitted.

In the unlikely event that the author did not send a complete manuscript and there are missing pages, these will be noted. Also, if material had to be removed, a note will indicate the deletion.



ProQuest 10391094

Published by ProQuest LLC (2017). Copyright of the Dissertation is held by the Author.

All rights reserved.

This work is protected against unauthorized copying under Title 17, United States Code
Microform Edition © ProQuest LLC.

ProQuest LLC.
789 East Eisenhower Parkway
P.O. Box 1346
Ann Arbor, MI 48106 – 1346



13403

COPY 2

ABSTRACT

The development of the modern space stations into large, highly complex orbital structures such as the International Space Station (ISS), has brought about a requirement for free-flying vehicles to perform various inspection and maintenance task on the exterior of the station. Concentrating on the ISS-Inspector vehicle, this thesis investigates the trajectory and mission planning required for a small free-flying vehicle operating in close proximity to the ISS. Two complimentary methods are presented to permit safe manoeuvring around the ISS. Ellipse of Safety trajectories enforce long-term passive safety requirements in the presence of differential air drag during the fly-around phases of the mission, used to transfer between the docking port and observation points. Short-range, close proximity manoeuvring is permitted through the use of Potential Field Guidance methods, enhanced through Velocity Selection strategies to provide passively safe trajectories where possible. Finally, a mission planning tool is presented to permit the integrated planning of ISS-Inspector missions, with automated scheduling and trajectory selection, designed to optimise the use of available manoeuvring methods to maximise overall mission safety. This facilitates the rapid planning and prototyping of Inspector missions from within a single tool, which is available both to operators on the ground and the crew onboard the ISS.

ACKNOWLEDGEMENTS

I would like to thank my supervisor Prof. Colin McInnes for his never ending patience and all the advice and encouragement he has given over the years. Also I would like to thank Emily Garman for the help she gave during my whole time in the Aerospace Engineering Department. I would have been lost without her.

Also, I would like to thank the following organisations for their sponsorship and assistance during the course of my research: EPSRC, The Cross Trust, The Royal Academy of Engineering, and of course all the people of the Department of Aerospace Engineering at the University of Glasgow. I would especially like to thank Detlef Wilde and Uwe Bruge of Daimler-Chrysler Aerospace in Bremen (now a part of EADS Astrium) for their invaluable help and assistance with the Inspector project.

Finally, I would like to thank all the people that have encouraged and supported me in the completion of this thesis. My Mum and Dad for their constant nagging (I needed it really, love Sandy), Ben Saunders for showing it can be done, Tom French and Niall MacDonald for their frequent joking at my progress, and Leslie Benzie for encouraging me to take time off work for writing up. Finally, I'd like to say a big thank you to my brother and sister, Neil and Kirsty Roger, for not asking me about my thesis and keeping me sane, you're the best!

CONTENTS

ABSTRACT	II
ACKNOWLEDGEMENTS	III
CONTENTS	IV
LIST OF FIGURES	VIII
NOMENCLATURE	XIII
CHAPTER 1: INTRODUCTION	1
1.1 INTRODUCTION	1
1.1.1 <i>Robotics and Autonomy</i>	2
1.2 PATH PLANNING	4
1.2.1 <i>Simple Reactive Path Finding and Collision Avoidance</i>	5
1.2.2 <i>The Configuration Space Approach</i>	8
1.2.3 <i>The Visibility Graph and Voronoi Diagram</i>	11
1.2.4 <i>Analytical Potential Fields (Potential Functions)</i>	14
1.2.5 <i>Harmonic Potential Fields</i>	18
1.2.6 <i>Discrete Solutions</i>	20
1.2.7 <i>Integrating Motion Constraints</i>	24
1.3 THESIS GOALS	25
1.3.1 <i>Required Manoeuvring Methods</i>	25
1.3.2 <i>Thesis Contributions</i>	27
1.3.3 <i>Software Tool Overview</i>	27
CHAPTER 2: ORBITAL DYNAMICS	30
2.1 PLANETARY AND SATELLITE MOTION	30
2.2 TWO-IMPULSE MANOEUVRES	36
2.2.1 <i>The Effect of Transfer Time τ</i>	37
2.2.2 <i>Optimisation of Two-Impulse Trajectories</i>	38
2.3 MULTI-WAYPOINT MANOEUVRES	41
2.3.1 <i>Applications for Multi-Waypoint Paths</i>	41
2.3.2 <i>Optimisation of Multi-Waypoint Manoeuvres</i>	43
2.3.3 <i>Comparison with Two-Impulse Cost</i>	47
2.4 ERRORS	48
2.4.1 <i>Linearised Equation Errors</i>	48
2.4.2 <i>Thruster Impulse Errors</i>	49
2.4.3 <i>Additional Perturbing Forces</i>	50

CHAPTER 3: THE ISS-INSPECTOR MISSION	52
3.1 PREDEFINED INSPECTOR MANOEUVRES	54
3.1.1 <i>ISS Flight Rules</i>	55
3.1.2 <i>R-Bar Forced Motion Approach</i>	55
3.1.3 <i>Approach Safety Envelope</i>	57
3.1.4 <i>Additional Standard Manoeuvres</i>	59
3.2 OBSERVATION POINT SELECTION	60
3.2.1 <i>The Inspector Camera View</i>	61
3.2.2 <i>Lighting and Space Station Configuration</i>	61
3.2.3 <i>Spatial visualisation</i>	63
3.2.4 <i>Additional observation point requirements</i>	64
CHAPTER 4: ELLIPSE OF SAFETY MANOEUVRES	67
4.1 THE ELLIPSE OF SAFETY	67
4.1.1 <i>Rationale of the EOS</i>	69
4.1.2 <i>Ellipse Parameters</i>	71
4.1.3 <i>Construction of EOS</i>	72
4.2 THE EOS SEGMENT OF AN INSPECTOR MISSION	74
4.2.1 <i>Ellipse of Safety Sizing</i>	74
4.2.2 <i>Transfer to and Return from Observation Points</i>	75
4.2.3 <i>Transfer from Above to Below the ISS</i>	77
4.3 TRANSFER TO OBSERVATION	77
4.3.1 <i>EOS Selection</i>	79
4.3.2 <i>Retreat from Docking</i>	81
4.3.3 <i>Injection into required EOS</i>	82
4.3.4 <i>Forced motion to Observation Point</i>	83
4.4 RETURN TO DOCKING	83
4.4.1 <i>Manoeuvre to Safe Retreat Position</i>	85
4.4.2 <i>Retreat from Observation Point</i>	86
4.4.3 <i>EOS Transfer back to Docking Position</i>	87
4.4.4 <i>R-Bar Forced Motion Approach to Docking</i>	90
4.5 EOS MANOEUVRE COST	90
CHAPTER 5: POTENTIAL FIELDS	93
5.1 THE LAPLACE ARTIFICIAL POTENTIAL	94
5.1.1 <i>The Laplace Equation</i>	94
5.1.2 <i>Discretising the Laplace Equation</i>	96
5.1.3 <i>Example Paths through the Laplace Potential Field</i>	98
5.1.4 <i>Merits of the Method</i>	101
5.1.5 <i>Specification of Obstacle Boundary Array</i>	104
5.2 THE WAVE-FRONT COST METHOD	105
5.2.1 <i>The Wave-Front Algorithm</i>	106

5.2.2	<i>The Step Cost Function</i>	107
5.2.3	<i>Example Paths through the Cost Field</i>	109
5.2.4	<i>Merits of the Method</i>	110
CHAPTER 6: POTENTIAL FUNCTION GUIDANCE		111
6.1	INTRODUCTION	111
6.2	PATH OF STEEPEST DESCENT	112
6.2.1	<i>Potential Field Interpolation</i>	112
6.2.2	<i>Gradient Extraction</i>	113
6.2.3	<i>Following Path of Steepest Descent</i>	117
6.3	GRADIENT IMPULSE MANOEUVRING	118
6.3.1	<i>The Method</i>	119
6.3.2	<i>Example Gradient Impulse PFG Manoeuvres</i>	121
6.3.3	<i>Merits of the Method</i>	124
6.4	PATHS FROM COMPLIMENTARY POTENTIAL FIELDS	125
6.4.1	<i>Gradient Magnitudes</i>	125
6.4.2	<i>The Effect of Changes in the Potential Field</i>	127
6.5	VELOCITY SELECTION FOR SAFETY	131
6.5.1	<i>The Aim of Velocity Selection</i>	131
6.5.2	<i>Velocity Selection Criteria</i>	132
6.5.3	<i>Impact on Manoeuvre Time and Propellant Cost</i>	133
6.6	NAVIGATION PROBLEMS AND SOLUTIONS	138
6.6.1	<i>Navigation Errors/Noise</i>	139
6.6.2	<i>Smoothing and filters</i>	141
6.6.3	<i>Backup Navigation Methods</i>	143
CHAPTER 7: MISSION PLANNING		145
7.1	INTRODUCTION	145
7.2	THE VEHICLE ROUTING PROBLEM (VRP)	147
7.2.1	<i>The Travelling Salesman Problem</i>	148
7.2.2	<i>A Dynamic Programming Solution to the TSP</i>	150
7.2.3	<i>Mission Scheduling Constraints and the VRP</i>	152
7.2.4	<i>The ISS-Inspector VRP</i>	153
7.3	MISSION PLANNING TOOL	155
7.3.1	<i>Observation Point Selection Interface</i>	156
7.3.2	<i>Path Planning of Mission Elements</i>	158
7.3.3	<i>Mission Sequencing</i>	162
7.3.4	<i>Mission Safety Analysis and Final Plan</i>	164
7.4	MISSION TEST CASES	166
7.4.1	<i>Case A: A Single Target Inspection Mission</i>	166
7.4.2	<i>Case B: A Two Target Inspection Mission</i>	175
7.4.3	<i>Case C: A 6 Target Inspection Mission</i>	184

CHAPTER 8: CONCLUSIONS	196
8.1 REVIEW	196
8.2 SUMMARY	200
8.3 RECOMMENDATIONS	202
APPENDIX I – SPACE STATION DEVELOPMENT	205
<i>Space Station History (1971-1990's)</i>	205
<i>The Mir Space Station</i>	207
<i>The International Space Station ISS (1998 - Future)</i>	208
<i>Space Station Statistics</i>	210
APPENDIX II: STATE OF THE ART ROBOTICS	213
<i>X – Mir Inspector</i>	214
<i>Mars Pathfinder – The Sojourner Robot</i>	216
<i>Space Shuttle Robotic Arm</i>	218
<i>Japanese Robotic Experiments</i>	219
<i>Terrestrial Robots</i>	221
<i>C.M.U. Autonomous Helicopter Project</i>	221
<i>Subsea Robots</i>	222
<i>Current Development Projects</i>	223
<i>ISS – Inspector</i>	224
<i>NASA AERCam</i>	226
<i>NASA Personal Satellite Assistant</i>	228
APPENDIX III: THE CLOHESSEY WILTSHERE EQUATIONS	229
<i>Non-linear Equations of Motion</i>	229
<i>Linearised Equations of Motion – The Clohessy Wiltshire Equations</i>	232
APPENDIX IV: THE ISS INSPECTOR HARDWARE SYSTEM	234
<i>Vehicle Capabilities</i>	234
<i>Docking and Berthing</i>	236
<i>Navigation</i>	237
<i>Communications and Data Links</i>	238
<i>Control Architecture</i>	239
REFERENCES	242

LIST OF FIGURES

Figure 1-1	The International Space Station	1
Figure 1-2	A Basic Path Finder	6
Figure 1-3	Sensor/Actuator Connection Structure	6
Figure 1-4	Wall Following Behaviour Weighting	7
Figure 1-5	Dijkstra's Algorithm Operation	9
Figure 1-6	The V-Graph and Sub-V-Graph	12
Figure 1-7	The Generalised Voronoi Diagram	13
Figure 1-8	The Potential Surface	15
Figure 1-9	Potential Function Combinations	17
Figure 1-10	Local Minimum Formation	18
Figure 1-11	The A* Algorithm	22
Figure 1-12	The D* Algorithm	23
Figure 1-13	Mission Planning Software Schematic	28
Figure 2-1	ISS Fixed Co-ordinate System	30
Figure 2-2	Orbital Ellipse geometry	31
Figure 2-3	Relative Motion between Circular and Elliptic Orbits	33
Figure 2-4	Free-Drift from a Stationary Position	35
Figure 2-5	An Example CW Trajectory	35
Figure 2-6	Increasing Transfer Time Comparison	37
Figure 2-7	ΔV Required vs Transfer Time τ	38
Figure 2-8	ΔV Distribution for Varying Start Co-ordinates	39
Figure 2-9	Transfer Cost for Varying Time Cost Weighting	40
Figure 2-10	Single Waypoint Obstacle Avoidance	42
Figure 2-11	Multi-Waypoint Path Following	43
Figure 2-12	Optimised Two Step Transfers	44
Figure 2-13	Deviation from Planned Path	45

Figure 2-14	Two Step Vs Single Step Transfers	47
Figure 2-15	Lincarisation Errors over Drift from (0,0)	49
Figure 2-16	The Result of Initial ΔV Errors	50
Figure 3-1	The ISS-Inspector	52
Figure 3-2	Defined Visiting Vehicle Safety Zones	55
Figure 3-3	Docking Approach Cone	56
Figure 3-4	Approach Braking Profile	56
Figure 3-5	Safe Drift from Station-Keeping	57
Figure 3-6	Growth of the Approach Safety Envelope	58
Figure 3-7	3-D Approach Envelope	59
Figure 3-8	EOS Orbit Timing with Lighting Direction	63
Figure 3-9	External View Example	64
Figure 3-10	Inspection Camera View	66
Figure 3-11	ISS and Inspector External View	66
Figure 4-1	The Ellipse of Safety	68
Figure 4-2	In-Plane Ellipse Drift due to Atmospheric Drag	69
Figure 4-3	EOS Trajectory with Drag	70
Figure 4-4	Standard Ellipse Geometry	72
Figure 4-5	EOS Ellipse Width Sizing	75
Figure 4-6	Inspector Ellipse of Safety Plan	76
Figure 4-7	Outward Phase Plan	78
Figure 4-8	EOS Safety Clearance Over S_2 Range	79
Figure 4-9	EOS Coverage of ISS	80
Figure 4-10	Calculation of the S_2 Point	80
Figure 4-11	Free-flyer passive drift from Docking Release	81
Figure 4-12	Return Phase Plan	84
Figure 4-13	The Effect of Small Phase Changes on the EOS	85
Figure 4-14	Transfer to a Safe Retreat Position Examples	86

Figure 4-15	Drifting Ellipse Retreat Trajectories	87
Figure 4-16	Solution of the Z Motion for R_i	89
Figure 4-17	Ellipse of Safety Examples	91
Figure 5-1	A Potential Minimum	95
Figure 5-2	The Laplace Potential Field	97
Figure 5-3	Example 2D Laplace Paths	98
Figure 5-4	Example 3D Paths around the ISS	100
Figure 5-5	Path Variations from Small Changes in Coordinates	101
Figure 5-6	Safe Path Finding Behaviours	102
Figure 5-7	A Discrete Time Representation of the Solar Array Configuration	103
Figure 5-8	The Boundary Definition of a Circle	105
Figure 5-9	Expanding the Wave-Front	106
Figure 5-10	The Calculated Cost Field	107
Figure 5-11	Obstacle Distance Component Influence	108
Figure 5-12	Wave-Front Path Shaping	109
Figure 6-1	Bi-linear Interpolation	113
Figure 6-2	Path Direction Discontinuities	115
Figure 6-3	The Calculation of Nodal Gradients	116
Figure 6-4	Path Differences due to Increased Interpolation Accuracy	116
Figure 6-5	ATV Potential Function Guidance	118
Figure 6-6	Gradient Switching Criterion	120
Figure 6-7	Example GI-PFG Paths using the Laplace Potential Field	122
Figure 6-8	A Demonstration of the Advantages/Disadvantages of GI-PFG	123
Figure 6-9	GI-PFG Path Variations from Small Changes in Co-ordinates	124
Figure 6-10	Potential and Cost Gradients	126
Figure 6-11	Paths around the COF Module, with Alternate Potential Fields	127
Figure 6-12	Reverse Paths around the COF Module	128
Figure 6-13	Path between ISS Elements, with Alternate Potential Fields	129

Figure 6-14	GI Path Shaping	130
Figure 6-15	Velocity Selection Application to COF Transfer	134
Figure 6-16	Velocity Selection Application to Extended Transfer	136
Figure 6-17	GI Path Velocity Profile	139
Figure 6-18	Sensed Free-Flyer Path with Random Noise Errors	140
Figure 6-19	Sample Rate Adaptation	141
Figure 6-20	A Smoothed Navigation Path	143
Figure 7-1	The Travelling Salesman Problem	148
Figure 7-2	Decimal Sequence Checking	149
Figure 7-3	The Multi-Windowed Interface	156
Figure 7-4	Observation Point Selection Interface	157
Figure 7-5	Observation Point Confirmation	157
Figure 7-6	Manoeuvre Selection Segmentation Map	159
Figure 7-7	PFG Manoeuvre Categories	160
Figure 7-8	ISS Configuration Relative to Orbital Plane	162
Figure 7-9	Mission Sequencing Interface	163
Figure 7-10	Free-Drift Path Propagation (With Errors)	165
Figure 7-11	Case A: Inspection Target and Observation Points	167
Figure 7-12	Case A: Observation Point Selection Procedure	169
Figure 7-13	Case A: Transfer Optimisation Dialogue	170
Figure 7-14	Case A: Overview of Mission Trajectory	171
Figure 7-15	Case A: PFG Trajectories	172
Figure 7-16	Case A: EOS Trajectories	173
Figure 7-17	Case B: Inspection Target 1 and Observation Points	175
Figure 7-18	Case B: Inspection Target 2 and Observation Points	176
Figure 7-19	Case B: Target 1 Observation Points	178
Figure 7-20	Case B: Target 2 Observation Points	180
Figure 7-21	Case B: Transfer Optimisation Dialogue	181

Figure 7-22	Case B: Mission Trajectory Overview	181
Figure 7-23	Case B: PFG Trajectories below the ISS	182
Figure 7-24	Case B: EOS Trajectories	183
Figure 7-25	Case C: Observation Point Overview	186
Figure 7-26	Case C: Observation Point Selection Screens	189
Figure 7-27	Case C: Transfer Optimisation Dialogue	190
Figure 7-28	Case C: Mission Trajectory Overview	191
Figure 7-29	Case C: PFG Trajectories	193
Figure 7-30	Case C: EOS Trajectory in X-Y Plane	194
Figure I-1	Skylab from Orbit	206
Figure I-2	The Mir Space Station	207
Figure I-3	ISS Construction Sequence	209
Figure I-4	The Evolution of Space Stations	211
Figure II-1	The X-Mit Inspector Systems Diagram	215
Figure II-2	The Mir – Progress – Inspector Mission Overview	216
Figure II-3	The Mars Sojourner Rover	217
Figure II-4	SRMS Assists in the Assembly of the ISS	219
Figure II-5	The Inspector Product Family	225
Figure II-6	ISS Inspector Preliminary Mission Concept	226
Figure II-7	AERCam Sprint	227
Figure III-1	Frames of reference for relative motion	229
Figure IV-1	Inspector Free-Flyer Configuration	235
Figure IV-2	The Inspector Docking Port	236
Figure IV-3	Inspector Control Systems Configuration	240

NOMENCLATURE

AE	Approach Ellipsoid
ATV	Automated Transfer Vehicle
AUV	Autonomous Underwater Vehicle
CAM	Collision Avoidance Manoeuvre
COF	Columbus Orbital Facility
CRV	Crew Return Vehicle
CW	Clohessey Wiltshire
DHS	Data Handling System
EOS	Ellipse of Safety
EVA	Extra Vehicular Activities
GA	Genetic Algorithm
GI-PFG	Gradient Impulse PFG
GNC	Guidance Navigation and Control
GPS	Global Positioning System
ISS	International Space Station
JEM	Japanese Experiment Module
KOS	Keep Out Sphere
MCS	Monitoring and Control Station
PFG	Potential Field Guidance
R Bar	Orbit Radius Vector
RGPS	Relative GPS
ROV	Remotely Operated Vehicle
RVD	Rendezvous and Docking
SRMS	Shuttle Remote Manipulator System
SSRMS	Space Station Remote Manipulator System
TDRSS	Tracking and Data Relay Satellite System

TM/TC	Telemetry / Telecommand
TSP	Travelling Salesman Problem
V-Bar	Orbital Velocity Vector
VRP	Vehicle Routing Problem
VV	Visiting Vehicle
D_o, D_p	Cost Field Obstacle Shaping Constants
F	Applied Force
F_{ij}	Array of TSP costs
G	Universal Gravitational Constant ($6.673 \times 10^{-11} \text{ m}^3.\text{kg}^{-1}.\text{s}^{-1}$)
\underline{R}	Position Vector Relative to ISS Frame of Reference
S	Set of Nodes
T	Orbit Period
a	Ellipse Semi-Major Axis
b	Ellipse Semi-Minor Axis
e	Ellipse Eccentricity
f_x, f_y, f_z	External Perturbing Forces
k_t	Time Cost Weighting
k_{v0m}	Default Velocity Scalar
m	Mass
r	Range
\underline{r}	Position Vector Relative to Earth Frame of Reference
s_i	Velocity Scale Multiplier
ζ_{\max}	Ellipse of Safety Width
ΔV	Required Velocity Change
ϕ	Potential Magnitude
μ	Gravitational Parameter of System $\mu = G(m_1+m_2)$
θ	Maximum Trajectory Deviation Angle

σ	Standard Deviation
τ	Transfer Time
ω	Orbital Angular Velocity Vector
$\sum \underline{f}$	Sum of External Force Vectors

CHAPTER 1: INTRODUCTION

1.1 Introduction

Ever since the first orbital flight by Cosmonaut Yuri A. Gagarin onboard Vostok 1 in 1961 increasingly complex structures have been launched into space, capable of supporting greater numbers of astronauts for extended durations. With increasing size and capabilities, come increased assembly and maintenance requirements, demanding enhanced support and assembly techniques. In December 1998 the first two modules of the International Space Station (ISS), Unity and Zarya, were docked in orbit to complete the first step in the assembly of the next generation of space station, and at the time of writing a further 12 major station element have joined these modules. An artist's impression of the completed structure, pictured with the European ATV supply vehicle docking at the rear of the station, is shown in Figure 1-1.

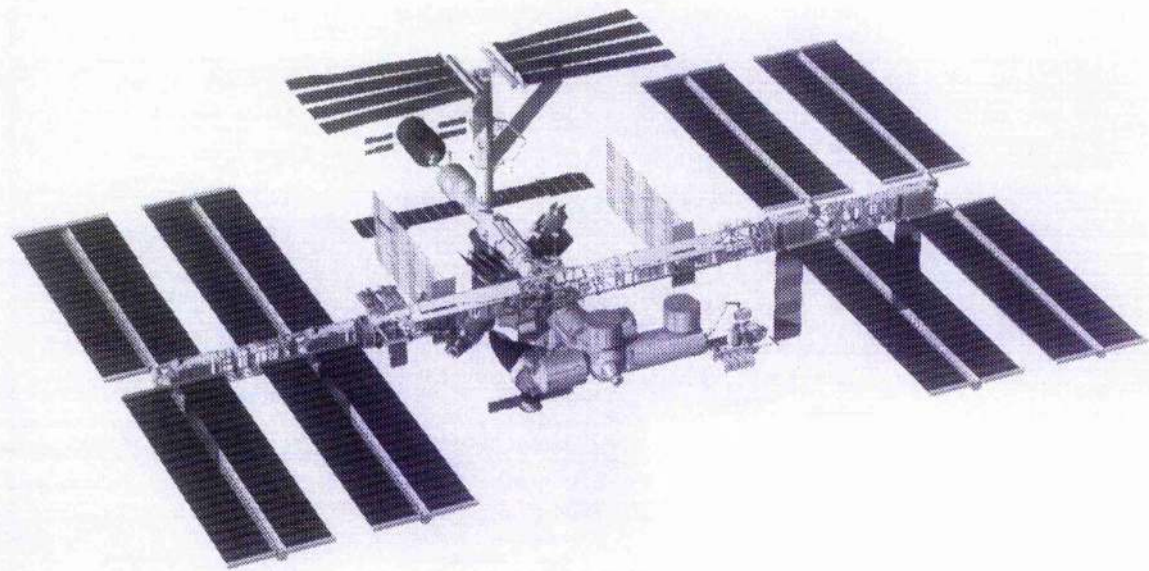


Figure 1-1 The International Space Station (Source: NASA)

The ISS is the latest in a long line of crewed space stations, and benefits from the combined expertise of not only the U.S. and European space agencies, but also that of Russia, Japan and the many other ISS partner nations. As such it is largest scale orbital program ever undertaken, requiring a large number of assembly flights to launch the planned 18+ modules into orbit. Compared to the previous generation of space station, the Russian Mir station, the ISS will have three times the pressurised volume, three times the power generation

capabilities, and up to double the crew of Mir. A brief overview of the history and development of orbital space stations is given in Appendix I at the end of this thesis.

As the assembly of the ISS continues there will be a need for a large number of external inspection missions, both during the lengthy construction phase and throughout its operational life. Some of these inspections will be made by external cameras mounted either on the ISS structure or on the station robotic arm. However because of the size and complexity of the ISS, the entire station exterior is not visible from station mounted cameras. A free-flying vehicle outside the station would be capable of making inspections of any point on the ISS structure and supporting astronaut EVA operations, as well as providing desirable documenting capabilities in the latter stages of station assembly to recording accurate reference information on the final ISS configuration. Once the station is operational these vehicles could also enable possible robotic maintenance and repair operations; for example, the case of the Mir accident on 25th June 1997 [1][2], when an unmanned *Progress* supply vehicle impacted on the Mir station while performing a manual re-docking operation. The collision punctured the Spektr module and damaged a number of solar panels and power cables, but the damage was not fully inspected until some three months later. In this situation, a rapid inspection of the damage made by an external free-flying camera would have been invaluable for assessing the accident.

1.1.1 Robotics and Autonomy

Many tasks and activities that require intelligence, but are required to take place in environments hazardous to humans, have been subject to the development of robotic entities - either remotely controlled or possessing their own form of intelligence to perform these tasks. Such tasks range from the inspection of radioactive or chemically contaminated sites, to the maintenance of underwater pipelines. A variety of autonomous robots have under development to fulfil these requirements, and a number of these state of the art robots are described in Appendix II. In addition, a lesser degree of autonomy is often applied to robotics and control systems to reduce the workload of a human controller, by automating simple tasks such as the monitoring of battery power supply levels or the execution of a pre-planned sequence of manoeuvres. This level of automation, which is already in common use, is distinct from the goal of overall robot autonomy which remains in the early stages of development. However, the automation of increasingly complex tasks is an important stage in the development of fully autonomous robots.

The orbital environment outside of the ISS is particularly suited to the use of robots to help reduce the workload on the crew, by avoiding unnecessary EVA's and actively supporting

the astronauts during EVA missions using a range of inspection cameras and other instruments. The problems encountered in the space environment such as high energy radiation and extreme variations in temperature are well documented [3], and robotic vehicles can be shielded against these hazards, while the structure of the ISS and any surrounding vehicles will be known in advance, facilitating manoeuvring around the space station.

Vehicles such as the German *DASA Inspector* and the American *NASA AERCam* are already under development to fulfil some of these ISS support tasks. However, one of the major obstacles to operating free-flying vehicles in close proximity to large crewed space structures such as the ISS is manoeuvring the vehicle within the constraints of safety, time, and propellant usage. In order to free astronauts onboard the ISS from some of the workload of controlling these free-flying vehicles, the vehicle operations can be enhanced through the use of autonomy, especially in such procedures as extended transfers between docking points and observation/inspection points. Previous ESA/ESTEC contract work at the University of Glasgow has developed a real-time controller for similar types of path constrained proximity operations [4].

This thesis presents a set of tools and techniques that have been developed to assist mission planners on the ground and astronauts on the station to quickly plan inspection missions. The missions are planned within the constraints of the observation geometry and safety requirements imposed by tight rules. In addition to this, an active manoeuvring phase of the mission may be used for onboard control through pre-calculation of an artificial potential, which can then be uploaded to the free-flyer for use by the vehicle for active guidance during constrained manoeuvring at observation points.

Development for this thesis was based on the planned Inspector vehicle. The author spent 6 months in 1998 working with Daimler-Chrysler Aerospace (now Astrium), at which time the desired manoeuvring requirements and restrictions were defined by the project engineers[5]. During this time the use of Ellipse of Safety trajectories, that will be developed in Chapter 4, as a strategy to move from point to point was developed by the author along with the observation point selection tool - which incorporates an approximately rendered representation of the space station, with visual observation point constraint indicators, to permit the interactive selection of observation points. Details of the X-Mir Inspector mission, a precursor to the ISS-Inspector which was designed to test the operation of a free-flying camera equipped robot in proximity to a large orbital space structure, and details of the planned ISS-Inspector vehicle are included in Appendix III.

1.2 Path Planning

The automation of any tasks requiring some degree of human skill or intelligence is usually grouped under the general heading of artificial-intelligence (AI), and AI research can be broken down into a small number of key fields:

- Problem Solving Methods
- Processing Sensory Data
- Language Processing

Of these, problem solving is the broadest aspect of current AI, as summarised by Nilsson in 1971 [6], and has been the primary focus of much of the AI research performed in the past 30 years. Furthermore, one of the key applications of a wide range of problem solving techniques has been the specific problem of path planning.

The path planning problem can be defined as the task of finding a continuous sequence of robot configurations between an initial configuration (start) and a target configuration (goal) while satisfying any obstacle constraints. Basically this describes the task of finding a collision-free path from an initial configuration or position to the goal configuration through an environment of known obstacles. In addition there are a number of factors that may influence the development of a path planning method, such as the manner of collision avoidance, optimality of motion of the resulting paths, and the ability of the method to find a path to the goal if one exists.

Path planning may be applied to a range of moving robot configurations, from the simplest problem of a small circular or point vehicle moving in a sparsely populated plane, to a large complex robot configuration with 6 degrees-of-freedom (DOF) moving in a tightly constrained environment. Typically the moving robot problem is applied to non-deformable or rigid-body vehicles, and often the robot vehicle itself can be considered as a point by expanding the obstacles by the radius of the robot, thus simplifying the problem. This modification is particularly applicable to configurations where there is a relatively low obstacle density, or a desire for the robot to maintain a distance from any obstacles and not attempt passage through narrow gaps. Rotational DOF only need be considered in highly constrained environments or when the robot's means of locomotion is highly dependent on orientation direction, however the path planning problem's complexity increases exponentially with each additional DOF.

One of the first defining problems in path planning, that of finding a collision free path for a 3d rigid object that can translate and rotate in 3d space, is often known as “The Piano-Mover’s Problem” [7]. Given a tightly constrained obstacle environment such as the interconnected rooms of a house, the path planner must determine the sequence of rotations and translations required to move a piano between the rooms of the house without hitting anything. Most methods of solving this problem however have had to ignore the dynamics and other differential constraints in order to solve these tight geometrical constraints with 6 DOF.

The path planning problem is also frequently applied to robotic arms which are fixed in translation but possess only rotational degrees of freedom in their joints. Robotic arms have been a popular subject of research due to the relatively constrained range of motion, scalable complexity arising from the range of DOF given by the number of joints of the arm, and uses in a wide range of applications, including space robots [8]. Most basic techniques of path planning however are equally applicable to either rigid body moving robots or robot arms.

1.2.1 Simple Reactive Path Finding and Collision Avoidance

To find a collision-free path from an initial position to a specified goal, even a method as simple as moving in a random direction until, either an obstacle is encountered and a new random direction is chosen, or the goal is reached, will provide a solution given sufficient time. However this is obviously highly inefficient and it would be preferable to make as much use as possible about the surrounding environment to optimise the search and the resulting path. The simplest step would be to move directly in the direction of the goal in the absence of any obstructions, in fact if there are no obstacles between the start and goal this method will yield an optimal solution. If an obstacle is encountered, the path can then side-step the obstacle until a direct route to the goal is once again clear. For obstacle configurations consisting of well spaced convex objects, this technique is relatively efficient. However, concave obstacles can trap the path finder, as shown in Figure 1-2, preventing the goal from being reached.

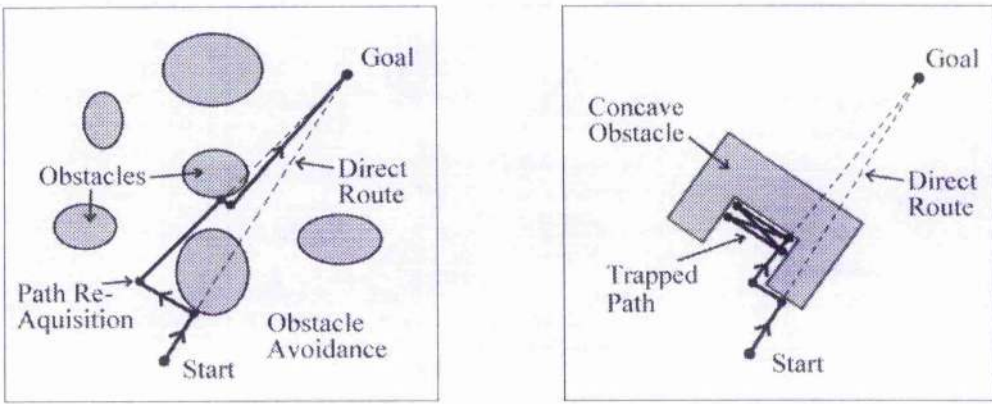


Figure 1-2 A Basic Path Finder

An alternative method for real-time path planning algorithms makes use of reactive obstacle avoidance techniques, such as those based on Braitenberg's theory [9]. This theory utilises direct connections between a vehicle's sensors and its actuators, to produce a behaviour that reacts directly to sensed objects. In the case of a free-flying vehicle such as Inspector, this could be implemented using proximity sensors situated on the exterior of the vehicle, directly connected to the control system as shown in Figure 1-3, so that a detected obstacle triggers a thruster firing in the direction of the obstacle and a corresponding acceleration in the opposite direction. On its own, the Braitenberg obstacle avoidance behaviour will only ensure that the free-flyer stays away from obstacles, but when coupled with an attraction toward the goal point, it will result in a free-flyer behaviour that moves toward the goal while being automatically repelled by obstacles.

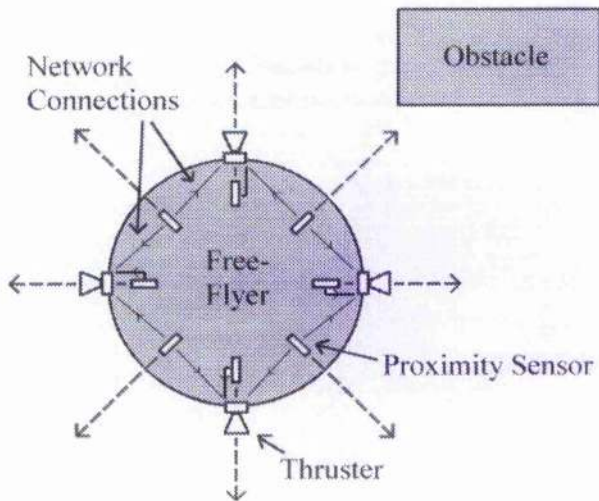


Figure 1-3 Sensor/Actuator Connection Structure

This simple technique has the advantage that no prior knowledge of the obstacle configuration is required, and even in the absence of navigation data obstacles will still be avoided autonomously. The problem of getting trapped behind large or convex obstacles can be solved by adding a wall following behaviour [10] to the control system to guide the free-flyer around large obstacles [11]. Similarly, the ability to add additional behaviours to the system permits the integration of human controller input, or even a secondary path finding algorithm, into the final control system behaviour [12]. Each behaviour is then weighted depending on current information such as obstacle proximity and available navigation and control data. Then for example when the free-flyer is in open space the goal attraction or path finder will be in control, but when an obstacle is approached the obstacle avoidance and wall following behaviours will take precedence. This ensures the safety of the free-flyer, even in the event of inaccurate navigation information or human controller error, for as long as propellant is available. However, the stability of these methods is highly dependent on the weightings of the relative controls, and the nature of the competing control actuations may produce undesirable excessive thruster firings under certain circumstances. Figure 1-4 shows the effect varying the weighing of the wall following behaviour. With the wall following weighting over 100% the path follows the wall at a fixed distance, but with a reduced weighting the path is pushed away by the obstacle avoidance behaviour, and leaves the obstacle on route towards the goal earlier.

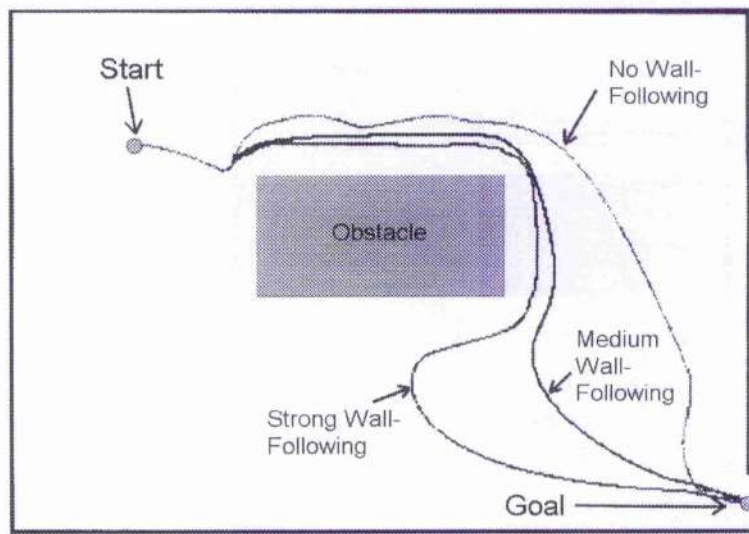


Figure 1-4 Wall Following Behaviour Weighting (adapted from [11])

The methods described above are purely reactive and require no prior knowledge of their surrounding environment other than some means of detecting obstacle proximity. They are not forward looking such that there is no real planning involved in the path finding. This

results in a number of limitations. Paths are prone to becoming trapped and there is no control over the optimality of the paths produced. In addition, these reactive methods tend to result in paths that pass in close proximity to and obstacles they avoid and often require rapid last-minute changes of direction to perform obstacle avoidance. It is often desirable in path planning to produce paths by planning ahead so that obstacles may be avoided in advance, and optimal paths with sufficient separation from obstacles may be produced.

1.2.2 The Configuration Space Approach

A key early development in path planning was the concept of the configuration-space approach introduced by Lozano-Perez [13] and the free space approach developed by Brooks [14] [15]. These methods recognise the key to path planning solutions as being the representation of the obstacle environment with respect to the robot configuration. This enabled the first unification of the path planning of both holonomic mobile robots and robot arms. The configuration-space is the space of all possible configurations of the robot, so for robot that can be represented by a point moving in a plane this would simply be a 2d map of the environment, whereas for a robotic arm the configuration space would be given by a multidimensional map with an axis for each rotational DOF of the robot with areas representing configurations which result in a collision between the arm and its surrounding environment. In this manner, the problem of determining the motion and interaction between both rotating rigid bodies or jointed manipulators and their environment can be reduced to the problem of determining the motion of a point in higher dimensional space. The free-space approach uses a representation of natural pathways between obstacles represented by a union of geometric shapes, in the case of the original papers these shapes were limited to generalised cones, allowing path-finding to be performed by following these collision free routes.

A common feature of many problem representations is their generation of a configuration-space graph as an intermediary stage to planning a path to the goal. A graph consists of a set of nodes, with certain pairs of nodes connected each other by arcs with a given cost for transfer in each direction across the arc. For the purposes of path planning each node on the graph represents a region of free-space, with the connection arcs between them defining the ability to transfer from one region to another and the costs for this transfer. Given a graph of the configuration-space, a path can then be found from a start point within one region of free space to the goal point within another region by finding a path between the corresponding nodes on the graph.

There are a large number of algorithms available to find a path through the graph, with the choice of a suitable method defined by the size and connectivity of the graph and the computational power available. One of the earliest methods is Dijkstra's algorithm [16]. Given a graph consisting of a small set of sparsely connected nodes V , Dijkstra's algorithm can be used to find the optimum route from any node to the goal, and in fact the best path between all nodes and the goal for the same calculation cost. Given the traversal cost between each connected node on the graph the algorithm works by first giving an estimate of the shortest path distance to each node, usually zero for the goal node and ∞ for all others, and then through a process called 'Relaxation' updating the distance estimate of the nodes adjacent to nodes for which the shortest paths have already determined. This operation can be seen in the sequence shown in Figure 1-5. The algorithm maintains two lists of nodes, the set S of nodes whose shortest paths have been determined, and the remaining nodes $V-S$. While $V-S$ contains nodes the distance estimate at nodes connected to the last member of S are updated, and the closest of these nodes is added to the end of S . The process is then repeated until $V-S$ is empty and the correct minimum distance from the goal to each node is determined. A path can then be found from any node by simply stepping along the nodes with the lowest distance to the goal.

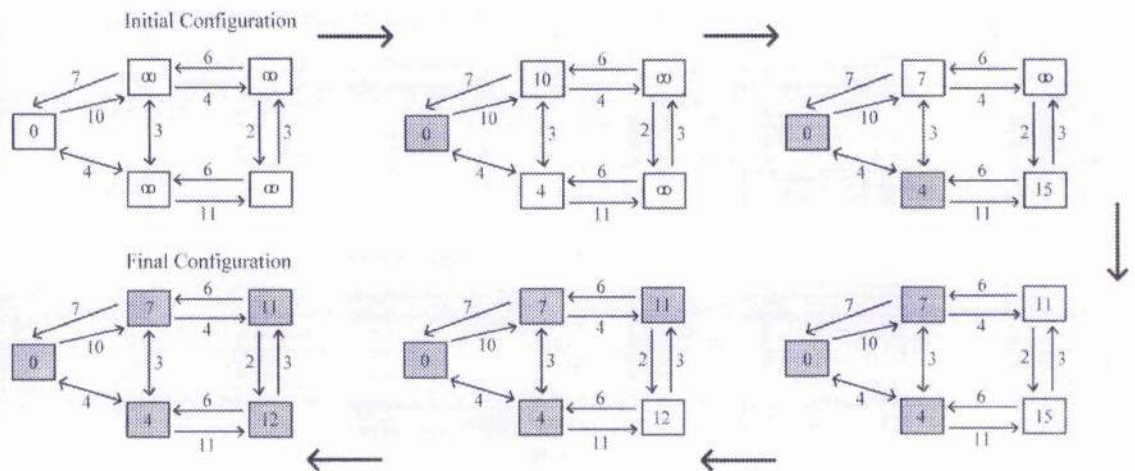


Figure 1-5 Dijkstra's Algorithm Operation

The results of a path planning traversal of the configuration-space graph can be viewed as planning a sequence of discrete state transitions its initial state to a goal configuration. Unfortunately this is a very rigid path definition, referring to an abstracted global representation of configuration space, and not necessarily easily applicable to freely moving vehicle taking consideration of its resulting motion. From this discrete path, some form of motion planning must therefore be applied to obtain a smooth path between these discrete states while respecting the movement capabilities of the robot. However, recent

research has developed a number of local methods that integrate both initial path planning and motion planning into a single stage, in many cases resulting in a more efficient overall solution.

A wide range of algorithms have been developed to solve the configuration-space or free-space representation and path planning problem, but in general all of these can be separated into two categories distinguished by the method's global or local representation of the configuration space. Global (or exact) methods, such as that used in the original work by Lozano-Perez and Brooks, essentially attempt to solve the path planning problem through the precise representation of the configuration-space. The most common of these approaches use "cell decomposition", which separates the set of free configurations into a finite number of cells, usually utilizing geometrical shapes to define these closed and free-space areas, and generating a graph containing the interconnectedness of all its free-space zones. A path may then be found by simply traversing the graph to reach the desired goal configuration. The representation is known as global since the entirety of the configuration space is encapsulated within in the graph. These methods are exact since they are guaranteed to find a path to the goal or prove that none exists within their representation, however they tend to have high complexity which increases both with the number of DOF of the robot and with the complexity of the obstacle environment. For this reason they are efficient for sparsely populated environments, but costly to apply to complex obstacle configurations.

Local methods simplify the representation of the configuration-space by constraining it to a local subset of space. This permits the use of a wider range of obstacle representations of configurable resolution, such as discrete grids or potential fields, so that the problem of path planning in configuration-space is abstracted into this alternative representation. These local methods often simplify the difficulty of representing the obstacles, but shift the problem to finding a path through this new representation. Local methods potentially offer greater flexibility however, both in integrating dynamic constraints into the paths found, and in controlling the general characteristics of these paths, to for example optimise movement costs or favour certain routes.

Research has also been performed to combine the use of individual global and local methods [17] [18]. This enables the use of a global method for high level planning to find a route between large areas of free-space, with a local method then used for the path planning within and between each individual free-space area. In Ii Wang and Ahuja (1992) the global and local configuration space representations are in fact generated using the same potential field method. In the global case a graph of the free-space regions is generated from the network of minimum potential valleys in the potential field, and this is used to generate a path

to the goal. The local path planner then uses the potential field directly navigate through each potential valley, ensuring collision avoidance and allowing the path to optimise the length and smooth the motion of the path. Further overall surveys of path planning methods may be found in [19] and [20].

There have been a wide range of alternative exact methods developed using geometrical representations of the global configuration-space problem. Earlier global approaches to path planning in three-dimensions have concentrated on specifying surfaces of obstacles in the configuration-space, and using these configuration surfaces to search for collision-free paths [21]. Critical curves were employed in the original piano movers' problem [7] but require a double exponential run time in the number of required DOF. This calculation cost has been reduced to single exponential time [22]. Other exact approaches have used Jacobian based representation of free-space [23], Integral curves or Flows [24], Polygonal obstacle representations [25], and retraction methods [26], but all these methods have similar exponential time complexities.

1.2.3 The Visibility Graph and Voronoi Diagram

The global configuration-space representation originally used by Lozano-Perez and Wesley [27] utilised the concept of a visibility graph (V-graph). Based on the vertices of polygonal obstacles, the visibility graph basically consists of a graph of all the visible connections between every vertex (node) in the configuration-space, as shown below in Figure 1-6. Defined more rigorously, the visibility graph is a graph of nodes, including a node at each obstacle vertex, and a set of links between nodes such that each straight line segment does not intersect any obstacle in the configuration space. Given this graph, the shortest path from any start point to the goal can be obtained by finding the shortest path in the V-graph between the corresponding start and goal nodes.

The first efficient algorithms for constructing visibility graphs were first developed by Lee [28] and Sharit and Schorr [29], and more recent results have improved on this efficiency [30] while being able to give optimum results in the worst case [31]. By illustration, the technique employed by Welzl functions by creating a set of line segments joining each node to every other node in the configuration-space, and then sorting the connections from each node to its surrounding nodes by angle. During the sorting of each node p , the algorithm maintains $\text{VIS}(p)$ which is the line segment seen just before the last sorted node, and each consecutive line segment from node p to the next sorted node q can be determined to be part of the visibility graph if q lies closer to p than $\text{VIS}(p)$ or if q is an endpoint of $\text{VIS}(p)$.

Given that the computational complexity of finding the optimal path through the V-graph is dependent on the size of the graph, a number of approaches have also been developed for creating a smaller sub-V-graph which still contains the shortest path. A popular method of achieving this is to “prune” the fully calculated V-graph [32], but a new technique presented by Fu and Lui [33] also optimises building of the V-graph itself by selecting only a subset of obstacle vertices and rejecting other obviously “occluded” obstacles and obstacles whose vertices are never possibly part of the shortest collision-free path, as shown in Figure 1-6.

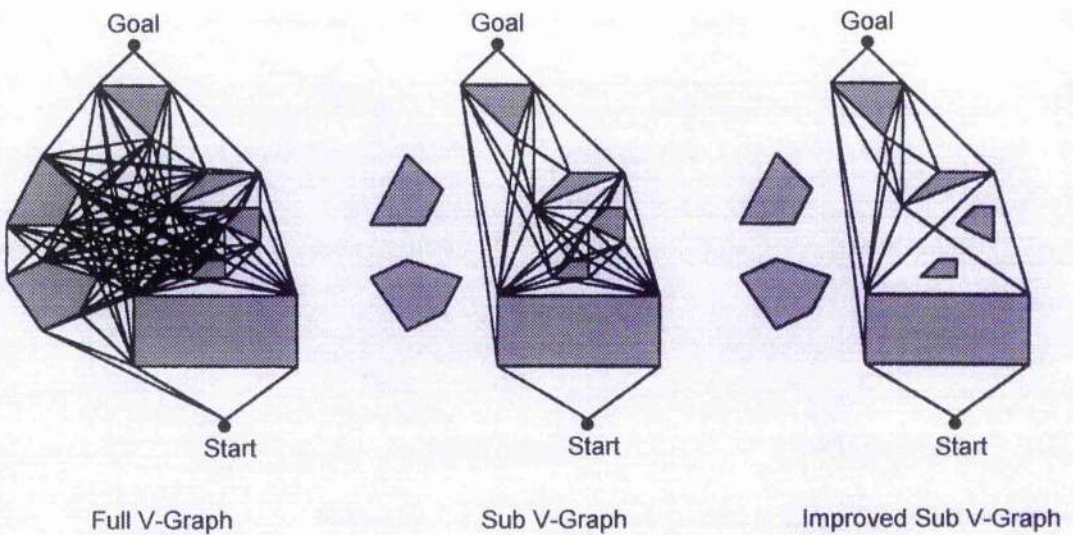


Figure 1-6 The V-Graph and Sub-V-Graph (adapted from [33])

The fact that the generation of the visibility graph requires a polygonal representation of the obstacles, as well as the fact that it produces only straight-line paths can drawbacks for certain applications. A further disadvantage of the method is that since nodes in the graph are located primarily on the surface of obstacles, the paths produced will inherently pass close to these objects at each point on their route, which may be a problem for applications where greater obstacle clearance is desirable. A comprehensive overview of visibility graphs, along with two new efficient methods for computing visibility graphs is given in Overmars and Welzl [34].

An alternate method that solves the problem of passing close to obstacles by generating routes that follow distance contours between obstacle surfaces is the generalised Voronoi diagram [35] [26]. The nodes of the two dimensional Voronoi diagram represent points that are equidistant from three or more obstacle surfaces in the configuration-space,

and these nodes are joined by edges which are one-dimensional curves along contours that are themselves equidistant from two obstacle surfaces, as shown in Figure 1-7.

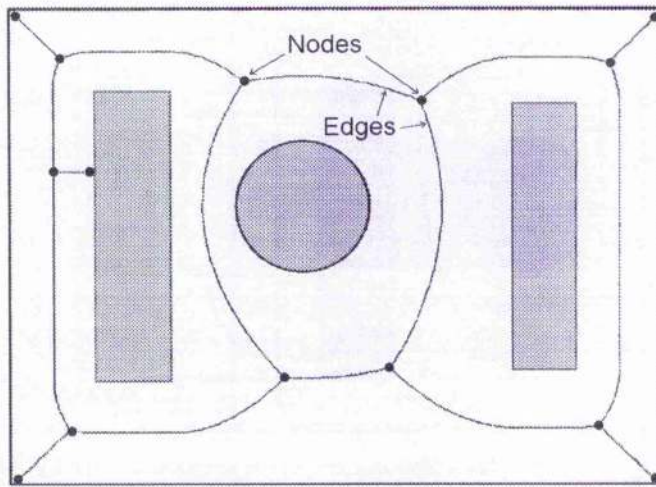


Figure 1-7 The Generalised Voronoi Diagram

The nodes and edges of the Voronoi diagram can be calculated discretely by propagating “waves” corresponding to contours of the distance from the surface of each obstacle along with the configuration space boundaries. The edges of the diagram are given as the set of points where the distance waves meet, and the nodes as the points where the edges between different obstacles intersect.

The geometric structure of the Voronoi diagram is of a form used for path-planning called a roadmap [22]. Roadmaps are used to plan a path by first finding a path from the start point to access the roadmap, then through the roadmap network, before departing the roadmap to reach the goal point. This describes the key properties of a roadmap, accessibility, connectivity, and departability. Given an arbitrary start point it was shown in O’Dunlaing [26] that there always exists a direct collision-free path onto the Voronoi diagram, guaranteeing accessibility. In addition it has been shown in Choset and Burdick [36] that all points in free-space are within at least one edge of the Voronoi diagram, giving departability provided that the robot can traverse the whole of the diagram. Finally, the Voronoi diagram is connected [37] ensuring a path between the start and goal can be found through the diagram. However, the roadmap structure does not itself contain information concerning the traversal costs of the edges of the diagram since the edges are not straight, and although maximum clearance between obstacles is maintained there are no comparisons made between the relative proximities of alternate routes. The question of traversal costs was solved by Barraquand and Latombe [38] by combining the Voronoi diagram with a separate distance cost potential propagated from the goal point over the same discrete workspace, which was then used to

choose routes through the Voronoi diagram. The method was extended to the three-dimensional Voronoi graph in [39], giving a graph consisting of equidistant faces between obstacle surfaces which can be treated in a similar way to the edges of the Voronoi diagram.

1.2.4 Analytical Potential Fields (Potential Functions)

The concept of path finding using a potential field is based upon being able to define a scalar potential function that represents the obstacles in the configuration-space. The potential field must have a global minimum at the goal point, and areas of high potential representing obstacles, so that a path to the goal may be found by traversing through the potential toward the minimum at the goal avoiding high potential areas. Potential functions are a specific case of a potential field that can be represented by an analytical closed form expression from which scalar potential values may be directly obtained. By comparison a more general potential field would typically require the pre-calculation of some discrete representation of the potential field before values of the potential at an arbitrary point can be obtained.

Potential functions have been investigated previously for applying controller feedback [40] and constraints [41], or direct obstacle avoidance [42], but the earliest application of potential functions for path planning was due to Khatib in 1985 [43] applying potential fields to provide real-time control for robotic arms. In space applications, potential fields have been applied to a range of problems, including spacecraft pointing controls [44] and docking approach controls [45]. A summary of potential field applications to spacecraft guidance and control is given in [46].

An example of a global potential function, in the absence of any obstacles, would be to define the potential ϕ at any point (x, y) , as

$$\text{Eqn 1-1} \quad \phi(x, y) = (x - a)^2 + (y - b)^2$$

This describes a potential field that increases as the square of the distance from the goal point (a, b) . By differentiating the potential function equation, the potential gradient at any point can also be obtained in each axis, as

$$\begin{aligned} \text{Eqn 1-2} \quad \frac{\partial \phi}{\partial x}(x, y) &= 2(x - a) \\ \frac{\partial \phi}{\partial y}(x, y) &= 2(y - b) \end{aligned}$$

Finding a path to the goal is then a simple case of traversing down the potential gradient to reach the minimum potential. Unlike the methods described previously that generate a configuration graph of nodes and edges as a means of finding a collision-free path to the goal and then applying the robot's motion to follow the chosen path, the potential field method provides a continuous method of control across the configuration space, eliminating this intermediate path finding step, and allowing a robot to directly navigate to the goal. Provided the control laws of the robot, or the path planner, are designed to ensure the rate of decent of the path through the potential field remains always negative, then by Lyapunov's theorem [47], the path is guaranteed to converge to the global minimum potential at the goal. Provided there is a single minimum of the potential field, this gives the important result that the method will be able to find a collision-free path to the goal, if one exists.

Obstacles in the potential field are represented by areas of high potential, shown in Figure 1-8, so that the increasing potential gradient approaching the obstacles will force the path planner around them.

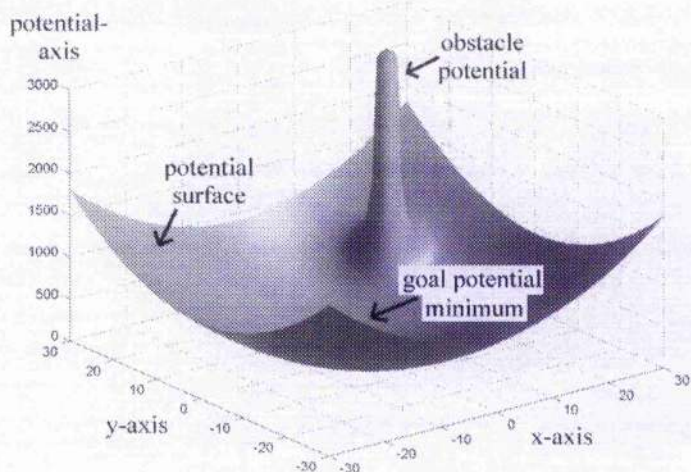


Figure 1-8 The Potential Surface

A good analogy for the two dimensional case is that the potential field represents a height field surface, and to reach the goal the path will travel down the surface to the lowest point. In the absence of any vehicle dynamics the path will travel directly down the steepest direction toward the goal, but with real world dynamics the path will, like the path of a ball rolling down the imaginary slope, follow a route dependent on the applied forces whilst still being guided toward the goal. This illustrates one of the major advantages of the potential field method, its ability to integrate with vehicle dynamics to provide continuous guidance, independent of the exact path followed. For a free-flying vehicle in space this flexibility is

important since it would be costly in terms of propellant to attempt to follow a path planned without respect to the relative orbital dynamics acting on the free-flyer.

The main problem in the potential field method is that if there are any additional minima in the potential field other than the goal, the path finder may get trapped at these points and be unable to find a route to the goal. The aim in defining the potential is then to accurately represent the obstacles present in the potential field, whilst avoiding the creation of any unplanned local minima in the field that might prevent the goal from being reached.

The use of potential fields generated from analytical potential functions has already been demonstrated for path planning and guidance at the ISS by the research performed at the University of Glasgow for the European ATV project [4]. In the ATV software the potential field was created by summing a number of potential functions consisting of a goal potential to guide the path to the target, and individually shaped potential functions to represent each obstacle. The goal potential ϕ_{goal} is described by a quadratic function increasing with distance from the goal point, as given in Eqn 1-1. Each obstacle potential function is then chosen to decrease (or increase) rapidly as the position retreats (or approaches) the obstacle. The global potential function away from any obstacles should then approximate ϕ_{goal} .

A number of different potential function types can be used to approximate different obstacles, but the primary obstacle potential is based on a Gaussian probability distribution. The general form of the Gaussian potential function is given by

$$\text{Eqn 1-3} \quad \phi_{gauss} = C_{gauss} \exp \left[- \sum_{i=1}^n \sum_{j=1}^n \frac{1}{\sigma_{ij}} (x_i - a_i)(x_j - a_j) \right]$$

Where C_{gauss} and σ_{ij} are constants, and x_i and a_i represent the current co-ordinate and obstacle co-ordinate in the i axis respectively. This is the approximate equivalent of a multi-dimensional Gaussian probability distribution with standard deviations σ_{ij} and cross deviations σ_{ij} ($i \neq j$). The distribution of the Gaussian potential function can then be shaped along each axis through the matrix constant σ_{ij} to represent the individual obstacle shape, and the size of the potential is controlled by the constant C_{gauss} . Another alternative to represent obstacles is the Power Law potential function, given by the form

$$\text{Eqn 1-4} \quad \phi_{pow} = \frac{C_{pow}}{\sum_{i=1}^n |x_i - a_i|^N}$$

where C_{pow} is again the obstacle sizing constant, and the constant N is chosen to ensure that the function's influence in the global potential decreases rapidly away from the obstacle. The characteristics of the Gaussian and power law potential functions can be seen by looking at the profile of the combined global potential field in one dimension. Figure 1-9 shows potential fields consisting of a quadratic goal potential function and a range of obstacle potential functions.

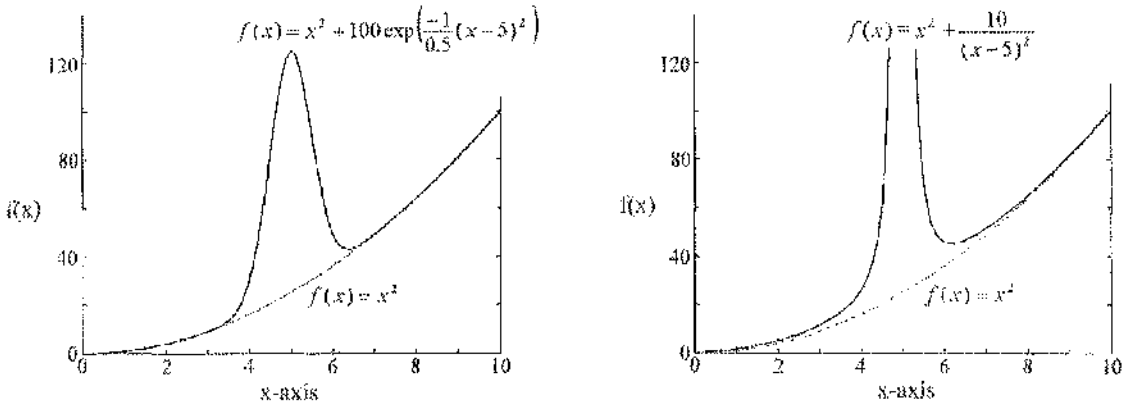


Figure 1-9 Potential Function Combinations

Potential fields generated from analytical potential functions also support the use of alternative potential functions to represent obstacle shapes [48], but the range of geometric shapes is still constrained to a limited number of specific Euclidean shapes such as spheres and stars and combinations of these. Potential functions have also been constructed based on ideal fluid flow [49], utilising the representation of a fluid sink as the attractive goal potential, fluid sources for obstacles with vortex potentials to provide a preferred direction of motion about obstacles.

The use of analytical functions to describe the potential field has many advantages for real-time control in terms of speed of definition and calculation. No pre-calculation is required for path finding beyond specifying the type and size of potential functions used to represent the obstacle configuration. Furthermore, since obstacle positions are represented as variables in their respective potential functions, moving obstacles are inherently supported. Updating the potential field to add newly detected obstacles is also simply achieved by adding additional potential functions. For large numbers of obstacles however, calculation time may become significant in a real-time onboard control system.

The main difficulty with the potential function method is in the formation of local minima in the potential field. From the one dimensional profile shown in Figure 1-9 it can be seen that the combination of a single obstacle potential with the goal quadratic potential forms a saddle point in the global potential field on the far side of the obstacle. In two dimensions

this is not critical since the potential will still decrease about either side of the saddle point, $\frac{\partial\phi}{\partial x} > 0$ but $\frac{\partial\phi}{\partial y} < 0$, so the path finder cannot be trapped. However, if a second obstacle potential is placed beside the first so that their influence on the global potential combines, a stable local minimum area between the two obstacle potentials may be formed, $\frac{\partial\phi}{\partial x} > 0$ and $\frac{\partial\phi}{\partial y} > 0$, as shown in Figure 1-10.

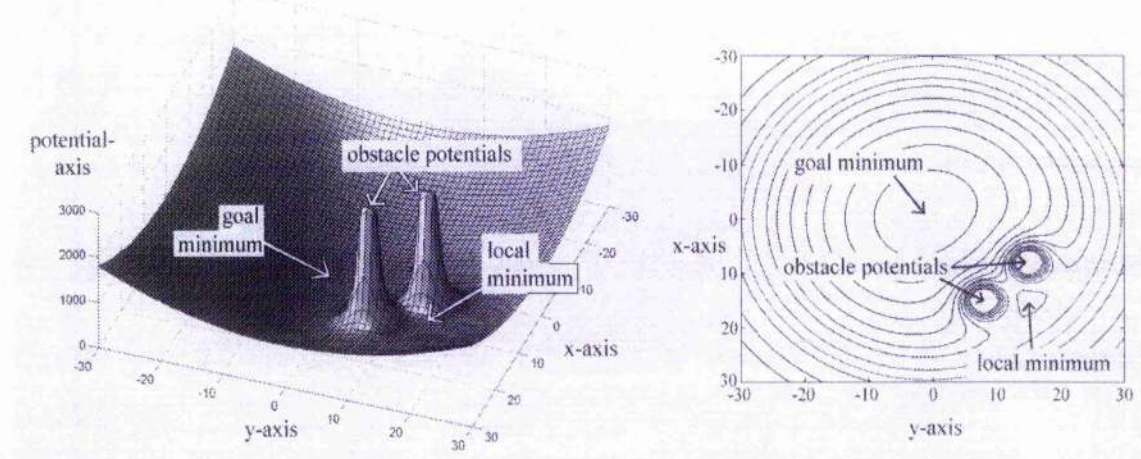


Figure 1-10 Local Minimum Formation

For configurations consisting of well separated obstacles, each represented by an individual potential function, this is not a problem. And, for isolated cases of local minima, techniques have been developed that use random motion to escape from a local minimum area [50], and alternative potential functions have been employed to attempt to avoid the creation of these minima [51][52][53]. However, for complex configurations of obstacles, such as that required to represent the International Space Station, high numbers of local minima become prohibitive to the use of a potential function field. Another factor against the use of potential functions for path finding close to the ISS is that the position of the goal minimum in the global potential field relies on the influence of the obstacle potential functions being negligible at the goal. For the large combination of potentials required to represent the ISS this may not be the case, especially for goal positions relatively close to the space station structure.

1.2.5 Harmonic Potential Fields

The formation of undesirable local minima in many potential functions, which can prevent a path to the goal from being found, has lead to the development of alternative

potential field representations to avoid the formation of such minima. The most popular of these use a harmonic function to generate the potential field and guarantee the absence of local minima. A harmonic function ϕ on a domain $\Omega \subset \mathbb{R}^n$ is a function that satisfies Laplace's equation

$$\text{Eqn 1-5} \quad \nabla^2 \phi = \sum_{i=1}^n \frac{\partial^2 \phi}{\partial x_i^2} = 0$$

The closed domain Ω represents the configuration space of the path planning problem, with the function ϕ used to calculate the potential field. The obstacle and goal points provide boundary conditions for the calculation of the potential field, with obstacle boundaries fixed at high potential values, and a low potential value fixed at the goal. The resulting harmonic potential satisfies the "Maximum Principal" [54] guaranteeing there are no local minima in the function. It is this property that makes harmonic potentials highly attractive and lead to the choice of a Laplace potential function as one of the primary methods for close proximity path planning in this thesis.

The application of harmonic or Laplace potential functions to path planning was introduced by Sato [55], and developed independently by Akishita et al. [56] and Connolly et al. [57]. Akishita et al. presented an analytical potential function based on the hydrodynamic potentials for a pair of moving obstacles in simplistic closed space. Connolly et al. chose to represent the potential field discretely, iteratively applying the Laplace equation over the configuration space to obtain the potential field. This discrete representation of the configuration space has been popular for the calculation of harmonic potential fields [58] [59] thanks to its easy application to arbitrarily complex obstacle configurations and the order that is imposed upon the environment [60]. Typically the potential across a discrete grid is computed by a method called "relaxation" [61] which iteratively calculates the potential at each point as the average of the surrounding potential values, while maintaining the high and low potentials at the boundary and goal points respectively. The calculation of potential fields based on the Laplace equation will be investigated fully in Chapter 5.

Although harmonic potentials are generally pre-calculated based on a specific obstacle configuration space and goal configuration, efforts have also been made to apply discretely calculated harmonic potential fields to environments where the obstacles are either moving or not fully known [62]. In this paper Zelek proposes the application of discrete potential fields to a dynamic environment through the modification (recalculation) of the potential field while combining existing potential values and new results during computation, to guarantee proper control while the new potential field is being calculated.

The link has also been made between the uses of harmonic potentials for path planning and collision probabilities for random walks within the same configuration space [63]. The probabilistic interpretation of harmonic functions was investigated by Doyle and Snell [64] in terms of lattices, but was applied directly by Connolly to discrete grids, who generated potential field values using random walk collision statistics for each node on the grid to demonstrate the equivalence of path planning using collision statistics. This result is important for the application of harmonic functions to path planning for safety critical applications, since it proves that the paths found using these methods will automatically choose a path with the minimum chance of a collision in the event of any uncertainty in the execution of the motion. In practice it ensures that paths generated from a harmonic potential field will provide good clearance away from obstacles boundaries wherever possible, unlike alternative methods that may produce paths that travel close to obstacles.

The first applications of harmonic functions to path planning were based on hydrodynamic theory [65], and this physical representation of the configuration space has been used in a range of subsequent work [66] [67] [68]. However a number of alternative physical representations whose steady state satisfies the Laplace equation have also been used to derive harmonic potential fields. Common alternative representations include molecular diffusion [69] and thermodynamic or annealing solutions [70] [71]. The solution of diffusion and fluid flow problems through direct representation by analogue electrical circuits was developed previously [72], and more recently this has lead to the harmonic potentials represented by electrical fields [73], and the use of inductive circuits to quickly and directly calculate harmonic potential fields [74].

1.2.6 Discrete Solutions

Although potential field methods are often computed over a discrete grid in order to obtain specific solutions to complex potential functions, there are also a wide range of problem solving methods that can be applied directly to this discrete representation of the configuration space. Dijkstra's algorithm has been mentioned previously as a solution to path planning though a graph of nodes, however for a large set of highly interconnected nodes such as a regular grid there are far more efficient methods available. Like Dijkstra's algorithm however all these alternative methods function by calculating across the grid some form of estimate for the distance or cost to transfer from each node to the goal. A path can then be found by stepping to each successive lowest cost node until the goal node is reached. This cost field can be considered similar to the potential field calculated using a harmonic potential function since the results can be used in the same manner to solve the path planning problem.

Dijkstra's algorithm is an example of a depth first search algorithm since it only expands a single node of the graph at a time, moving on to the next best cost node and updating that until all nodes have been calculated. Conversely a breadth first search is performed by starting at a single node, expanding the cost values at each of its surrounding nodes, and then using these nodes to expand the cost values of all of their surrounding nodes, until all nodes have been updated. Both of these blind-search methods are exhaustive techniques however, and while they will provide a path planning solution to reach the goal, in many situations they will expand too many nodes in the process. A solution to the problem of expanding unnecessary nodes is to use some extra information about the configuration space to direct the search in a more efficient manner. One of the most popular methods used in path planning is a directed breadth first algorithm known as A* [75], which has been widely applied to a range of applications from general AI problems [76] to path planning in computer games [77] thanks to its simplicity and ease of application. A* (pronounced "a-star") is a generic method that can be applied to any graph of nodes provided that some heuristic estimate of the remaining cost from a node to the goal node can be given. This gives the cost of any node on the graph by the function

$$\text{Eqn 1-6} \quad f(n) = c(n) + h(n)$$

where $f(n)$ is the cost at node n , and $c(n)$ and $h(n)$ are the cost to reach n and the estimated remaining cost to the goal, respectively. Typically $h(n)$ could be given by the direct distance remaining to the goal, or from a previous investigation. By searching only in the direction of the most promising nodes guided by the cost estimate $h(n)$, the A* path finder is directed towards the goal, as shown in Figure 1-11, rather than spreading across the entire control space as is the case for a wave-front expansion. The efficiency of the search in quickly finding a path to the goal point is dependent on the estimate of the remaining distance to the goal. Provided however that the estimation function $h(n)$ is admissible, that is the estimated distance is never greater than the actual distance to the goal, an optimum path to the goal will always be found.

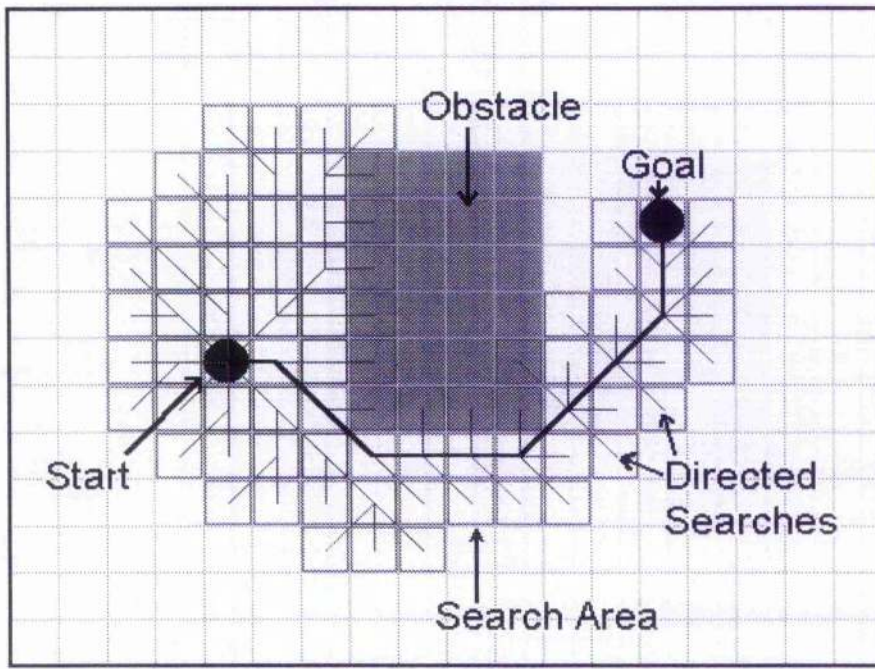


Figure 1-11 The A* Algorithm (adapted from [77])

Although A* methods have proved very popular, a significant amount of research has also performed into improving the exhaustive breadth first method. If it can be computed sufficiently quickly a breadth first search offers a number of advantages over A* because the cost field exists over the entire configuration space rather than the specific area searched. The breadth first search, also known as the wave-front method because of the wave of nodes propagated out from the goal during the search, has been developed in detail by Donald [78] and Dorst and Trovato [79]. Furthermore, the analogy of the propagation of wave-front methods to the extensively optimised flood-fill algorithms utilised in computer graphics was made by Pavlidis [80], which lead to the application of low-level computer rasterizing hardware to directly perform a breadth first search for path planning [81]. An additional solution to the problem of expanding large numbers of nodes is to reduce the total number of nodes used to represent the configuration space by grouping together areas of free-space [82]. This can be achieved for a grid based representation by using a hierarchical data structure, such as a quadtree structure, so that areas of free-space can be represented by a single node [83].

Both A* and wave-front methods have been further enhanced through the use of distance transforms in the formulation of the movement cost between nodes [84] [85]. The standard formulation of these methods does not discriminate between the proximity of free-space nodes of the grid to any obstacle nodes, unlike the Laplace method which ensures safe clearance of obstacles. However this can be provided by incorporating into the cost of

transferring to a node an additional cost based on the nodes proximity to obstacles or some estimate of the collision probability at the node [86] [87].

The final problem for discrete path planning solutions is how to deal with unknown or changing environments. A typical approach to partially unknown environments from other areas of path planning is to treat unexplored regions as obstacles and only enter if goal is there [88] [89], however this severely limits the paths that may be found and precludes finding optimal paths to the goal [90]. Boult presented an updatable A* method [91] which was later extended in [92]. The method maintains an optimal cost map from the goal to all states in the environment, so that when differences between the obstacle environment and then map are discovered, only the affected portion of the cost map needs updated. A new algorithm known as the D* algorithm (from Dynamic A*) [93] has also been developed from the A* algorithm to speed the recalculation of the cost field in a dynamic environment. This technique operates by limiting the required recalculation to the specific areas of the cost field that are affected by the change in obstacle configuration. So for example, if a new obstacle is introduced into the control volume, then only those nodes that are hidden, or shadowed, from the goal by the new obstacle need be recalculated, as shown in Figure 1-12.

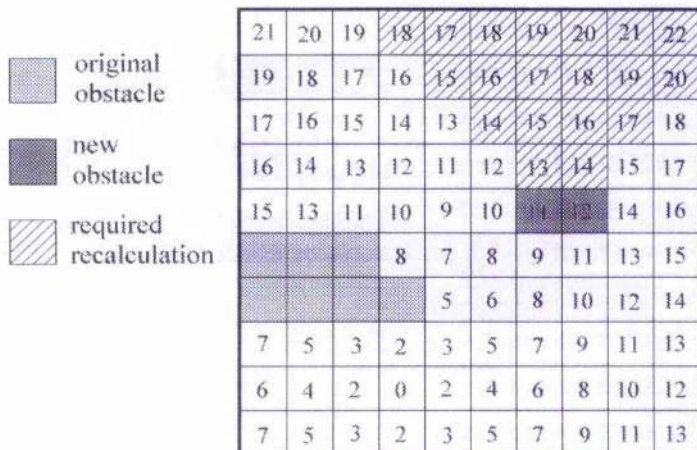


Figure 1-12 The D* Algorithm

Alternately, an adaptable quadtree representation of the grid and distance cost transforms were combined by Zelinsky [94] to provide an efficient discrete grid which can be easily updated when new obstacles are encountered, but avoids unnecessary nodes in the grid to speed up the calculation of the cost field.

1.2.7 Integrating Motion Constraints

Once a method has been found for planning a path to reach the goal configuration, it then remains to plan the actual motion of the robot to follow this path. In most cases a number of motion constraints will have already been applied in the generation of the configuration space, for example the range of motion of each joint in a robotic manipulator. Some additional constraints, such as the cost of traversing different terrain for a ground based vehicle, may also be integrated into the original path planning problem [95] [96] [97]. These papers also distinguish between the incline and slope direction of the terrain, allowing uphill and downhill sections to be assigned different costs to take account of the acceleration and braking capabilities of the vehicle. However other factors such as acceleration restrictions for a free-flying vehicle, or turning circle constraints for a wheeled vehicle, will limit the paths that may be followed.

For global search methods such as the V-graph that produce a graph of nodes for path planning, the paths produced only define direct motion from point to point through the graph, and often there will be sharp changes in direction between segments of the path. While this type of motion may be possible for a highly manoeuvrable vehicle with precise navigation, in most cases such a path could only be followed approximately. Since the configuration space graph itself does not contain any information concerning collision probabilities outside of the nodes and edges of the graph, the original method must therefore be formulated to include a defined path following error, and the motion used to follow the path constrained to within this error margin from the prescribed path.

Conversely analytical potential functions naturally provide path planning information over the whole configuration space, with the result that they are ideally suited to motion planning since the path can be allowed to follow its natural motion constraints while path planning control is continuously applied using the potential values [46]. The continuous nature of this type of path planning is also highly suited to on-line path finding and guidance control. The robot can be allowed to traverse the configuration space, with the potential function used to supply direct control inputs based on the robot's current configuration to guide the robot along a path to the goal, automatically incorporating any motion errors since the robot's true position rather than pre-planned position is used throughout, ensuring a collision-free path. Nevertheless, safe collision avoidance still is dependent on the ability of the robot to satisfy the requested motion from the potential function path planner, so the stability of the system is critical. Typically this can be ensured by imposing strict limits on the velocity of the robot, and shaping the magnitude of the control inputs supplied from the potential function [98].

Like graph based methods, discrete potential field or grid based methods (such as A*) also often plan paths from point to point through the configuration space. Depending on the setup of the grid this can often produce undesirable path characteristics since the route can only follow axis aligned or diagonal directions. An attempt has been made to overcome this limitation with applications to free-flying space robots through randomisation of the grid node placements with impressive results [99], however the method requires a high resolution grid which limits its usefulness. Unlike generic graph results however, grid based methods do provide additional path planning information away from the primary path thanks to the potential or cost data stored in the surrounding nodes. This can be used by interpolating the data between nodes to obtain a continuous potential or cost field, which can be used in a similar fashion to analytical potential functions to provide integrated path planning and motion planning, with applicability to on-line path planning [59]. This method of interpolating a discrete potential or cost field to provide continuous path planning and guidance will be developed in Chapter 6 for use in this thesis for close proximity path planning at the International Space Station.

1.3 Thesis Goals

The primary goal of this thesis is to develop the techniques and tools that will be required to manoeuvre a free-flying inspection vehicle safely around the exterior of the ISS. The development of these techniques will focus specifically on the ISS Inspector vehicle, and the design of the associated ISS Inspector project systems. As demonstrated earlier in this chapter, there is a pressing need for such a free-flying vehicle to reduce the need for astronaut EVA and to support external missions. However, many of the problems involved in operating a free-flying vehicle based ISS have yet to be fully investigated, specifically the problem of safety constrained path planning for a vehicle moving in close proximity to the structure of the space station.

1.3.1 Required Manoeuvring Methods

The types of manoeuvres required for the Inspector free-flyer are determined by the ISS-Inspector mission profile, which calls for the vehicle to transfer between its docking port and various observation positions around the ISS. The manoeuvring strategies developed here to achieve this will be broken up into two distinct phases; long range transfers to and from docking and between observation points on opposite sides of the ISS, and short range local manoeuvring between adjacent pairs of observation points. The main priority of both of

these phases must be to preserve the safety of the space station at all times. However, the cost of each transfer in terms of duration and propellant usage must also be optimised in order to achieve mission goals within the finite capabilities of the free-flying vehicle.

Constraints on the long range manoeuvring strategy are that it should provide the best available long term passive safety, to ensure the safety of the ISS in the event of any malfunction, but still be able to approach the ISS structure for docking and close observation phases of the mission. To achieve this, a strategy using an Ellipse of Safety (EOS) transfers will be exclusively developed in this thesis for long range manoeuvres. The EOS is concept that was used in the X-Mir Inspector mission to provide a safe trajectory to fly-around the Mir space station, but has not to the authors knowledge been utilised for point to point transfers. Being a pre planned sequence of manoeuvres it should be possible to demonstrate, through an investigation of each element of the transfer, that the complete manoeuvre will be entirely passively safe.

The second stage of ISS Inspector manoeuvring consists of path planning and manoeuvring between observation points in close proximity to the ISS structure. Path planning methods using both discrete Laplace potential fields and discrete wave-front cost fields will be adapted and applied to the problem of path planning in a relative orbital co-ordinate frame attached to the ISS. The dynamics of the resulting relative motion problem in this rotating co-ordinate frame will be investigated, and the results used to develop a gradient impulse manoeuvring method combined with a pre-calculated potential or cost field to plan the motion required to reach each observation point. The focus during this phase will be placed upon the passive safety of the collision avoidance strategy and the minimisation of potential collision impact velocities.

To simplify the path planning problem a number of approximations and assumptions will be made to the dynamic model of the Inspector vehicle. First the vehicle model will be constrained to consider only translational degrees of freedom. This is a valid assumption for collision-free path planning since the ISS Inspector vehicle itself is a relatively compact shape that can be easily approximated by a sphere, and is capable of providing thruster control in any direction independent of orientation. From a control point of view, Inspector attitude control using reaction wheels will be relatively decoupled from any translational control actions until the reaction wheels become saturated, which is unlikely given the relatively short mission duration unless some significant external torque is applied to the Inspector vehicle. In addition, all Inspector manoeuvres will take place with a relatively long transfer time between each thruster action, allowing an extended period of free-drifting for attitude control to take place. The low relative magnitude of the velocity changes required compared available

thrust also allows the thrusters actuations to be approximated by impulse manoeuvres - velocity changes of negligible duration at a point [100]. Finally it will be assumed for development that accurate relative positional and velocity information is available, and that thruster actuations are also accurate. The effects of errors in each of these systems must also be considered and investigated, however, to verify the integrity of any developed methods.

1.3.2 Thesis Contributions

The contributions made in the development of these tools and methods can be described in a number of areas, primarily concerned with the advancement of passively safe manoeuvring techniques of a free-flying robot close to the ISS. The primary contributions can be listed as;

- The Ellipse of Safety point to point transfer method, developed from a simple fly-around trajectory into a fully passively safe manoeuvring method for point to point transfers.
- The first application of both harmonic potential fields and a discrete cost field to path planning for a free-flying space robot. The suitability of these functions for path planning in close proximity to a complex obstacle structure such as the ISS is also demonstrated in the results.
- The development of a new velocity selection manoeuvring method, to use potential field information to generate paths while observing dynamic constraints to minimise impact velocities in case of failure, with the aim of providing enhanced passive safety for the ISS.
- The development of an interactive graphical software interface to enhance mission planning, and enforce safety constraints such as passive station keeping safety using visual indicators.
- The use of prior information about obstacle structure (ISS configuration) at a high level to perform pre-selection of optimal manoeuvre types, and automatic scheduling of transfers to observation points using this information.

Combined with the predefined ISS-Inspector manoeuvres such as forced motion along the R-bar and collision avoidance manoeuvres, an overall strategy providing highly safe transfers to and from docking and to any point around the exterior of the ISS is provided.

1.3.3 Software Tool Overview

In addition to the development of the individual manoeuvres required for the ISS Inspector, the objective is to make use of these manoeuvres in a cohesive manner for overall

mission planning. By combining the selection of suitable observation co-ordinates, the optimisation of the choice and sequence of transfers between docking and the chosen observation points, and the visual analysis of the final mission plan, the rapid development of ISS Inspector missions will be possible. An integrated tool will therefore be developed for rapid mission prototyping and planning. This tool should be able to demonstrate the operational use of the developed manoeuvring techniques, as well as investigating feasibility of the ISS Inspector mission concept. An overall schematic of the mission planning software is given in Figure 1-13.

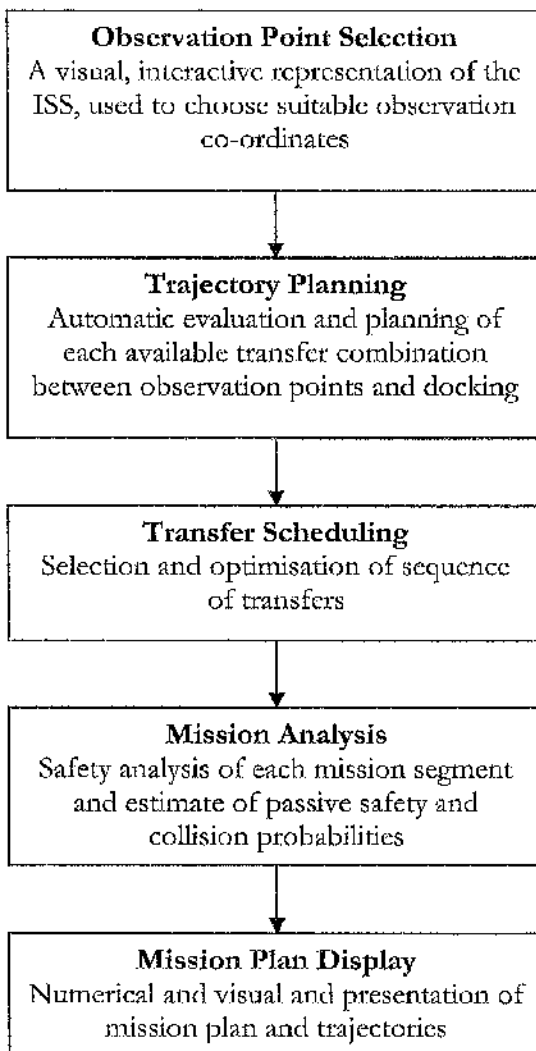


Figure 1-13 Mission Planning Software Schematic

One of the key requirements is that the tools developed for mission planning must be portable to the computing facilities available onboard the ISS, so that missions can be investigated by astronauts on-orbit as well as mission planners on the ground. In addition, if rapid inspection of the ISS is to be successful the problem of mission specification, the

selection of suitable inspection positions within operational as well as visual constraints, must be addressed. Finally the tool must be able to provide results of the planned mission, both quantitatively and visually, and with a brief analysis of the passive safety of each element of the mission.

CHAPTER 2: ORBITAL DYNAMICS

2.1 Planetary and Satellite Motion

To plan motion for a free-flying vehicle at the International Space Station we must first consider the motion of the ISS in its orbit about the earth. The ISS flies in a circular orbit approximately 400km above the surface of the earth, and rotates 360 deg throughout each orbit to maintain it's orientation with respect to the earth below. Over the course of its life the station's orbital radius will vary as the orbit decays under the influence of atmospheric drag and is periodically re-boosted. For the duration of an individual free-flyer mission however, it is acceptable to approximate the orbit radius as constant. To perform ISS-Inspector path planning relative to the ISS we therefore wish to refer to the Inspector position and motion in a co-ordinate system fixed relative to the ISS, as shown below in Figure 2-1.

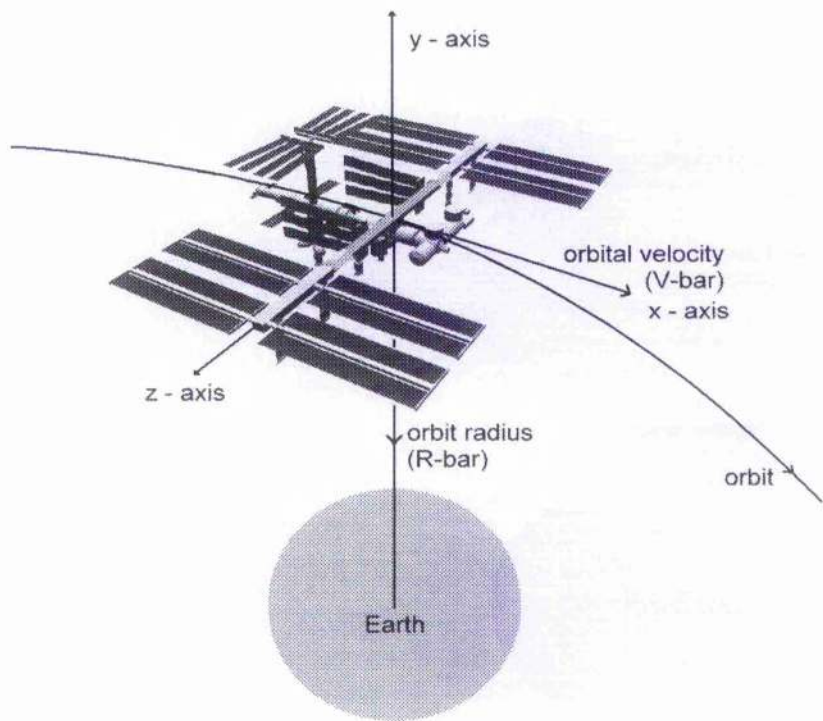


Figure 2-1 ISS Fixed Co-ordinate System

The local co-ordinate system to be used has its origin fixed at the ISS co-ordinate reference point, located at the ISS centre of mass near the centre of the main truss structure. The axis system is then orientated so that the x-axis is aligned along the positive orbital velocity vector (referred to as the V-bar), the y-axis is aligned along the outward radial

direction (opposite to the R-bar), and the z-axis completes the triad. This axis orientation is used since this is the co-ordinate system adopted by EADS Astrium for the Inspector programme to comply with their Russian partners RSC Energia in the project. It should be noted however that the standard co-ordinate system used by NASA for the ISS has the z-axis aligned along the inward radial direction (negative y-axis in Figure 2-1), and the y-axis replacing the z-axis from the Russian configuration.

Before we investigate the relative motion of a free-flying vehicle in this ISS fixed coordinate system it is useful to first consider the relative motion of the two bodies' orbits about the earth. The geometry of an elliptical orbit about the earth can be described can be described by the mathematics of conical sections. The ellipse is one form of conic section, along with the parabola and hyperbola, which though also applicable to interplanetary spacecraft trajectories are not relevant to this investigation of orbital dynamics. The premise of conic sections is that the shape of any ellipse may be found by taking a section through a 3-dimensional cone [101]. One property of these conic sections is that they have two foci, which can be used to generate the ellipse using a line segment of length $2a$ attached to each focus. This is shown by the two lines $2a-p$ and p in Figure 1-2, with the Sun or planetary body located at one of the foci.

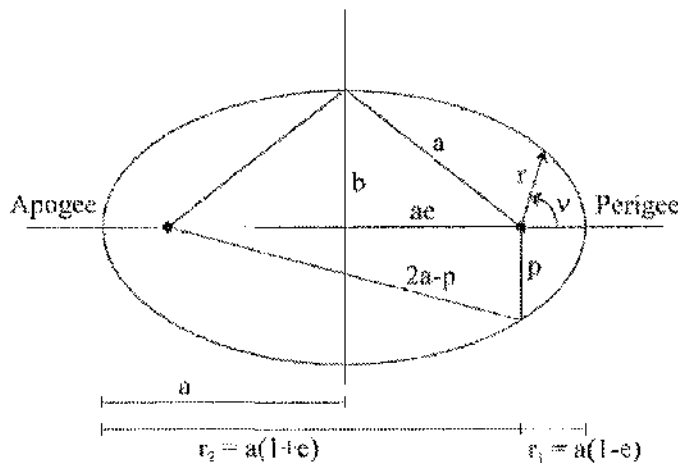


Figure 2-2 Orbital Ellipse geometry

Any ellipse may be completely described by two parameters, the semi-major axis a and the ellipse eccentricity e . These can be calculated from the radius of the orbit at the furthest and closest points on the ellipse to the central body, the apogee and perigee.

$$\text{Eqn 2-1} \quad a = \frac{1}{2}(r_1 + r_2)$$

$$\text{Eqn 2-2} \quad e = \frac{r_2 - r_1}{r_2 + r_1}$$

In addition the speed at any point on the orbit can be determined by

$$\text{Eqn 2-3} \quad V = \sqrt{\mu \left(\frac{2}{r} - \frac{1}{a} \right)}$$

Or for a circular orbit where $r = a$, the speed reduces to

$$\text{Eqn 2-4} \quad V_{\text{circular}} = \sqrt{\frac{\mu}{r}}$$

Kepler's third law states that the radius vector between the two bodies sweeps an area at a constant rate dA/dt . This can be calculated from the angular momentum of the orbit as $dA/dt = H/2$, with the angular momentum (per unit mass) H equal to the vector product of the radius and velocity vectors at any instant. The ellipse orbital period can then be calculated by dividing the ellipse area, given by $A = \pi ab$, by dA/dt . Using the equation for the angular momentum

$$\text{Eqn 2-5} \quad H = \sqrt{\mu a (1 - e^2)}$$

gives the orbital period as

$$\text{Eqn 2-6} \quad T = \frac{2\pi a^2 \sqrt{1 - e^2}}{\sqrt{\mu a (1 - e^2)}} = \frac{2\pi}{\sqrt{\mu}} a^{3/2}$$

The time taken for a complete orbit is dependent, therefore only on the semi-major axis of the ellipse, and notably, not on the eccentricity. If the free-flyer is on a circular orbit of a different radius to the ISS, it will have a different orbital period from the station and will either drift ahead or behind of the station. However, an elliptical orbit with a semi-major axis size of a will have the same orbital period as a circular orbit of radius a . This allows a vehicle moving relative to a target vehicle in a circular orbit to use elliptical orbits to move around the target vehicle, without continually moving away from the target because of a difference in orbital periods. Motion on an elliptical orbit will cause a periodic relative motion between the free-flyer and the ISS in its fixed circular orbit, that will drift with each orbit if the orbit periods differ. This drifting elliptical motion can be seen in Figure 2-3, which shows the relative motion between a circular orbit and an elliptical orbit with a longer orbital period. If the orbit periods were the same, the relative motion would itself describe an ellipse about the centre of the ISS reference frame.

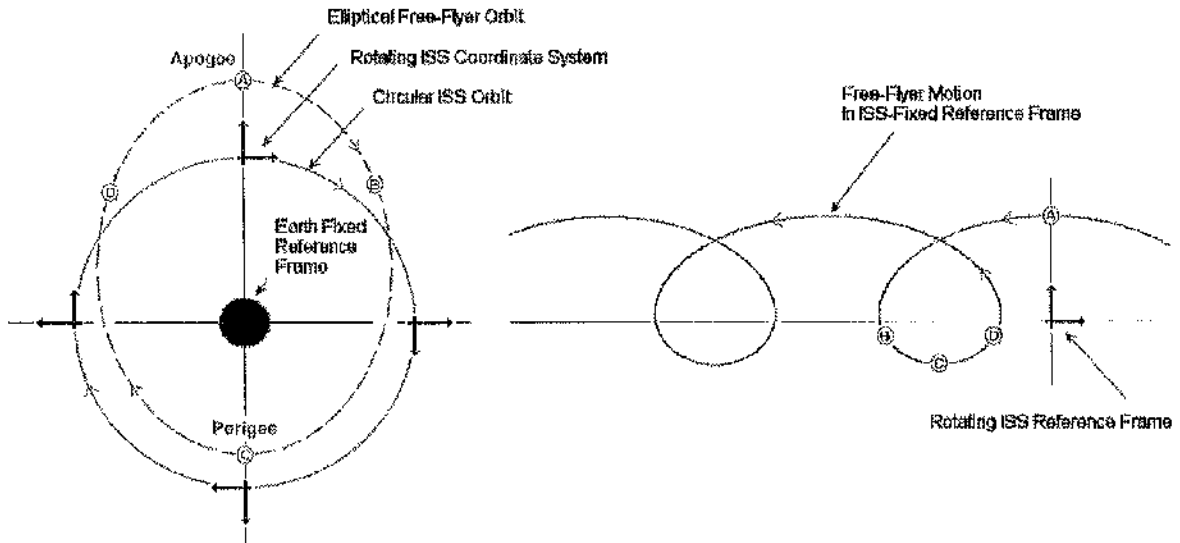


Figure 2-3 Relative Motion between Circular and Elliptic Orbits

The equations of motion of a free-flying vehicle moving relative to another vehicle in orbit about a planetary body are given by a set of non-linear equations [102] that can only be solved for the free-flyer motion using numerical methods. They cannot be easily manipulated further to derive equations to predict and plan trajectories in the orbital co-ordinate frame. However these equations were linearised by Clohessy and Wiltshire [103] by making the assumptions that the origin of the co-ordinate frame is on a circular orbit, and that the positional offset of the free-flying vehicle in this co-ordinate frame is small relative to the frame's orbital radius. The derivation of the full equations of motion and their linearisation is provided in Appendix III, to give

$$\begin{aligned}
 \ddot{x} &= -2\omega\dot{y} + f_x \\
 \text{Eqn 2-7} \quad \ddot{y} &= 2\omega\dot{x} + 3\omega^2 y + f_y \\
 \ddot{z} &= -\omega^2 z + f_z
 \end{aligned}$$

These equations are known as the Clohessy Wiltshire (CW) Equations, regardless of the frame of reference in which they have been obtained. It can be seen that the two equations describing the in plane motion (x y plane) of the free-flyer are coupled together, while the out of plane motion (z -axis) is completely separate.

The CW equations can now be solved by integration [104], given some initial position (x_0, y_0, z_0) and velocity components $(\dot{x}_0, \dot{y}_0, \dot{z}_0)$, for the free-flyer position at time t

$$x(t) = x_0 - 6(\omega t - \sin \omega t)y_0 + \left[\frac{4}{\omega} \sin \omega t - 3t \right] \dot{x}_0 - \frac{2}{\omega} (1 - \cos \omega t) \dot{y}_0$$

Eqn 2-8

$$+ \left[\frac{4}{\omega^2} (1 - \cos \omega t) - \frac{3}{2} t^2 \right] f_x - \left[\frac{2}{\omega} t - \frac{2}{\omega^2} \sin \omega t \right] f_y$$

$$y(t) = (4 - 3 \cos \omega t)y_0 - \frac{2}{\omega} (\cos \omega t - 1)\dot{x}_0 + \frac{1}{\omega} (\sin \omega t)\dot{y}_0$$

Eqn 2-9

$$- \left[\frac{2}{\omega^2} \sin \omega t - \frac{2}{\omega} t \right] f_x + \frac{1}{\omega^2} (1 - \cos \omega t) f_y$$

$$z(t) = z_0 \cos \omega t + \frac{\dot{z}_0}{\omega} \sin \omega t + \frac{1}{\omega^2} (1 - \cos \omega t) f_z$$

Eqn 2-10

and for the free-flyer velocity at time t

$$\dot{x}(t) = 6\omega (\cos \omega t - 1)y_0 + (4 \cos \omega t - 3)\dot{x}_0 - 2 \sin \omega t \dot{y}_0$$

Eqn 2-11

$$+ \left(\frac{4}{\omega} \sin \omega t - 3t \right) f_x - \frac{2}{\omega} (1 - \cos \omega t) f_z$$

$$\dot{y}(t) = 3\omega \sin \omega t y_0 + 2 \sin \omega t \dot{x}_0 + \cos \omega t \dot{y}_0$$

Eqn 2-12

$$- \frac{2}{\omega} (\cos \omega t - 1) f_x + \frac{1}{\omega} \sin \omega t f_y$$

$$\dot{z}(t) = -\omega \sin \omega t z_0 + \cos \omega t \dot{z}_0 + \frac{1}{\omega} \sin \omega t f_z$$

Eqn 2-13

These equations illustrate the somewhat counter-intuitive nature of the free-flyer motion in this reference frame. For example, Eqn 2-11 demonstrates that the free-flyer velocity in the x direction, whilst initially dependent on \dot{x}_0 , quickly becomes influenced to a great extent by the initial velocity in the y direction as well as the initial y offset from the V-bar ($y = 0$). Therefore, no initial velocity in the x direction is required to produce motion in the x direction at a later time. In fact, to travel to a point along the positive x-axis it may even be necessary to make an initial ΔV in the negative x direction. The relationship between the direction of the initial velocity and the shape of the resulting motion does, however, follow a pattern since the in plane relative motion will always be part of an elliptical path.

As expected, the initial x co-ordinate x_0 has no effect on velocity since the motion is independent of where on the circular ISS orbit it takes place, the resulting trajectory is simply shifted along the x-axis. This has the important result that the free-flyer can remain stationary with respect to the ISS, known as station keeping, at any point on the V-bar without requiring any propellant to maintain its position. Any other position relative to the ISS however, will

need continuous thruster activity to counteract the accelerations acting on it. This is shown in the velocity equations as the y_0 and z_0 contributions to the velocity components. The effects of these accelerations can be seen in Figure 2-4, showing the path taken by the free-flyer when allowed to drift from an initial stationary position. The resulting path drifts away from the origin on a looping path, in a direction dependent on the initial y co-ordinate.

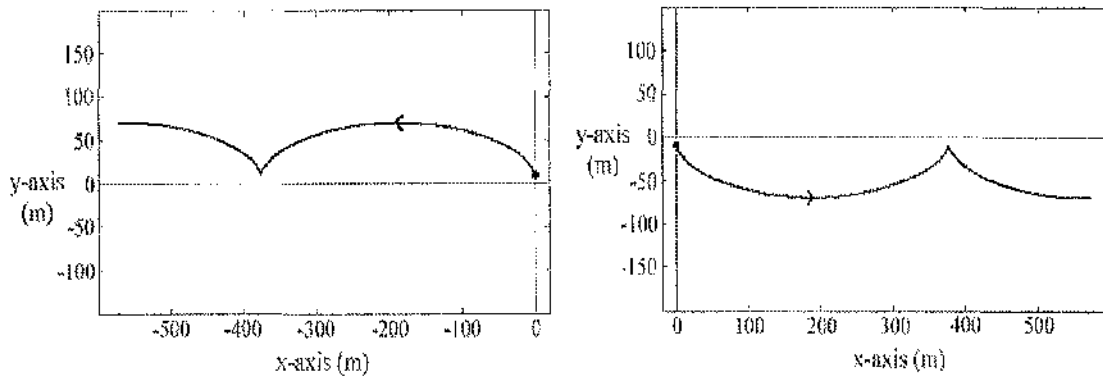


Figure 2-4 Free-Drift from a Stationary Position

If the initial velocity is non-zero, the free-flyer may enter an elliptical path at a different point on the ellipse and can control the size and shape of the final ellipse. Figure 2-5 shows a typical example, calculated using the CW equations over one complete ISS orbit.

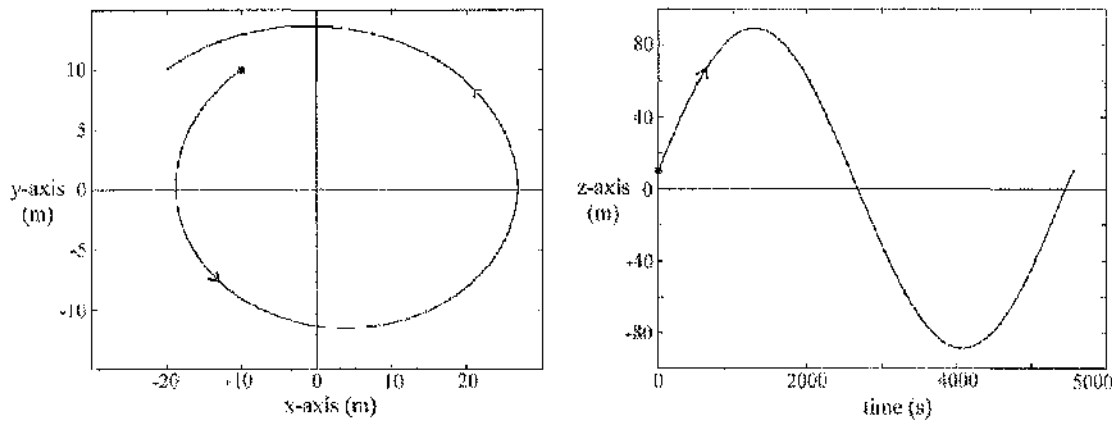


Figure 2-5 An Example CW Trajectory

In this example, the free-flyer has started from the co-ordinates $(-10.0, 10.0, 10.0)$ m with a velocity of $(0.02, -0.01, 0.10)$ m s^{-1} . This resulted in an in-plane ellipse, drifting in the negative x direction by approximately 10 metres per orbit, and a periodic out-of-plane motion which returned the free-flyer to its initial z co-ordinate after one orbit.

In general, all paths in the rotating frame of reference used to calculate relative motion describe an elliptical path, the centre of which may be drifting parallel to the x axis.

2.2 Two-Impulse Manoeuvres

In addition to using the CW equations to predict the motion of the free-flyer, there is a requirement to calculate the change of velocity and hence thruster activity required for the free-flyer to follow a desired path and reach its goal position. Eqn 2-8, Eqn 2-9, and Eqn 2-10 above, determine the free-flyer position after time t given an initial position and velocity. These equations can be re-arranged to give the initial velocity required to reach a target position after time $t = \tau$, from a given initial position. Using these equations it is then possible to plan a manoeuvre to move from one position to new target position, and calculate the velocities required to accomplish this.

Substituting for $t = \tau$, and introducing F_1 and F_2 to simplify the result

$$\begin{aligned} F_1 &= 3\omega\tau \sin \omega\tau + 8(\cos \omega\tau - 1) \\ \text{Eqn 2-14} \quad F_2 &= (y_t - y_0)/(\cos \omega\tau - 1) \end{aligned}$$

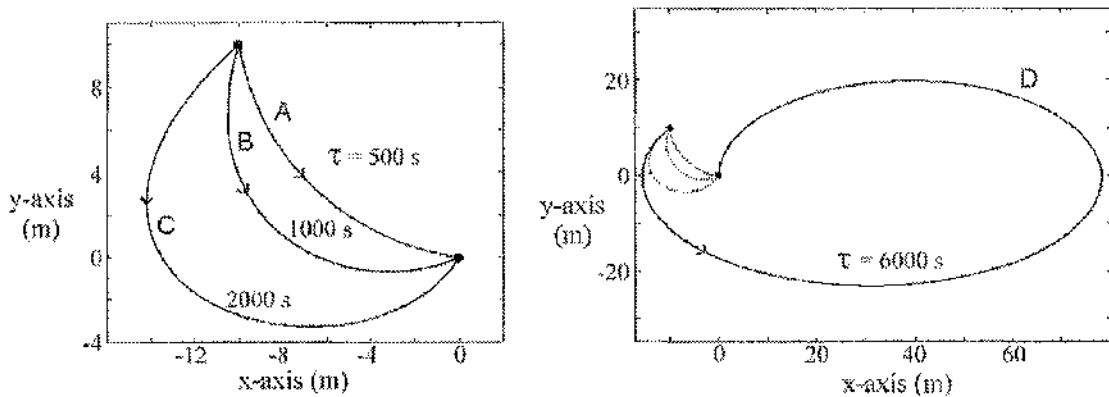
it can be shown that

$$\begin{aligned} \dot{y}_{0_{\text{req}}} &= -\frac{\omega}{F_1}(\cos \omega\tau - 1)[2(x_t - x_0) + 4F_2 \sin \omega\tau - 3\omega\tau(F_2 - y_0)] \\ \text{Eqn 2-15} \quad \dot{x}_{0_{\text{req}}} &= -\frac{\omega}{2} \left[3y_0 + F_2 - \frac{\dot{y}_{0_{\text{req}}}}{\omega(\cos \omega\tau - 1)} \sin \omega\tau \right] \\ \dot{z}_{0_{\text{req}}} &= \frac{\omega}{\sin \omega\tau}(z_t - z_0 \cos \omega\tau) \end{aligned}$$

which gives the initial change in velocity ΔV_1 . For a given a starting position and target coordinates, the required initial velocity and the path followed is therefore depended solely on the time taken to reach the target τ . Furthermore it can be shown that as the transfer time $\tau \rightarrow 0$ then each equation is approximated by the distance to the target along that axis, divided by the transfer time τ , as expected. The final change in velocity required to reach the final state ΔV_2 , can also be calculated by substituting for the transfer time and initial velocity in Eqn 2-11 - Eqn 2-13, to give the total required velocity change ΔV_{total} .

2.2.1 The Effect of Transfer Time τ

The transfer time used to plan a manoeuvre between two points has a dramatic effect both on the propellant requirements for the manoeuvre and on the path the free-flyer will follow to reach its target. The effect of increasing τ can be seen in Figure 2-6, which details the trajectory between two sets of co-ordinates for a range of transfer times.



Path	τ (sec)	\dot{x}_0 (ms^{-1})	\dot{y}_0 (ms^{-1})	ΔV_1 (ms^{-1})	ΔV_2 (ms^{-1})	ΔV_{total} (ms^{-1})
A	500	0.0059	-0.0334	0.0349	0.0288	0.0637
B	1000	-0.0074	-0.0247	0.0257	0.0167	0.0424
C	2000	-0.0168	-0.0154	0.0227	0.0116	0.0343
D	6000	-0.0235	-0.0204	0.0311	0.0242	0.0553

Figure 2-6 Increasing Transfer Time Comparison

As the transfer time increases, the path taken to the target deviates increasingly from the direct line to the target. All the trajectories shown represent an ellipse segment, the size and eccentricity of which is dependent on the target co-ordinates, and the fraction of an orbit over which the manoeuvre takes place. For the case shown in Figure 2-6(D), τ exceeds the ISS orbital period of 5560 seconds, and the free-flyer path must complete a full ellipse before arriving at its target. This pattern continues if the transfer time is extended past two orbits, with the resultant path executing an additional ellipse for each additional orbit on its path to the target.

The cost of each two impulse transfer in terms of propellant can be determined by the total change in velocity or ΔV required for the manoeuvre. A two impulse transfer consists of two parts, the initial velocity change ΔV_1 to start the free-flyer on the desired trajectory, and the final velocity change ΔV_2 to bring the free-flyer to rest at its goal. In the first three examples shown ΔV_1 , ΔV_2 , and ΔV_{total} , decrease with increasing transfer times, although this

trend does not continue as Figure 2-6 demonstrates. Also, a decrease in the initial impulse ΔV_1 may not necessarily result in a corresponding reduction in ΔV_2 since the magnitude of the second impulse is simply dependent on the free-flyer velocity at the target, which will vary as the free-flyer travels around its elliptical path. Looking at the individual component velocities in the x and y axes, it can be seen that the direction of the initial applied ΔV also changes dramatically as the transfer time varies. In the example transfer shown, the required x velocity component is initially positive moving the free-flyer in the direction of the target for $\tau = 500$ s, but changes as the transfer time increases so that for $\tau = 2000$ s the initial x velocity is actually directing the free-flyer away from the target.

2.2.2 Optimisation of Two-Impulse Trajectories

To choose a transfer time for any specific manoeuvre, it may be desirable to optimise τ with respect to some cost function for the manoeuvre [105] [106]. The most obvious cost for a trajectory is the propellant required to perform the manoeuvre, which is proportional to the ΔV for the two impulse transfer, and varies with τ . For each manoeuvre there will be a transfer time which requires the minimum possible ΔV . Figure 2-7 illustrates the variation of ΔV against τ for the manoeuvre from $(-10, 10)$ to $(0, 0)$ described in Figure 2-6.

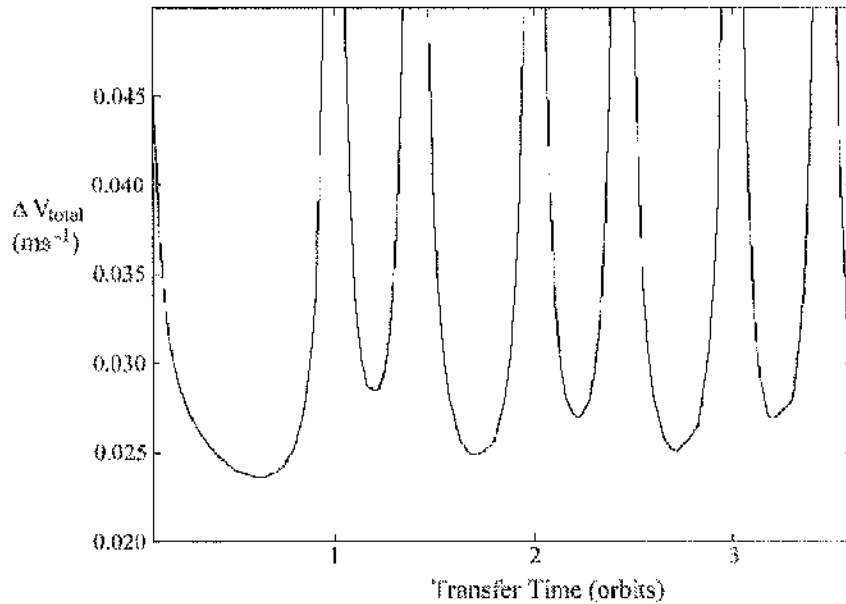
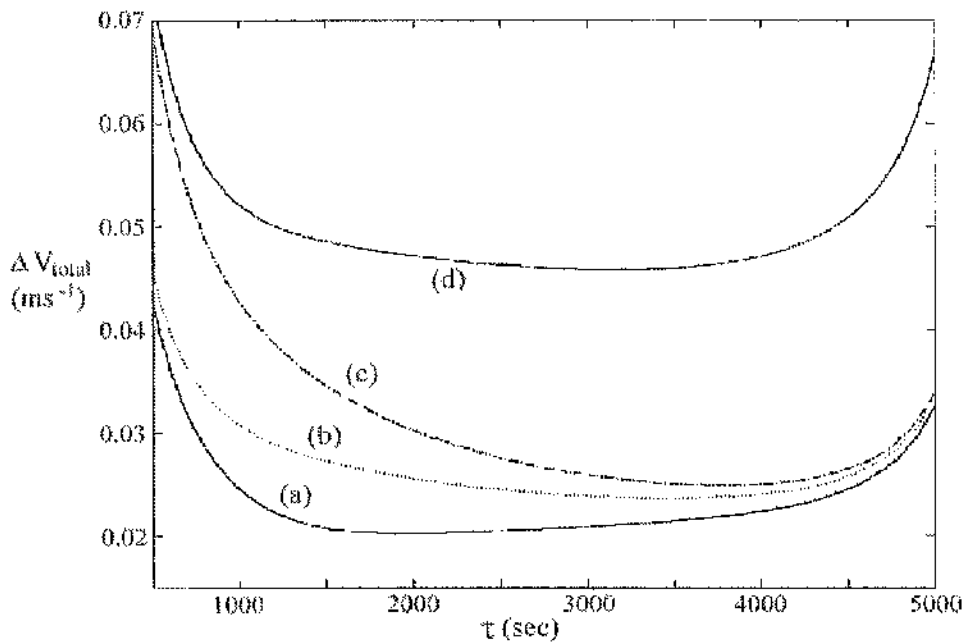


Figure 2-7 ΔV Required vs Transfer Time τ

The transfer times shown range from 500 to 20,000 s, encapsulating nearly four complete orbits of the reference frame. It can be seen that the cost varies periodically, with one cycle and hence one minimum in the first orbit, and one minimum every half orbit from there on.

It can also be seen that in this case the minimum of the first cycle appears to be the global minimum for the whole function. The only exception to this cycle of minima in the cost function comes from transfers between two sets of co-ordinates which lie at the same orbit radius, i.e. the same y co-ordinate. In this case a drifting ellipse is able to reach the target point relatively efficiently in exactly one orbital period, if the drift of the ellipse in a single orbit is equal to the distance to the target point. For transfers between differing orbit radii, a transfer time equal to one orbit is not possible, since the orbital dynamics determine that any elliptical path will always return to the same orbit radius after each orbital period. This can be demonstrated using Eqn 2-14. If the transfer time τ is equal to the orbital period of the reference frame, then the term $\omega\tau$ becomes 2π . The term P_2 therefore tends towards infinity, except in the case of $y_t = y_0$ where it equals zero.

Nevertheless, it is reasonable to assume that in general the optimum transfer time for a two impulse transfer lies within one orbit period. The distribution of the ΔV over this period is variable for different combinations of start and goal co-ordinates. This is illustrated in Figure 2-8, showing ΔV as a function of transfer time for a range of start co-ordinates to reach a constant target point.



Line	(a)	(b)	(c)	(d)
Start Co-ordinates	(-10,10)	(10,10)	(-20,10)	(-10,20)
Goal Co-ordinates	(0,0)	(0,0)	(0,0)	(0,0)

Figure 2-8 ΔV Distribution for Varying Start Co-ordinates

An additional factor to the overall cost function is the cost of the time taken for each manoeuvre. Time constraints are an important factor during both crewed and automated missions, and a wide range of factors will determine the cost of transfer time, including:

- Crew time for tele-operated free-flyers controlled from the ISS.
- Astronaut movements for EVA support missions.
- Crew time for automated free-flyer supervision.
- Time windows for specific lighting conditions.

Including the cost of time, a linear example of a cost function for a two impulse transfer can be given by

$$\text{Eqn 2-16} \quad \text{Cost}(\tau) = \Delta V_{\text{total}} + k_t \tau$$

The choice of weighting of the time constant k_t , which represents the relative cost of the transfer time to the ΔV or propellant requirement, is important in influencing the optimal transfer time as can be seen in Figure 2-9.

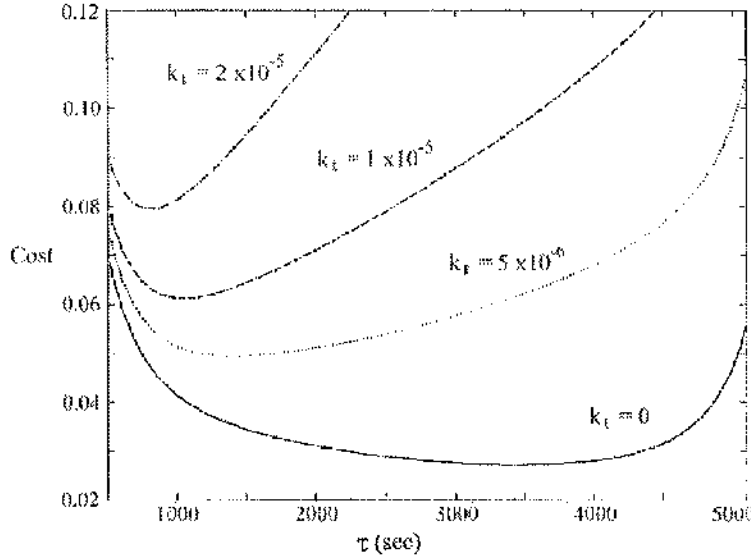


Figure 2-9 Transfer Cost for Varying Time Cost Weighting

Increasing the time cost has the effect of displacing the total cost distribution towards lower transfer times, resulting in faster optimal solutions. This allows for a certain amount of flexibility for mission planning in the case of emergencies where time is critical, or for cases where time is limited by operational constraints. For normal missions though, despite the

high cost of astronaut time, the even higher propellant costs dictate that the total cost is primarily driven by the ΔV requirement, and savings in transfer time have only a small impact on the final cost of a manoeuvre. This is even more important for automated free-flyers, where astronaut demands are reduced and lower ΔV requirements lead to enhanced mission capabilities and mission durations.

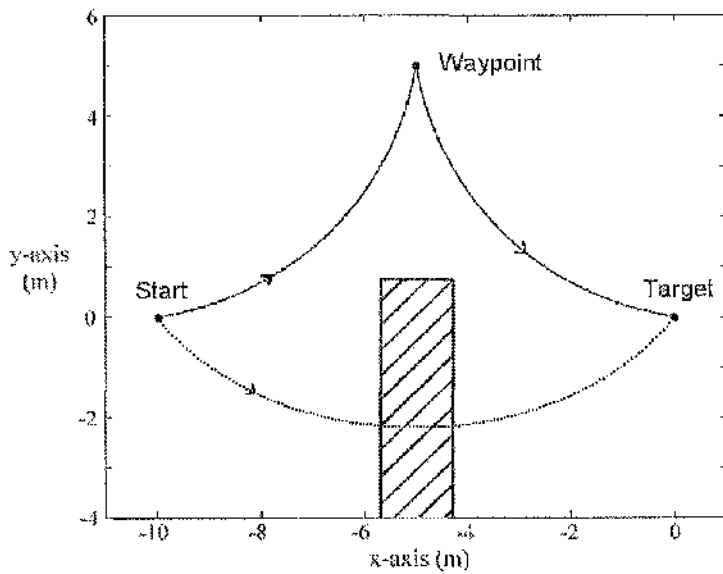
2.3 Multi-Waypoint Manoeuvres

There are, for manoeuvres in the vicinity of other objects, many conceivable scenarios for which a single step two-impulse transfer would not be suitable. For example, an obstacle may lie in front of the target co-ordinates or along the planned two-impulse trajectory. While some obstacles may be avoided by manually adjusting the transfer time of a manoeuvre to alter the path, this trial and error process is time consuming and cannot be easily automated. Furthermore, manipulating the transfer time to avoid obstacles may compromise other mission goals, such as time windows or ΔV limitations. For problems involving complex obstacles such as the ISS, many transfers simply cannot be solved by a two impulse manoeuvre, or cannot be performed with adequate safety clearance.

The simple solution to this problem of collision avoidance is to use multiple two-impulse transfers between a number of waypoints to reach the target. These waypoints may be placed manually by a mission planner, or automatically through planning software to reach the goals of the mission. Each instance of a manoeuvre between waypoints is then essentially a distinct two impulse transfer, except that it carries over the velocity from the end of the previous step.

2.3.1 Applications for Multi-Waypoint Paths

The primary application of waypoints is to avoid obstacles in the path of the free-flyer. If the vehicle were manoeuvring in free space, there would be little reason to split up a transfer except for possible navigation issues. The ISS structure however presents a highly complex obstacle configuration to be traversed by the free-flyer. The simplest example of obstacle avoidance would be a two-step transfer with a single waypoint, used to bypass an object in the normal path of a two impulse transfer, as shown in Figure 2-10.



Path Type	τ (sec)	ΔV_1 ($m s^{-1}$)	ΔV_2 ($m s^{-1}$)	ΔV_3 ($m s^{-1}$)	ΔV_{total} ($m s^{-1}$)
Single Step	1000	0.0109	-	0.0109	0.0217
Two Step	500,500	0.0144	0.0344	0.0144	0.0632

Figure 2-10 Single Waypoint Obstacle Avoidance

There is no means of avoiding the obstacle in Figure 2-10 with a single two impulse transfer, as the orbital dynamics of the problem will always force the path to curve below the target point. Yet a single waypoint enables the path to be easily diverted above the obstacle, so that the target can be safely reached. The penalty for this added control is an increased ΔV requirement for the transfer.

For more complex obstacle avoidance problems, a larger number of waypoints may be used, following a pre-defined safe path to the target. This ‘safe’ path can be generated, independently of the orbital dynamics of the problem, and then broken down into steps using waypoints between each section, so that the desired path can be followed by the free-flyer. This strategy permits a high degree of flexibility in the technique used to find a safe path, and can be easily configured for different obstacle configurations. In addition, the planning of such multi-waypoint paths is suitable for automation, unlike the single waypoint technique described above, which requires a degree of understanding of the equations of motion to be used effectively. An example of path following using waypoints can be seen in Figure 2-11, which shows a path generated using a two dimensional Laplace function based path planner, before being converted into a series of waypoints.

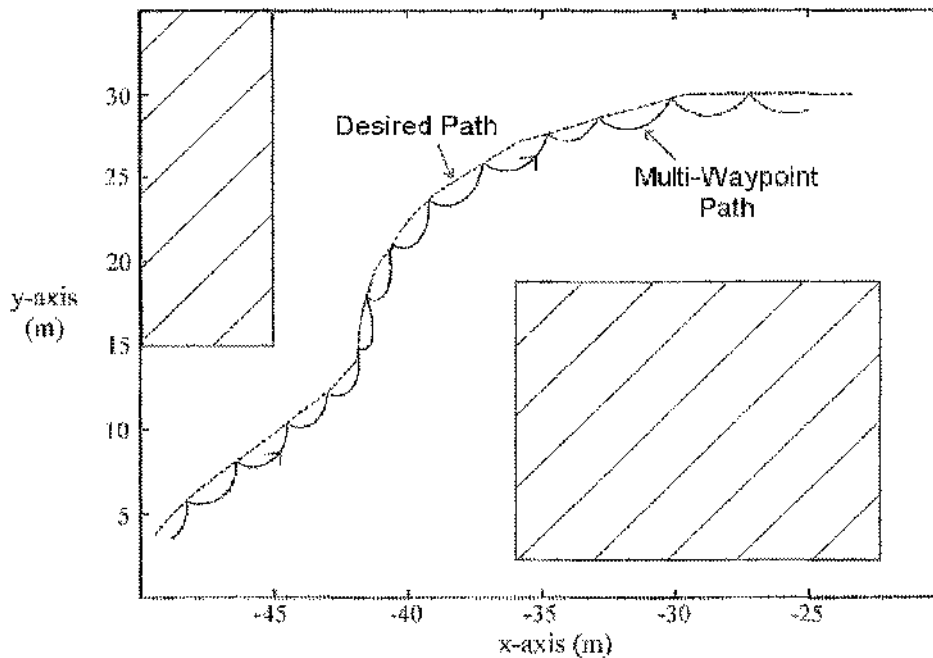


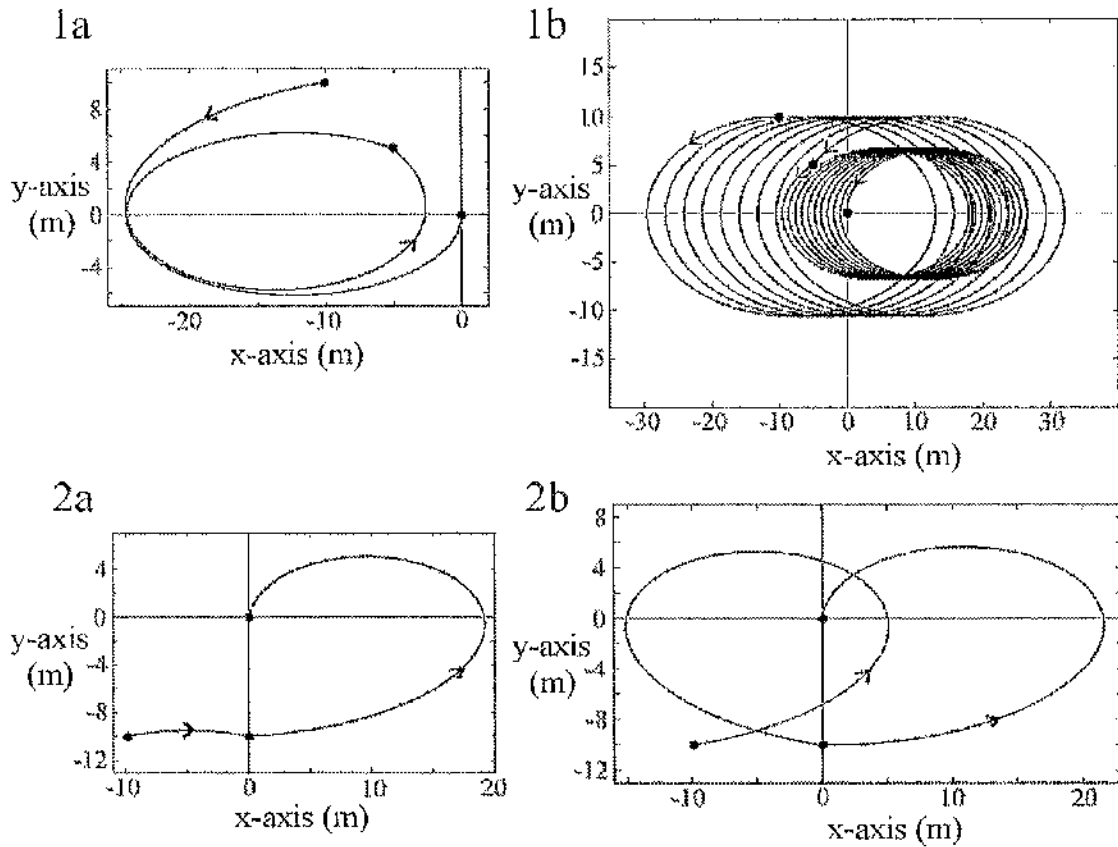
Figure 2-11 Multi-Waypoint Path Following

Multi-step manoeuvres have other possible applications, especially in rendezvous and docking missions. For crewed missions, using smaller steps rather than one large transfer to approach a target along the V-bar, minimises the deviation from the V-bar and hence from the line of sight to the target making it easier for a human pilot to control. The use of smaller steps during the approach also allows the closing velocity to the target vehicle to be independently controlled at each waypoint, facilitating braking gates so that as the free-flyer nears the target the potential impact velocity in the event of a failure is reduced. Finally, multiple waypoints allow controlled manoeuvring along the R-bar, since as previously noted, the elliptical motion of the free-flyer can only drift naturally in the V-bar direction. This allows additional docking approaches from above and below the ISS to be safely performed since the free-flyer will drift away from the target in the event of a failure.

2.3.2 Optimisation of Multi-Waypoint Manoeuvres

Unfortunately the difficulty of optimising a multi-waypoint manoeuvre increases proportionally to the power of the number of steps. The problem is essentially a function optimisation of the n variable cost function, where n is the number of transfer times. The only case for which simple optimisation techniques are practical therefore, is a single waypoint, two

step transfer. Figure 2-12, shows two example manoeuvres optimised using a simplex method optimisation routine in Matlab [107] [108].



Transfer	1a	1b	2a	2b
τ_1 / τ_2 (sec)	4100/4728	45377/56347	743/3759	4878/3942
ΔV_1 ($m s^{-3}$)	0.0215	0.0228	0.0114	0.0214
ΔV_2 ($m s^{-3}$)	0.0049	0.0050	0.0079	0.0032
ΔV_3 ($m s^{-3}$)	0.0070	0.0076	0.0082	0.0086
ΔV_{total} ($m s^{-3}$)	0.0334	0.0354	0.0304	0.0331

Figure 2-12 Optimised Two Step Transfers

Two results are detailed for each transfer to show the range of solutions that can be found depending on the initial estimate given to the optimisation routine. The global minimum is consequently very difficult to find because of local minima in the cost function, even in the simple case of a transfer with a single waypoint considered here. It may be the case, as with the single two impulse manoeuvre, that the global optimum is obtained from the first minima of the function. This is supported by the results shown, and consequently, small initial estimates for the transfer functions are recommended.

The main problem resulting from the optimisation of multi-waypoint manoeuvres, however, is that the extended paths resulting from longer more efficient transfer times, may impinge upon the obstacles that the waypoints were initially designed to avoid. Care is therefore required in manipulating transfers to optimise propellant usage, not to compromise the safety of the trajectory. In fact, for many multi-waypoint manoeuvres the safety factor, rather than the ΔV , may be the primary cost criteria used to evaluate trajectories. This is an important problem since for any set of manoeuvres used to approximate a pre-calculated safe path there will always be a certain amount of deviation from the desired path between waypoints. It is necessary to ensure that this deviation is constrained sufficiently to maintain the obstacle avoidance of the original plan. As with the optimisation of ΔV , this may be achieved by adjusting the transfer time to control the maximum deviation within any step of the manoeuvre. It may also be necessary to insert extra waypoints, if the maximum deviation criteria cannot be maintained because of the safe path curving in the opposing direction to the orbital dynamics, as shown in Figure 2-13.

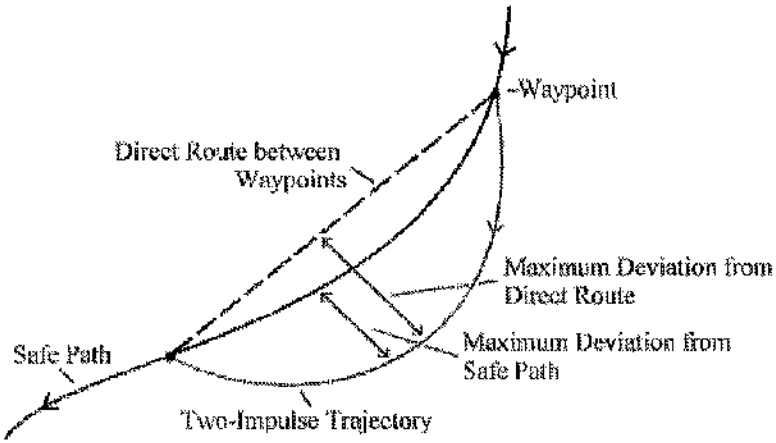


Figure 2-13 Deviation from Planned Path

This method of optimisation only considers each step of the manoeuvre individually though, and makes no attempt to optimise the propellant cost either locally or globally. One possible optimisation to the ΔV cost would be to take the safe path generated by the maximum deviation routines, and use further techniques to attempt to minimise the ΔV by varying the transfer times within certain limits. One such set of techniques, suitable to the optimisation of a function of a large number of variables, are Genetic Algorithms (GA) [109] [110]. Genetic algorithms function by maintaining a population of solutions to a given problem stored in a chromosome-like data structure, and applying recombination operators [111] to the population to preserve critical information and generate new members of the

population. By applying an evaluation function to each member, the population can then be pruned, with the better members preserved and given more chances to reproduce than the poorer members.

In the case of the optimisation of a multi-waypoint transfer, the variables that make up the chromosome structure will be the transfer time for each individual point to point transfer of the manoeuvre. An evaluation function is easily provided by the cost of the complete manoeuvre in terms of ΔV and total transfer time. Given an initial population of transfer time sets based on the maximum deviation results, successive generations would evolve with improved sets of transfer times to give a better total ΔV cost. Genetic algorithms have the advantage of being independent of the number of variables used, enabling their use for manoeuvres with a large number of waypoints, which will slowly optimise the solution whilst staying relatively close to the initial population, rather than quickly diverging. Relatively large savings in the total ΔV can then be made with relatively small changes in the transfer times for individual steps, without dramatically changing the path or compromising safety. The results of a preliminary solution obtained using the GA package *Genesis* (version 5.0) [112] are given in Table 2-1. The table compares the original results of a path planned using a Laplace potential field based path planner and converted into a multi-waypoint path with transfer times derived from the maximum deviation criteria, and the results of a GA optimisation of this multi-waypoint path.

Optimisation Routine	Number of Waypoints	Total Transfer Time τ_{total} (sec)	Total ΔV (ms^{-1})
Deviation Criteria	29	2432	1.3467
Genetic Algorithm	29	3804	0.4873

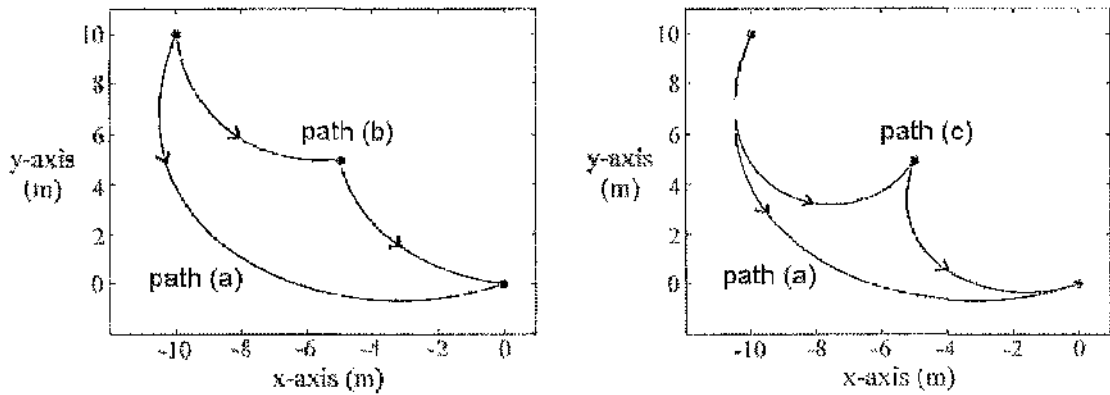
Table 2-1 A Genetic Algorithm Optimisation

The added deviation from the initial path introduced by the GA optimisation is minimal, but the optimisation has reduced the total ΔV cost by nearly a factor of three. This is an impressive result and would suggest that genetic algorithms may represent a promising direction for investigation in the optimisation of multi-waypoint transfers, and in fact GA optimisation has already been applied to spacecraft trajectory optimisations for rendezvous manoeuvres [113]. However, it should be noted that this method of trajectory optimisation is not necessarily repeatable, and includes no provision to constrain the safety of the resulting paths. To do this would require some form of collision evaluation to be incorporated into the trajectory cost evaluation function used for GA chromosome evaluation, which is expected to be prohibitively computationally expensive. Furthermore, the method of using specific pre-

planned waypoints for manoeuvring around the ISS is undesirable for reasons of navigation and thrusters errors which will be investigated in Chapter 5. For these reasons the use of GA trajectory optimisations is has been left for future research.

2.3.3 Comparison with Two-Impulse Cost

Comparing the cost of fully optimised multi-waypoint transfers with optimised two-impulse manoeuvres is not particularly useful, since optimising the ΔV independent of other aspects of the mission may jeopardise the reasons for using waypoints. To obtain a basic understanding of the potential cost of using waypoints however, we can compare the results of simple transfers carried out by single and multi step manoeuvres, using comparable transfer times. As such, Figure 2-14 shows a transfer from co-ordinates (-10,10) to (0,0), performed using a single step two-impulse trajectory with a transfer time of 1000 s, and a two step transfer with an intermediate waypoint at (-5,5), and transfer times of 500 s for each of the sections. In addition, since the cost for a single two impulse manoeuvre of 500 s would be expected to be high compared to a 1000 s transfer, giving an unfair penalty to the two step transfer, the manoeuvre is also shown using transfer times of 1000 s for each step.



Path	τ_1, τ_2 (sec)	$\Delta V_1 (\text{ms}^{-1})$	$\Delta V_2 (\text{ms}^{-1})$	$\Delta V_3 (\text{ms}^{-1})$	$\Delta V_{\text{total}} (\text{ms}^{-1})$
(a)	1000, n/a	0.0257	-	0.0167	0.0424
(b)	500, 500	0.0217	0.0220	0.0144	0.0581
(c)	1000, 1000	0.0206	0.0245	0.0084	0.0534

Figure 2-14 Two Step Vs Single Step Transfers

In both cases shown the ΔV requirement for the multi part manoeuvre is significantly greater than for the single step trajectory. Also interesting is the relatively small saving in ΔV obtained using 1000 s transfers rather than 500 s. This is due to the increased intermediate impulse ΔV_2 required by the larger change in direction at the waypoint for the longer path.

With a larger number of steps, the ΔV saving at each waypoint for more direct transfers may favour faster transfer times in spite of the larger initial and final impulses. The trend of increased ΔV requirements for multi-waypoint transfers over the single step two-impulse equivalent continues for other example missions, as each additional step must incur the hefty ΔV penalty of a change of direction at each waypoint [114]. Single step two-impulse trajectories therefore represent the maximum achievable optimality for a point-to-point transfer, against which developed path planning tools can be compared.

2.4 Errors

The Clohessy Wiltshire equations provide a simple and highly accurate description of the orbital dynamics of the free-flyer. It is important, however, to understand where deviations and errors from the CW result may occur, and design missions to minimise the impact of these effects. For the most part, especially for relatively short term missions, many errors may be neglected. But for longer duration missions, such as extended station keeping, or free drift after a malfunction and the shut down of free-flyer systems, cumulative errors become more critical.

2.4.1 Linearised Equation Errors

The Clohessy Wiltshire equations themselves are a linearised approximation to the full non-linear equations of motion. Errors will therefore be present between the free-flyer position predicted using the CW equations, and its actual position as it drifts in the orbital frame of reference. The magnitude of these errors will therefore increase the further the free-flyer travels from the origin of the reference frame at the ISS, as the assumptions used to linearise the equations of motion become less valid. However, it can be shown that for transfers in the relatively close vicinity to the ISS, where the free-flyer is designed to operate, these errors are very small. Figure 2-15 illustrates this, showing the drift trajectory of the free-flyer from the origin with an initial x velocity of 1 ms^{-1} .

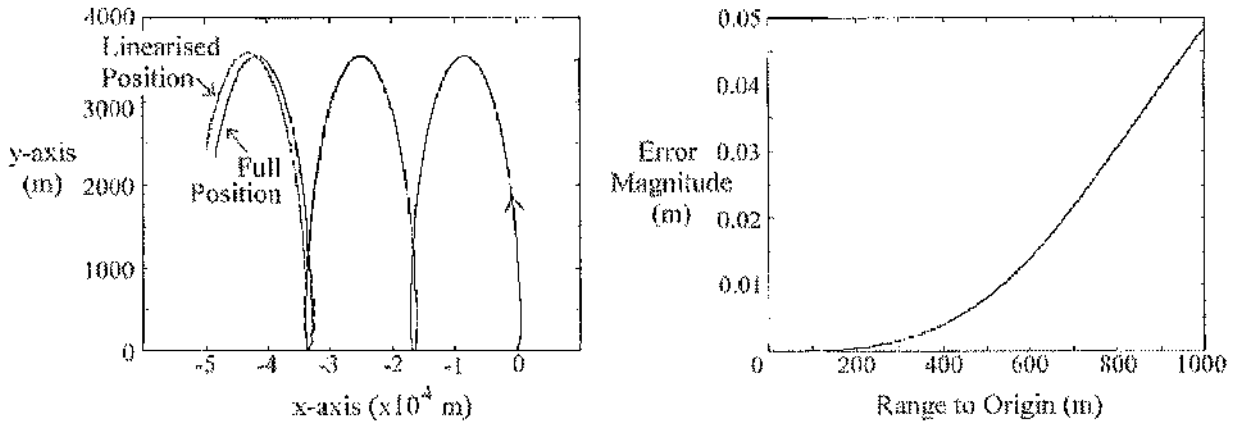


Figure 2-15 Linearisation Errors over Drift from (0,0)

Over large distances from the origin, the errors between the linear CW equations and the non-linear result become quite significant. However, within the range of operations of the Inspector free-flyer up to 500m from the ISS, the maximum error is approximately 0.01m as shown in Figure 2-15, less than the expected Inspector navigation sensor error of 0.025m as given in Appendix IV. In addition, the accumulation of errors over time would be negated during a mission through the updating of position information, and the CW results are only required to give an estimate of position for mission planning. Higher order solutions to the relative equations of motions have also been found [115] [116], however the added complexity of these equations makes further solutions more difficult, and as has been shown above the increased accuracy is not necessary for ISS-Inspector manoeuvres within 500 m of the ISS.

2.4.2 Thruster Impulse Errors

The Clohessy Wiltshire equations show that the motion of the free-flyer is dependent on both the initial position, and its initial velocity. The thrusters used to provide this initial velocity are, however, subject to tolerances in the accuracy of the change in velocity they can deliver to the vehicle. The effect of such errors in the initial velocity given to the free-flyer on its evolving trajectory must therefore be addressed. Figure 2-16 shows the result of an error in the initial velocity of $\pm 1 \text{ cm}^{-1}$ in each axis from a desired velocity of 10 cms^{-1} , generated by plotting the results of the extremes in initial velocity error at a number of intervals.

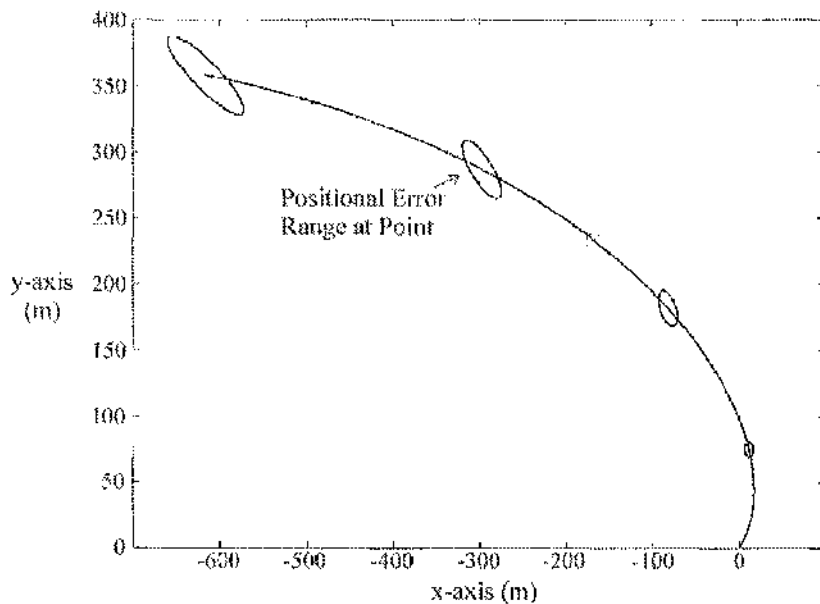


Figure 2-16 The Result of Initial ΔV Errors

The deviation from the desired path increases along the trajectory, to a maximum position error of 52 m after 2000 s for the example shown. For the relatively low impulse thrusters likely to be used on a small vehicle such as a free-flying camera, the maximum error in ΔV should be significantly less than 1 cms^{-1} , but the average magnitude of the free-flyer velocity should also be less than 10 cms^{-1} , so the percentage error gives a good representation of the expected free-flyer response to thruster errors.

The techniques used to guide the free-flyer must therefore take this positional error into account, to ensure that the maximum error at the end of any free-drift segment is smaller than the closest distance to any obstacles. A model of the possible deviation due to initial velocity errors should therefore be included, to be used by collision detection algorithms. In addition, the path planner should not rely on reaching any specific point at the end of each trajectory as this would require many costly corrections to the path during free-drift. Rather, the control strategy should be flexible enough to easily re-plan each step, based on the actual terminal position at each waypoint.

2.4.3 Additional Perturbing Forces

Other errors in the path followed by the free-flyer come from any additional external forces acting on the free-flyer and the ISS. These forces, as represented by the f_x , f_y , f_z terms in the non-linear equations of motion (reference non-linear equations in Appendix III) may come from perturbing forces on the Earth orbit such as atmospheric drag and variations in

gravitational field caused by the Earth's oblate and non-uniform shape. In addition, external forces such as solar light pressure, and the gravitational influence of the Sun and Moon will also act on the free-flyer and the ISS. In general however all of these forces, with the exception of air drag, will be acting on both the ISS and the free-flyer orbits so the differential effect between the two is extremely small for most cases. With the exception of air drag, all the perturbing forces are also periodic over each orbit of the reference frame, averaging their long term influence on the motion of the ISS and free-flyer.

The deceleration due to atmospheric drag for each vehicle is primarily dependent on the ratio of their cross-sectional area to total mass. For the ISS this deceleration should be smaller than for a free-flyer since the space station has a very large mass aligned deliberately along the V-bar to minimise cross-sectional area, whereas the free-flyer is more general cube shaped shape. It is therefore expected that the Inspector will experience greater deceleration due to its passage through the upper atmosphere. As an example, for the ISS with a cross-sectional area of 92 m^2 and mass 454,000 kg in a circular orbit of velocity 7671.3 ms^{-1} , using an atmospheric density of $10^{-11} \text{ kgm}^{-3}$ and a drag coefficient of 2.2, results in a drag force of 0.596 N [3] or a deceleration of $1.313 \times 10^{-6} \text{ ms}^2$. For the Inspector vehicle of cross-sectional area 0.5 m^2 and mass 210 kg, using a similar drag coefficient gives a drag force of 0.0065 N or an deceleration of $1.541 \times 10^{-5} \text{ ms}^2$ applied to Inspector. The drag forces are generated due the orbital velocity, and hence the forces produced will act only in the negative V-bar direction. The net effect on the free-flyer in the relative equations of motion will therefore be a small force applied in the negative x direction, resulting in a slow drift over time along the V-bar. A strategy is therefore required to guard against the long term effects of this drift, and will be discussed in Chapter 4.

CHAPTER 3: THE ISS-INSPECTOR MISSION

As discussed in Chapter 1, the target for the development of mission planning tools in this thesis is specifically for the ISS-Inspector mission. At this point therefore, it is necessary to investigate the requirements of the Inspector project and the capabilities and constraints of the ISS-Inspector vehicle, shown in Figure 3-1, as defined by the project leaders EADS Astrium and NASA.

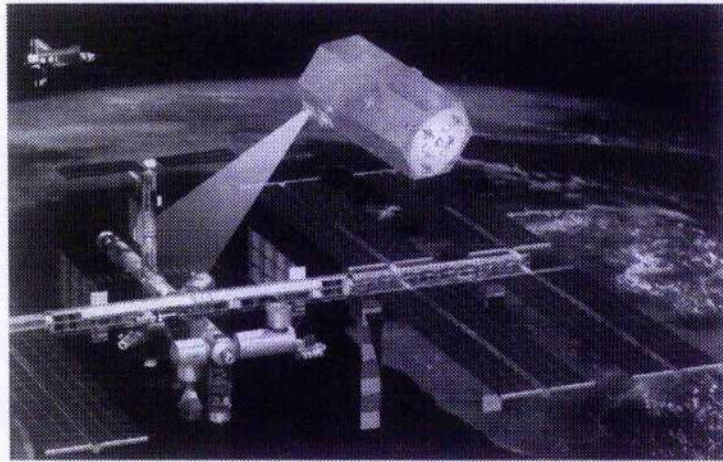


Figure 3-1 The ISS-Inspector (source: EADS Astrium)

Planned as the second step in the Inspector product family and developed from the X-Mir Inspector, the ISS-Inspector will have greatly enhanced capabilities over its predecessor in order to fulfil its role at the International Space Station. However, performing numerous inspection missions about the complex station will require an enhanced flexible control strategy to utilise the capabilities of the new vehicle. The planned ISS-Inspector system itself consists of a number of integrated elements [117] [118]:

- The Inspector Free-Flying Vehicle (hereafter known as the Inspector Free-Flyer, Inspector, or described by the generic term ‘free-flyer’) with integrated visual inspection cameras, and additional payload capacity.
- Supplementary non-visual inspection and environmental monitoring payloads.
- A docking port, attached to the ISS to provide vehicle services, and a storage facility for Inspector while docked between missions.
- The Central Data Handling System (DHS), based on the ISS to distribute data between the Inspector Free-Flyer and the control stations onboard the ISS and on the ground.
- A Monitoring and Control Station (MCS), onboard the ISS.

- ‘The Ground Control segment, with mission planning and control stations.

These elements provide all the services required support Inspector, and allow operation both from the ground and onboard the ISS.

The safety requirements for the Inspector Free-Flyer operating at the crewed space station are the same as for any vehicle visiting the ISS, as defined by NASA. Therefore Inspector must be able to satisfy the stringent requirements defined in the “Interface Definition Document for International Space Station Visiting Vehicles” [119]. Accordingly, mission safety is a critical part of the design of any free-flyer system. For the Inspector Free-Flyer, fault tolerant systems are used to, at a minimum, satisfy the basic visiting vehicle safety requirements of two fault tolerant systems for catastrophic failure risks, and single fault tolerant systems for critical risks. The importance of the safety aspect of the free-flyer mission is illustrated by the technical definition of safety used in the interface definition document:

- **Catastrophic Hazard:** Any hazard that may cause a disabling or fatal personnel injury, or the loss of either the Orbiter or the Space Station. NOTE: For safety failure-tolerance considerations, loss of the International Space Station (ISS) is to be limited to those conditions resulting from failures or damage to elements of the station that render it unusable for further operations – even with contingency repair or replacement of hardware – or which render the ISS in a condition which prevents further rendezvous.
- **Critical Hazard:** Any hazard that may cause a non-disabling personnel injury or severe occupational illness; lose a major ISS element, on-orbit life-sustaining function, on emergency system; or involve damage to the Orbiter. NOTE: For safety failure-tolerance considerations, critical hazards include the loss of ISS elements that are not in the critical path for station survival or that can be restored through contingency repair.

In most instances, the requirements for fault tolerant systems will be exceeded by the Inspector vehicle. Inspector safety is further enhanced through mission planning and design to ensure that the free-flying vehicle utilises passively safe trajectories wherever possible, or can perform a simple collision avoidance manoeuvre (CAM) to safely retreat from the station otherwise. However, the interface definition document for visiting vehicles described above, which is the closest available documentation for an Inspector type vehicle, was originally intended for vehicles visiting the station from outside of ISS controlled space rather than a free-flyer *based* at the space station [120]. As such it assumes that the vehicle will maintain a minimum distance of 200 m from the ISS throughout its mission, only coming closer on a tightly defined docking approach or release trajectory. This is in contradiction to the planned mission of the ISS Inspector, which is to fly around in close proximity to the ISS in order to make detailed inspections of the structure. It is planned therefore to perform as much Inspector manoeuvring as possible on the edge of this 200 m distance, only approaching the

station for docking or inspections, with only short range manoeuvres permitted once at close range.

3.1 Predefined Inspector Manoeuvres

As discussed earlier, the Inspector control strategy requires a number of predefined trajectories to be performed by Inspector to fulfil the mission objectives. These sets of manoeuvres are defined in the ISS-Inspector Design Definition (and developed by the author where noted) as

- The creation of a free flight fly-around trajectory, with an out-of-plane separation to ensure long term safety (developed in Chapter 4: Ellipse of Safety (EOS) Trajectories)
- Approach to station-keeping observation points from the EOS fly-around trajectory to within the 200 m inner perimeter of the ISS, performed via a forced motion trajectory along the R-bar wherever possible.
- Transfer to the docking port using an EOS followed by a standard forced motion R-bar approach (developed in Chapter 4).
- Automated station-keeping relative to the ISS structure.
- Safe translation along or around an inspected ISS element (developed in Chapter 5 and 6: Potential Function Manoeuvring)
- A single impulse collision avoidance manoeuvre (CAM), leading to a permanently safe retreat from the station after failure or an operator command.

Some of these manoeuvres, such as the r-bar forced motion approach, have been developed extensively for the ISS-Inspector and other vehicles, and will be briefly detailed here. Other manoeuvres and flight rules, such as the development of EOS trajectories and the use of potential function guidance for translating around ISS elements, will be the subject of subsequent chapters of this thesis. Finally, the station-keeping and CAM tasks are the subject of continued development by the Inspector project team, since these manoeuvres are highly dependant on the final Inspector Free-Flyer navigation and propulsion hardware configuration. Examples of both will however be given later in this chapter to indicate the potential cost and design considerations concerned.

3.1.1 ISS Flight Rules

Although not technically a Visiting Vehicle (VV), being based at the ISS, the Inspector Free-Flyer may be subject to some of the station requirements defined by NASA for such vehicles. These requirements are categorised primarily by the range of the vehicle from the station, divided into two categories as shown in Figure 3-2. The first safety zone a visiting vehicle will enter is the Approach Ellipsoid (AE), defined by a 2×4 km ellipsoid around the station. At this point, command of the vehicle must be taken over by the ISS Visiting Vehicle Control Centre. The inner safety zone, known as the Keep out Sphere (KOS), is a 200m sphere centred on the ISS. Visiting vehicles are only permitted to enter the KOS during a docking manoeuvre, during which they must keep to tightly defined docking approach cones to the docking point.

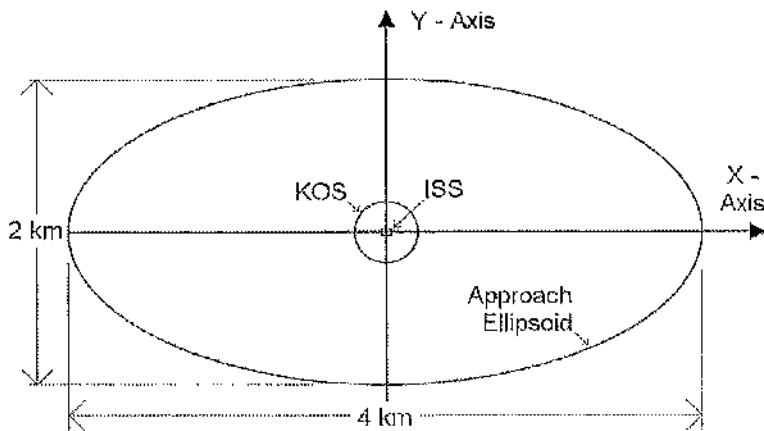


Figure 3-2 Defined Visiting Vehicle Safety Zones

All of the planned Inspector operations will take place within the Approach Ellipsoid since the free flyer is based at ISS, requiring that the Inspector ground control station be situated at a VV control centre. Furthermore, most operations will take place close to or even inside the KOS, especially during the detailed inspection phase. For the Inspector Free Flyer to be permitted to manoeuvre to its observation points and fulfil its objectives, new safety guidelines for such ISS based free-flyers will be needed.

3.1.2 R-Bar Forced Motion Approach

The R-bar forced motion approach has been developed over many years as a standard rendezvous and docking approach technique [121] [122]. In the context of the ISS, an approach corridor has been specified for visiting vehicles such as the ATV, which is also applicable for the Inspector Free-Flyer, especially as Inspector will typically be approaching

the station from an EOS trajectory on the edge of the KOS. This approach corridor consists of a cone orientated along the R-bar direction, with a maximum approach angle of 10° for 200 – 50 m range, and 5° for the final 50 – 0 m to docking, as shown in Figure 3-3.

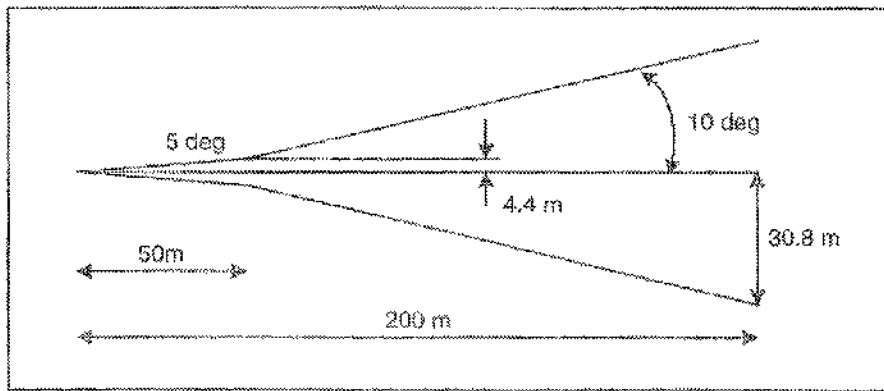


Figure 3-3 Docking Approach Cone

The velocity along the R-bar approach towards the station must also be controlled, to maintain the passive safety of the manoeuvre [123]. This is done using pre-calculated braking gates to ensure that the closure rate is kept within the safe approach profile, as shown in Figure 3-4. These velocity limits along the R-bar are calculated to ensure that in the event of a failure, at a given distance from the ISS, the free-drift trajectory will reverse its direction and drift safely back away from the station without collision.

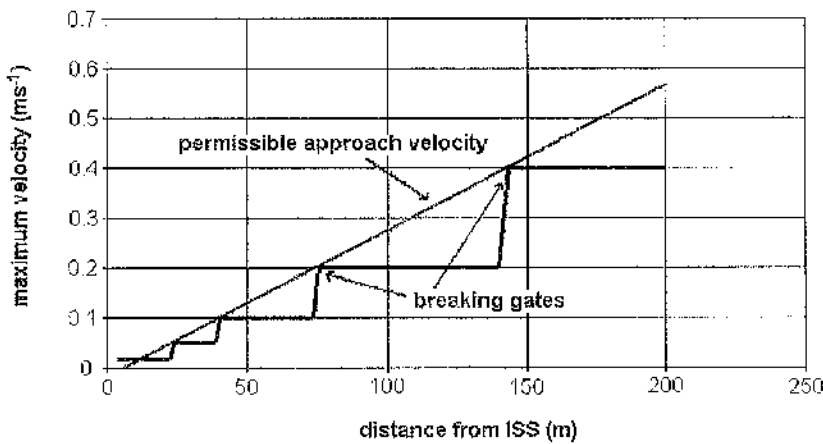


Figure 3-4 Approach Braking Profile

The time and ΔV cost of the forced motion approach is dependant on both the initial and final y co-ordinates, and on the constant out-of-plane position of the manoeuvre. As an example, a nominal approach from 200m to docking will take approximately 21 minutes and require a total ΔV of 0.8 ms^{-1} , contributing a significant fraction of the overall ΔV cost of a

mission. Due to the pre-calculated braking gates however, the approach is continuously passively safe to a range of approximately 13 m from the docking port. Naturally, the final stage of any docking manoeuvre cannot be passively safe, since the goal is a controlled impact with the docking mechanism.

3.1.3 Approach Safety Envelope

To ensure safe station-keeping close to the ISS structure during the observation phase, we can calculate a safety envelope around the station outside which station keeping at any point will be passively safe in case of a free-flyer failure. Fortunately, the configuration of the ISS places the majority of the station structure along the x-z plane, resulting in observation points mostly situated either above the ISS with a positive y co-ordinate, or below the station with a negative y co-ordinate. This means that the resulting drift from station-keeping points above the station will take the free-flyer further above and safely away from the station, and positions below the station will also drift further below and away, as shown in Figure 3-5. The required safe station-keeping distance from the ISS in these cases is therefore mainly dependent on the level of control of the station-keeping control system.

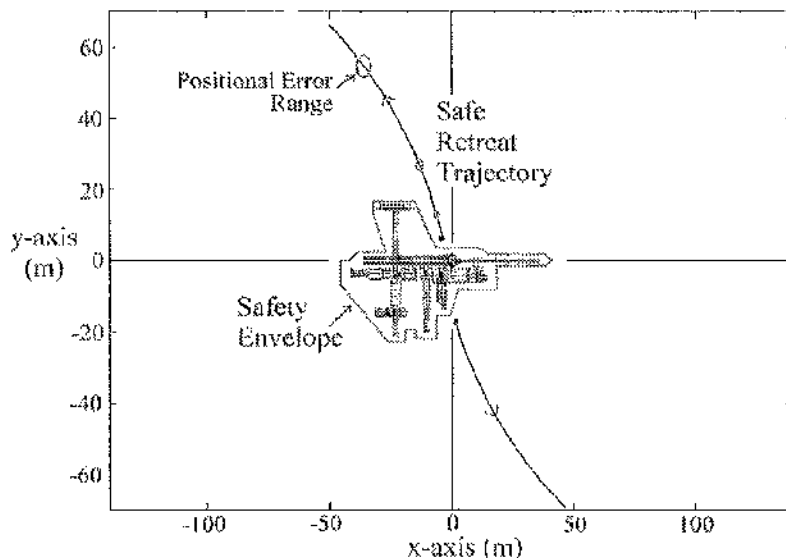


Figure 3-5 Safe Drift from Station-Keeping

Unfortunately, though the station-keeping envelope is safe for maintaining a static position close to the ISS, the problem remains that the limits of this envelope may still be unreachable by a passively safe approach, since approach requires an initial motion towards the ISS. The extent of the increase in the boundaries of the safe envelope for an R-bar approach is dependant on the velocity of the approach in the r-bar direction, as shown in

Figure 3-6. Figure 3-6 shows the minimum approach distance envelope around the ISS, to ensure passive safety during approach, for a range of initial velocities in the R-bar direction of $0.0 - 0.05 \text{ ms}^{-1}$. This demonstrates that positions close to the original station-keeping envelope can be reached using a reduced approach velocity, at the cost of an extended transfer time. For practical purposes however, constrained mission times require that a minimum approach velocity of 0.03 ms^{-1} be selected to reduce the maximum approach time.

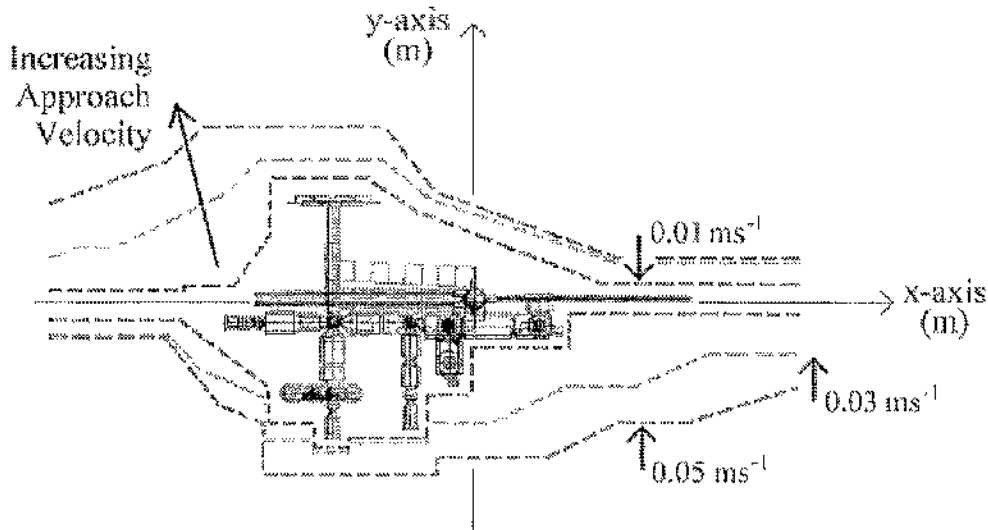


Figure 3-6 Growth of the Approach Safety Envelope

The approach safety envelopes shown were developed by the author during time spent working with EADS Astrium, to investigate the areas around the ISS within which the Inspector Free-Flyer would be able to operate safely. The results were obtained by a grid based method, creating a network of test points surrounding the ISS structure and checking the free-drift trajectory at each point, for each approach velocity, to determine the closest safe points. Extending this planar envelope method, the approach envelope can also be built up around the ISS in three dimensions, to visually describe the areas around the space station inaccessible to the free-flyer via a forced motion approach. This representation, an example of which is given in Figure 3-7, can then be used by mission planners to develop an awareness of the potential problem areas around the station in terms of the passive safety of observation points.

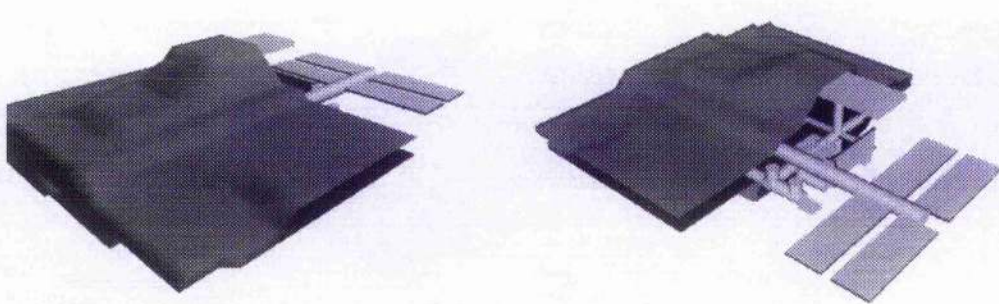


Figure 3-7 3-D Approach Envelope

3.1.4 Additional Standard Manoeuvres

The techniques required for automated station-keeping have been developed over many years for a wide range of satellite applications [124] [125]. Unlike satellites on free-drift orbits, automated station-keeping of the Inspector Free-Flyer relative to the ISS will have the harder task of maintaining the free-flyer on a non-Keplerian orbit. To do this, Inspector's thrusters must compensate for the constant accelerations experienced by the free-flyer due to its y-z position relative to the origin of the relative co-ordinate system, as given by the equations of motion (eqn 2-30). It is these accelerations that will have the primary influence on the cost, in terms of ΔV , of the station-keeping phase. The performance, in terms of positional accuracy, of the station-keeping system will on the other hand be dependent on the accuracy of the available navigation data. For station-keeping close in to the ISS this will rely on the chosen navigation strategy. Visual navigation may be particularly suited to maintaining a fixed position, as the technique has already been demonstrated for underwater ROV's using image centring methods [126].

The main application for station-keeping during the Inspector mission is for close proximity ISS inspections, and EVA mission support. Whilst station-keeping outside the inner perimeter of the ISS is possible, wide angle observations can be easily made from an EOS trajectory at no cost, so the prohibitive ΔV cost of station-keeping at larger distances from the station will limit their application to shorter periods of time. For close observations, the free-flyer must be capable of station-keeping for a full 7 hr EVA mission. Examples of the relative cost of these applications are detailed in Table 3-1, calculated from the applied accelerations, in-plane and out-of-plane, at typical close and far observation co-ordinates.

Station-Keeping position (m)	Time Period (hrs)	ΔV Cost ($m s^{-1}$)
In-Plane $y = 30$	7	2.75
Out-of-Plane $z = 30$	7	0.92
In-Plane $y = 60$	1	0.78
Out-of-Plane $z = 50$	1	0.22

Table 3-1 Station-Keeping Cost

The ISS-Inspector safety strategy requires that at all times a Collision Avoidance Manoeuvre (CAM) must be available in case of a failure of the free-flyer. This CAM consists of a single impulse to initialise a safe permanent retreat from the ISS, and must be capable of being performed even under the worst case of two thruster failures, or an unwanted thruster action [127]. The CAM manoeuvre itself will be similar to the retreat from observation developed in Chapter 4, except that there is no need to size the retreat ellipse to enable subsequent manoeuvres. However, a CAM must be continuously available at positions around the station, which is difficult to achieve in certain areas. It is therefore planned that standard CAM manoeuvres be pre-calculated to handle difficult areas of the ISS and to allow pre-flight verification of each trajectory.

Furthermore, due to the extensive use of passively safe trajectories in the planning of the ISS-Inspector manoeuvres, the reliance on collision avoidance manoeuvres for safety should also be reduced to being an emergency backup. Since the Inspector Free-Flyer will already be safe without any collision avoidance, a CAM should only be required to provide longer term safety if desired, or to provide safety coverage for any non-passively safe portions of close manoeuvring.

3.2 Observation Point Selection

The initial planning stage of any Inspector mission will be in the selection of the required observation positions to view the target location. Each mission will have one or more target points on the ISS exterior which must be inspected, or at which EVA activities will take place that must be supported. In each case, an observation position must be found for the Inspector Free-Flyer to provide an optimum view of the target through Inspector's cameras. Suitability criteria for these points include not just a good viewing angle of the target free from obstructions, but also that the target has sufficient illumination either from the Sun or the Inspector's onboard spotlight during the observation period to be clearly visible. In

addition, a viable observation point must also be passively safe during station-keeping, and provide unbroken radio coverage for transmission of the video inspection pictures to the ISS.

The task of simultaneously satisfying all these constraints cannot be easily performed with manual data sheets and station plans. Therefore a specialised tool is needed to assist in planning the observation points for a mission. The observation point selection tool presented here was developed by the author during a six month placement as part of this PhD, at DASA-RI (now EADS Astrium) in Bremen, Germany in 1998. As such, it implements the planned requirements of the ISS-Inspector mission and the planned ISS configuration at that time. The tool was coded by the author in ANSI standard C++ code [128], using the OpenGL graphics libraries [129] for rendering tasks and the GLUT libraries to handle the windowing interface. The use of these standards and widely available libraries permitted the tool to be compiled without any code changes on a variety of machines from pc based Windows and Linux systems to SGI workstations running the Unix based Irix operating system.

3.2.1 The Inspector Camera View

The primary component of the observation point selection tool is a virtual view provided through the Inspector camera, and the ability to interactively aim and translate the camera/free-flyer through this camera view. Moreover, the view also allows the camera to track a chosen target position while translating the camera, simplifying the task of optimising the view of a specific observation target. Target tracking can also be used to visualise a translational observation phase around or along a target element, or to choose multiple views of a chosen target to give a range of viewing angles. Besides translating and rotating the camera, the view also provides the ability to zoom the viewing angle within the limits of the camera, enabling the range between Inspector and the observation target to be chosen with respect to the camera's physical characteristics to give the required detail and viewing angle for each particular inspection task.

This virtual camera view forms the basic observation point selection tool, which is then enhanced through additional options, and visual feedback of the current Inspector point suitability in terms of the other observation requirements such as passive safety and the integrity of the communication links.

3.2.2 Lighting and Space Station Configuration

One important factor affecting the suitability of any inspection camera view is the lighting conditions available at the target. While not directly critical for a non-visual

inspection of the target with environmental monitoring instruments, bad lighting can still have an adverse effect on any visual navigation system or in the loss of tracking of the target position. Most importantly, for a visual inspection mission good lighting conditions are crucial to successful imaging of the target. The Inspector camera view must therefore provide the ability to vary the lighting of the ISS model to present a more accurate representation of the view available to Inspector at any time. It is not however intended to be an accurate simulation of the resulting image that would be viewed by the camera since this would be dependent on many surface properties of the ISS structure that are not available at this time, and would be highly computationally expensive which would make it too slow for interactive view selection.

The illumination direction from the Sun can be varied either by choosing to specify a particular light vector, for example derived from the planned position on the ISS orbit, or directly by rotating the angular position of the light source in the sky. Once the ISS orbit is defined, it would be possible to relate the illumination direction directly to the time of day on the ISS orbit, enabling the lighting conditions to be viewed throughout the planned mission duration. The desired lighting conditions, and hence the preferred time window for each observation point, can then form an additional observation requirement to be used for subsequent mission planning and scheduling. One important feature that is not incorporated into the lighting model is the influence of shadowing from each ISS component on the overall view. This could be implemented using the OpenGL model by pre-rendering a shadow texture for each individual station component to a stencil buffer, which could then be applied to the model as it is rendered [129]. However, it should be noted that rendering hardware that supports stencil buffers would be required for this approach to be viable without having a drastic impact on rendering performance.

As well as determining the lighting conditions, the movement of the Sun across the sky will also have an influence on the physical configuration of the ISS as Sun orientated components, such as solar panels, rotate to track the Sun's position. Sun tracking is necessary to maintain the efficiency of all the solar energy dependent photo-voltaic arrays on which the station depends for electrical power, and also the station's cooling radiators which must be angled away from the Sun. The most significant consequence of this is the rotation of the large main solar arrays mounted on the truss structure, which will rotate up to 180° about the truss during each orbital period. For observation point selection, the camera model automatically updates the station configuration with respect to any change in the lighting direction, linking the physical and lighting models at all times. For the inspection of any sun tracking components themselves, the timing of observation points will be vital to ensure a

good view of the target, though for a critical phase such as this, safety constraints may require the rotating components to be fixed for the duration of the mission. An alternative would be to make inspections of any solar tracking components from an EOS orbit about the ISS, with the EOS position timed to be synchronous with the light direction to provide constant illumination conditions as Inspector orbits the station, as planned for the X-Mir Inspector mission shown in Figure 3-8 below.

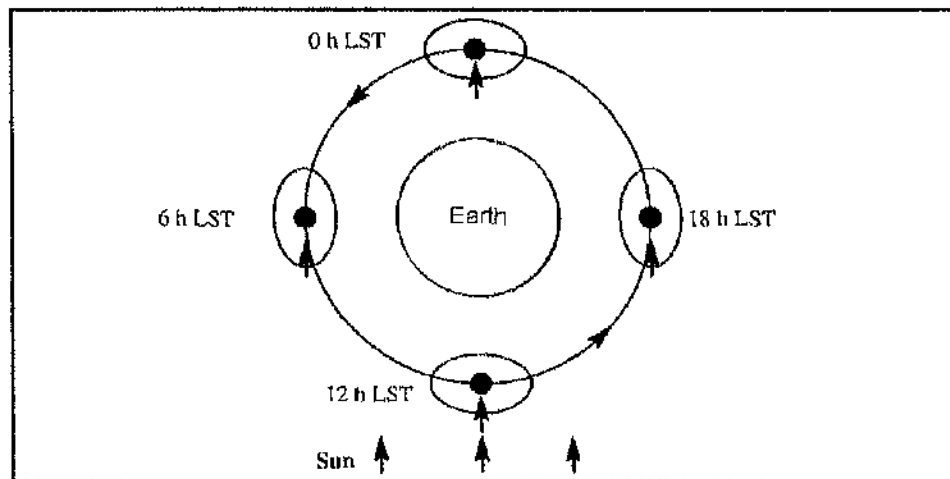


Figure 3-8 EOS Orbit Timing with Lighting Direction (source: EADS Astrium)

With the launch of the ISS-Inspector planned during the lengthy construction phase of the ISS, the configuration of the space station will also dramatically change throughout its assembly. To accommodate this, the observation point selection tool, along with all Inspector mission planning tools, must be able to represent the station at different stages of assembly. For the visual simulation, this is to be done by manually switching ISS modules and components on or off, and through the definition of a sequence of selectable station configurations used to represent specific stages of assembly. However, the planned ISS assembly sequence, like the final configuration, is under constant revision and the representations used in any Inspector tools must be easily modified to keep pace with current information.

3.2.3 Spatial visualisation

With only a view through the Inspector camera lens either for observation planning, or during a mission using live video images, it can be difficult for the operator to visualise the true position of the Inspector Free-Flyer due to variable camera zoom and range to the target, coupled with a lack of additional sensor input. To solve this problem, an external view of the ISS and Inspector Free-Flyer is provided for the observation planner to enhance spatial awareness of the Inspector position with respect to the station structure, as shown in Figure 3-9. In addition to showing the ISS and Inspector vehicles, the external view also gives a

representation of the field of view of the Inspector camera, shown as a cone with its vertex at the Inspector vehicle and its base centred on the observation target. This gives a clear visual indicator to the operator of the current camera zoom level, and target range, while emphasising the Inspector attitude with respect to the ISS.

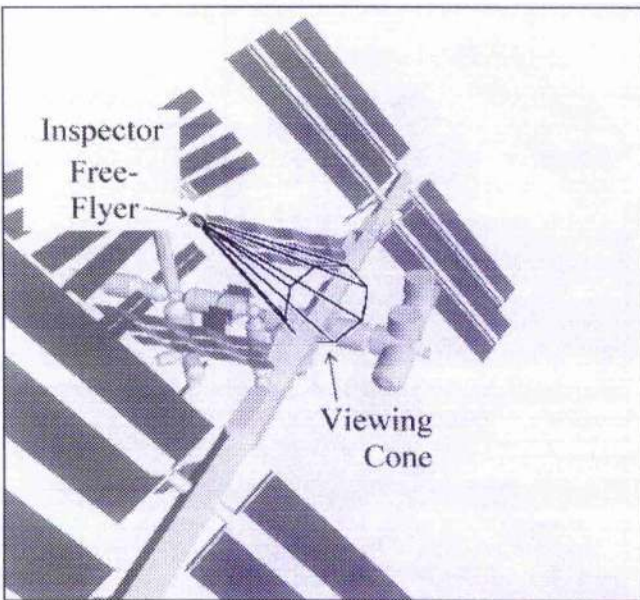


Figure 3-9 External View Example

As well as assisting mission planning, the external view can also be integrated into supervision, monitoring and control software both onboard the ISS and on the ground, to provide an extra aid in detecting potentially dangerous events during manoeuvring.

3.2.4 Additional observation point requirements

The final component of observation point selection is to ensure both the passive safety of the chosen position, and the integrity of communications links at that point. The integration of these parameters into the Inspector camera simulation simplifies the selection of valid observation points by allowing the operator to continually verify the availability of communications links and station-keeping safety, while manoeuvring the camera position.

The calculation of station-keeping safety, and optionally observation point approach safety, is calculated numerically by propagating the free-drift trajectory with the CW equations, and checking for collisions with the ISS structure along the path. For station-keeping the drift trajectory is calculated with the free-flyer initially at rest at the observation co-ordinates, while for approach safety the free-flyer will have an initial velocity in the r -bar direction, toward the station. Unfortunately, collision detection between the free-flyer trajectory and the ISS is not possible analytically due to the complex configuration of the space station structure. The

numerical method used relies on a discrete representation of the ISS structure, stored in a 'boundary' array, which can then be checked against the Inspector position along its drift trajectory. This boundary array is developed fully in Chapter 5 for use in computing the discrete potential fields for path planning and guidance. The free drift path need only be propagated and checked for one full orbit from release, since if a collision has not occurred by then the free-flyer will have drifted safely away from the station.

Calculation of the radio coverage between Inspector and the communications antennae on the ISS is based on determining signal interference from parts of the station structure, along the line-of-sight from Inspector to the antenna in use. Similarly to the station-keeping safety analysis, this is achieved by determining intersections between the line-of-sight communications link and a discrete model of the ISS structure. To account for the different interference models of the two radio wavelengths utilised, two models of the ISS are used to represent the station components capable of shadowing each radio signal. While not providing a strictly accurate simulation of the complex radio interference model around the station, this technique does produce a reasonable first approximation of overall communications coverage, which can then be verified by more accurate models later.

These three observation point requirements are now displayed to the operator as coloured icons in the camera display: Green for constraint verification, Red for constraint violation. This gives a simple observation point selection rule of finding a suitable observation position for viewing the target with good lighting conditions, which also gives three green lights to satisfy all the operational constraints. Figure 3-10 and Figure 3-11 show an example of the observation point selection tool with all the features described above.

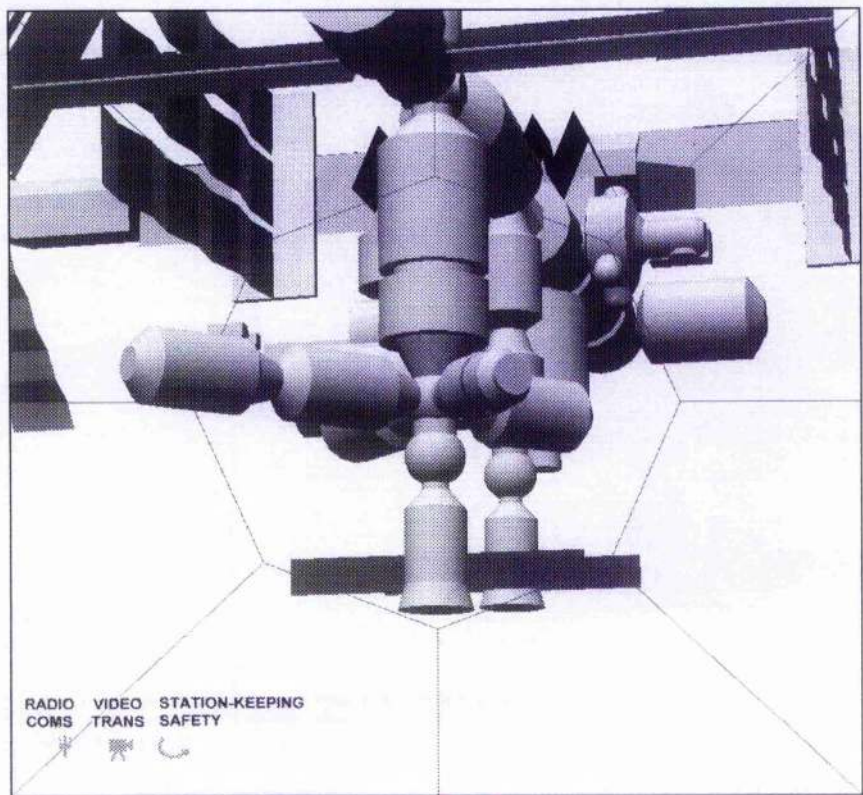


Figure 3-10 Inspection Camera View

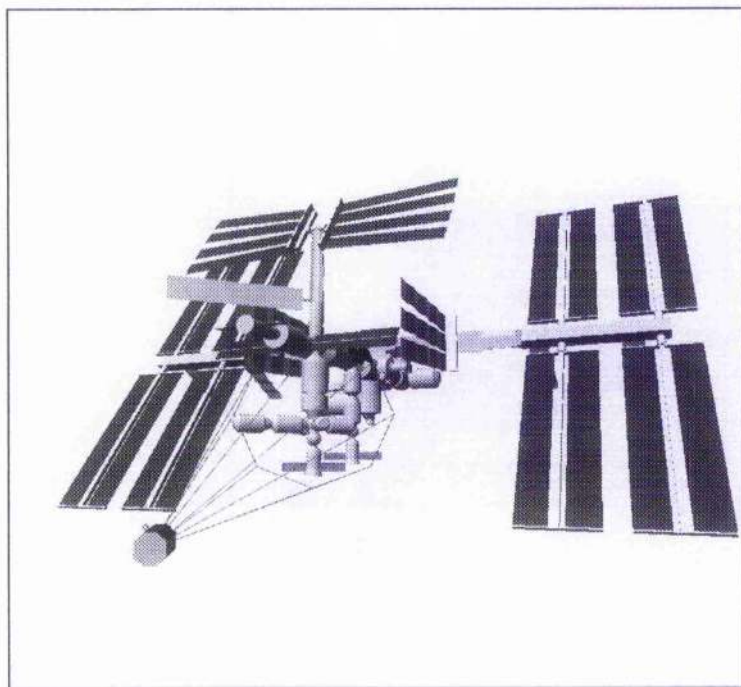


Figure 3-11 ISS and Inspector External View

CHAPTER 4: ELLIPSE OF SAFETY MANOEUVRES

After considering the general Inspector mission scenario, it is a natural step to divide the Inspector mission into two distinct parts. There are large amplitude manoeuvres at the start and end of a mission to transfer between the docking position and the observation area, and smaller manoeuvres taking place at the observation point to provide different viewing geometries or make observations of different targets in the vicinity. In comparison to the limited manoeuvring at the observation point, transfers to and from docking will typically traverse at least half of the station. In addition, pre-planned sequences are preferable from a safety point of view for the retreat from docking to allow initial diagnostic checks of the vehicle, and for the docking return to ensure a safe approach to latch the docking mechanisms. Given the important flight safety constraints at the ISS, the guidance strategy to be used for these long transfers at the beginning and end of missions must be as passively safe as possible, even in the long term under disturbing influences such as atmospheric drag, as discussed in section 2.5.3.

The core strategy chosen by Astrium to satisfy these long term safety goals is to use Ellipse of Safety (EOS) trajectories to safely transfer around the ISS, and a forced motion approach to translate in from the ellipse toward the observation point close to the station. The classification of ellipses in the orbital plane described in relative co-ordinates was achieved by Mueller in 1962 [130]. However, the EOS concept was first utilised in the X-Mir Inspector mission, as a simple fly-around trajectory to demonstrate long distance inspections of the Mir space station [131]. The use of EOS trajectories for the ISS Inspector, as developed by the author, is the first application of such ellipses for point to point manoeuvring and will be detailed in this chapter.

4.1 The Ellipse of Safety

In Chapter 2 it was demonstrated that the relative motion between the free-flyer and the ISS results in an in-plane (plane containing both the V-bar and R-bar) motion describing an elliptical path around the station. Ellipse of Safety trajectories make use of this in-plane ellipse, whilst introducing an additional motion in the z axis, carefully synchronised with the in-plane motion to produce a secondary ellipse around the ISS normal to the orbit. Since the dynamics of the in-plane and out-of-plane motion are uncoupled, the velocities required for

these two parts of the EOS may be considered separately. The timing between the two is however crucial to the effectiveness of the EOS in providing long term safety. The resulting combination of the in-plane ellipse and out-of-plane periodic motion is shown in Figure 4-1, detailing the elliptical motion in the x-y and y-z planes, and the phasing in the x-z plane.

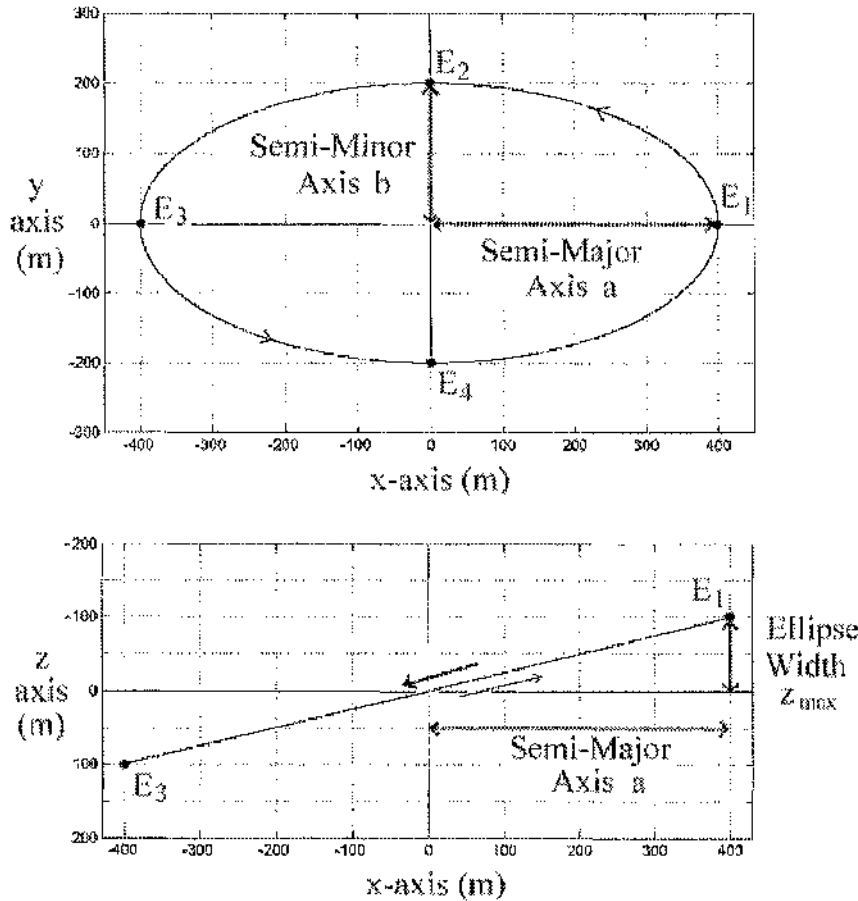


Figure 4-1 The Ellipse of Safety

The ellipses in the x-y and y-z planes, are used to provide clearance around the ISS for both in-plane and out-of-plane motion. The phasing of the ellipse is initiated so that as the in-plane path crosses the V-bar ahead of or behind the ISS, the deviation from the V-bar in the z-axis is at a maximum. Accordingly, the z co-ordinate vanishes only as the in-plane path crosses directly above or below the station, as shown in Figure 4-1.

The size and shape of any EOS can be completely described by two parameters. The in-plane ellipse size is defined by the semi-minor axis b . The out-of-plane motion, i.e. motion along the z -axis, is entirely decoupled from motion in the x-y plane, and is therefore best described by its maximum deviation from the V-bar, since the motion is always centred over $z = 0$. We have chosen to call this dimension the EOS width, z_{\max} .

4.1.1 Rationale of the EOS

The aim of the secondary ellipse in the y-z plane of the EOS is to guard against the long term effects of atmospheric drag. In the absence of air drag, the clearance around the ISS provided by the in-plane ellipse would be sufficient to provide long term safety, even under the influence of other periodic disturbing forces. However, as noted in section 2.5.3, the differential drag force experienced by the ISS and the free-flyer due to their difference in mass and cross-sectional area, will result in a decelerating force along the V-bar applied to the free-flyer relative to the ISS [132]. The effect of this deceleration, acting in the negative x-direction, will be that the in-plane ellipse will drift over time along the x-axis, as shown in Figure 4-2.

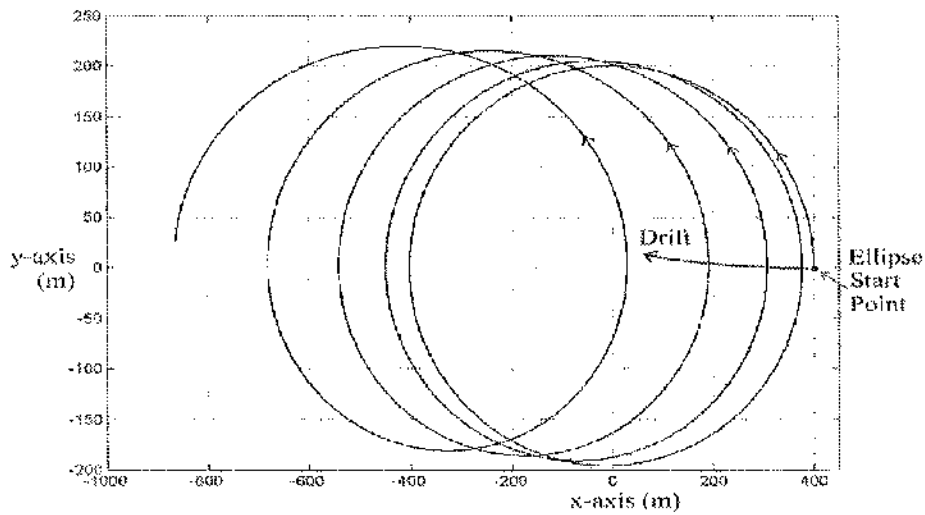


Figure 4-2 In-Plane Ellipse Drift due to Atmospheric Drag

In the absence of any out-of-plane motion, this drift would result in the free-flyer colliding with the ISS, though the time taken for this to occur is dependent on the magnitude of the relative acceleration.

The Ellipse of Safety strategy avoids this potential collision by ensuring that during the arcs of the ellipse where the y co-ordinate is small, and the in-plane ellipse may collide with the ISS, the z co-ordinate is large enough to avoid collision. The resulting trajectory, with drag, then describes a helical spiral, shown in Figure 4-3 passing safely around the ISS as it drifts along the x axis. As the relative drag force only acts in the x direction, the acceleration will have no effect on motion in the z-axis, ensuring that safe clearance around the ISS provided by the ellipse in the y-z plane will be preserved as the in-plane ellipse drifts [133]. Furthermore, this safety is independent of the magnitude or sign of the force applied along the x-axis.

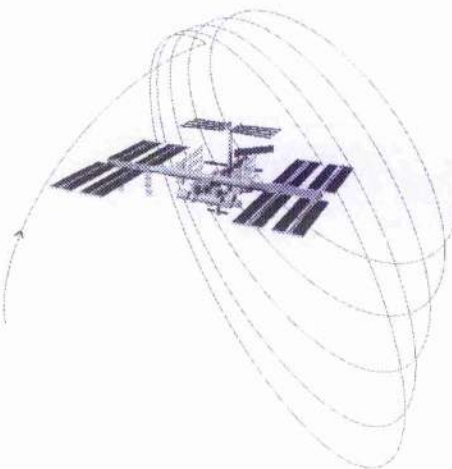


Figure 4-3 EOS Trajectory with Drag

The examples shown in this section use a constant relative acceleration due to drag of $1 \times 10^{-6} \text{ ms}^{-2}$ in the -x direction. In practice the relative acceleration experienced by the free-flyer with respect to the ISS will not be constant, as it is highly dependent on both the density of the atmosphere and the station configuration. Atmospheric density varies periodically throughout each orbit, seasonally as the Earth orbits the Sun, and randomly due to solar activity. The result of this density variation on the ISS and free-flyer can be as much as two orders of magnitude. In addition, the acceleration experienced by the ISS is highly dependent on the orientation of the main solar arrays. These large, flat panels rotate during each orbit to track the Sun. When the Sun is directly overhead, the panels will be orientated in the x-z plane, minimising their cross-sectional area in the y-z plane. However, when the Sun is in front or behind the station, the panels will be positioned vertically, presenting the largest possible area normal to the velocity vector. The total effective cross-sectional area of the ISS will therefore vary by a factor of two during each orbit. In fact this effect has even been suggested as a method for maintaining station-keeping between co-orbiting satellites, using the angle of their solar arrays to their velocity specifically to control relative position [134].

The safety of the EOS is also affected by the accuracy of the phasing between the primary in-plane ellipse and the out-of-plane motion. Correct phasing is necessary to preserve the secondary ellipse in the y-z plane which provides clearance around the ISS as the EOS drifts along the V-bar. Providing that the initial size of the EOS is sufficient, there is a reasonable margin for error between the correct phasing that will still provide sufficient safety. Beyond this however the EOS will not function correctly. Taken to the extreme where the

phasing is 90° in error, the resulting motion will describe a planar ellipse inclined at 45° to the local vertical, passing directly through the ISS.

Once the properly phased EOS has drifted past the ISS, it is completely safe until the free-flyer has drifted a complete orbit ahead of the station to return to the origin from the opposite direction. Unfortunately, it is unlikely that the free-flyer, and the ISS for that matter would be on the same orbit after such a lengthy period, so avoidance through the original EOS would not be expected, and a possible collision is difficult to predict. Action must therefore be taken either to remove the inactive free-flyer before this event, or to alter the ISS orbit to give an acceptable separation from the free-flyer orbit. For a differential deceleration of $1 \times 10^{-6} \text{ ms}^{-2}$ on the free-flyer, the time required to complete one complete orbit relative to the ISS, at an altitude of 400 km, is approximately 100 days, giving adequate time for the necessary action to ensure the safety of the ISS.

4.1.2 Ellipse Parameters

In order to evaluate the EOS trajectories, it is useful to rearrange the solutions of the CW equations to describe the motion on the ellipse by parameters independent of time. Equations 2-39 and 2-40 in section 2.2.2 describe the in-plane motion of a drifting ellipse, whose dimensions are elongated such that the ellipse semi-major axis a is twice the size of the ellipse semi-minor axis b , whose centre remains at a constant altitude with respect to the orbital frame of reference, and drifts in the x -direction with a velocity given by

$$\text{Eqn 4-1} \quad v_c = -3(\dot{x}_0 + 2\omega y_0)$$

From equations 2-39 and 2-40, the location of the centre of the ellipse can be obtained by eliminating periodic terms and neglecting the external forcing terms, to obtain

$$\begin{aligned} \text{Eqn 4-2} \quad x_c &= x_0 - 2\dot{y}_0 / \omega \\ y_c &= 4y_0 + 2\dot{x}_0 / \omega \end{aligned}$$

Referring to the geometry of the ellipse, shown in Figure 4-4, we can express positions on the ellipse, for example x_0, y_0 , relative to the ellipse centre position as

$$\begin{aligned} \text{Eqn 4-3} \quad \alpha &= x_0 - x_c = 2\dot{y}_0 / \omega \\ \beta &= y_0 - y_c = -3y_0 - 2\dot{x}_0 / \omega \end{aligned}$$

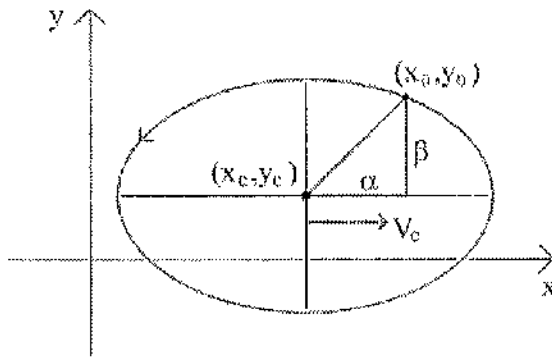


Figure 4-4 Standard Ellipse Geometry

Due to the fixed shape of the ellipse of safety, having a semi-major axis twice the size of the semi-minor axis, b can therefore be obtained from any ellipse position (α, β) , by

$$\text{Eqn 4-4} \quad b = \sqrt{\beta^2 + (\alpha/2)^2} = \sqrt{(3y_0 + 2\dot{x}_0/\omega)^2 + (\dot{y}_0/\omega)^2}$$

also giving the semi-major axis $a = 2b$.

The out-of-plane motion of the EOS is described by the maximum out-of-plane position on the ellipse, the ellipse width z_{\max} . This is obtained from equation 2-42, solving for $z = z_{\max}$, to obtain

$$\text{Eqn 4-5} \quad z_{\max} = \sqrt{z_0^2 + (\dot{z}_0/\omega)^2}$$

Using these equations, the size and shape of the Ellipse of Safety can now be selected.

4.1.3 Construction of EOS

Now that the desired size and eccentricity of the EOS have been chosen, the initial velocities required to initiate the planned EOS must be calculated. By definition, the drift velocity of the EOS must be zero, so the ellipse drift equation, Eqn 4-1, can be rearranged to provide the required initial x-velocity at the start of the ellipse

$$\begin{aligned} \text{Eqn 4-6} \quad 0 &= -3(\dot{x}_0 + 2\omega y_0) \\ &\Rightarrow \dot{x}_0 = -2\omega y_0 \end{aligned}$$

Given \dot{x}_0 , the equation for the ellipse semi-minor axis b , Eqn 4-4, can then be used to find the initial y-velocity

$$\begin{aligned} \text{Eqn 4-7} \quad (\dot{y}_0 / \omega)^2 &= b^2 - (3y_0 + 2\dot{x}_0 / \omega)^2 \\ \Rightarrow \quad \dot{y}_0 &= \omega \sqrt{b^2 - (3y_0 + 2\dot{x}_0 / \omega)^2} \end{aligned}$$

which, substituting for \dot{x}_0 , becomes

$$\text{Eqn 4-8} \quad \dot{y}_0 = \omega \sqrt{b^2 + y_0^2}$$

Using Eqn 4-6 and Eqn 4-8, the free-flyer velocity can now be initialised at any point to start the trajectory on a non-drifting, in-plane ellipse of semi-minor axis b . The easiest position to perform this manoeuvre is at the E_1 point depicted in Figure 4-1. This point, situated on the V-bar ($y_0 = 0$), simplifies the manoeuvre considerably since Eqn 4-6 becomes $\dot{x}_0 = 0$, and Eqn 4-7 then reduces to $\dot{y}_0 = \omega b$. In addition, making the in-plane EOS manoeuvre at E_1 has the advantage of minimising the ΔV cost of initialising the ellipse, since the in-plane velocity on the EOS is at a minimum at this point.

The initial z-velocity component required to set the out-of-plane motion of the EOS can now be easily determined by rearranging Eqn 4-5, to give

$$\text{Eqn 4-9} \quad \dot{z}_0 = \omega \sqrt{z_{\max}^2 - z_0^2}$$

However, to ensure that the correct phasing with the in-plane motion is met, the timing of this manoeuvre with respect to the free-flyer position on the in-plane ellipse is crucial, and is also dependent on the initial z co-ordinate z_0 . The easiest position to perform the inclination manoeuvre is at the apogee (E_2) or perigee (E_4) of the in-plane ellipse, where the EOS phasing requires that the z co-ordinate is zero. Eqn 4-9 then becomes

$$\text{Eqn 4-10} \quad \dot{z}_0 = \omega z_{\max}$$

Depending on the initial free-flyer position in the z axis, an earlier manoeuvre may be required to ensure the $z = 0$ condition is met at E_2 or E_4 . The EOS cannot therefore be completely initialised until the E_2 position is reached, $\frac{1}{4}$ orbit after E_1 , and full passive safety is only available from this point. Depending on the trajectory up to E_1 however, it may be possible to initialise the EOS inclination $\frac{1}{4}$ orbit earlier, enhancing the overall safety of the manoeuvre.

4.2 The EOS Segment of an Inspector Mission

To make use of EOS trajectories in an ISS Inspector mission, a strategy is required to utilise the EOS manoeuvres in transfers to and from arbitrary observation positions around the ISS. As described in Chapter 3, this can be achieved by using EOS trajectories to transfer to a point above or below the target position, with a forced motion approach along the R-bar to then reach the target. The planning problem therefore, is to manipulate the EOS so that the trajectory will pass over a desired observation position, in effect to find the particular EOS that passes through the desired observation co-ordinates in the x-z plane. This must be done, however, without compromising the basic safety of the EOS.

4.2.1 Ellipse of Safety Sizing

The minimum size of the in-plane ellipse of the EOS used about the ISS is determined by operational constraints such as navigation data availability, as detailed in Chapter 3, requiring that the semi-minor axis b must be at least 200 m. While it would be possible to increase b without violating any of these constraints, there would be a cost to the manoeuvre both in the ΔV required to initialise the ellipse and on the time and ΔV cost of a longer forced motion approach from the EOS to the ISS. Since these costs would not be offset by the limited control over the path of the EOS provided by varying b , it is advantageous to fix the semi-minor axis size at 200 m, simplifying further analysis.

The minimum ellipse width is then sized by the dimensions required to provide clearance around the ISS in the y-z plane. This must also take into account the changing profile of the station as its configuration changes to track the Sun. For the worst case where the solar arrays are orientated in the y-z plane, the approximate minimum safe ellipse width, as shown in Figure 4-5, is found to be 100 m.

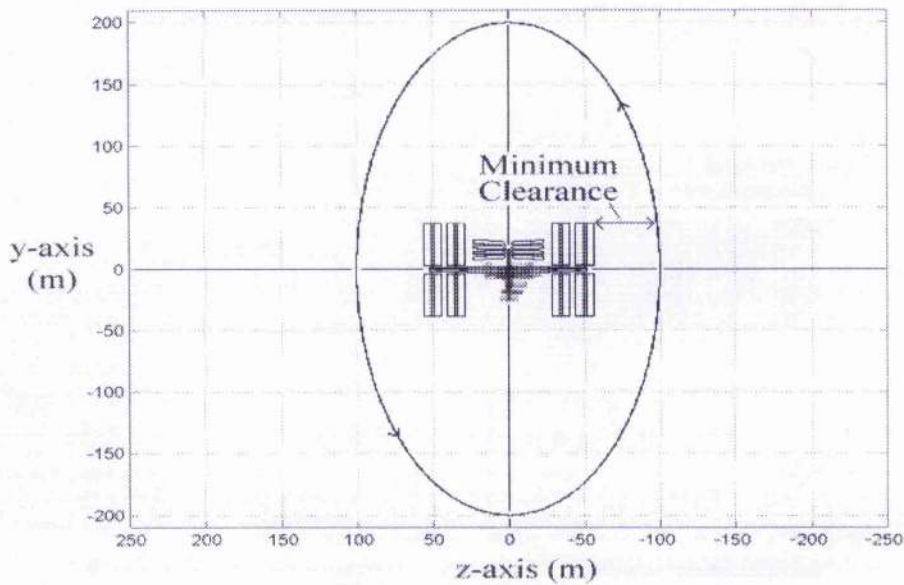


Figure 4-5 EOS Ellipse Width Sizing

Though increasing the ellipse width would increase the safety clearance of the EOS as it drifts past the ISS, the cost in terms of ΔV of doing so is prohibitively high, as will be shown later in this section. This requires z_{\max} to be fixed at the minimum safe value to limit the cost of the mission. This use of fixed EOS dimensions, while restricting the possibilities for reaching the observation point, helps greatly by simplifying both trajectory calculation, and safety verification.

4.2.2 Transfer to and Return from Observation Points

For an Inspector mission, the primary EOS segments of the mission will be standard transfers from the docking attachment on the ISS to an observation point, and subsequent return to docking. Since the start co-ordinates for the outbound manoeuvre and the target for the return are fixed, these trajectories can be standardised to incorporate elements such as the mechanical release from docking, and the retreat from the observation point, and integrate them into the final EOS trajectories. A standard EOS transfer and return is shown below in Figure 4-6.

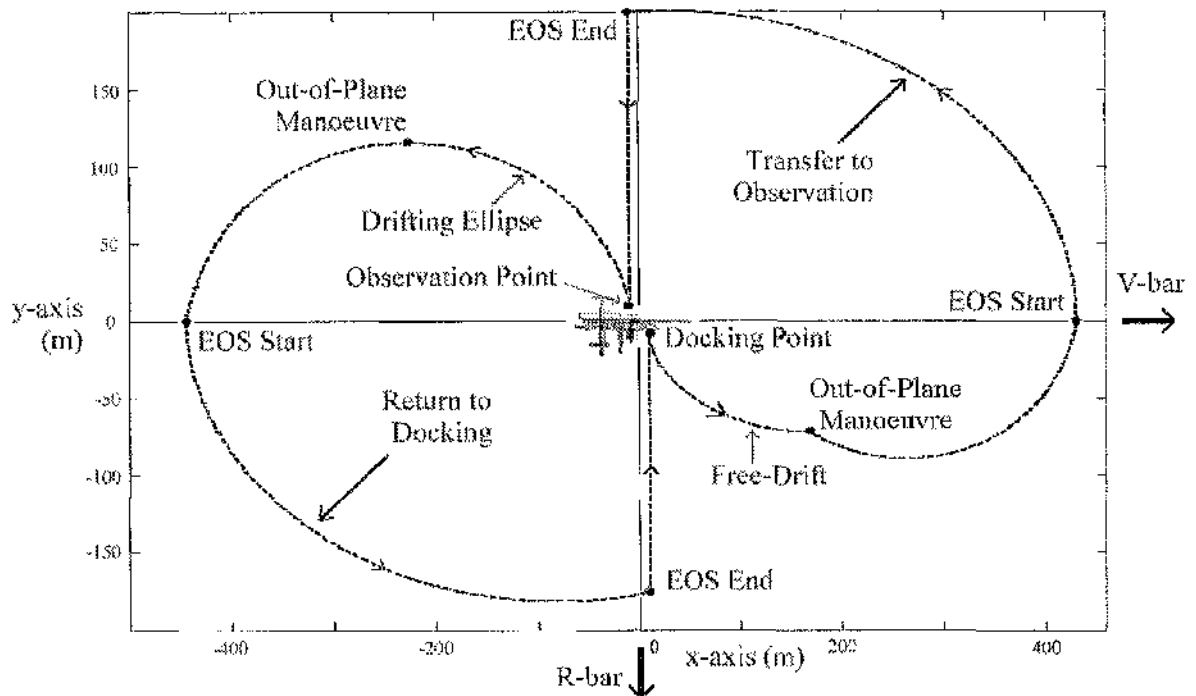


Figure 4-6 Inspector Ellipse of Safety Plan

The transfer to the observation point is initiated by the release from docking and a mechanical push-off from the docking mechanisms. No control occurs within this period of free-drift following release, as communication and system checks are performed by the Inspector vehicle, and initial navigation data is obtained. In case the vehicle does not checkout, the trajectory resulting from the initial push-off must be passive safe, so that the free-flyer will safely drift away from station. Once the systems checks have been completed, manoeuvres may then be performed by Inspector to transfer onto the EOS required to pass above or below the observation point. Once this point is reached, the free-flyer must negate its relative velocity, and use a standard forced motion approach in the R-bar direction to the observation phase of mission. Although the plan shows the path stopping instantaneously at this point, implying infinite accelerations, the relatively low velocity on the EOS trajectory at this point (approx $0.4 - 0.5 \text{ ms}^{-1}$) and the fact that small errors in positioning will easily be adjusted during the R-bar approach, make this a reasonable approximation.

For the return from the observation point, it is preferable in terms of efficiency and safety, to make a single ΔV to retreat from the ISS on a safe, drifting ellipse. Once clear of the station structure, manoeuvres can be safely made to set up the EOS required to return to below the docking port. Nevertheless, the drifting ellipse used for the retreat ensures that in the event of any of these manoeuvres not being performed, the trajectory will remain passively

safe. As the Inspector passes under the docking co-ordinates, the free-flyer can then stop and again utilise a forced motion approach to return to docking.

4.2.3 Transfer from Above to Below the ISS

For inspection missions with multiple observation points, spaced sufficiently far apart, it may be preferable to use additional EOS manoeuvres to transfer between certain observation co-ordinates. The most appropriate example of this is for transfer between a high observation point above the station, and a second observation point located below the V-bar, with the ISS separating the two. In this case, it would be difficult to provide sufficient passive safety using potential function guidance techniques described in section 6.2, due to the proximity of the desired path to the station and, importantly, to the V-bar. For this category of manoeuvre, a further development of the previously discussed EOS return to docking trajectory could be applied. This would enable the free-flyer to safely retreat from the first observation point, and make use of an EOS trajectory to transfer around the ISS to the second observation point below the station.

This manoeuvre is effectively the same as a return to docking, but with variable target co-ordinates for the EOS trajectory, and would provide passive safety for the free-flyer throughout. The time required for the EOS would be longer than using a more direct Potential Field Guidance transfer however, and the ΔV cost would also be considerably greater due to the cost of the initialisation of the EOS and the forced motion approach. The relatively high cost of using additional EOS transfers must therefore be balanced against the safety limitations of a potential function guidance transfer for each specific case.

4.3 Transfer to Observation

The transfer of the Inspector free-flyer from its docking port on the ISS, to the first inspection point, is a critical phase of the mission. This phase is highly dependent on the use of passively safe trajectories, since it is only during this initial period after the free-flyer has been released from the station that it has its first real opportunity to verify many of its mission critical systems. Although a number of systems can be checked prior to a mission, many, such as navigation sensors, cannot be fully tested while docked to the ISS. The opportunity must therefore be available to test these systems under safe conditions, where any possible failure will not endanger the ISS or its crew. The need for such systems checks carried out under passively safe conditions was fittingly demonstrated during the X-Mir inspection mission,

when the navigation sensors were initially unable to acquire a reference attitude from the star camera. In this example the X-Mir Inspector flight rules suspended any active manoeuvring of the free-flyer in the absence of navigation data, leaving Inspector to safely drift away from the Mir station.

The plan for the outward phase of the mission can be described by the position of the three manoeuvres required to complete the desired trajectory, as shown in Figure 4-7 below. For initial observation positions above the ISS, the transfer will take approximately 1 orbit to complete, with observation points below the ISS, the free-flyer will remain on the EOS transfer for an extra $\frac{1}{2}$ orbit, in order to pass below the station.

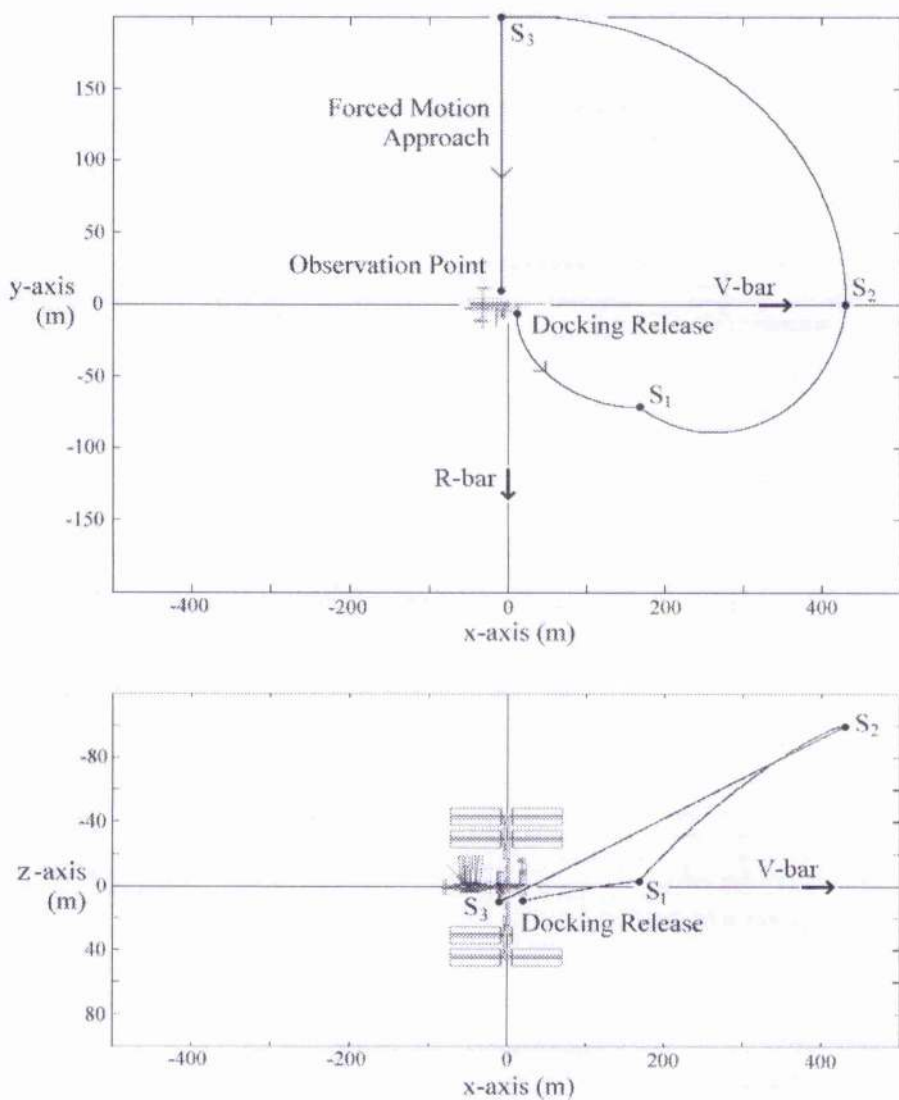


Figure 4-7 Outward Phase Plan

4.3.1 EOS Selection

The strategy to enable the EOS to cross the desired observation point for this phase of the mission is to translate the entire ellipse, of fixed semi-minor axis b , and width z_{\max} along the x-axis until the trajectory passes over/under the desired co-ordinates. This movement of the ellipse is achieved by varying the start point of the ellipse, denoted S_2 on the mission plan. The possible range of the S_2 position is limited by the relative dimensions of the EOS so that the ellipse can maintain safety clearance around the ISS. For the Inspector EOS semi-minor axis and width of 200 and 100 m respectively, this gives an allowable position for S_2 of 200 to 600 m along the positive x-axis, whilst maintaining sufficient clearance to the station at all times, as demonstrated in Figure 4-8 below.

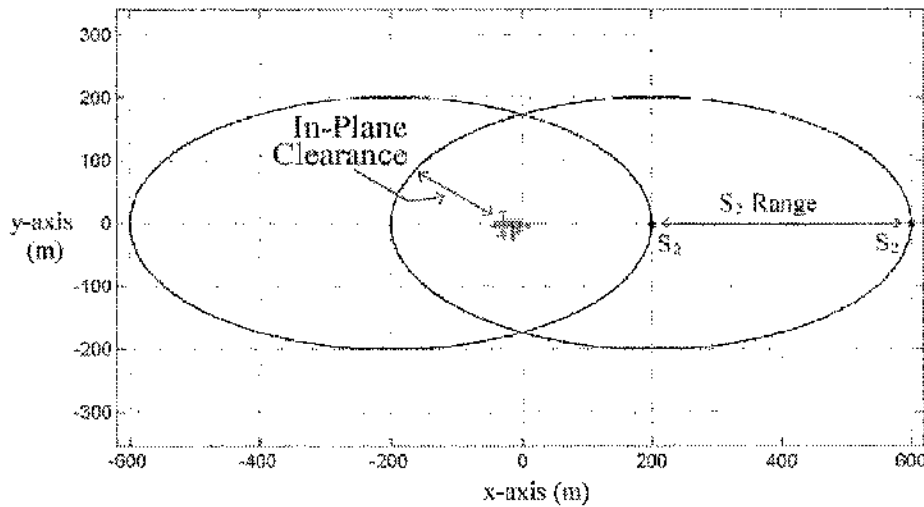


Figure 4-8 EOS Safety Clearance Over S_2 Range

This flexibility in the location of the S_2 point achieves full coverage by the EOS of all positions on the ISS. However, some of the extremes of the station, such as the outside tip of the main solar arrays, are close to the limits of coverage. For these critical areas, the available coverage of the EOS can be extended by reversing the direction of the out-of-plane motion of the ellipse, so that the ellipse is inclined to the right as it passes ahead of the station, rather than to the left. This can be seen in Figure 4-9, which shows the limits of the coverage provided by moving the S_2 point, and by reversing the inclination.

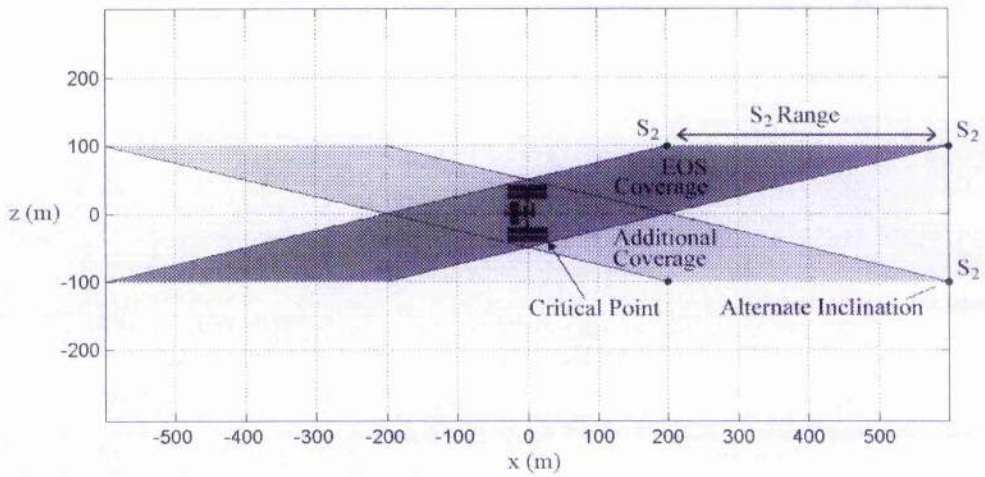


Figure 4-9 EOS Coverage of ISS

The co-ordinates along the x-axis of the S_2 point required to reach a specific co-ordinate on the ISS can be calculated using the geometry of the EOS to project the ellipse over the desired goal point. The easiest way to achieve this is to first shift all the co-ordinates by z_{\max} (100 m) in the z-direction, to account for all possible goal co-ordinates on both sides of the x-axis. Now that all the points lie on the +z side of the x-axis, the S_2 x co-ordinate can be found by simply projecting the goal back across to the x-axis at the same angle as the EOS. This angle is defined by the ratio of the ellipse width to the semi-major axis size $z_{\max}/2b$. The x co-ordinate where the projected line crosses the x axis is then equal to the S_2 position, as illustrated in Figure 4-10.

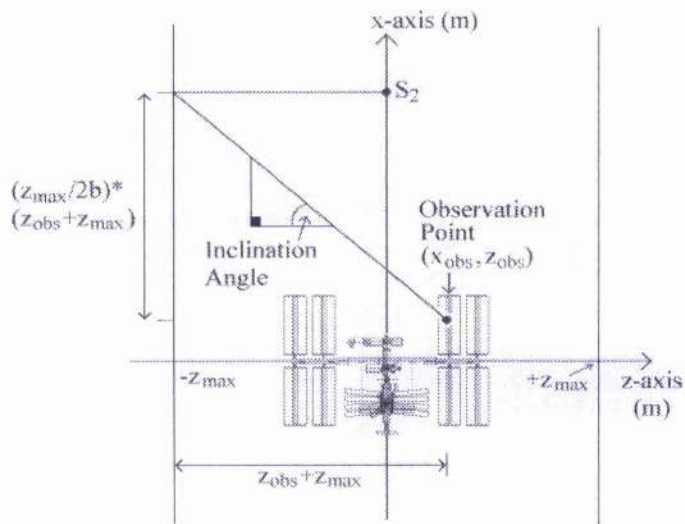


Figure 4-10 Calculation of the S_2 Point

Numerically, from the diagram above, the S_2 x co-ordinate is given by the sum of the goal z co-ordinate and the x distance required to project the goal to the x-axis, given by

$$\text{Eqn 4-11} \quad S_2 = x_{obs} + \frac{2b}{z_{max}}(z_{obs} + z_{max})$$

For the alternate inclination case, the co-ordinates must be shifted to the negative side of the z-axis, and then projected back to the x-axis in the same manner, to give the S_2 co-ordinate as

$$\text{Eqn 4-12} \quad S_2 = x_{obs} + \frac{2b}{z_{max}}(z_{max} - z_{obs})$$

4.3.2 Retreat from Docking

For the ISS Inspector mission the nominal planned docking port is located on the end of the European C&O module at the front of the station, as described in section 3.1.2. The planned docking release uses a fixed velocity mechanical push-off from the docking port, to provide Inspector with an initial downwards velocity of 0.05 ms^{-1} in the negative y direction. This initial velocity, combined with the position of the docking port below the V-bar, results in a forward drifting ellipse, which over time safely drifts ahead of the ISS as shown in Figure 4-11.

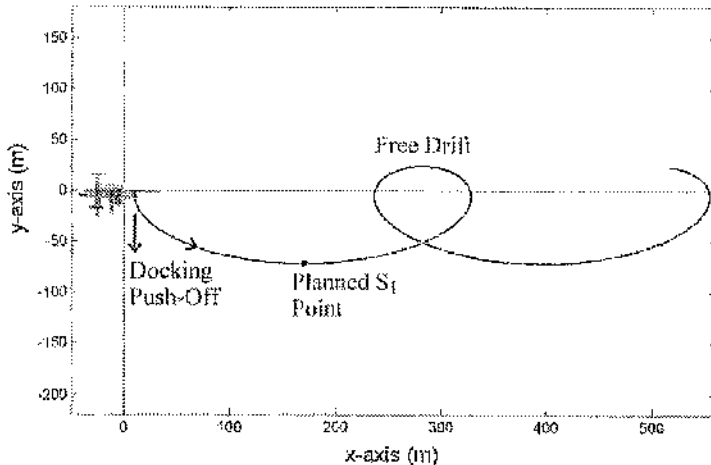


Figure 4-11 Free-flyer passive drift from Docking Release

For alternative free-flyer mounting positions on the ISS, the docking release strategy would have to be revised to ensure the safety of the retreat from the station. In some cases the entire EOS transfer and return plan may even have to be changed, as the safety of these manoeuvres is highly dependent on the start and return co-ordinates.

The Inspector free-flyer is allowed to drift from the docking release while all its systems are being checked-out and initialised. Once fully operational, the desired position for the first active manoeuvre is at the lowest point (in the y-axis) of the natural retreat ellipse, given as the S_1 point. The timing for this manoeuvre can be calculated by noting that at this position the free-flyer velocity in the y direction is zero. Eqn 2-43 can then be solved for $\dot{y}(t) = 0$ to give the time to reach S_1 after docking release where $\dot{x}_0 = 0$, as

$$\text{Eqn 4-13} \quad \tau_{s_1} = \omega \tan^{-1}(-\dot{y}_0 / 3\omega y_0)$$

This will be approximately $\frac{1}{4}$ of an orbit after release, though slightly less because of the initial downward velocity.

4.3.3 Injection into required EOS

At the S_1 point, the initial manoeuvres must be made to reach the start of the desired EOS at S_2 . The x co-ordinate of S_2 has already been found in Section 4.3.1, and from the fixed EOS parameters the y and z co-ordinates can be given as 0 and 100 m respectively. Forcing the z co-ordinate as 100 m at S_2 has the advantage that the full ellipse inclination will be already set up by this point, ensuring passive safety is initiated as early as possible. The velocities to reach S_2 can then be calculated using the targeted form of the CW equations, given in Eqn 2-46. For this, the last variable needed is the transfer time to be used for the transfer from S_1 to S_2 . Since at S_1 the y-velocity is already zero, being the turning point of the y-motion in the ellipse, and at S_2 the x-velocity will be zero as this is the start of the EOS ellipse, a transfer time of $\frac{1}{4}$ orbit is used since this should result in an efficient $\frac{1}{4}$ ellipse, making appropriate use of the previous and subsequent ellipse velocities without requiring a full optimisation of the manoeuvre.

The second set of manoeuvres, at S_2 , must then initialise the free-flyer onto the planned EOS to take it above/below the observation point. As the dimensions of the EOS are fixed, this manoeuvre will be the same regardless of the actual position of S_2 or the observation point. The z-position at S_2 should be equal to the required ellipse width, and so the only out-of-plane manoeuvre is to remove any z-velocity. In-plane, any x-velocity at S_2 must also be removed to ensure a non-drifting ellipse, and the only ΔV that need be calculated is the required y-velocity. Due to the position of S_2 on the x-axis, the required initial y-velocity can be easily calculated, as derived in Section 4.1.3, from

$$\text{Eqn 4-14} \quad \dot{y}_0 = \omega b$$

4.3.4 Forced motion to Observation Point

As Inspector on its EOS trajectory, approaches the position directly above or below the target observation co-ordinates at S_3 , the free-flyer velocity is removed to bring it to a standstill at this point, and a forced motion approach is then used to move in the R-bar direction to the observation point. This forced motion approach to the ISS is a standard Inspector manoeuvre, as detailed in Chapter 3. The ΔV cost and time required for the approach will depend on the distance to be traversed from S_3 on the EOS to the observation point, and on the final range to the station structure. As an example, a typical transfer of 150 m along the R-bar to a range of 20 m from the V-bar using a forced motion manoeuvre would take approximately 1300 seconds and require a total ΔV of 0.8 ms^{-1} .

4.4 Return to Docking

The return from observation point back to docking is slightly different from the outward phase because the co-ordinates of starting position of the manoeuvre, the observation point, are not fixed, whereas the target co-ordinates, the docking point, are. Thus, rather than a sequence of manoeuvres from a standard starting position to move the EOS over the desired goal, there is a sequence of manoeuvres from an arbitrary start point, designed to get onto a fixed EOS that passes under the fixed goal co-ordinates. This phase can also be described by a number of points where manoeuvres must be performed to follow the desired path, shown in Figure 4-12.

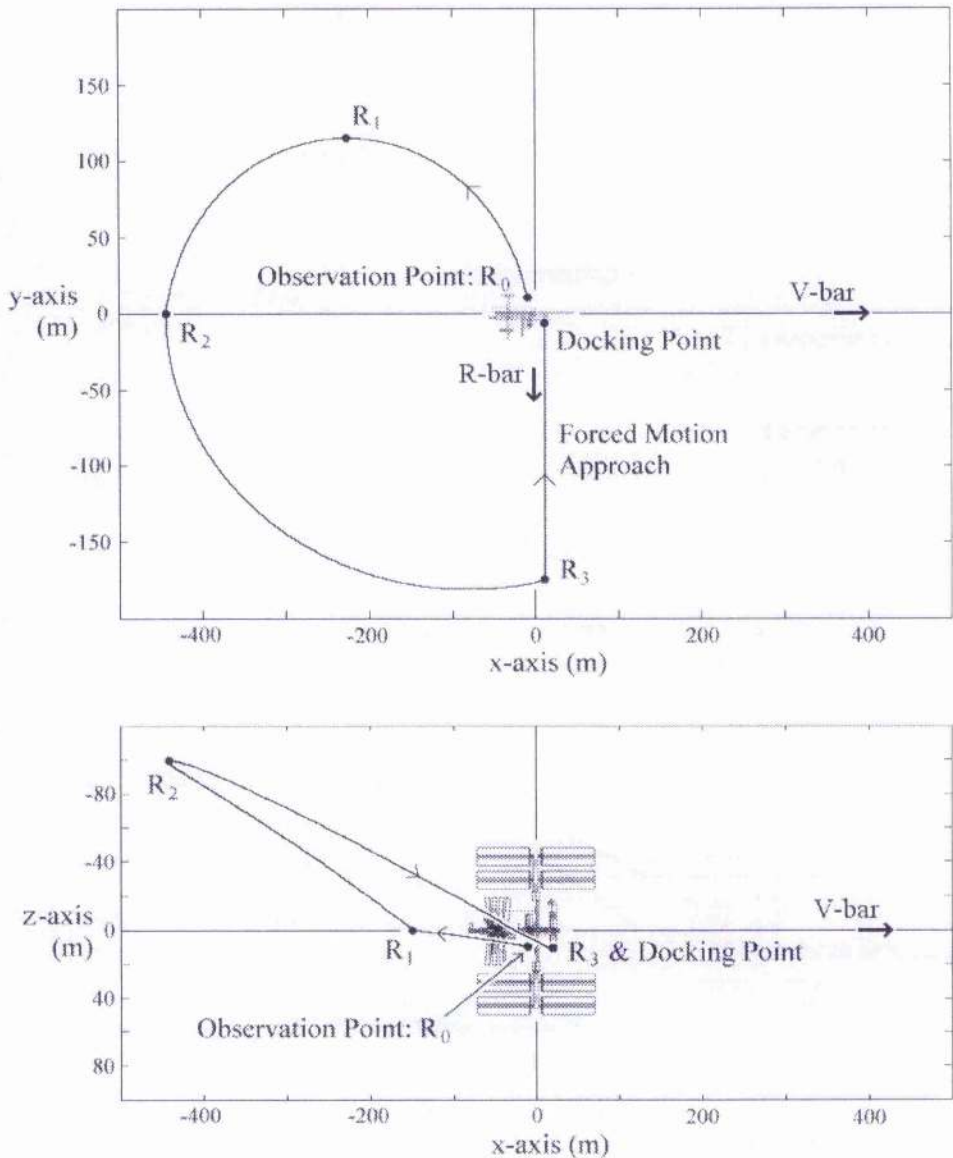


Figure 4-12 Return Phase Plan

The retreat from the observation point to the start of the return EOS at R_2 is made on a drifting ellipse, sized to guarantee safe avoidance of the ISS in case the R_2 manoeuvre cannot be made. Unfortunately this means that the position of R_2 , and hence the position of the final EOS relative to the station and the docking port, is dependent on the observation point R_0 . The position of the EOS cannot then be controlled as with the outward phase, to pass under the docking point. To overcome this limitation, the path of the ellipse can instead be controlled by small alterations in the phasing between the in-plane ellipse and the out-of-plane motion, allowing the docking target co-ordinates to be reached. The effect of this change in the phasing is to effectively tilt the entire EOS ellipse about the x-axis. As the free-flyer will

pass under the docking port at, or close to the lowest point of its ellipse, a relatively small angular tilt in the EOS will have a relatively large effect on the free-flyer path in the y-axis, as shown in Figure 4-13. Since the docking position is relatively close to the origin of the frame of reference, this allows the EOS to reach the target from a wide range of R_2 positions with a minimum required phase change.

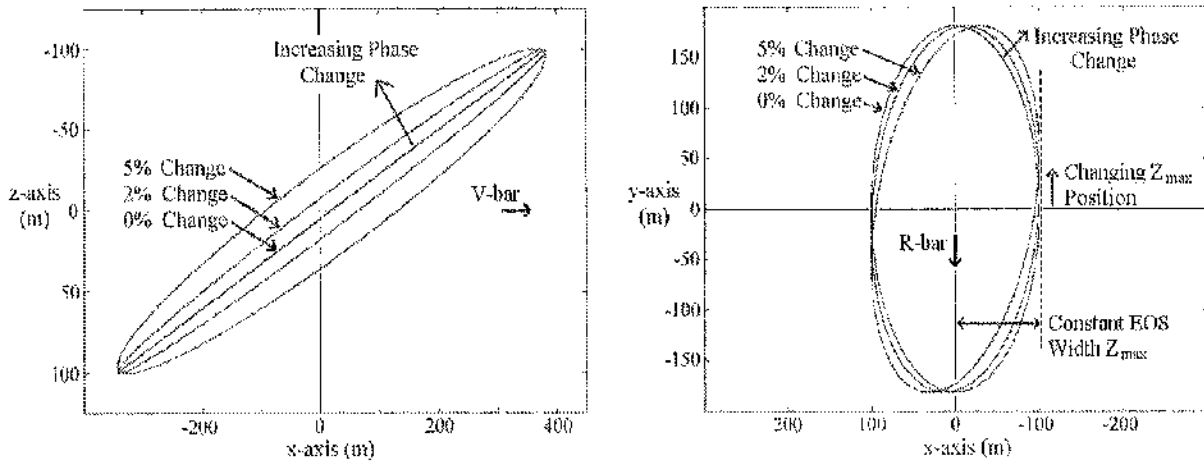


Figure 4-13 The Effect of Small Phase Changes on the EOS

Despite the small phase changes required, there will nevertheless be an impact on the safety clearance of the EOS in the y-z plane as the ellipse tilts. Fortunately, as shown in Figure 4-13, for the limited change required it can still provide acceptable safety for the ISS.

4.4.1 Manoeuvre to Safe Retreat Position

Before the first manoeuvre can be made to retreat from the observation point however, it must be checked that the standard retreat trajectory can be followed without danger to the ISS. If not an additional transfer using potential function guidance techniques must be made to move to a safe retreat position before the EOS retreat manoeuvre can be executed. A safety envelope around the ISS is therefore pre-calculated, to determine which areas around the station are unsafe for a single impulse retreat, as developed in section 3.2.3.

If an immediate retreat is not available, the easiest solution would be to use potential function manoeuvring to return to the initial observation position from the start of the observation phase. This position, chosen to be easily accessible from the first EOS, should also be suitable for an impulse retreat. For missions where extended manoeuvring has taken place during the observation phase, for example due to well separated multiple observation positions, it may be more efficient to move directly outside the retreat safety envelope. In this case, the exit position is simply found as the closest point calculated to be outside the envelope, with the transfer to this point performed with potential function manoeuvring.

Alternatively, specific safe retreat waypoints can be defined, for which unsafe retreat points in the vicinity can transfer to non-standard trajectories, before retreating onto the EOS. Examples of these three options for transfer to a safe retreat position are shown below in Figure 4-14.

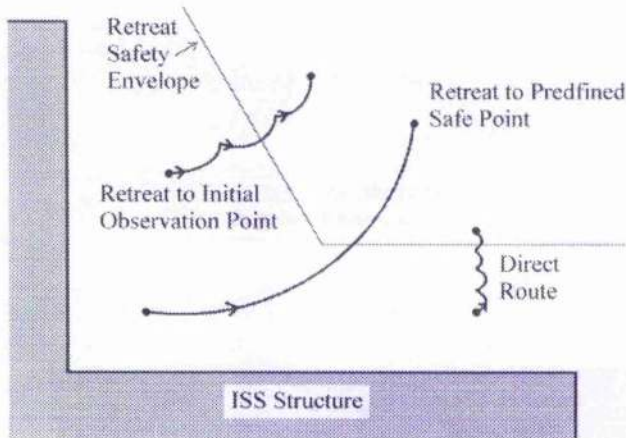


Figure 4-14 Transfer to a Safe Retreat Position Examples

4.4.2 Retreat from Observation Point

Once the safe retreat position R_0 is reached, manoeuvres may then be executed to initialise the ellipse to retreat from the ISS. The drift ellipse retreat trajectory itself is designed so that the ellipse semi-minor axis b is the same as that of the standard EOS at 200 m, but the ellipse centre will drift along the x-axis at a displacement of $4b$ per orbit. This drift rate ensures that the ISS will be outside the path of the ellipse by the end of the first orbit, thus maintaining passive safety throughout the retreat manoeuvre. The required direction of the ellipse drift is dependent on the sign of the y co-ordinate at R_0 since this value will also establish the initial direction of the free-flyer motion on the ellipse. For positions above the station, the retreat ellipse starts on the top half of the ellipse moving up and behind the ISS, requiring an ellipse drift in the positive x-direction, i.e. behind the station as shown in Figure 4-15. Conversely, R_0 positions below the ISS require a drift velocity in the positive x-direction.

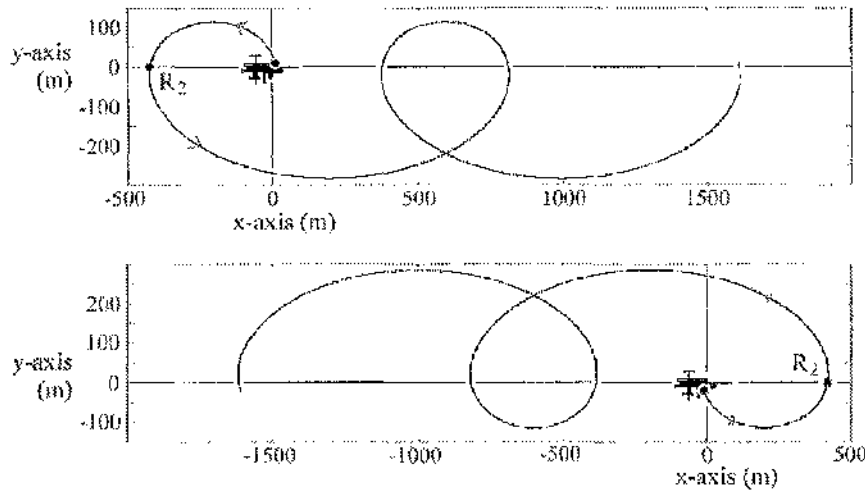


Figure 4-15 Drifting Ellipse Retreat Trajectories

The velocities required to initialise the retreat ellipse can then be calculated by first setting the drift velocity, $v_c = 4b$, in Eqn 4-1 to give the initial x-velocity as

$$\text{Eqn 4-15} \quad \dot{x}_0 = -2(3b + \omega y_{R_0})$$

Eqn 4-4 can then be rearranged to give the initial y-velocity, as

$$\text{Eqn 4-16} \quad \dot{y}_0 = \omega \sqrt{(3y_{R_0} + 2\dot{x}_0/\omega)^2 - b^2}$$

where y_{R_0} is the y co-ordinate of the observation point. As with other passively safe trajectories using ellipse drift, the trajectory will eventually traverse a complete orbit however, and further action must be taken to ensure the continued safety of the ISS.

In addition to the in-plane manoeuvre to initiate the retreat ellipse, a small out-of-plane ΔV is also performed at R_0 to ensure that at the next point R_1 , the z co-ordinate will be zero, enabling the main inclination increase manoeuvre. The magnitude of this ΔV can be calculated using the targeted CW equation 2-46. However, until the complete manoeuvre has been calculated the exact timing of the R_1 point cannot be determined since it is the timing of the R_1 manoeuvre that is used to control the EOS phasing.

4.4.3 EOS Transfer back to Docking Position

The final step in setting up the in-plane portion of the EOS required to pass under the docking point is to remove the drift velocity of the retreat ellipse. To minimise the ΔV required, this manoeuvre takes place as the free flyer path crosses the x-axis at R_2 . From Eqn

4.1, this gives $\dot{x}_0 = 0$ at R_2 requiring a ΔV along the x-axis, while the y-velocity is left unchanged.

The manoeuvre at R_2 , once performed, completes the construction of the in-plane ellipse, leaving only the calculation of the out-of-plane motion required to synchronise the two ellipses to pass under the docking point. As previously mentioned, this synchronisation is controlled through the correct timing of the R_1 manoeuvre. To determine this timing, the first step is to propagate the in-plane ellipse from R_2 to find the time at which the trajectory passes under the docking point, by solving the CW equation 2-39 for $x = x_{\text{dock}}$. This completely defines the time at R_3 , from which we can work back via the out-of-plane motion to find the time at R_1 . At R_1 , $z = 0$ and the EOS inclination is set to the fixed value of $z_{\text{max}} = 100$ m. The out-of-plane motion can therefore be propagated using Equation 2-42 from this point, to find the time after R_1 that the z-position is equal to the docking target z co-ordinate. It must however be ensured that the correct root is found when solving the CW equation for $z = z_{\text{dock}}$, as the periodic z motion may also cross the goal co-ordinate at an earlier time while the in-plane motion is on a different part of the ellipse. The z-solution is therefore only searched for within a certain time envelope defined by the in-plane motion of the EOS, as shown in Figure 4.16.

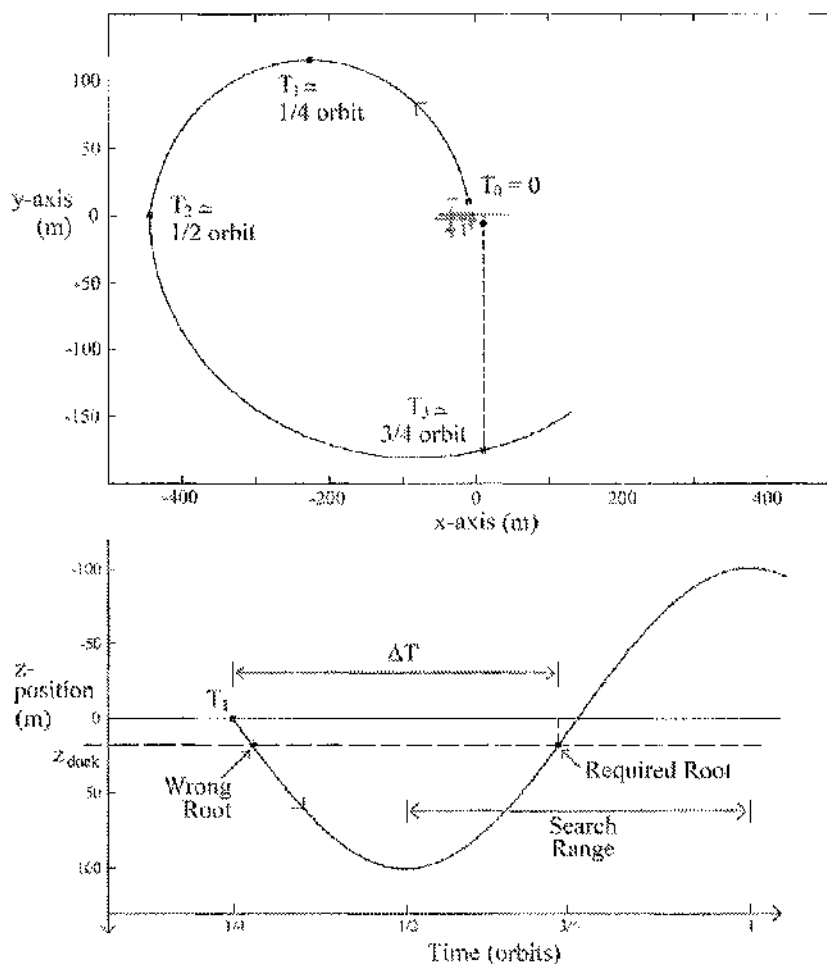


Figure 4-16 Solution of the Z Motion for R_1

For initial R_0 positions above the ISS this strategy requires a solution to $z = z_{\text{dock}}$ within $\frac{1}{4}$ to $\frac{3}{4}$ orbits after R_1 , or for R_0 positions below the ISS within $\frac{3}{4}$ to $1\frac{1}{4}$ orbits after R_0 , since the path must complete an additional $\frac{1}{2}$ orbit around the station before passing under the target. Given the time at R_3 from the in-plane calculations, and the time required by the out-of-plane motion to reach R_3 from R_1 , the time at R_1 can be obtained by subtracting the out-of-plane duration (ΔT in Figure 4-16) from the in-plane R_3 time. With the time at R_1 known, the z axis ΔV required at R_0 to reach R_1 at $z = 0$ can then be determined, completing the calculation. The full sequence of calculations required for this complex phase, is detailed below in Table 4-1.

Calculation Type	Position in Plan	Aim of Calculation
ΔV : in-plane	R_0	Set up 200 m EOS with $V_c = 4bd$
Propagate path (in-plane)	R_0 to R_2	Calculate time to cross x axis to get time at R_2
ΔV : in-plane (x axis only)	R_2	Remove ellipse drift
Propagate path (in-plane)	R_2 to R_3	Calculate time to pass under docking target to get time at R_3
ΔV : out-of-plane	R_1	Set EOS width to z_{\max}
Propagate path ^a (out-of-plane)	R_1 to R_3	Calculate time within specified limits after R_1 for $z = z_{\text{dock}}$ to get time from R_1 to reach R_3
Calculate time	R_1	Subtract to get time at R_1
ΔV : out-of-plane	R_0	Calculate initial z velocity required to reach R_1 with $z = 0$

^aSolve within correct interval: $y(R_0) > 0$ then R_1 to R_3 limit $1/4$ to $3/4$ orbits

$y(R_0) < 0$ then R_1 to R_3 limit $3/4$ to $1\frac{1}{4}$ orbits

Table 4-1 Calculation Sequence for Return Trajectory

4.4.4 R-Bar Forced Motion Approach to Docking

The forced motion approach used to transfer up from the EOS point below the docking co-ordinates is another example of a standard Inspector approach manoeuvre. In comparison to the approach to the observation point, the main difference is that in docking the free-flyer must manoeuvre to the ISS structure itself, increasing the safety constraints at the end of the transfer. During this approach however, the Inspector free-flyer will have access to enhanced guidance and navigation sensors, used specifically for docking manoeuvres. Alternatively the free-flyer may be berthed using the ISS - SSRMS robotic arm rather than directly docking with the station, as discussed in Chapter 3.

4.5 EOS Manoeuvre Cost

Some of the range of possibilities for an EOS transfer and return from a single observation position are demonstrated in the following examples, shown in Figure 4-17 below. These examples illustrate the use of the EOS strategies to transfer between the docking port situated on the COF module, and observation points over a range of positions both above and below the ISS structure.

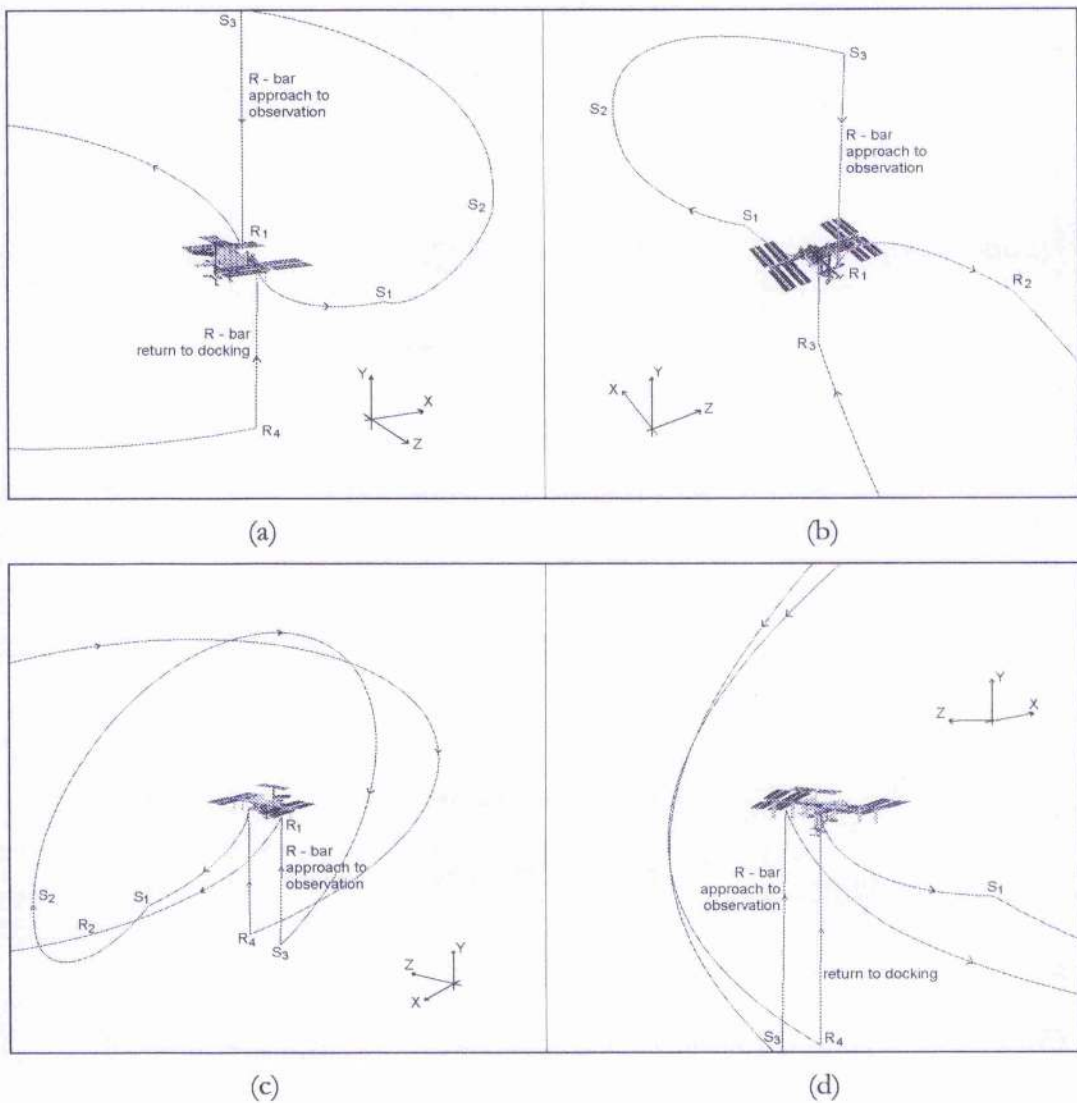


Figure 4-17 Ellipse of Safety Examples

The costs of these missions, both in terms of the total time taken and the ΔV required for each stage of the manoeuvre, are detailed in Table 4-2.

Example	(a)	(b)	(c)	(d)
Start/End Co-ordinates	10.0, -6.0, 10.0	10.0, -6.0, 10.0	10.0, -6.0, 10.0	10.0, -6.0, 10.0
Observation Co-ords	-6.0, 10.0, 15.0	-36.0, 5.0, 0.0	-16.0, -18.0, 20.0	0.0, -7.0, 35.0
Total Transfer Time (s)	11,969	12,187	16,777	16,818
$S_1 \Delta V (\text{ms}^{-1})$	0.1566	0.1144	0.1042	0.2111
$S_2 \Delta V (\text{ms}^{-1})$	0.4809	0.4885	0.4989	0.4831
$S_3 \Delta V (\text{ms}^{-1})$ (to stop before forced motion)	0.4660	0.4700	0.4628	0.4475
$R_0 \Delta V (\text{ms}^{-1})$	0.2137	0.2123	0.2226	0.2209
$R_1 \Delta V (\text{ms}^{-1})$	0.0897	0.1140	0.0521	0.0416
$R_2 \Delta V (\text{ms}^{-1})$	0.0484	0.0484	0.0484	0.0484
$R_3 \Delta V (\text{ms}^{-1})$ (to stop before forced motion)	0.4196	0.4118	0.4261	0.4239
Total Transfer $\Delta V (\text{ms}^{-1})$	1.8749	1.8594	1.8151	1.8765

Table 4-2 EOS Costs

The interesting result is that although the transfer time taken varies considerably between observation points above and below the station, the total ΔV for the manoeuvres is relatively constant throughout. This is due to the fixed EOS dimensions used, requiring similar velocities to initialise the EOS trajectories regardless of the target position. The increased transfer time for observation co-ordinates below the ISS comes from the additional time spent on the EOS trajectory to transfer under the station during the approach, and the additional transfer above the station during the return to docking. The cost of the forced motion approach manoeuvres will also have a significant effect on the total cost of the mission. Due to the fixed ellipse size, this cost will however be mainly dependent on the range of the desired observation co-ordinates from the x-z plane, and hence the distance travelled using forced motion. However, this will be balanced by the increased station-keeping cost of an observation position further from the V-bar.

CHAPTER 5: POTENTIAL FIELDS

For the ISS-Inspector mission, the project leaders Astrium would like to enhance the inspection capabilities of the Inspector Free-Flyer by providing the ability to manoeuvre between different observation points while close to the space station. This capability would allow multiple observation points to be planned to inspect one target from multiple viewpoints, or multiple inspection targets to be grouped together in a single mission. To enable manoeuvring during the inspection phase a guidance strategy is therefore needed to satisfy the constraints of path finding and obstacle avoidance, and ensure the safety of trajectories close to the ISS structure.

Previous work at the Department of Aerospace Engineering at the University of Glasgow, under a European Space Agency contract, demonstrated the use of potential functions for real-time control and obstacle avoidance of the European ATV during an autonomous approach to the ISS [4]. This work dealt mainly with the autonomous avoidance of a small number of discrete obstacles, such other free-flyers or co-orbiting satellites, throughout the ATV approach from entering the Approach Ellipsoid at 4km up to the edge of the Keep Out Sphere at 200m and through the docking approach cone to the ISS. For these tasks the potential function technique proved successful in attaining target co-ordinates and safely avoiding both stationary and mobile obstacles under a full non-linear simulation of the ATV. For the Inspector vehicle however, the potential function method used for the ATV is unsuitable for guidance at close range to the ISS. This is due to the problems associated with the creation of local minima in the global potential field, as described in section 1.2.4, which occur frequently when trying to represent a complex non-convex obstacle such as the ISS using analytical potentials.

An overall review of the field of path planning was given in chapter 1, but in this chapter, two specific artificial potential field methods will be developed for use in the off-line path planning of manoeuvres within a control volume close to the ISS. This control volume is defined as a manoeuvring space containing start and goal points and the obstacle configuration in the volume, which provides a finite space within which to calculate the potential fields, whilst also constraining manoeuvres to within this volume. These potential fields provide the basis for the path planning of the Inspector Free-Flyer during the observation phase. The use of the potential field for detailed trajectory planning and real-time guidance will be fully developed in Chapter 6.

5.1 The Laplace Artificial Potential

The first potential field method that will be developed for the close manoeuvring of the Inspector Free-Flyer utilises a discrete potential field based on the Laplace function. The Laplace equation and other harmonic functions have been the subject of development for path finding in a number of papers since they circumvent the local-minima problem that affects many other techniques. Typically the methods developed either satisfy the Laplace equation through the use of a fluid flow representation [66] with a combination of Laplacian potential function elements such as sources and sinks (as described previously), or alternatively by applying a discrete form of the Laplace equation to a discrete representation of the obstacle configuration space [59] [63]. An alternative approach has also been developed to use harmonic functions based on the Laplace equation in a panel method, similar to that used in the numerical calculation of the flow over an airfoil, to represent obstacles of an arbitrary shape [68].

For the Inspector path finder, a discrete approach to satisfying the Laplace equation was chosen for easy application to sets of large complex obstacles such as the ISS. While the fluid flow representation has the advantage of a lack of pre-processing, the problems associated with representing the ISS structure as a combination of flow elements precludes its use for Inspector path finding. Similarly, representation of the ISS by the panel method while possible (the graphical representation shown in Chapter 3 is also comprised solely of flat panels), is limited by the large number of panels required which would be prohibitive from a global storage and calculation perspective. A discrete representation of the obstacles in the control space also has the advantage of being available for use by other mission planning elements such as collision safety checking and radio link interference calculations, as discussed in Chapter 3.

5.1.1 The Laplace Equation

Laplace's differential equation is important in a wide field of research areas because the final steady-state of many physical phenomena can be expressed by a solution to this equation. For example, the solution can be used to represent many different potential fields, from electrostatic and magnetic potentials, to temperature, gravitational, and velocity potentials. Laplace's equation itself, states that for a steady state solution the second derivative of the potential must equal zero over the control volume.

This can be written as

$$\text{Eqn 5-1} \quad \nabla^2 \phi = \frac{\partial^2 \phi}{\partial x^2} + \frac{\partial^2 \phi}{\partial y^2} + \frac{\partial^2 \phi}{\partial z^2} = 0$$

If Eqn 5-1 is satisfied, then the potential ϕ is harmonic over the control space, and can have no local minima in the potential. This can be proved analytically, however for the purposes of this discussion it can also be demonstrated by looking at the definition of a minimum potential point, shown in Figure 5-1.

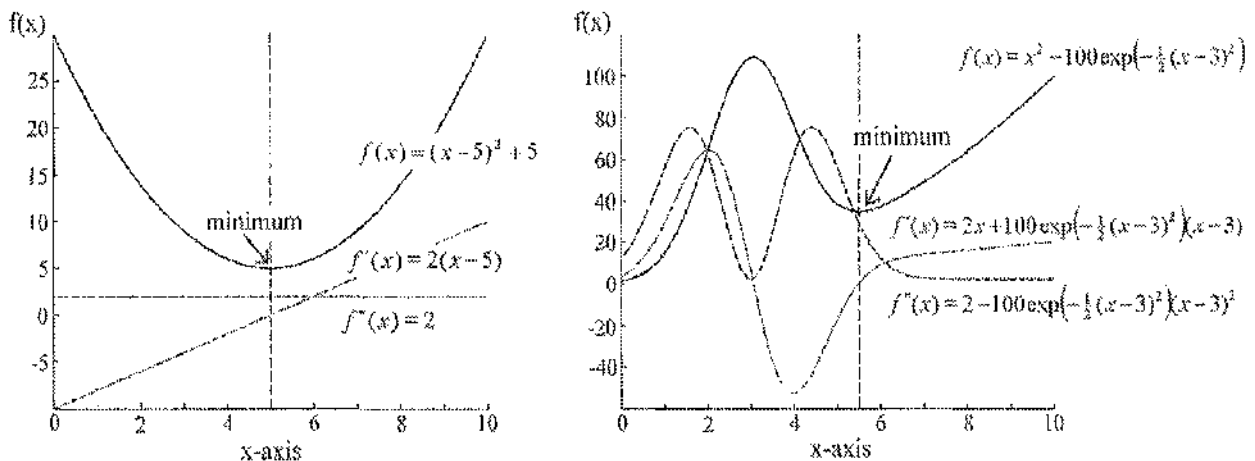


Figure 5-1 A Potential Minimum

Any potential minimum point must by definition have a zero potential gradient, and both a positive potential gradient on one side and a negative gradient on the other, as shown above. This changing gradient can then only be possible if the second derivative is non-zero, which violates the Laplace equation. So, for Eqn 5-1 to be satisfied there must be no local minima in the control volume.

For path finding, we apply Laplace's equation to a potential field over the control volume, which contains both the start and goal positions. If an artificial low potential is introduced at the goal point before the Laplace equation is applied to the control volume, the resulting potential field will then have a single minimum located at the goal point. This guarantees that a path will be found from any position in the control volume to the goal, if a path is possible. A continuous potential field can then be obtained from the discrete results by interpolating between the calculated nodal potentials.

5.1.2 Discretising the Laplace Equation

For obstacle structures as complex and changeable as the ISS, it is not feasible to globally solve the Laplace equation by analytical methods. The control volume surrounding the manoeuvre start and goal points is therefore divided into a discrete mesh, upon which the obstacle boundary points can be defined, before a discrete form of the Laplace equation is applied iteratively to the potential mesh. The Laplace differential equation Eqn 5-1 can be replaced by a difference equation, given by

$$\text{Eqn 5-2} \quad \left(\frac{\phi_{i+1,j,k} - \phi_{i,j,k}}{\Delta x, \Delta x} - \frac{\phi_{i,j,k} - \phi_{i-1,j,k}}{\Delta x, \Delta x} \right) + \left(\frac{\phi_{i,j+1,k} - \phi_{i,j,k}}{\Delta y, \Delta y} - \frac{\phi_{i,j,k} - \phi_{i,j-1,k}}{\Delta y, \Delta y} \right) + \left(\frac{\phi_{i,j,k+1} - \phi_{i,j,k}}{\Delta z, \Delta z} - \frac{\phi_{i,j,k} - \phi_{i,j,k-1}}{\Delta z, \Delta z} \right) = 0$$

where $\phi_{i,j,k}$ is the Laplace potential at node (i,j,k) , and $\Delta x, \Delta y, \Delta z$ are the step sizes between mesh points in each direction. If the mesh is equally spaced, that is, the step sizes are equal in each direction, then Eqn 5-2 can be simplified to give

$$\text{Eqn 5-3} \quad \phi_{i+1,j,k} + \phi_{i-1,j,k} + \phi_{i,j+1,k} + \phi_{i,j-1,k} + \phi_{i,j,k+1} + \phi_{i,j,k-1} - 6\phi_{i,j,k} = 0$$

or

$$\text{Eqn 5-4} \quad \phi_{i,j,k} = \frac{1}{6}(\phi_{i+1,j,k} + \phi_{i-1,j,k} + \phi_{i,j+1,k} + \phi_{i,j-1,k} + \phi_{i,j,k+1} + \phi_{i,j,k-1})$$

At the start of the calculation, the initial potential at each node is set to a value of 1, and the potential at the specified goal point is set to 0. The value of the potential at any node in the mesh that is defined as either an obstacle node, an edge node, or the goal node is then fixed so that these potentials will remain at the highest value of 1 (or at 0 in the case of the goal) throughout the calculation of the Laplace potential field. The Laplace equation is then solved over the free-space nodes by iteratively applying Eqn 5-4 to each node. The use of an initial potential value of 1 at all nodes means that as the iterations progress, the lower potential value at the goal gradually propagates out around the surrounding obstacles, as shown in Figure 5-2, while ensuring that no local minima are formed.

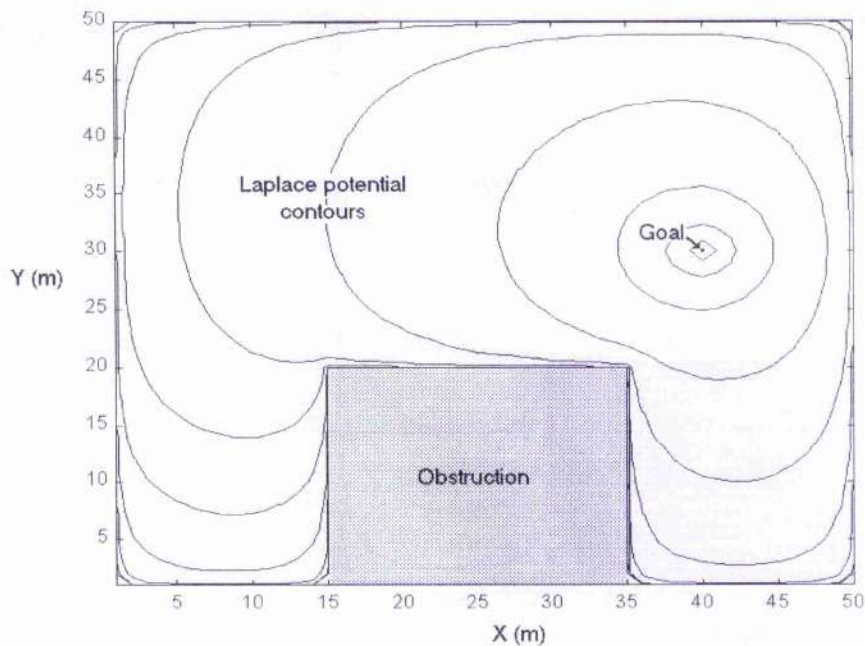


Figure 5-2 The Laplace Potential Field

The use of equal step sizes in the control volume mesh is not absolutely necessary for the formulation of the discrete Laplace equation shown above or for other discrete potential fields for that matter. For example, many discrete path finders use a ‘quadtree’ approach to add extra nodes, and hence extra detail, to complex areas while reducing the number of nodes used to represent large obstacle free areas to reduce storage and calculation requirements [94]. However, many quadtree implementations lose significant intermediate nodes between obstacles and the control volume boundaries, which may result in reduced safety clearances from obstacles. Discrete grids with randomly positioned nodes have also been proposed, mainly as a solution in path finders that step directly between nodes, to reduce the negative effects of being limited to traversing in axial and diagonal directions. In our case, the use of equally spaced nodes simplifies the formulation and application of the Laplace equation, while ensuring a minimum available detail both at obstacles and in the intermediate space. And since the path finder is not to be constrained to stepping between nodes, there is little advantage to be gained from randomisation.

One problem that can affect the iterative calculation of the Laplace potential is the difficulty of propagating through small gaps between obstacles. Given a gap between obstacles that only has one free node between fixed boundary nodes on either side, it becomes hard for a low potential area on one side of the gap to propagate to the other side of the obstacles. This comes about from the formulation of the discrete Laplace potential function, which calculates each potential as an average of the surrounding potentials. If a number of

these surrounding potentials are fixed at a value of 1, then it will take a much larger number of iterations for a single low potential on one side to significantly propagate across this point. Fortunately this problem mainly affects the two dimensional case since 2 of a possible 4 surrounding potential nodes may be fixed at 1. In three-dimensions, it is highly unlikely that more than 2 out of a possible 6 would be boundaries, and low potentials are more likely to be able to propagate around the problem area.

5.1.3 Example Paths through the Laplace Potential Field

With the Laplace potential calculated at each node, a path can then be found by following the path of steepest descent through the potential to reach the goal. The two examples in Figure 5-3 show paths found using a Laplace potential field over a 2-dimensional control space. Figure 5-3(a) demonstrates the ability of the Laplace potential to find paths around concave obstacles that would produce potential minima in other methods, and Figure 5-3(b) shows a potential field used to find paths to the goal point from a range of starting positions in the control volume. Four examples of 3-dimensional paths found using the Laplace potential are also shown in Figure 5-4. Figure 5-4(a) & (b) show paths generated around and along the surface of two elements of the ISS structure, the COF module and a solar array respectively. While Figure 5-4(c) & (d) demonstrate the path finder's ability to travel between obstacles to reach the goal, if necessary for the mission. The examples shown in Figure 5-4 also illustrate the control volume and discrete obstacle representation used to determine the Laplace potential field by the obstacle nodes.

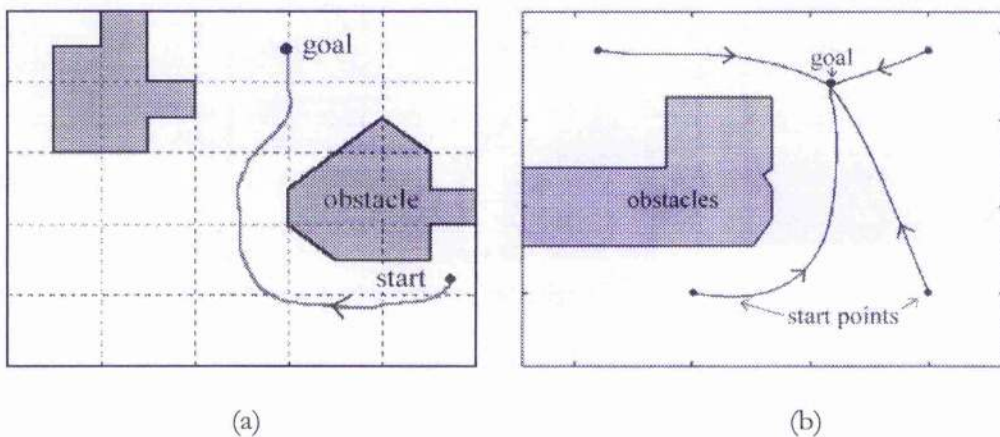
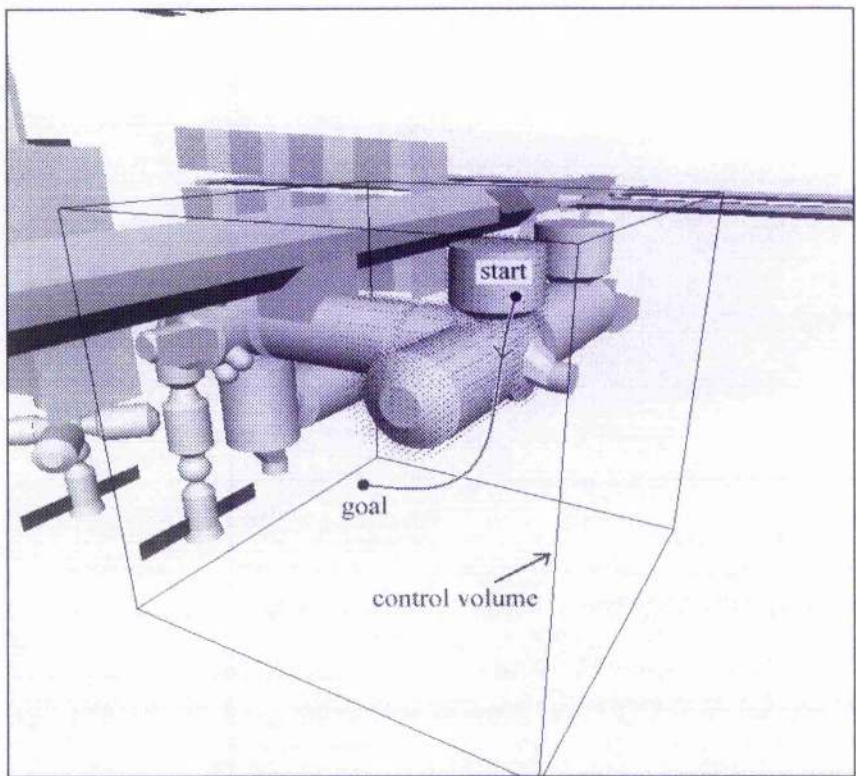
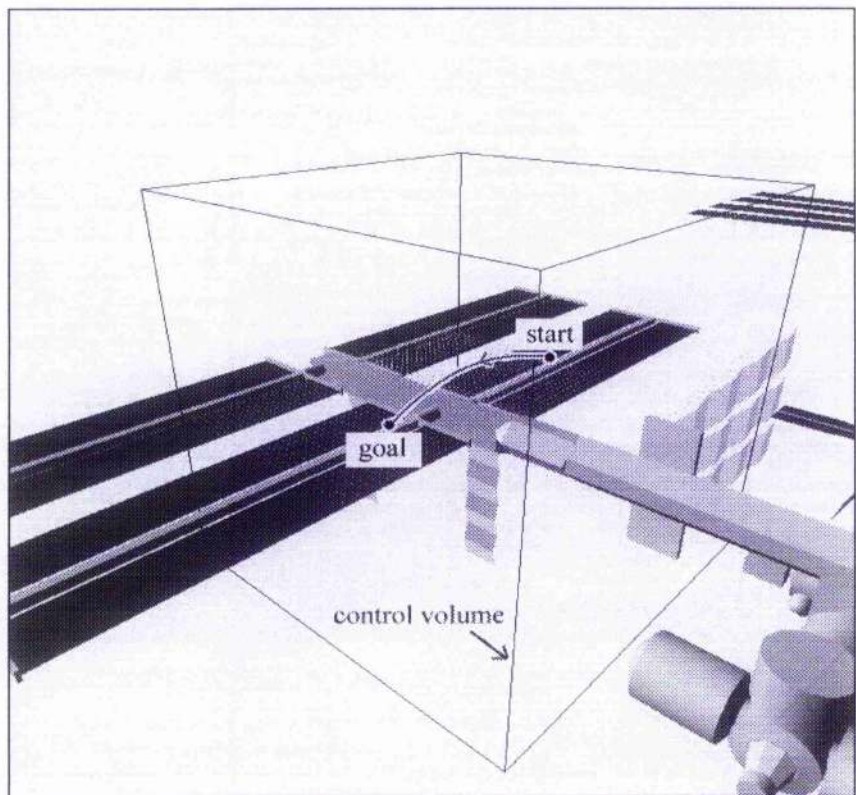


Figure 5-3 Example 2D Laplace Paths

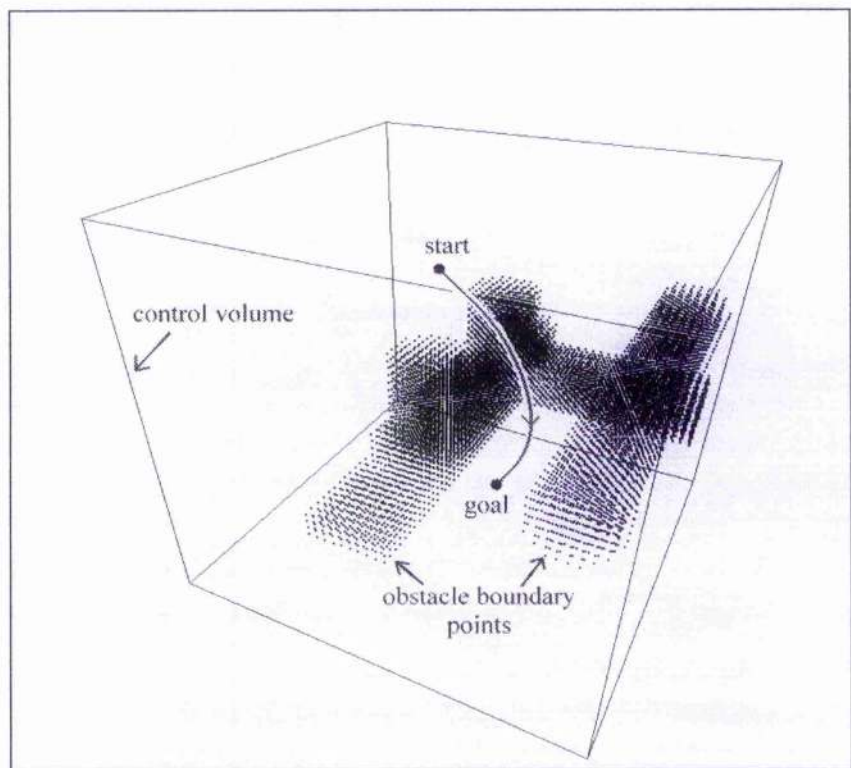


(a)

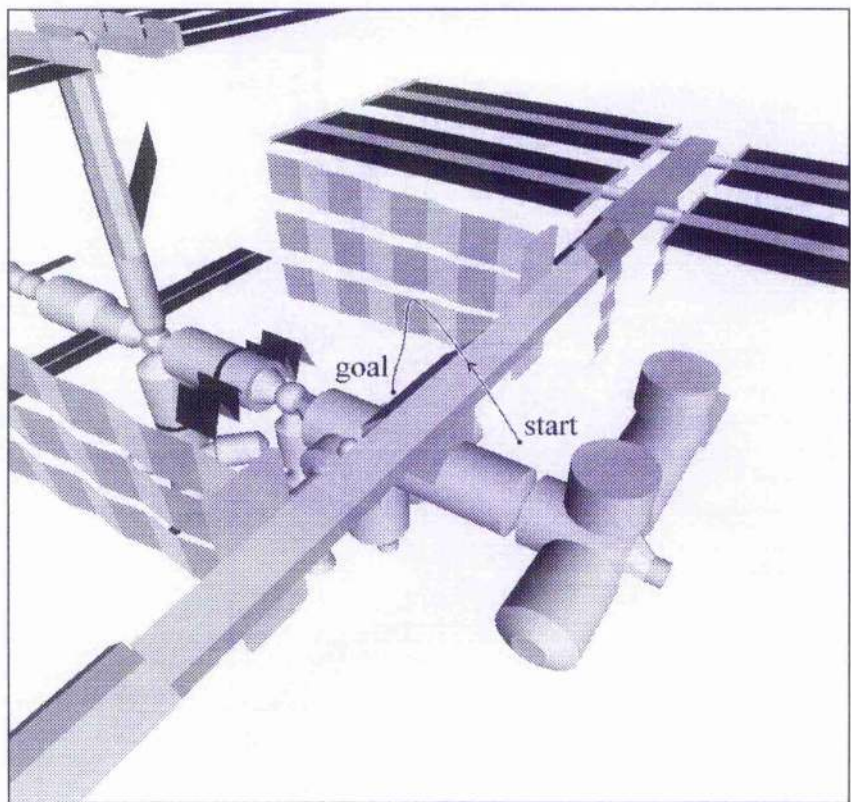


(b)

Figure 5-4 Example 3D Paths around the ISS



(c)



(d)

Figure 5-4 Example 3D Paths around the ISS

All of these examples show the characteristic of the Laplace potential to produce paths that maintain an optimum safety clearance between the path and the surrounding obstacles at all times. The effects of a small change in path co-ordinates on the final path are illustrated in Figure 5-5, showing the alternative paths available in a complex obstacle environment such as the ISS, giving a range of options for a safe path to the goal while avoiding the main truss structure.

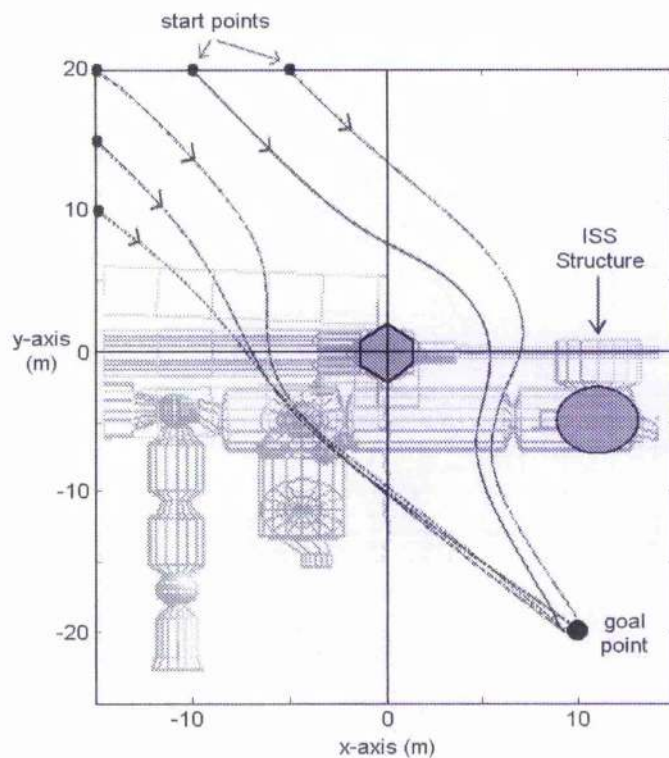


Figure 5-5 Path Variations from Small Changes in Coordinates

5.1.4 Merits of the Method

The main advantages of the discrete Laplace equation method are in the ease of formulation and calculation of the potential, giving a potential field with one single minimum guaranteed at the goal point. For free-flyer manoeuvring and safety, the Laplace potential provides smooth continuous control throughout the control volume, and produces paths with good clearance from obstacles while being constrained within the defined volume. Unlike some potential function methods where obstacle potentials must be designed to quickly fade outside the obstacle boundary to avoid undesirable effects on the global potential, the influence of obstacles in the Laplace potential field extends far from their actual boundaries. This gives a global potential field that can recognise the presence of obstacles from a distance, and plan paths to avoid them from an early stage, rather than travelling directly toward a hazard and then skirting around its boundaries as can happen with other potential fields.

Another aspect of this behaviour is that paths starting from positions close to obstacles will tend to move safely away from the obstacle while finding a path to the goal instead of remaining close to the hazard. These behaviours can both be seen in Figure 5-6, which shows a contour plot of the two dimensional potential field generated around an adversely orientated concave obstacle. Path A demonstrates the ability of the Laplace path finder to recognise the presence of the obstacle and flow a path to avoid it from the start of the manoeuvre. Similarly, Path B shows how a path starting effectively inside a concave obstacle can move away from the obstacle walls into safe free-space before proceeding towards the goal. It is these behaviours which ensure good safety clearance of paths found using Laplace potential fields that make the method well suited to path finding for the safety critical ISS-Inspector Free-Flyer mission.

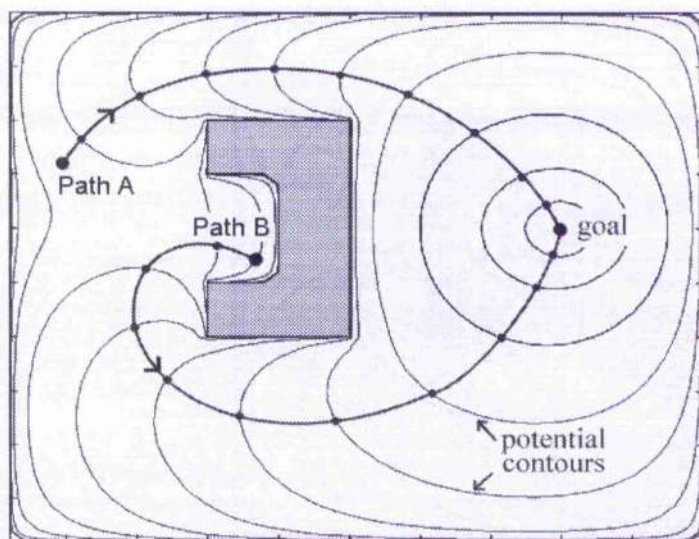


Figure 5-6 Safe Path Finding Behaviours

As we have already seen, the Laplace potential can be easily extended to 2 and 3 dimensions, and in fact the formulation of the Laplace equation makes it easy to extend to higher dimensions. For a discrete solution however, extension even to 4 dimensions becomes quickly limited by both the storage requirements for the potential mesh, and the calculation time required. As an example, in the case of the Inspector path finder a three-dimensional mesh size of $50 \times 50 \times 50$ nodes is used, giving a storage requirement of 1,000,000 bytes (for 8 byte double variables) just for the potential values, and additional storage is required to define the obstacle boundaries. So implementing a fourth ‘time’ dimension, even with a low resolution of 100 seconds, would require a huge 36 Mb of memory to represent a time span of one hour. For such a large number of nodes, the computational time required to iteratively apply the Laplace equation also becomes a significant limitation on the usable mesh size.

Though this limits the use of a time dimension to represent a rapidly changing obstacle configuration, it is possible to represent a set of slowly moving obstacles with a relatively small number of points along the time axis by defining the position of an obstacle in each time step by the total volume covered during this interval. For example, the changing orientation of the main ISS solar arrays, which rotate through 360° during each orbit, could be represented by four intervals in the time axis each describing the space occupied by the panels in a $\frac{1}{4}$ orbit, as shown in Figure 5-7. Combined with a real-time path finder or guidance algorithm, this can be used to permit the Inspector Free-Flyer to follow paths over the solar panels while autonomously avoiding collisions with these rotating obstacles.

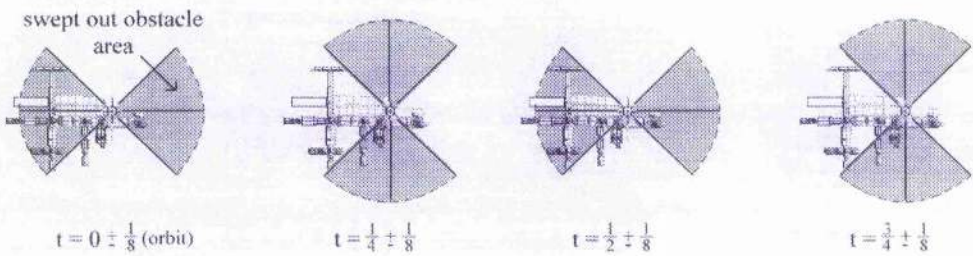


Figure 5-7 A Discrete Time Representation of the Solar Array Configuration

Other than the rotating ISS elements, moving obstacles in the vicinity of the ISS structure, such as other free-flying vehicles or astronauts, are unsuitable for representation in this manner since their motion is unlikely to be known at the Inspector mission planning stage. In any case, the representation of free-flyer motion would be seriously limited by the available time scale.

As demonstrated by the previous discussion, the main disadvantages of the discrete Laplace potential method are in the computational calculation time and storage requirements of the potential field. The computational iteration requirements are partly reduced by using double precision values for storage and calculation of the nodal potential values, since the extra accuracy obtained permits small potential gradients to propagate through the potential field more quickly. This increased calculation speed is offset however by the increased storage requirements for double's over standard single precision floating point variables, typically 8 bytes compared to 4 bytes for floats. For a fixed $50 \times 50 \times 50$ potential mesh this is not problematic, however for larger mesh sizes such as for a four dimensional mesh, float variables may be used to reduce mesh storage requirements at the cost of an increased number of iterations to calculate the potential field. One further disadvantage is that though a calculated potential field can be used to find a path from any position in the control volume to the goal, it is only valid for a fixed goal position, and in the case of a three dimensional mesh,

for a fixed obstacle configuration. Any change in the goal or obstacles therefore requires a complete recalculation of the potential field.

Fortunately, for mission planning operations at ISS ground stations, computational power will be readily available, reducing many of the inherent Laplace potential disadvantages. This, along with the use of fixed mesh dimensions, scaled to the control volume around the start and goal points, reduces potential field calculation times to the point where complete recalculations of the potential are executed in semi-real time. For example, for a PC based on a Pentium 166 MHz processor, calculation time of the Laplace potential field for the $50 \times 50 \times 50$ mesh is of the order of 1 sec, while for a Celeron 500 MHz based PC this is reduced to approximately 0.1 sec. Given these baselines, even the laptop based control station onboard the ISS would have sufficient processing power to recalculate Laplace potential fields if required.

5.1.5 Specification of Obstacle Boundary Array

A critical part of the calculation of any discrete potential field is the definition of a boundary array to describe the potential nodes that represent obstacle points. This boundary definition must, as previously determined, be easily modified and updated to take account of changing ISS obstacle configurations, and specifically must also support angular updates to take account of rotating, Sun orientated components. To simplify this process, a system of functions has been developed allowing standard shapes such as Cylinders, Spheres, Cuboids, and Panels to be easily added to the boundary mesh. Each of these functions correspond the functions used to graphically draw the ISS modules and elements in the Inspector Camera Simulation discussed in section 3.3. For example, for a cylindrical ISS element such as the COF module drawn in the graphical model, a corresponding element can be added to the ISS boundary mesh by calling the boundary Cylinder function with the same dimensions and position. The applied function then attempts to define the best representation of the required shape, by assigning specific nodes in the boundary mesh as obstacle nodes, subject to a specified representation type. For example, in two dimensions a circle would be defined on the boundary mesh as shown in Figure 5-8, either by the most conservative ‘safe’ method of assigning the set of boundary nodes required to completely enclose the circle, or by assigning a ‘best fit’ set of nodes that most closely represents the circle shape.

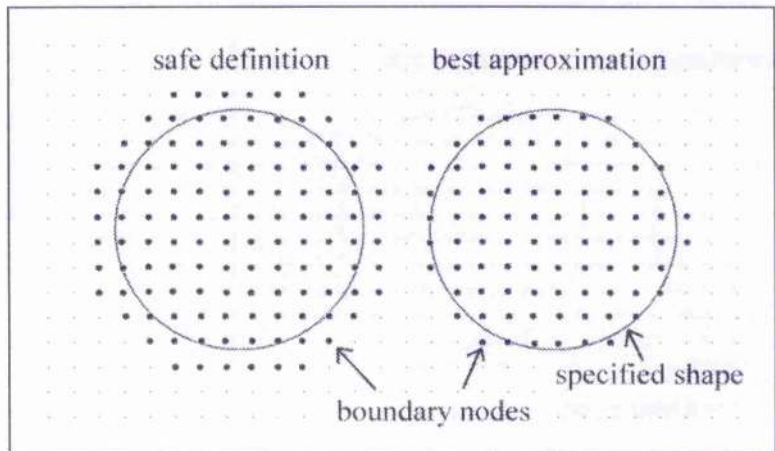


Figure 5-8 The Boundary Definition of a Circle

The use of such a set of functions allows the obstacle boundary mesh used to calculate the potential field to be specifically tied to the graphical model of the ISS, through the use of comparable model data files, ensuring compatibility between the complimentary models.

5.2 The Wave-Front Cost Method

The second path finding method developed for the ISS-Inspector mission planner makes use of a wave-front algorithm as an alternative to the discrete Laplace equation, to generate a cost field instead of a potential field. The method used is essentially a development of a simple distance transform algorithm rather than an actual potential field, where each node is assigned a cost based on the shortest calculated distance to the node from the goal point. The ‘wave-front’ name comes from the nodal cost calculation method which determines the shortest distance or cost at each node by propagating an expanding wave-front of minimum cost points from the goal node [94]. This distance transform wave-front is actually an application of the simplest case of another method, the A* algorithm discussed in section 1.2.6, and works similarly to other methods of this type, by assigning nodes a cost based on the lowest distance to get to each point from the start point.

The A* search uses a heuristic estimate of the remaining distance to reach the goal to optimise the search through the nodes towards the goal. Unfortunately, the directed search that makes the A* algorithm efficient in searching for a single optimum path in a discrete world, also makes it unsuitable for planning arbitrary safe paths to the goal point in a continuous volume. For the Inspector Free-Flyer, path planning and navigation requires that a potential field be able to provide guidance toward the goal from any position in the control volume, not just along the best route from its initial position. The distance transform method

developed is an instance of the A* algorithm where the cost estimate is equal to zero at all points. As a result the search is therefore undirected and will extend over the entire discrete mesh of nodes. Furthermore, by propagating the wave-front from the goal point outwards, rather than from the start toward the goal as usually the case in an A* search, the cost field obtained will have a single minimum point at the goal, allowing it to be used in the same way as the Laplace potential field. Finally, though the use of fixed mesh step sizes actually has little effect on the calculation of the cost field, many of the same arguments as for the discrete Laplace potential may be applied, such as the preservation of detail between boundaries. So a fixed step size will also be used for the wave-front cost method, providing the added advantages of ensuring compatibility with the previously developed obstacle boundary array, and with subsequent potential function guidance techniques.

5.2.1 The Wave-Front Algorithm

The operation of the wave-front cost algorithm is in fact relatively simple, and relies on maintaining a list of the current nodes in the wave-front as it expands from the goal point. Initial cost values, as with the Laplace potential are assigned the maximum allowable cost, although in this case the cost range is not known prior to calculation so the maximum cost must be given by a predefined limit. The goal point is assigned a cost of zero, and added to the wave-front list as the initial node. The wave-front is then allowed to expand by checking the adjacent nodes of each node in the current wave-front list, as shown in Figure 5-9. A new cost for each adjacent node is calculated as the cost at the previous node, plus the distance or cost to move from there to the new node. If the new cost is lower than the existing cost at the new node, then its cost value is updated and the node is added to the wave-front list. Otherwise it is left unchanged.

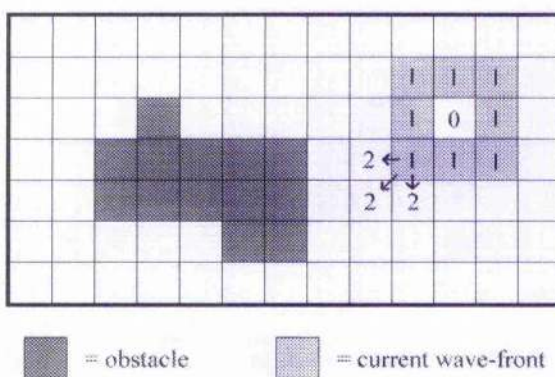


Figure 5-9 Expanding the Wave-Front

Once all the adjacent nodes from a single node on the wave-front list have been checked and updated, this original node is then removed from the current list, allowing the wave-front to expand through the new nodes. The final result once the wave-front has expanded over the complete control volume is a cost field containing the cost to travel to each node from the goal, as shown in Figure 5-10. A path can then be found from any point to the goal by simply descending through the cost field in a similar way to descending through a potential field.

22	20	18	16	14	12	10	8	6	5	4	5	6
21	19	17	15	13	11	9	7	5	3	2	3	5
22	20	18		12	10	8	6	4	2	0	2	4
24							7	5	3	2	3	5
26							8	6	5	4	5	6
25		21	19	17			9	8	7	6	7	8
24	22	20	18	16	14	12	11	10	9	8	9	10

Figure 5-10 The Calculated Cost Field

5.2.2 The Step Cost Function

The key to the successful use of the wave-front method for free-flyer path planning, comes from the formulation of the cost function used during the wave-front expansion to calculate the additional cost of travelling from one node to another. During the expansion, from each node w on the wave-front list, the cost $c(n)$ at each adjacent node n is given by the formula

$$\text{Eqn 5-5} \quad c(n) = c(w) + f(n, w)$$

where $f(n, w)$ is the cost of transferring from n to w . Since the wave-front is expanded outwards from the goal node to the start, the direction of the required movement cost is from the new node n to the previous node w , since this is the direction the path will follow from the start to the goal. In the case of a simple distance travelled cost this will make no difference, however it should not be assumed that movement costs are always reversible.

The simplest example of a transfer cost function is given by the direct distance between the two nodes. This reduces the cost field to a simple distance transform field of the shortest distance to the goal from each node, similar to that shown in Figure 5-10. In common with other minimum distance algorithms this has the disadvantage of finding paths that pass close to obstacles rather than favouring safer open space. Fortunately, with the wave-front method this can be easily solved by adding to the cost function an additional cost

based on the current proximity to the nearest obstacle. For example, the cost function can be modified to give

$$\text{Eqn 5-6} \quad f(n, w) = (w - n) + \frac{D_n}{r_n^{D_p}}$$

where r_n is the range to the closest obstacle node from node n , and D_n, D_p are constants used to shape the influence of the obstacle distance term. D_n controls the magnitude of the obstacle distance component, while D_p determines the extent of its influence. Through careful choice of these constants, the cost potential can in fact be shaped to closely imitate the behaviour of the Laplace potential field in finding smooth safe paths around obstacles, as shown in Figure 5-11.

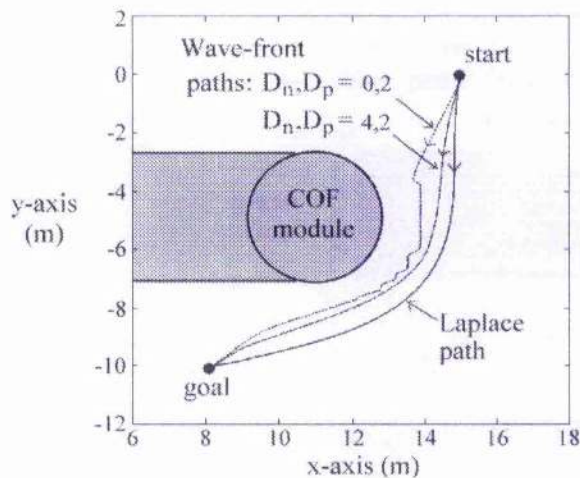


Figure 5-11 Obstacle Distance Component Influence

The uneven path that is shown by the pure distance transform result ($D_n, D_p = 0, 2$) is the result of the path attempting to travel directly along the cell boundaries between two nodes, and reacting to the small discontinuities in the interpolated cost gradient on either side of the boundary. For a smoothly calculated cost or potential field, this is not a problem.

So, with a distance transform and an obstacle range cost the wave-front cost field displays all the main characteristics of the Laplace potential field, and can therefore be used as a direct alternative for path planning. Ensuring the formation of only one global minimum in the cost field and avoiding the formation of any local minima, is performed in a similar manner to the calculation of the discrete Laplace potential, by initialising all nodal costs to an arbitrarily high value that is considered a maximum cost by the algorithm, setting the goal node cost to zero, and fixing the values of nodes that contain obstacles or the goal during calculations. Provided the combined cost function is always positive, i.e. $f(n, w) > 0$ for all

nodes n, w belonging to the control volume, the low cost wave will spread out from the goal point with monotonically increasing cost values, precluding the formation of any future minima. The flexibility of the transfer cost function means that the cost field can be enhanced to incorporate many more mission characteristics than the simple Laplace potential. For example, an additional cost can be added based on the availability of radio TM/TC and Video links at each node. Similarly a cost can also be incorporated to represent the calculated risk of travelling between nodes not just in terms of the proximity to obstacles described above, but also calculated from the free-drift characteristics of the free-flyer. The addition of such costs allows the cost field to be shaped to favour paths away from undesirable areas of the control volume in terms of any desired mission parameters.

5.2.3 Example Paths through the Cost Field

In general, the paths found by following the route of steepest descent through the wave-front cost field are similar to the Laplace results. The main deviations are where the cost function has been changed to avoid particular areas. One example of this, shown in Figure 5-12, demonstrates the use of an increased obstacle proximity cost to avoid passage between two relatively close obstacles.

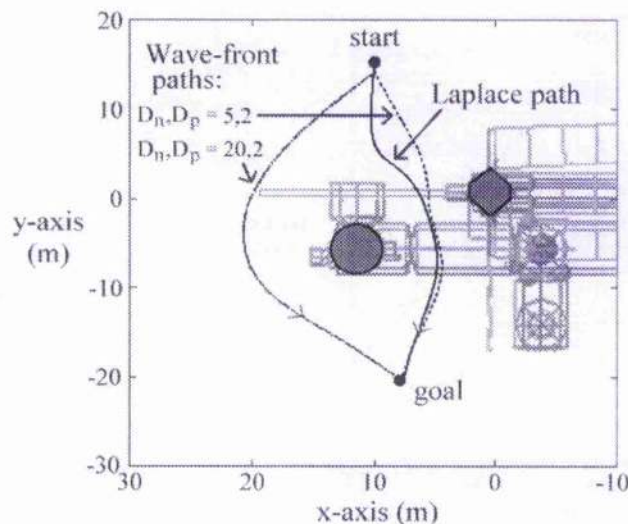


Figure 5-12 Wave-Front Path Shaping

As can be seen in the figure however, the proximity cost weighing must be dramatically increased before the resultant path will take the extended route around both the obstacles.

5.2.4 Merits of the Method

The primary advantage of the wave-front cost method over the Laplace potential field is in the flexibility of the cost function, and its ability to integrate weightings based on real mission parameters, other than the obstacle configuration, into the cost field. In addition, like the Laplace potential the wave-front method guarantees the formation of a single minimum in the cost field, as described above, calculated over the entire control volume to ensure path guidance toward the goal point from any position in the control volume. Also, by the addition of an obstacle proximity cost, the method can be adapted to favour safer open volumes in a more controllable manner to the Laplace potential.

As was the case for Laplace potential fields, the main disadvantage of the wave-front cost method is in the calculation time and storage requirements of the cost field and the need for recalculation of the field for a change in the obstacle configuration or goal point. A significant percentage of the calculation time of the wave-front is required to determine the range from any node to the closest obstacle. This element can be enhanced by pre-calculating the obstacle proximity values for each node, which has the further advantage of greatly speeding a cost field recalculation if required. Nevertheless, the calculation time for the wave-front is in general greater than for the Laplace potential field, especially with the addition of extra mission elements to the cost function. For this reason, along with the additional setup of distance and cost variables required to optimise the wave cost field to find the best paths for the Inspector vehicle, the Laplace potential field was selected as the default choice for Inspector path planning.

6.1 Introduction

With the development of potential and cost fields in Chapter 5, which allow paths to be found between any two points around the ISS, the next step is to investigate guidance techniques that can use these potential fields to manoeuvre the Inspector Free-Flyer to the goal in as safe and efficient a manner as possible. Throughout this chapter the techniques and methods developed will be referred to as acting on potential fields and potential gradients. However, all these methods are equally applicable to cost fields calculated with the wave-front method. The possible differences in applying the guidance methods developed to different classes of potential or cost fields will also be discussed later in the chapter.

In order to develop a guidance strategy for the ISS Inspector certain assumptions about the Inspector vehicle capabilities must first be made. Firstly it is assumed, as discussed in previous chapters, that the relatively small magnitude ΔV changes required to manoeuvre the free-flyer compared with relatively high thrust levels available, allow ΔV manoeuvres to be considered as impulse changes in velocity, of negligible duration and infinite acceleration [100]. In addition, it is also assumed that the Inspector Free-Flyer is able to provide these ΔV impulses in any direction, irrespective of the vehicle attitude. This allows the attitude control problem to be removed from current guidance considerations. In practice this is a reasonable assumption due to the design of the Inspector vehicle, which provides an array of thrusters, aligned around the vehicle in each axial direction.

The goal is therefore to develop a guidance strategy to take the available navigation information at any position in the control volume, and produce ΔV requirements to be linked to the vehicle reaction control system to guide the free-flyer to the goal. For the final Inspector vehicle, the control hardware required for the low-level execution of control will be integrated onboard the free-flyer. This can increase reliability by allowing higher level guidance commands to be carried out autonomously by Inspector rather than relying on external control software located in the MCS onboard the ISS or on the ground. Nevertheless, it should not be assumed that requested ΔV manoeuvres will be carried out precisely as required by the Inspector control systems, due to unavoidable thruster errors. Similarly it should be expected that the navigation system will only be able to supply the relative position or velocity of Inspector to a varying degree of accuracy, as any navigation

system will be inherently subject to noise and error bias in its measurements. Any guidance technique must therefore be able to accommodate these inaccuracies and restrictions while maintaining the safety of the resulting trajectory.

6.2 Path of Steepest Descent

The basic method of finding a path through a potential field, as used to produce the example results in Chapter 5, is to simply follow the path of steepest descent through the potential without considering the orbital dynamics of the problem. This path can be found by calculating the potential gradient and then making incremental steps in the direction of the negative gradient until the goal is reached. Despite the lack of reference to the orbital dynamics of the problem, the dynamics can still be applied at a later stage in order to follow the steepest descent path to the goal.

For any continuous path finder or guidance technique using discrete potential fields, the first step that must be taken is to interpolate between the available discrete potential values at the nodes of the grid, to obtain both the potential and potential gradient at any position within the control volume.

6.2.1 Potential Field Interpolation

Interpolation of the discrete potential values to approximate a continuous potential field is achieved by linearly interpolating the nodal potentials of the mesh cell surrounding the required position. The mesh cell is defined by the volume of discretised space in the control volume as represented by the potential mesh, within which the required point resides. This can be found by simply rounding down the current co-ordinates to the closest lower mesh node to get the cell coordinates. Given the current cell (i, j), the potential at a given co-ordinate in two dimensions can then be calculated by applying a bi-linear interpolation formula [135], given by

$$\begin{aligned} \phi(x, y)_{i,j} = & \phi_{i,j} \cdot (i+1-x)(j+1-y) \\ & + \phi_{i-1,j} \cdot (x-i)(j+1-y) \\ \text{Eqn 6-1} \quad & + \phi_{i,j+1} \cdot (i+1-x)(y-j) \\ & + \phi_{i-1,j+1} \cdot (x-i)(y-j) \end{aligned}$$

This effectively performs a combination of linear interpolations in each axis to give the resultant potential at the desired point, as shown in Figure 6-1.

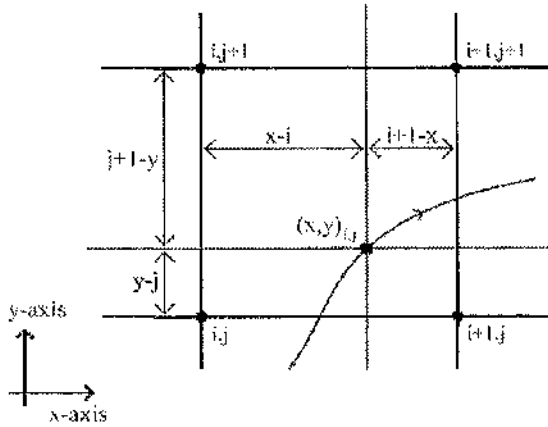


Figure 6-1 Bi-linear Interpolation

Bi-linear interpolation can then be extended to three dimensions, giving a tri-linear interpolation formula. The potential at co-ordinates (x, y, z) in cell (i, j, k) are given by

$$\begin{aligned}
 \phi(x, y, z)_{i,j,k} = & \phi_{i,j,k} \cdot (i+1-x)(j+1-y)(k+1-z) \\
 & + \phi_{i+1,j,k} \cdot (x-i)(j+1-y)(k+1-z) \\
 & + \phi_{i,j+1,k} \cdot (i+1-x)(y-j)(k+1-z) \\
 & + \phi_{i+1,j+1,k} \cdot (x-i)(y-j)(k+1-z) \\
 & + \phi_{i,j,k+1} \cdot (i+1-x)(j+1-y)(z-k) \\
 & + \phi_{i+1,j,k+1} \cdot (x-i)(j+1-y)(z-k) \\
 & + \phi_{i,j+1,k+1} \cdot (i+1-x)(y-j)(z-k) \\
 & + \phi_{i+1,j+1,k+1} \cdot (x-i)(y-j)(z-k)
 \end{aligned}
 \tag{Eqn 6-2}$$

6.2.2 Gradient Extraction

For potential field guidance it is the potential gradient that is important to finding a path to the goal. Unfortunately, the discrete potential field only contains values for the potential at each node, not the gradient, which must be constructed from this limited information. The primary method of doing this is to take the bi-linear or tri-linear method used to interpolate potential, and then differentiate Eqn 6-1 or Eqn 6-2 in each axis to give the potential gradient components in the axial directions [136]. For three dimensions, partial differentials of Eqn 6-2 gives the potential gradient along the (x, y, z) axes as

$$\begin{aligned}\frac{\partial \phi}{\partial x}(x, y, z)_{i,j,k} = & -\phi_{i,j,k} \cdot (j+1-y)(k+1-z) \\ & + \phi_{i+1,j,k} \cdot (j+1-y)(k+1-z) \\ & - \phi_{i,j-1,k} \cdot (y-j)(k+1-z) \\ & + \phi_{i+1,j+1,k} \cdot (y-j)(k+1-z)\end{aligned}$$

Eqn 6-3

$$\begin{aligned} & - \phi_{i,j,k+1} \cdot (j+1-y)(z-k) \\ & + \phi_{i+1,j,k+1} \cdot (j+1-y)(z-k) \\ & - \phi_{i,j+1,k+1} \cdot (y-j)(z-k) \\ & + \phi_{i+1,j+1,k+1} \cdot (y-j)(z-k)\end{aligned}$$

$$\begin{aligned}\frac{\partial \phi}{\partial y}(x, y, z)_{i,j,k} = & -\phi_{i,j,k} \cdot (i+1-x)(k+1-z) \\ & - \phi_{i+1,j,k} \cdot (i+1-x)(k+1-z) \\ & + \phi_{i,j+1,k} \cdot (x-i)(k+1-z)\end{aligned}$$

Eqn 6-4

$$\begin{aligned} & + \phi_{i+1,j+1,k} \cdot (x-i)(k+1-z) \\ & - \phi_{i,j,k+1} \cdot (i+1-x)(z-k) \\ & - \phi_{i+1,j,k+1} \cdot (i+1-x)(z-k) \\ & + \phi_{i,j-1,k+1} \cdot (x-i)(z-k) \\ & + \phi_{i+1,j+1,k+1} \cdot (x-i)(z-k)\end{aligned}$$

$$\begin{aligned}\frac{\partial \phi}{\partial z}(x, y, z)_{i,j,k} = & -\phi_{i,j,k} \cdot (i+1-x)(j+1-y) \\ & - \phi_{i+1,j,k} \cdot (x-i)(j+1-y)\end{aligned}$$

Eqn 6-5

$$\begin{aligned} & - \phi_{i,j+1,k} \cdot (i+1-x)(y-j) \\ & - \phi_{i+1,j+1,k} \cdot (x-i)(y-j) \\ & + \phi_{i,j,k+1} \cdot (i+1-x)(j+1-y) \\ & + \phi_{i+1,j,k+1} \cdot (x-i)(j+1-y) \\ & + \phi_{i,j+1,k+1} \cdot (i+1-x)(y-j) \\ & + \phi_{i+1,j+1,k+1} \cdot (x-i)(y-j)\end{aligned}$$

This gives a continuous value for the gradient available throughout the control volume, which can be used to find a path to the goal. However, since the potential interpolation function was a linear function of x, y, z , the differentiated gradient function is then only a constant function along each axis. The second derivative of the potential function

is therefore undefined in the control volume, leading to possible discontinuities in the gradient at cell boundaries. This means that while the calculated potential gradient is continuous over the control volume, the derivative of this gradient will not be, and there are likely to be distinct changes in gradient values between adjacent cells. This can be clearly seen in one of the two dimensional examples used to demonstrate Laplace potential path finding in Chapter 5, repeated in Figure 6-2. As the path crosses over the boundary between two cells, the direction of the path, given by the potential gradient at that point experiences a small but distinct change in direction, showing that the interpolated potential gradient field is not smooth at these points.

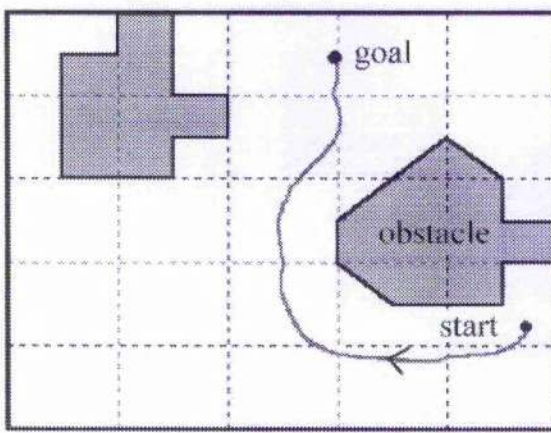


Figure 6-2 Path Direction Discontinuities

In order to provide the extra data required to satisfy the second derivative constraint and a smooth path, additional points must be used in calculating the potential gradient. This could be achieved globally for the potential field by using a higher order interpolation formula such as bi-cubic interpolation. However since extra accuracy is unnecessary for potential field values, the easiest way to achieve this for the potential gradient case is to introduce a pre-interpolation step that uses the surrounding nodes to the current cell to approximate the potential gradient at each node of the cell. The gradients can then be interpolated directly from these cell node gradients rather than trying to interpolate via the potential values, giving the equivalent of a cubic interpolation of the potential values. The gradient values at the cell nodes are calculated by a simple one dimensional linear approximation from the nodes on either side of the node in question, as shown in Figure 6-3.

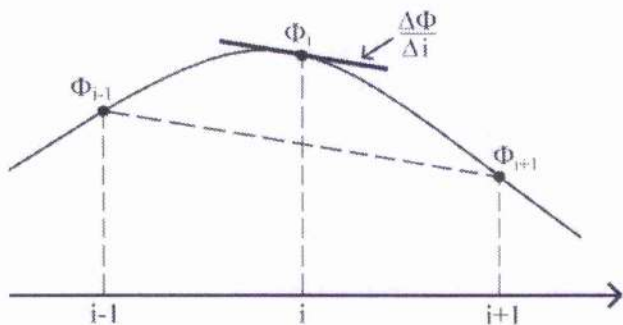


Figure 6-3 The Calculation of Nodal Gradients

A bi-linear or tri-linear interpolation as given in Eqn 6-1 and Eqn 6-2 respectively can then be applied to the gradients. Then, since the nodal gradients are calculated from the nodal potentials outside each specific cell, the gradient transition between cells will now be smoother. For three-dimensional potential functions such as those used for manoeuvring about the ISS, the advantages of using the enhanced gradient interpolation are not so pronounced as for the two dimensional example shown in Figure 6-2, since the larger number of available mesh nodes give a smoother representation of the potential field. The difference in the steepest descent path found can still be observed however, as shown in Figure 6-4, when a simple distance transform wave-front is used.

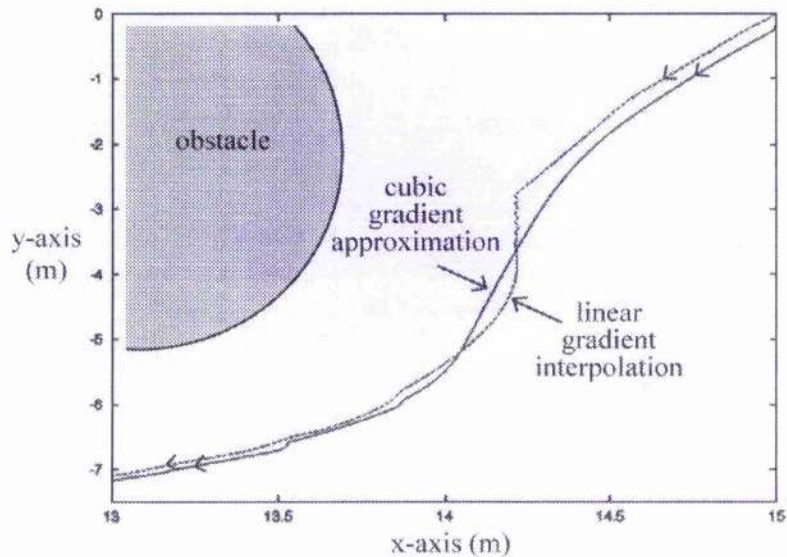


Figure 6-4 Path Differences due to Increased Interpolation Accuracy

6.2.3 Following Path of Steepest Descent

Given interpolated potential gradients, the path of steepest descent to the goal can then be found by iteratively applying a path equation, given below, to step toward the goal until the goal is reached [47].

$$\text{Eqn 6-6} \quad \underline{P}(n+1) = \underline{P}(n) + \Delta p \frac{\nabla \phi}{|\nabla \phi|}$$

where $\underline{P}(n)$ is the path position, Δp is the step size, and $\nabla \phi$ is the potential gradient vector, given in component form by

$$\text{Eqn 6-7} \quad \nabla \phi = \frac{\partial \phi}{\partial x} \underline{i} + \frac{\partial \phi}{\partial y} \underline{j} + \frac{\partial \phi}{\partial z} \underline{k}$$

Provided the step size is sufficiently small compared to the cell spacing, this will generate a smooth path from the start to the goal.

Though independent of vehicle dynamics, the formulation of the steepest descent path finder itself does present a possible direct application to free-flyer path finding. The definition of the path step size is an open issue, and in principle it may be possible to use a relatively large step size, especially if a very coarse grid is used, so that a 2-impulse transfer could be performed by the free-flyer to transfer along each step as the path is calculated. However, in reality the step size must be constrained to a relatively small distance, which would be impractical to follow with such a high frequency of 2-impulse transfers. This limitation on step sizes is required since the direction of each step is determined by the potential gradient at the start of the step without reference to changing potential values at the step end, and so small step lengths are required to maintain the validity of the safe direction of the path throughout each step.

To follow paths generated with the steepest descent method, a path must therefore be found using small steps, and then subsequently split up into longer steps to be followed by the free-flyer using 2-impulse transfers [137]. The resultant path is made up of a number of waypoints along the original steepest descent path, which can then be calculated either to optimise total manoeuvre costs or to minimise the free-flyer deviation from the original path, as discussed in Chapter 2. This method is applicable to off-line path planning only, as the planned sequence and position of manoeuvres must be calculated before the mission. There is however still a certain degree of flexibility in the execution of the mission in that the pre-planned waypoints do not necessarily require to be passed through precisely along the path. It should be sufficient to reach an approximate waypoint position before initiating the

subsequent 2-impulse transfer to the next waypoint, allowing a certain amount of error in the applied impulses over the manoeuvre to be accommodated. In conclusion, however, these techniques are limited by attempting to follow a predefined steepest descent path that does not represent the orbital dynamics of the problem. The result is a guidance method that does not make the safest or most efficient use of the free-flyer dynamics or the potential field.

6.3 Gradient Impulse Manoeuvring

Unlike the steepest descent path finder, the Gradient Impulse (GI) manoeuvring method [138] incorporates the free-flyer dynamics from the outset into a path finding technique that can, with a pre-calculated potential field, be employed equally well for real-time guidance as for off-line path planning. This Potential Function (or Field) Guidance (PFG) technique was originally developed for free-flyer guidance using potential functions as part of the ATV guidance software developed at the University of Glasgow [4]. It will now be adapted and developed as the chosen method for the Inspector Free-Flyer path planning and guidance. Required changes include the use of discrete potential fields, and attempting to satisfy the increased safety constraints of manoeuvring close to the ISS. An example of the ATV implementation of GI-PFG from [4], used to guide the ATV path around a repulsive obstacle potential function is shown in Figure 6-5.

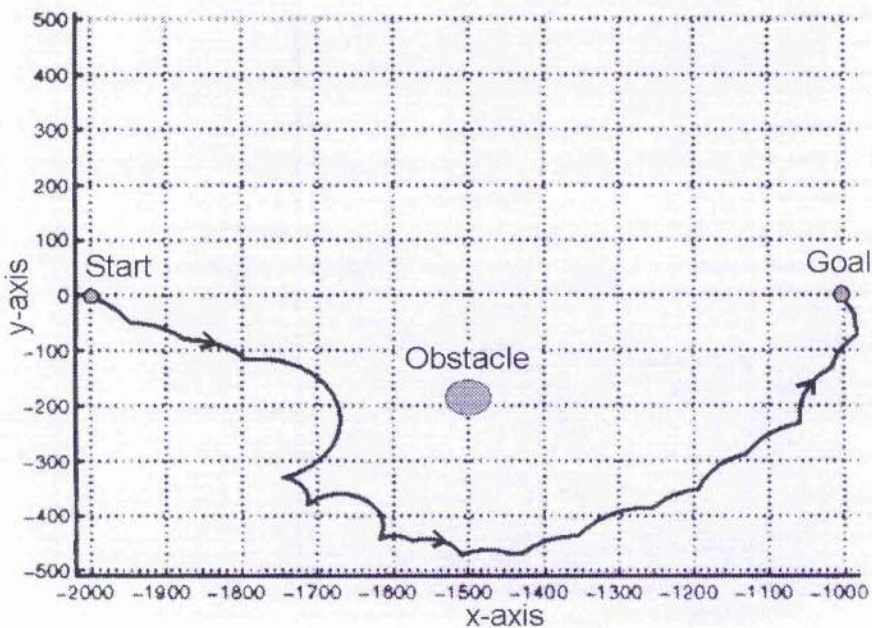


Figure 6-5 ATV Potential Function Guidance (from [4])

6.3.1 The Method

The GI-PFG method operates by using the potential gradient direction to directly generate the desired free-flyer velocity at that point. The required ΔV , given by the difference between desired velocity and current velocity, is then supplied to the free-flyer control system to guide the vehicle. Between control requests, the free-flyer is allowed to drift freely, allowing the orbital dynamics to shape the path until another control action is required to ensure that the potential monotonically decreases. For off-line path finding, the path planner must then simulate Inspector thruster and navigation characteristics, and propagate the path using the CW equations of motion. Or, in the case of real-time guidance, control demands based on state information from the navigation system can be supplied directly to the free-flyer control system to generate the trajectory.

The desired free-flyer velocity at any point can be calculated from the potential gradient as

$$\text{Eqn 6-8} \quad \underline{V} + \Delta \underline{V}_{req} = -k \frac{\nabla \phi}{|\nabla \phi|}$$

where \underline{V} is the current velocity vector, $\Delta \underline{V}_{req}$ is the required change in velocity, and k is a velocity shaping function, which can be constant or a function of the vehicle state. The potential gradient $\nabla \phi$, when normalised gives the direction of the desired velocity vector, while the shaping function k allows the velocity magnitude to be chosen with respect to vehicle and operational constraints, such as pre-defined velocity or thrust limits. It is desirable to use the normalised potential gradient rather than utilising a proportional gradient controller in order to negate the differences in gradient caused by alternate cost fields, discussed in section 6.4.1, and maintain control over the velocities applied to the vehicle.

The final element of the GI-PFG method concerns the criterion used to determine when a control action is required to ensure that the potential monotonically decreases. If a continuous switching strategy is applied, so that a control request based on Eqn 6-8 is produced every control cycle, the guidance method will effectively deliver a forced motion trajectory following the path of steepest descent. This is undesirable from a ΔV cost point of view since forced motion is inherently inefficient, and thruster and navigation errors will only exaggerate the cost, though it may be applicable to a continuous low thrust propulsion system [139]. The gradient impulse guidance strategy however uses a discrete switching criterion which only produces control requests when the potential is no longer decreasing. In a potential field method, this can easily be checked by referring to the rate of change of potential, so that as long as the potential change is always decreasing within desired limits, no

control action is required. If the potential rate of change does not satisfy this constraint, a discrete control request can then be applied to resume an admissible path.

The rate of change of potential can be determined in two ways. Firstly, the path finder can simply check that the given potential value at the current position is lower than at the previous step. This gives the basic switching criterion that if the new potential at some trajectory step n is not lower, a control impulse is required:

$$\text{Eqn 6-9} \quad \begin{cases} \phi_n < \phi_{n-1} & \Rightarrow \text{no action} \\ \text{else} & \Rightarrow \text{control required} \end{cases}$$

Alternatively, the rate of change of potential can be found by taking the scalar product of the current potential gradient and the free-flyer velocity vector. The result can then be used to implement a slightly more sophisticated switching criterion, to constrain the maximum angle from the steepest descent path permitted before a control action is required as shown in Figure 6-6, by

$$\text{Eqn 6-10} \quad \begin{cases} \frac{\underline{V} \cdot (-\nabla \phi)}{\|\underline{V}\| \|\nabla \phi\|} < \cos \theta & \Rightarrow \text{no action} \\ \text{else} & \Rightarrow \text{control required} \end{cases}$$

where θ is the maximum allowed deviation from the steepest descent direction. For the case $\theta = \pi/2$ the behaviour of Eqn 6-10 then becomes identical to that of Eqn 6-9, as shown in Figure 6-6. For a limit such that $\theta < \pi/2$ the controller will pre-empt manoeuvres, although unnecessary control activity can be activated. This method, which was applied to analytical potential functions in [4], will be applied here to Laplace and wave-front cost fields, with all further examples in this text will use a switching constraint of $\theta = \pi/2$.

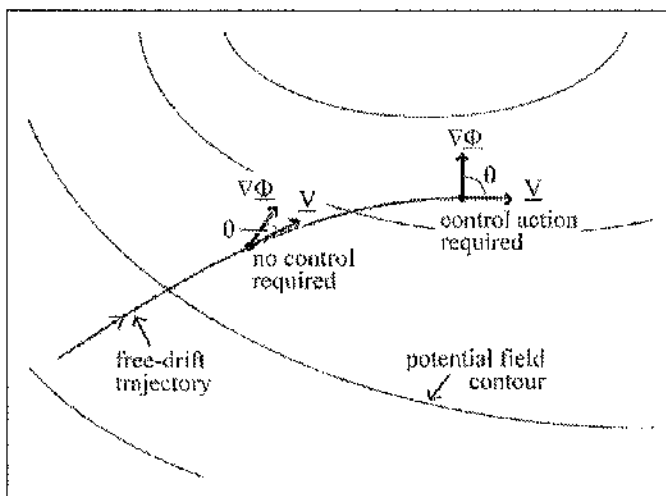


Figure 6-6 Gradient Switching Criterion

6.3.2 Example Gradient Impulse PFG Manoeuvres

Although paths found using GI-PFG may utilise the same potential fields, and have similar directional controls to purely steepest descent paths, the free-drift permitted between control impulses result in paths that can appear quite different to the smooth direct paths produced by the steepest descent method, even to the extent of taking an alternative route through the potential field to reach the goal. Figure 6-7 shows the paths found using GI-PFG for two example paths originally used to demonstrate the steepest descent path through the Laplace potential field in Chapter 5 (Figures 5-12(a) & (d) respectively). The actions of the PFG method can be easily seen in the shape of the resulting path, as the free-drift periods are shown by the smooth curving arcs, while each discrete control impulse is represented by a discontinuity in the direction of the path. Figure 6-7(a) also demonstrates how the path found using the Laplace potential field is constrained within the control volume as well as repelled by the obstacle points, ensuring a safe path to the goal. Figure 6-7(b) also shows the ability of the potential field to guide the free-flyer between obstacles using GI-PFG to reach the goal. This is a key result, as it shows that collision avoidance can be ensured using GI-PFG while convergence to the goal is also assured since ϕ has no local minima within the control volume.

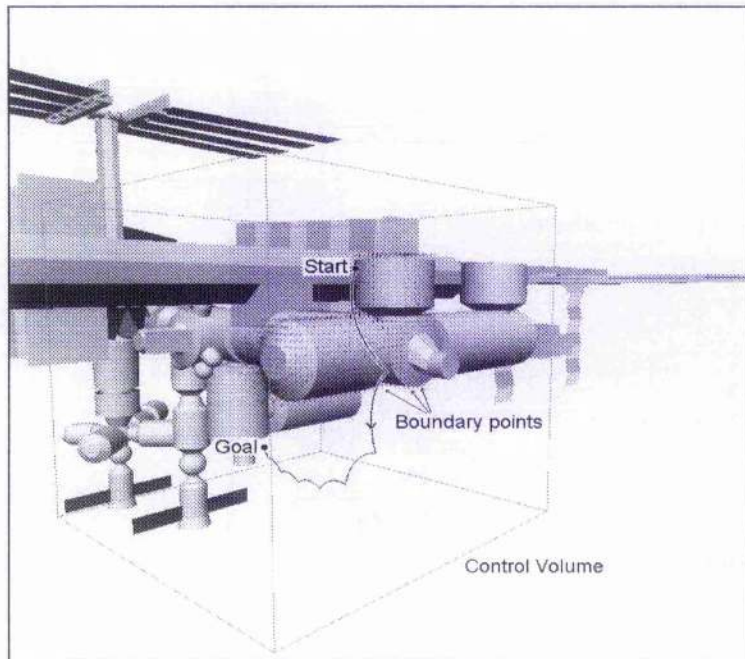
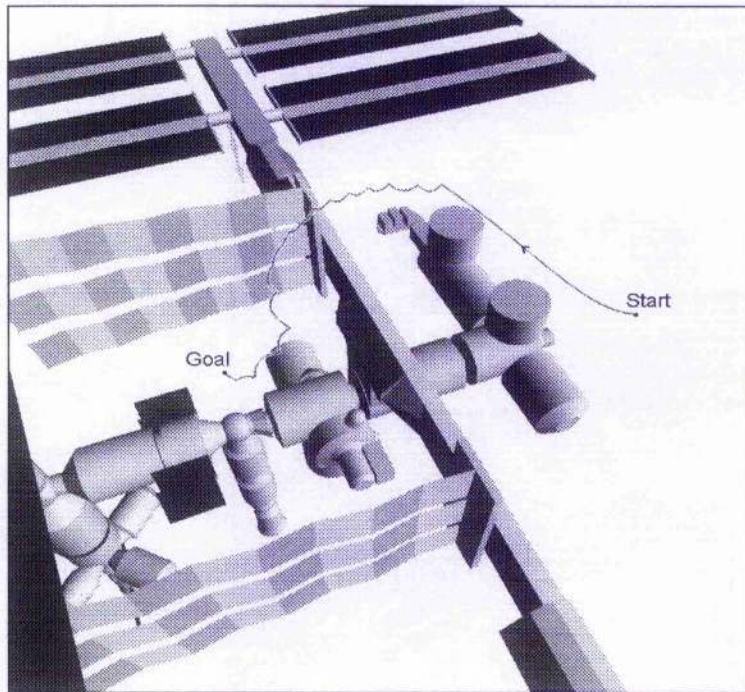


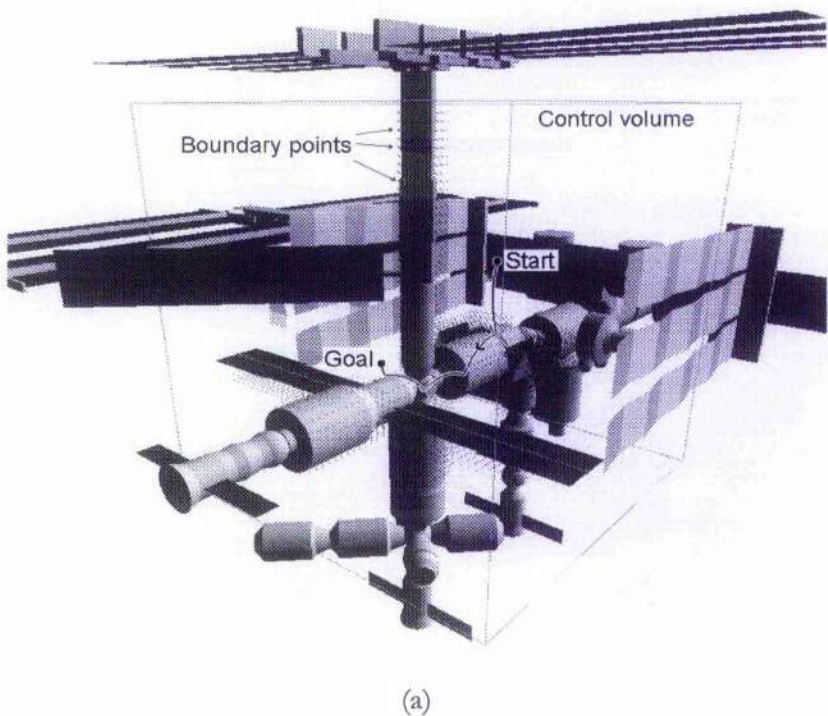
Figure 6-7 (a)



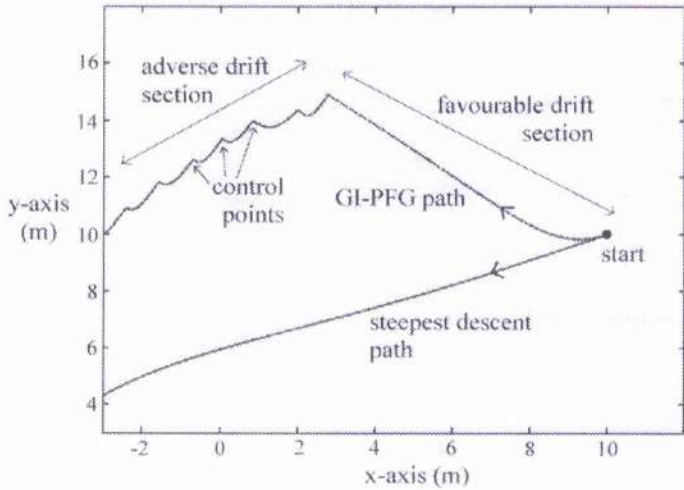
(b)

Figure 6-7 Example GI-PFG Paths using the Laplace Potential Field

Another feature of GI paths shown in Figure 6-7 is the length of the free-drift periods, which can vary dramatically between different paths, and in different sections of the same path. This variation occurs because of the natural tendency of the free-drift path to curve in a particular direction, due to the orbital dynamics of the problem. If the natural curvature of the drifting path coincides with the desired route through the potential field, then the path will be allowed to drift for an extended period as the rate of change of potential remains negative definite. However, if the free-drift direction opposes the required route toward the goal, frequent control impulses may be required to keep the free-flyer on an admissible trajectory. Another way of considering this is that the free-flyer may tend to drift safely around the ISS toward the goal, in which case no control action is required (or even desired), but if the free-flyer drifts towards the ISS, then action must be taken as often as required by the control law to avoid a collision. This behaviour can be more clearly seen by concentrating on the initial portion of the path in Figure 6-7(b) which demonstrates examples of both favourable and unfavourable free-drift elements. These unfavourable elements can also be seen in Figure 6-8(a). By contrast, Figure 6-8(b) shows a path where the free-drift characteristics of the free-flyer naturally avoid the obstacle between the start and goal, and the path must instead be constrained by the control volume boundaries in order to reach the goal.



(a)



(b)

Figure 6-8 A Demonstration of the Advantages/Disadvantages of GI-PFG

The effect of slightly different start positions on the trajectory found to the goal through the Laplace potential field was originally investigated for steepest descent paths in section 5.2.3, but the effects of using GI-PFG on chosen routes can also be demonstrated by applying the PFG method to the same test cases. The results given in Figure 6-9 show that for GI-PFG the final route is dependent as much upon the free-drift characteristics of the early portion of the path, as on the exact start position.

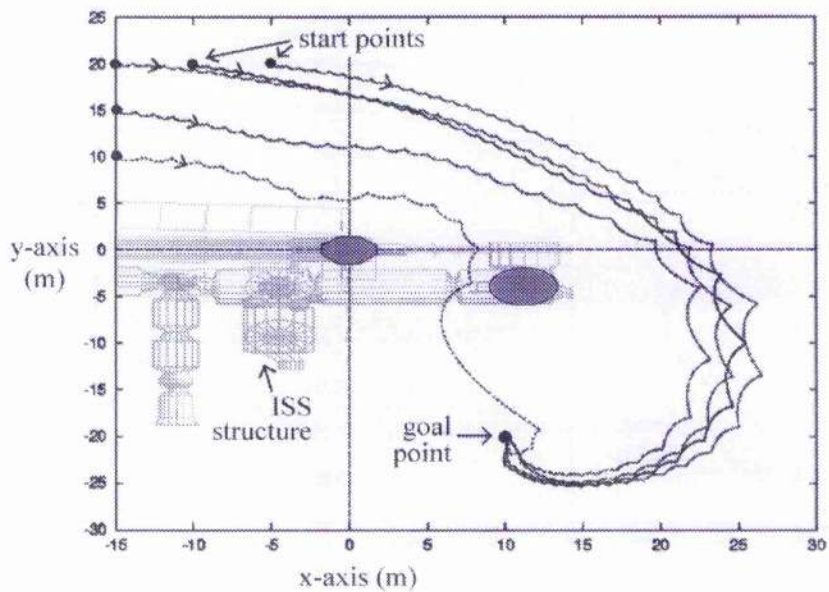


Figure 6-9 GI-PFG Path Variations from Small Changes in Co-ordinates

6.3.3 Merits of the Method

The main advantage of the gradient impulse guidance method is its flexibility in adapting to the orbital dynamics of the free-flyer motion, applying control impulses to guide the path to the goal while still taking advantage of the natural motion of the vehicle wherever possible. In fact, GI-PFG actually makes no prior assumptions about the free-flyer dynamics or control systems, only requiring being supplied current position, and optionally velocity information, to return the desired velocities to guide the vehicle to the goal. Any favourable free-drift motion is automatically taken advantage of through the discrete, gradient rate of change switching criterion, irrespective of the manner in which the vehicle drifts. The lack of reliance on any specific path being followed also means that the GI method is relatively unaffected by errors, either in the actual velocity changes supplied to the vehicle by its propulsion system, or in absolute navigation errors. In this sense the method is not model based and so is highly robust and failure tolerant.

Nevertheless, disadvantages do arise from the lack of direct control over the chosen path of the GI path finder. This is not seen as a major issue, but paths planned off-line as part of the mission planning phase before a mission may not correspond exactly to paths followed in real-time using the same potential field due to differing navigation and control errors in the real execution of the path. Off-line path planning therefore should only be used to produce an approximate path for a given transfer to obtain a predicted route and costs for that mission element. Unless of course the results of the off-line path planning step are to be used directly

to control the path of the free-flyer during mission execution, but this strategy would in any case undermine most of the primary advantages of the GI methods flexibility anyway.

One final problem with GI-PFG arises in the final section of the path to the goal point. Because of the relatively sharp changes in the potential field surrounding the goal point, the finite approach velocity of the free-flyer means that it may be unable to reach the exact goal point in an acceptable period of time. An approximate analogy would be of a ball bearing rolling around a bowl with a hole at the bottom, unless the ball happens to fall down the hole first time, it may take a number of cycles around the bowl before the ball falls down the hole. Fortunately for the GI path finder, there is an easy solution. Once the path reaches an acceptable pre-defined proximity to the goal, GI-PFG can be switched off and a single 2-impulse transfer used to transfer the remaining distance to the goal. Provided the maximum distance at which the 2-impulse transfer is used is small enough, for example if defined by the width of a single mesh cell, then it is safe to assume there are no obstacles between the current position and the goal, and a 2-impulse transfer can be used without compromising safety.

6.4 Paths from Complimentary Potential Fields

Some examples have already been given of the results of using GI-PFG manoeuvring in the Laplace potential field. These examples have shown how alternative paths can be found by the GI method compared to the route of steepest descent, through the same potential field. However, the relative performance of the GI method between different potential field types must also be addressed. In principle, both of the developed potential fields (Laplace potential and wave front cost fields) should generate safe paths to the goal, but in practice the formulation of each respective potential may affect the behaviour of the GI guidance scheme, making one or other potential preferable for guidance of the Inspector Free-Flyer. Furthermore, the application of different potential types to specific mission applications will also be investigated.

6.4.1 Gradient Magnitudes

The first aspect of using different potential fields for PFG that must be addressed is the fact that in addition to the varying potential across the control volume, the relative magnitudes of the potential gradient obtained in the Laplace potential field and the wave-front cost field are dramatically different over the control volume. This arises from the formulation of the Laplace potential function, which essentially averages the potential values across the

control volume, from a minimum of 0 at the goal, to a maximum of 1 at the edges and boundaries. As potential values are calculated further away from the goal point, the maximum possible change in potential effectively halves with each step from the goal, resulting in a potential gradient that falls exponentially from the goal point. At reasonable distances from the goal node, all Laplace potential values will therefore be very close to the maximum value of 1, and gradients close to zero. This emphasises the need for double precision variables in calculating the Laplace potential, in order to preserve the detail of the changes in potential values.

By contrast, the change in cost between nodes of the wave-front cost field is independent of the distance from the original goal. The cost gradient will have a guaranteed minimum value throughout the control volume, defined by the ratio of the step transfer cost to step distance, with increased gradient applied by additional cost elements to the total cost function. The comparison between wave-front cost gradients and Laplace potential gradients can be seen by looking at a surface plot of the respective potential and cost fields, as shown in Figure 6-10. The wave-front cost field shown is a simple distance transform cost with no additional proximity cost, so the gradient throughout the surface is actually constant except at the obstacle and boundary edges where it is steep. The effective gradient of the Laplace potential field must however be multiplied by two orders of magnitude before the shape of the obstacle can even be discerned.

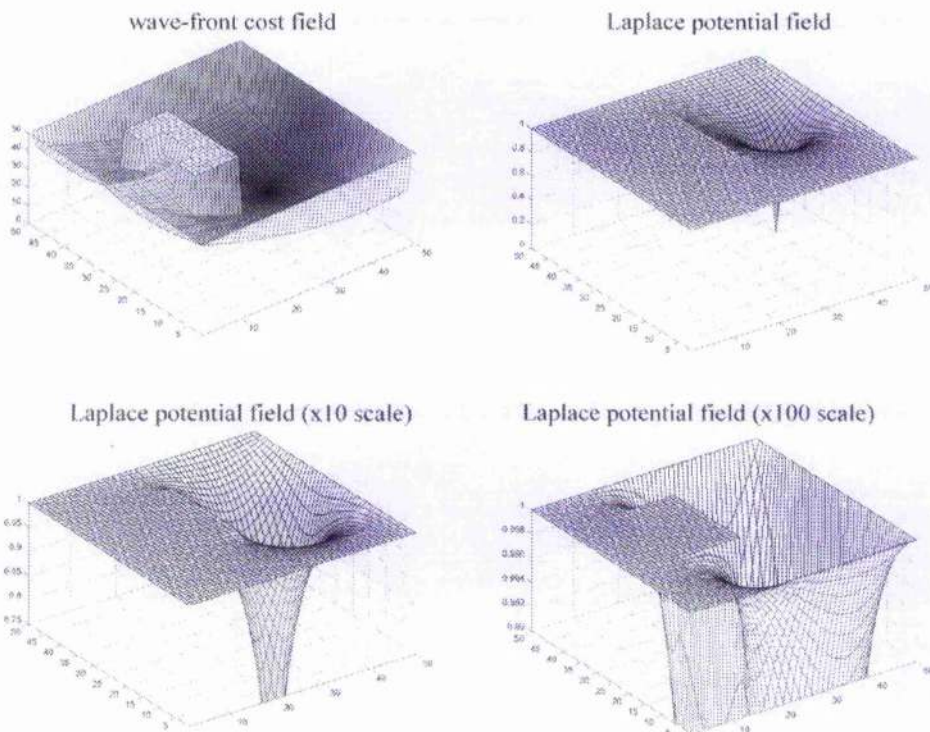


Figure 6-10 Potential and Cost Gradients

Fortunately the problem of large variations in potential gradient is solved by normalising the gradient $\nabla\phi$ to obtain the pure gradient direction for use in the path finder. It is useful however to be aware of the differences, so that no direct use is made of gradient potentials in the GI-PFG method that might limit the use of any particular potential field.

6.4.2 The Effect of Changes in the Potential Field

In section 5.3.2 the steepest descent paths generated for a transfer around the COF module of the ISS for a range of potential fields were demonstrated. The potential fields utilised for this example, shown in Figure 5-20, included the Laplace potential, and wave-front cost fields based on different obstacle proximity weightings. The result of the same test case repeated using the GI path finding method is shown in Figure 6-11, to give an example of the effect of using different potential fields for GI-PFG. It can be seen that the differences in potential field when using the GI method have a much lower effect on the resultant path than the orbital dynamics of the free-drift motion. However, in this example the natural free-drift motion is constantly curving the path away from the COF obstacle, so that the repulsive potential of the obstacle has less of an overall effect on the path. As a comparison, the GI guidance paths found for the reverse transfer (i.e. from the goal to the start point) along with the Laplace steepest descent path for this transfer are shown in Figure 6-12. In this case the orbital dynamics force the free-drift path towards the COF module, and the paths taken between different potential fields are dramatically different, with the two wave-front paths following a completely different route to the side of the COF module, shown as cutting through the module in the two-dimensional view and clarified in the three-dimensional view of the wave-front path.

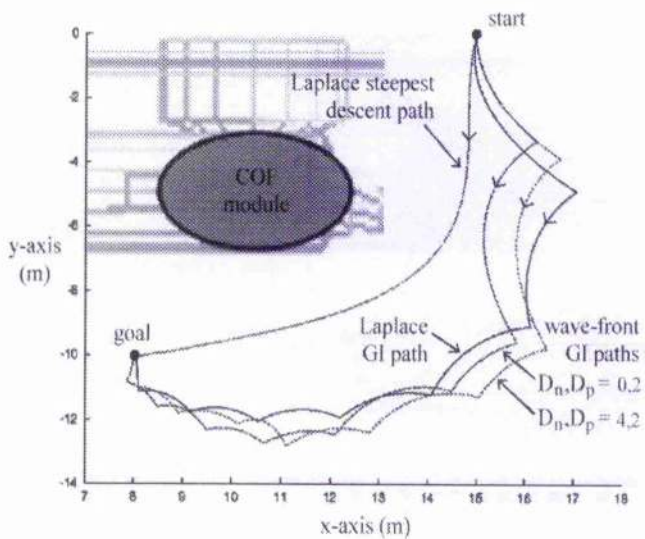


Figure 6-11 Paths around the COF Module, with Alternate Potential Fields

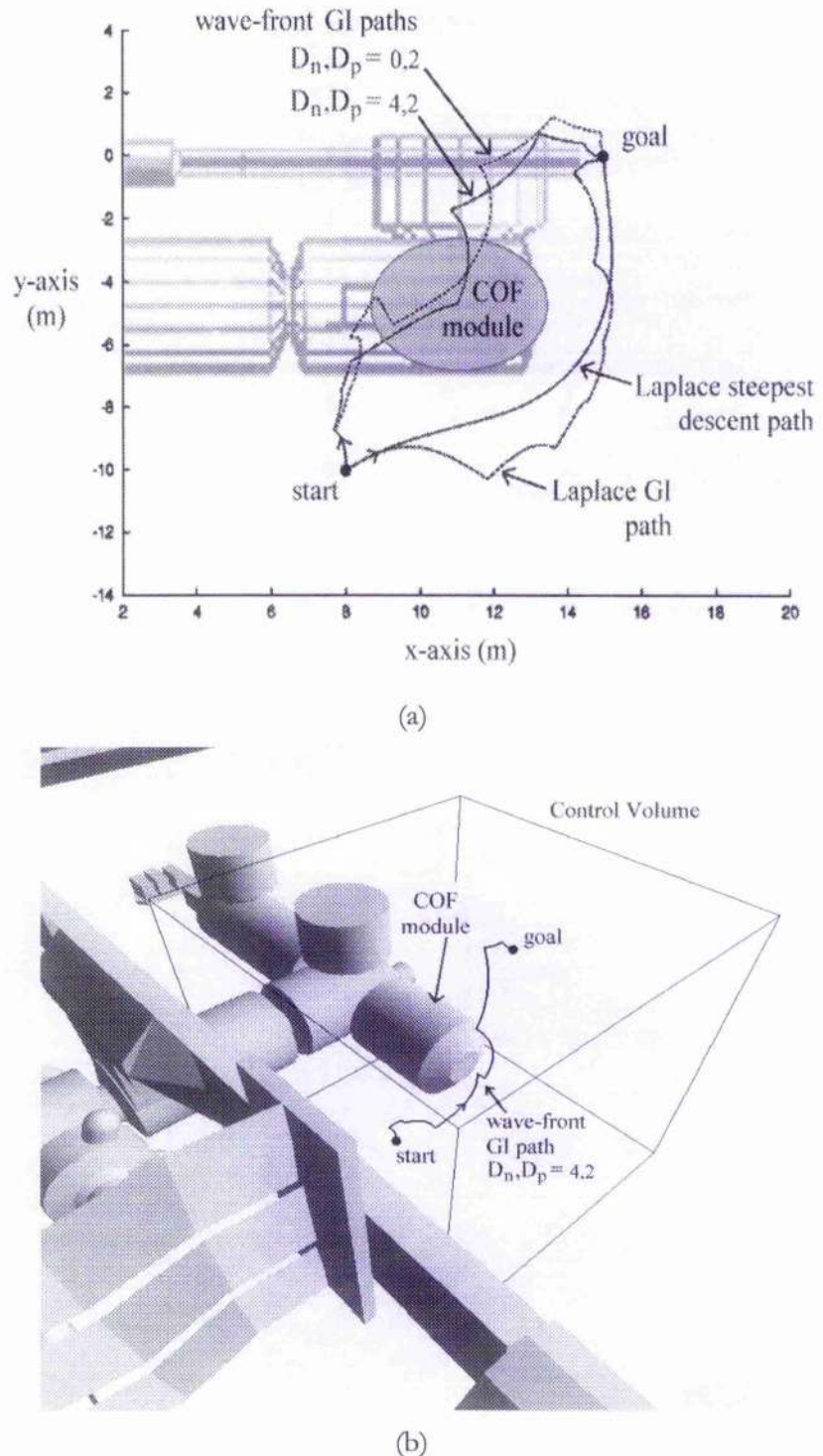


Figure 6-12 Reverse Paths around the COF Module

The second example used to demonstrate the application of alternate potential fields in Chapter 5 was that of a path passing between or around two close obstacles, shown in Figure 5-21. The results of this test case when solved by GI path finding, shown in Figure 6-13, are quite surprising. Contrary to the steepest descent results where only the wave-front

cost field with an exaggerated proximity cost component was forced around the two obstacles rather than passing in between, when the GI method is applied it is only the path found using the Laplace potential that passes around both the obstacles, while the two wave-front paths execute a route between the obstacles, passing considerably closer to the ISS structure as influenced by the natural free-drift characteristics which force the path towards the obstacle.

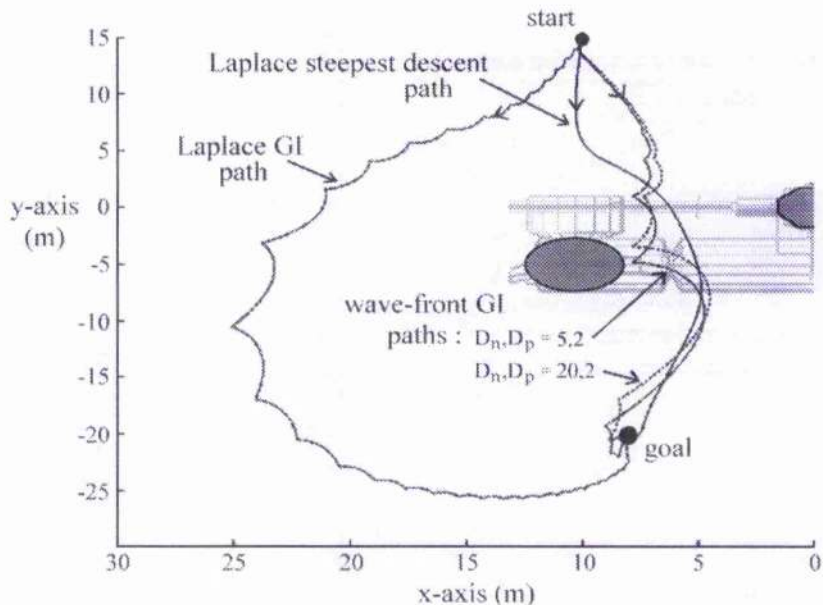


Figure 6-13 Path between ISS Elements, with Alternate Potential Fields

The final aspect of path planning using the GI method with differing potential fields is that of performing a transfer along an ISS element such as the main solar arrays, as previously shown in Figure 5-12(b). In this example, the aim is to manoeuvre the free-flyer along the solar panel, whilst maintaining a relatively close distance to the obstacle to facilitate a continuous inspection of the structure. As demonstrated in Figure 5-12(b) the Laplace potential achieves this reasonably well using steepest descent manoeuvring, however GI guidance applied to the same potential field results in an extended path that moves a considerable distance away from the target obstacle. This retreat from the obstacle is caused by the initial action of a potential field favouring points away from obstacle walls which pushes the path slightly to one side of the main body of the ISS structure, and once it begins to drift in this direction the characteristics of the orbital dynamics of the motion that cause the free-flyer to drift up and away from the solar panels combine with the influence of the potential field to follow an extended path around the original obstacle. One solution to the potential field problem of extended paths is to utilise a wave-front cost field with reduced obstacle repulsion, as shown in Figure 6-14(a). However, approach is dangerous since if the mission was orientated so that the free-drift characteristics forced the free-flyer toward the

obstacles rather than away from them, then the obstacle repulsion in the cost field may be insufficient to maintain adequate safety clearance from the ISS.

A better solution is to continue using the Laplace potential field, but to adjust the switching criterion so that the angle between the GI path and the steepest potential gradient is constrained to a smaller value. This will have the effect, as shown in Figure 6-14(b), of forcing the GI path closer to the steepest descent path, regardless of the free-drift dynamics of the manoeuvre.

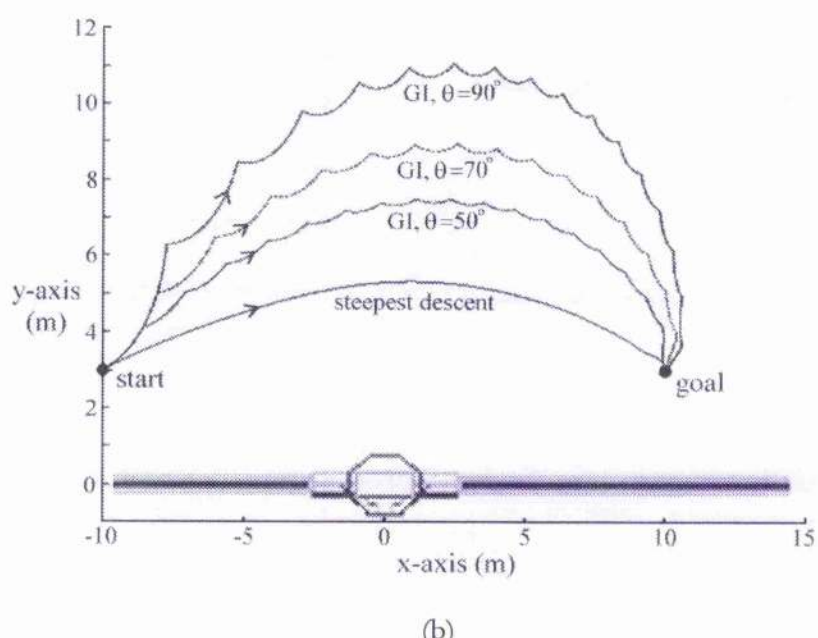
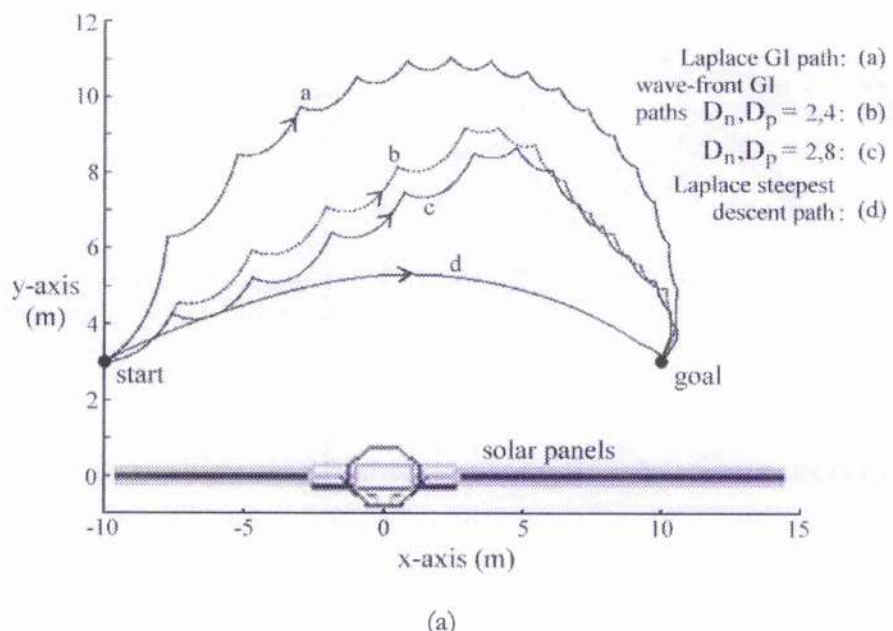


Figure 6-14 GI Path Shaping

6.5 Velocity Selection for Safety

One potential disadvantage in the application of the GI-PFG method to Inspector Free-Flyer path planning and guidance, is the fact that although free-flyer dynamics are incorporated into the method, there are no specific safety criteria implemented other than those inherent in the potential fields used. While the safety provided by potential fields, such as the Laplace potential, may be sufficient for many applications the safety, and in particular passive safety, of planned trajectories are of paramount importance. The GI-PFG method would therefore be made significantly more attractive for applications at the ISS, if it could be enhanced to improve the passive safety of the resulting trajectories, both in off-line path planning and under real-time control.

6.5.1 The Aim of Velocity Selection

The main mechanism of the GI method available to manipulate the path and safety of trajectories is in the velocity applied to the vehicle at each control request. As specified by Eqn 6-8, velocity demands are obtained from the direction of the potential gradient, and then scaled by the velocity shaping function k to give the requested velocity. It would not be advisable to alter the direction of the desired velocity obtained from the potential gradient, since this may affect the ability of the method to safely guide the path to the goal. However, the possibility of varying the absolute magnitude of the free flyer velocity is already included through the shaping function k . Since the action of k has no direct effect on the validity of the guidance method, and is in any case chosen for each specific application, the velocity magnitude can be shaped within the limits of the free-flyer without affecting the ability of the GI-PFG method to safely reach the goal.

The easiest way to shape the velocity profile would be to base the value of k directly on some function of the current vehicle position, such as the proximity to the ISS structure. Unfortunately this strategy does not take into account the direction of the requested velocity. For the proximity example one would assume that a velocity of 0.05 m s^{-1} toward the ISS is safer than a velocity of 0.05 m s^{-1} away from the space station. However, as has been discussed at some length already, the direction and magnitude of the initial vehicle velocity is not necessarily very representative of the subsequent free-flyer trajectory under the action of relative orbital dynamics at the ISS. The solution therefore, is to propagate the resulting free-drift trajectories using the orbital dynamics for a given range of velocity magnitudes in the current potential gradient direction at each control impulse, and evaluate the safety of each

potential trajectory. The resulting trajectory with the lowest collision likelihood, or in the event that passive safety is not possible the lowest impact velocity, can then be selected to optimise the safety of the subsequent path.

6.5.2 Velocity Selection Criteria

Before an optimum trajectory can be selected, the velocity magnitudes to be tested must first be defined. The upper and lower limits of vehicle velocity are first restricted by the available thrust and propellant load of the vehicle. However, further restrictions on the range of k must be enforced by other mission constraints, so that at the upper limit velocities cannot compromise the free-flyer's ability to obtain up-to-date navigation information or to process guidance commands. Also, high velocities which limit the free-flyer's ability to perform a CAM and retreat from the ISS in the case of a critical failure cannot be permitted. At the lower limit, a minimum free-flyer velocity is required to ensure that the free-flyer motion can overcome potentially adverse orbital dynamics to reach the manoeuvre position in a reasonable time period.

It is expected that for most applications it should be possible to find some nominal value for k which provides an acceptable compromise between finding good paths to the goal with reasonable time and propellant costs, for a range of missions. This nominal or 'preferred' value can then be used to define the test velocities by finding a requested number of equally spaced values on either side of nominal, between the pre-defined velocity limits. The GI velocity request equation, Eqn 6-8, then becomes

$$\text{Eqn 6-11} \quad \underline{V} + \Delta \underline{V}_{reg} = -s_i k_{nom} \frac{\nabla \phi}{|\nabla \phi|}$$

where k_{nom} is the preferred velocity value, and s_i represents a sequence of scale factors used to select velocities within the required range. In the case of the Inspector Mission Planner, k_{nom} was chosen by simulation to give a preferred free-flyer velocity of 0.01 m s^{-1} . The multiplier sequence that was used to test the velocity selection technique for the Inspector mission is then given by

$$\text{Eqn 6-12} \quad s_i = \{1.0, 1.5, 2.0, 2.5, 3.0, 4.0, 5.0, 0.95, 0.9, 0.85, 0.8, 0.75, 0.7, 0.6, 0.5, 0.4\}$$

The sequence is arranged so that the velocities are tested in order of preference. Obviously the nominal velocity k_{nom} must be tested first, since if this trajectory is passively safe the other options become redundant. For the Inspector mission, the next best option is to increase the tested velocity to the upper limit, since if safe this choice will result in a shorter mission time,

often with little extra overall cost in terms of ΔV . Finally, the tested velocity is reduced down to the lower limit to complete the spectrum of permissible trajectories.

For each test case, the resulting trajectory is propagated using the CW equations of motion for a period of two complete orbits, and checked for collisions along the path. If no collisions occur, then the tested velocity is deemed passively-safe within the requirements of the PFG observation manoeuvring segment of the mission, and that velocity is applied to the free-flyer. If however a collision does occur within this period, the free-flyer velocity at this point must then be determined and saved, so in the case that no passively-safe trajectory is found the option with the lowest impact velocity can be chosen.

Though the development of path finding using totally passively safe trajectories is one of the main objectives of the Inspector Mission Planner developed here, it must be recognised that to permit free-flyer manoeuvring in the vicinity of the ISS this cannot be achieved for all mission scenarios. By minimising the potential velocities of possible collisions however, in conjunction with duplex redundant vehicle systems and pre-planned CAM manoeuvres, the risk of free-flyer manoeuvring can be reduced to an acceptable level.

6.5.3 Impact on Manoeuvre Time and Propellant Cost

The application of velocity selection at each control request could result in potentially large effects on the final path followed by the GI-PFG method, compared to paths found with a fixed nominal value for k as shown in previous examples. These path differences should not, however, affect the ability of the path to reach the goal point. In order to show the effects of using velocity selection, two example transfers already used to demonstrate GI paths will be repeated with velocity selection enabled. These two examples, both using the Laplace potential field, have been chosen to represent as many distinct characteristics as possible of GI-PFG applications. In addition, it has been shown that the direction of travel for a given mission can also have a dramatic effect on the path and safety of the transfer. Therefore, each example will be tested in both directions to provide a range of both favourable and unfavourable free-drift behaviours.

The first example shown is that of a simple transfer around the front of the COF module at the front of the ISS structure. In the standard direction from above to below the module, this transfer demonstrates a path generated under favourable free-drift conditions that continuously guide the free-flyer away from the COF module. However, for the reverse transfer the opposite is true, with the orbital dynamics curving the path toward the COF structure for the second half of the transfer. The velocity selection results, shown in Figure 6.15, demonstrate that the overall path followed with velocity selection activated follows a

similar route to the goal as the original path, though the manoeuvres executed are not the same. In the forward direction, shown in Figure 6-15(a), the initial velocity applied to the free-flyer from the start position appears to be significantly lower than that of the original path, resulting in the second manoeuvre being made earlier in the path. However, after this point the velocities appear to be relatively similar. The reverse path, as shown in Figure 6-15(b), requires a significantly larger number of lower velocity transfers throughout much of the path, in order to increase the safety of the transfer.

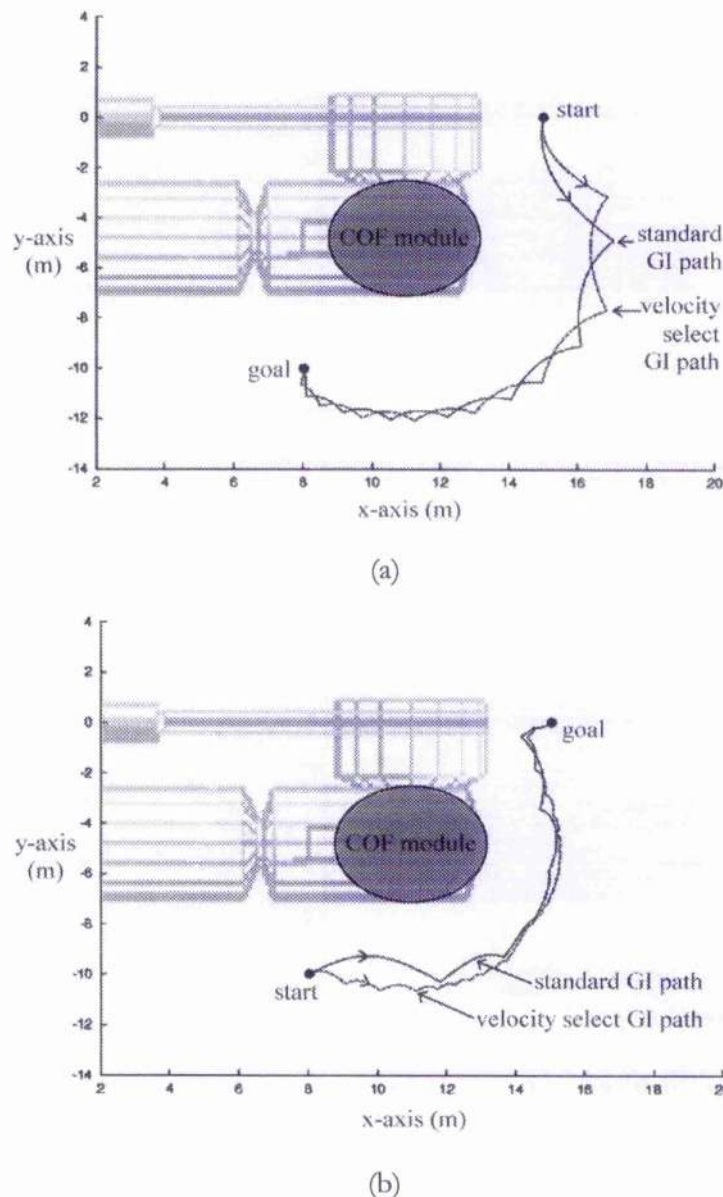
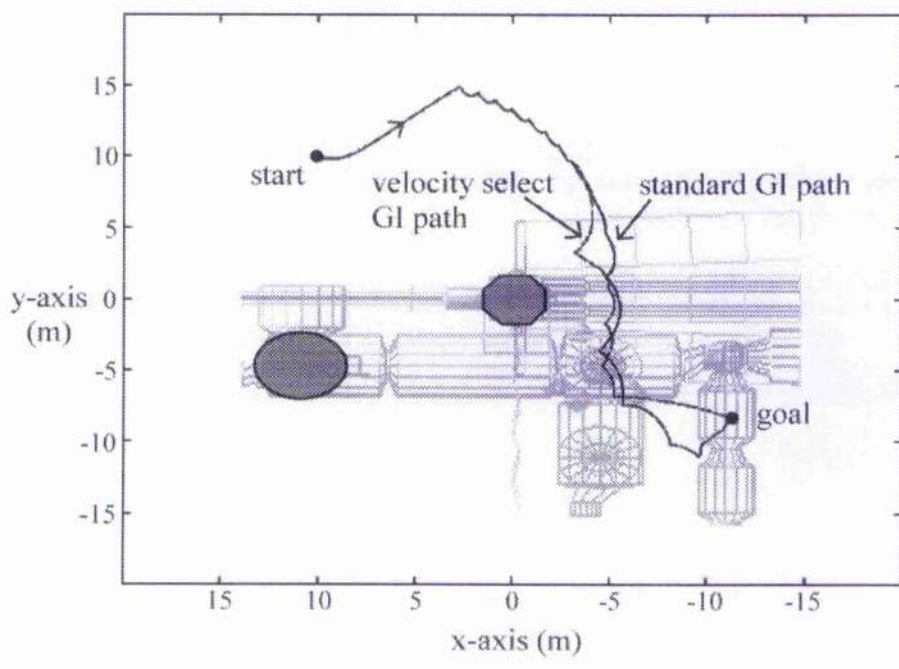


Figure 6-15 Velocity Selection Application to COF Transfer

The second example that will be used to demonstrate the application of velocity selection is a more extended transfer than the COF example, transferring from a position above and ahead of the ISS structure, through the centre of the main structure to a position to

one side of the lower portion of the ISS. This example, previously shown in Figure 5.12(d) and Figure 6-7(b), demonstrates GI guidance behaviours both in passing between elements of the ISS and in transferring between points above and below the station. Moreover, this transfer is also a good example to demonstrate varying free-drift behaviours through the path, since at the start of the transfer the free-flyer orbital dynamics produces a safe path that requires little control to continue toward the goal, while in later sections frequent control impulses are needed to guide the path safely to the goal. Using velocity selection the forward transfer path, shown in Figure 6-16(a), follows the original path almost exactly for the initial segment of the transfer, showing that the nominal k velocity must be passively safe for this period. The paths then diverge slightly as the velocity selection causes lower velocity requests to be made. Towards the end of the path the velocity selection path then makes a comparatively high velocity manoeuvre, causing the paths to diverge significantly, with the new path finally approaching the goal from a different direction. The reverse velocity selection transfer on the other hand, follows the original path very closely, with the exception of a higher frequency of lower velocity impulses in the first quarter of the transfer.



(a)

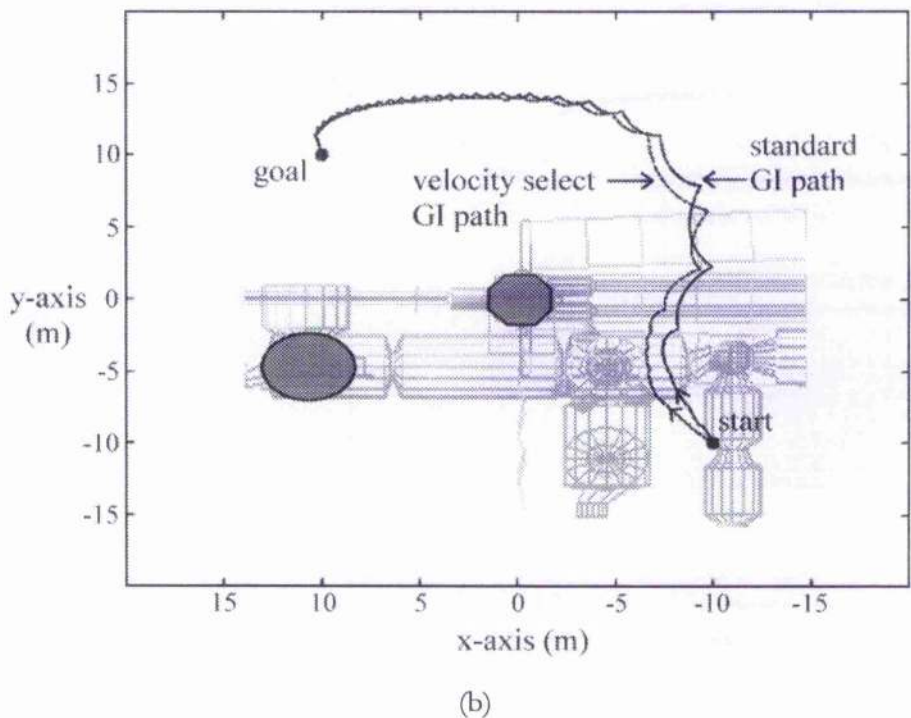


Figure 6-16 Velocity Selection Application to Extended Transfer

The paths followed by the GI-PFG method when using velocity selection only demonstrate the continued ability of the guidance method to find a path to the goal. The original purpose of the velocity selection technique was to enhance the safety of the GI method. The consequences of Inspector Free-Flyer impact velocities on the relative safety of the mission will be investigated later in section 7.3.4 to develop a method of analysing the safety of Inspector missions. However, this path safety analysis can be utilised here to assess the safety benefits of velocity selection. The results obtained, shown in Table 6-1, represent the safety of a path by the percentage of transfer time along which the free-flyer is on a passive impacting trajectory with the ISS. These percentages are then further broken down into three safety categories by velocity of impact, based on the safety categories defined in section 3.0. The categories consist of velocities that would present a *Catastrophic* hazard to the ISS, velocities that would result in a reduced but still *Critical* hazard (including *Catastrophic* results), and all collisions of any velocity (including both previous percentages).

No Velocity Selection

Path	Figure 6-15(a)	Figure 6-15(b)	Figure 6-16(a)	Figure 6-16(b)
Description	COF	Reverse COF	Extended	Reverse Ext.
Start (m)	(15,0,7)	(8,-10,7)	(10,10,10)	(-10,-10,-10)
Goal (m)	(8,-10,7)	(15,0,7)	(-10,-10,-10)	(10,10,10)
Control impulses	9	8	18	24
$\Delta V \text{ m s}^{-1}$	0.1281	0.0888	0.2379	0.3139
Total time (sec)	2021	2950	6094	6092
Impact safety	32.61 %	87.66 %	55.99 %	46.26 %
Critical safety	26.52 %	1.53 %	43.50 %	9.95 %
Catastrophic safety	0.00 %	0.00 %	18.54 %	7.37 %

With Velocity Selection

Path	Figure 6-15(a)	Figure 6-15(b)	Figure 6-16(a)	Figure 6-16(b)
Description	COF	Reverse COF	Extended	Reverse Ext.
Start (m)	(15,0,7)	(8,-10,7)	(10,10,10)	(-10,-10,-10)
Goal (m)	(8,-10,7)	(15,0,7)	(-10,-10,-10)	(10,10,10)
Control impulses	9	8	18	33
$\Delta V \text{ m s}^{-1}$	0.1266	0.1380	0.2811	0.3462
Total time (sec)	2363	5361	6297	8373
Impact safety	22.85 %	82.97 %	52.64 %	61.94 %
Critical safety	0.00 %	0.00 %	22.19 %	5.39 %
Catastrophic safety	0.00 %	0.00 %	0.00 %	0.00 %

Table 6-1 Velocity Selection Safety Results

The results show that for the examples given, the use of velocity selection manages to reduce the *Catastrophic* impact percentage to zero in all cases, and also significantly reduces the *Critical* percentage in every case. However this is at the cost of possible increases in total impact percentages, showing that although the technique can reduce the overall safety risk to the ISS, the generation of purely passively safe trajectories by this method is not possible. The cost to the example transfers in terms of ΔV and transfer times is relatively small in cases where approximately the same number of control impulses are performed. However, in cases where a significantly greater number of control actions are required, usually as a result of lower control velocities, the result can be a significant increase in transfer time, and occasionally ΔV requirements. In terms of the ISS-Inspector mission however, these increased cost should be seen as acceptable for the increase in safety achieved.

6.6 Navigation Problems and Solutions

One of the most significant problems that any autonomous guidance technique must deal with is errors, both in the navigation data supplied to the GNC system, and in the execution of manoeuvres requested by the guidance system. For a free-flying vehicle in orbit, using a discrete control method, navigation errors present a serious problem to the safe and reliable guidance of the free-flyer. Navigation errors are more significant than thruster actuation errors because while an actuation error will make a single discrete change to the subsequent free-flyer path, navigation errors are constantly and rapidly changing with limited reference to past data.

The trajectory deviation caused by a thruster actuation error is relatively easily detected as it will quickly become apparent to the GNC system as the trajectory progresses, allowing corrective manoeuvres to be performed if necessary. In fact small thruster errors, such as to be expected from an Inspector type vehicle, will be automatically corrected by the GI-PFG method. Since the guidance technique does not rely on a precise path being followed, small trajectory errors will merely result in subsequent control actions taking place at slightly different points. The GI technique is therefore robust enough that, so long as an initial portion of the trajectory does travel down the potential gradient, a route to the goal can still be found though an alternate route may be taken.

Failure of the GI-PFG method due to thruster errors will only occur if thruster errors become so large that the direction of the resultant velocity vector at a significant proportion of control points begins to be normal to the desired direction, or if the applied velocity magnitude becomes close to zero. However, due to the fault tolerant design of the Inspector vehicle and built in safety constraints, this scenario should never be permitted before a CAM manoeuvre is performed to remove the stricken Inspector Free-Flyer from the vicinity of the ISS. In any case, it would be nearly impossible for any autonomous guidance strategy to overcome such severe actuation errors.

Navigation errors on the other hand, directly affect a potential field guidance method's ability to determine the desired control action at any point, and if not dealt with can easily result in failure of the GI-PFG method.

6.6.1 Navigation Errors/Noise

For the ISS-Inspector Free-Flyer, navigation errors are particularly significant due to the relatively low velocity of the free-flyer throughout its PFG manoeuvring. In many cases, the total distance travelled in a given time-step will actually be smaller than the average positional error. This is a significant problem for GI guidance, since the method must be able to determine not only the potential and gradient at the current position to supply control demands, but also the current direction of motion so that the switching criterion can be determined. For a GI-PFG path found with a Laplace potential field, with velocity selection enabled, a typical example of the velocity profile is shown in Figure 6-17. The free-flyer velocity varies discontinuously at each control point as the safest velocity is applied by the velocity selection routine, and continuously between impulses due to the vehicle orbital dynamics. However the average velocity remains close the nominal requirement that $k_{\text{nom}} = 0.01 \text{ m s}^{-1}$.

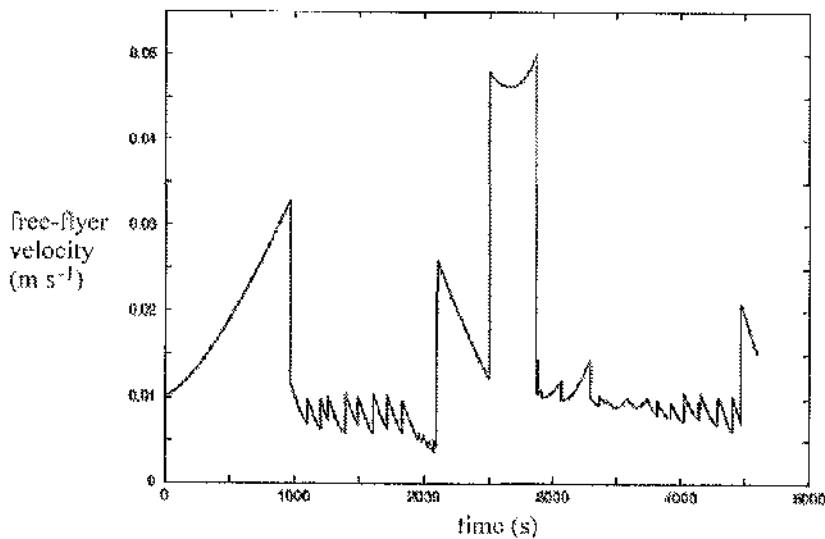


Figure 6-17 GI Path Velocity Profile

The errors experienced by the Inspector navigation system will, irrespective of the navigation method used, typically comprise of two elements, random noise and bias. Bias errors are specific to each specific navigation type, for example a RGPS system will experience error bias caused by the shadowing and interference effects of the ISS structure with the RGPS signals. This bias should produce a relatively consistent error within any given area around the ISS, but will vary with position around the structure. The specific and relatively unknown nature of bias errors makes it difficult to simulate their effect on the Inspector navigation results. Fortunately however, since these errors should only change relatively

slowly for slow free-flyer velocities, they do not pose a serious threat to the use of GI guidance. The problem of any significant bias errors affecting the final Inspector design as a result of the chosen navigation system will require compensation in the vehicle navigation system, and should not affect path planning and guidance.

Errors caused by random noise on the other hand will affect every navigation system in the same way, with only the relative magnitude of the noise varying between methods. It is these errors that will have the most significant effect on GI guidance, since even a relatively small magnitude random noise component can disguise the true short term motion of a slow moving free-flyer. Unlike bias errors, random noise can be simulated by applying a standard Gaussian distribution random number generator to the navigation data. To test the Inspector Mission Planner, the C random number library ‘Randlib.c’ was used to generate random errors with using normal distribution with a standard deviation σ chosen to match the expected navigation error range of 0.025 m [140]. The results of a free-drift path generated using a standard deviation of $\sigma = 0.025$ m, shown in Figure 6-18, clearly demonstrates the problem of random navigation errors. Because the path appears to step in different directions at each point, the application of GI-PFG to this path will only result in continuous control requests, triggered by the false directions supplied to the switching criterion.

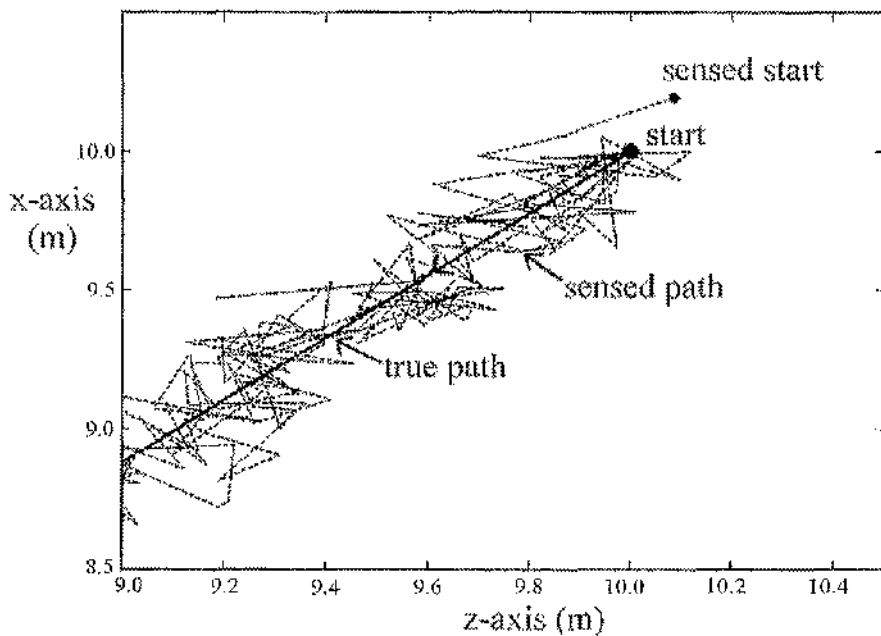


Figure 6-18 Sensed Free-Flyer Path with Random Noise Errors

The sensed path in Figure 6-18 appears stochastic because although the true path is only progressing at a rate of approximately 1 cm per second, the errors of ± 0.025 m in any direction completely mask this motion to jump forward and back with each step. Over a

longer period however, the sensed path does follow the average trend, and so a solution to obtaining improved directional estimates from the sensed path is to only sample the navigation data at longer intervals. This allows the true position to progress further between navigation cycles, and if the sample interval is sized by the expected velocity of the free-flyer so that the distance travelled between samples is greater than the maximum possible error, then the sensed path should progress, if a little unevenly, in the correct direction. This can be applied to the GI guidance method by using the applied velocity at each control impulse to adjust the navigation sample interval. The result is that even with random errors the GI-PFG method is now able to correctly determine the approximate direction of travel, and can guide the free-flyer to the goal. The results of scaling the sample rate by the applied velocity for a test trajectory are given in Figure 6-19, showing the sensed path approximating the true path, while rapidly jumping either side of the trajectory. Unfortunately however, this technique makes assumptions about the free-flyer velocity that may not hold throughout its free-drift path, and may result in overly long sample intervals that could compromise the safety of the, originally real-time, guidance method. In addition, the magnitude of the random noise must be known for the sample interval to be calculated.

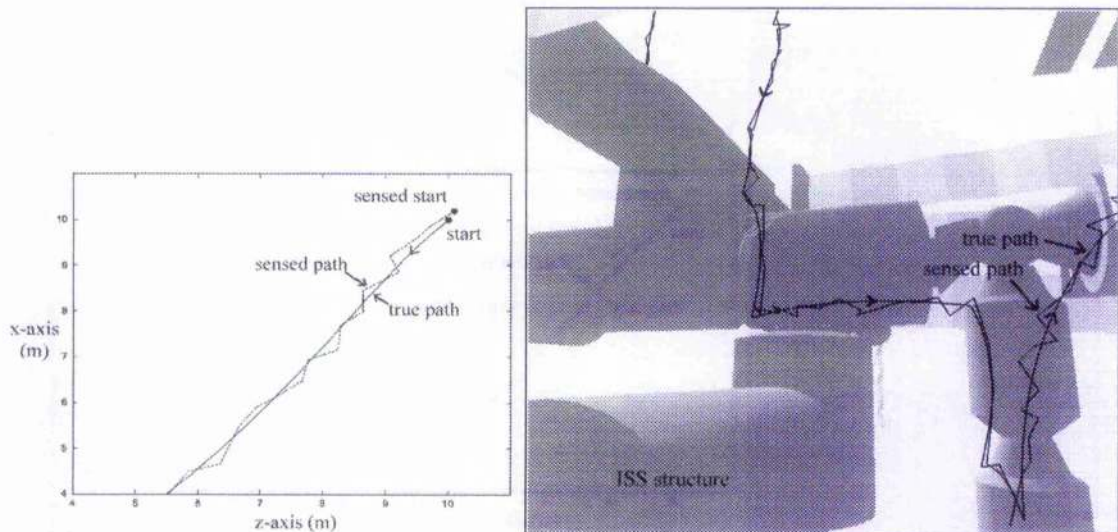


Figure 6-19 Sample Rate Adaptation

6.6.2 Smoothing and filters

To maintain a high sample rate and ensure the quick response of the GI-PFG method, a filter or smoothing routine is required to deal with random navigation noise before it can be used by the guidance system. The best solution would be to use a fast filter such as a Kalman filter [141], commonly used for GNC systems onboard spacecraft, which would be built into the Inspector Free-Flyer navigation system. In the absence of any such capacity however, it

was decided for test purposes to simulate the approximate effect of a navigation filter using simple data smoothing techniques. Unlike a Kalman filter, these smoothing techniques do not require models of the vehicle dynamics to provide estimates of vehicle state, and can be relatively easily implemented for free-flyers such as Inspector where the vehicle motion is smooth and undisturbed between control manoeuvres. In fact, particular exponential smoothing techniques are particularly suited to the smoothing of data that represents a continuing trend, such as that of free-drift free-flyer motion.

The basic form of exponential smoothing can be given by the Simple Exponential Smoothing method [142], which smoothes a series of values given by y_k as

$$\text{Eqn 6-13} \quad y'_k = ay_k + (1-a)y'_{k-1}$$

where ' represents the 'smoothed' value and a is the smoothing constant. This method is applicable to cases with no continuing trend, but where the most recent points carry more influence than earlier values. As smoothing progresses, the influence of previous data points, carried over in the y'_{k-1} term, decreases in an exponential fashion.

The Simple Exponential Smoothing method can then be extended to incorporate a linear trend into the exponential smoothing equations [143]. This method, commonly known as Linear Exponential Smoothing or Holt's method, is given by

$$\text{Eqn 6-14} \quad \begin{aligned} y'_k &= ay_k + (1-a)(y'_{k-1} + t_{k-1}) \\ t_k &= b(y'_k - y'_{k-1}) + (1-b)t_{k-1} \end{aligned}$$

where a is the level smoothing constant, and b is the trend smoothing constant. The term t_k is used to represent the trend of the sequence.

One further extension can then be made to Holt's method is to add a cyclic pattern to the smoothing equations to give

$$\text{Eqn 6-15} \quad \begin{aligned} y'_k &= a(y_k / s_{k-p}) + (1-a)(y'_{k-1} + t_{k-1}) \\ t_k &= b(y'_k - y'_{k-1}) + (1-b)t_{k-1} \\ s_k &= c(y_k / y'_k) + (1-c)s_{k-p} \end{aligned}$$

where a is the level smoothing constant, b is the trend smoothing constant, c is the seasonal smoothing constant, and p represents the seasonal period. This Seasonal Exponential Smoothing method is known as Winter's method, and was developed for use in weather forecasting since it works well for data that follows both a trend and a cyclic pattern.

To smooth the Inspector navigation data, Holt's method was chosen. Although the free-flyer motion will display a periodic pattern within each orbit, it is not accurately cyclic since the trajectory may not return to the same position after each ellipse, so Winter's method should not be applied. Besides, between each control impulse, sections of free-drift will be of a relatively short duration so that the periodic motion will not have a significant effect on the short period trend. In addition, though the smoother must be reset at each control impulse, as the new free-flyer velocity will be approximately known after each impulse, the initial trend term of Holt's method can be initialised to this velocity allowing the smoother to converge quickly to a good approximation of the free-flyer motion.

The results of GI-PFG using exponentially smoothed navigation data, under the same random noise conditions as Figure 6-18, are demonstrated in Figure 6-20. The smoothed results give a reasonable representation of the true free-flyer path in most cases, where in each case the largest positional error occurs at the control impulse point where the smoothed estimate must be reset to the current, corrupted position. The resulting navigation data is certainly sufficient to allow the GI guidance method to function, and find a safe path to the goal.

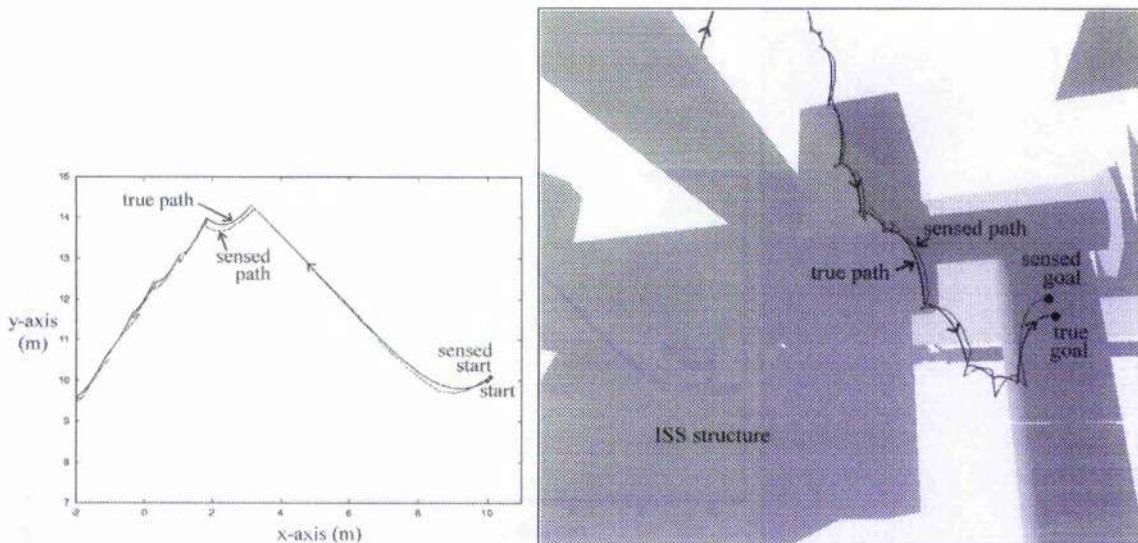


Figure 6-20 A Smoothed Navigation Path

6.6.3 Backup Navigation Methods

In the event of a complete loss of the RGPS signal or other primary navigation method, the baseline ISS-Inspector safety response as detailed in Chapter 3 is to perform a CAM to retreat from the ISS, potentially resulting in the total loss of the Inspector Free-Flyer if RPGS data cannot be restored before Inspector drifts away from the station. It may

therefore be useful to briefly consider alternative navigation methods that could be employed by Inspector as a backup in case of a primary navigation failure.

One possible alternative would be available if a visual system was available on-board Inspector for use in station-keeping during the observation phase. In this case, the same system could be activated during other mission phases if navigation is lost, not to provide navigation but to maintain the free-flyer's current position for a predefined waiting period, in order to allow the original navigation system to be re-acquired. If this cannot be achieved, then the CAM can be performed without safety having been compromised by the station-keeping period. But if navigation is restored, then the mission may still be completed, or at least the Inspector Free-Flyer could safely return to its docking port for servicing.

Another alternative would be to use a series of proximity sensors situated around the Inspector vehicle to provide a reactive control system, as described in section 5.1.2, to take over in the case of a navigation failure to keep the free-flyer safely away from the ISS structure. This reactive obstacle avoidance behaviour could then be combined with a simple visual beacon to guide Inspector safely back to its docking port without the need for any form of absolute navigation. Care must be taken however to preserve sufficient propellant supplies, so that in case a path to the docking port cannot be found, a manoeuvre can still be performed to safely remove the vehicle from the proximity of the ISS.

Despite these alternative navigation strategies to save the Inspector mission however, the safest strategy in the event of a loss of primary navigation data remains the complete removal of the Inspector Free-Flyer from the vicinity of the ISS with a pre-planned CAM.

CHAPTER 7: MISSION PLANNING

7.1 Introduction

The original goal of this work was to develop the methods and techniques necessary for mission planners and the ISS crew to operate the ISS-Inspector in close proximity to the International Space Station. Much effort has been made to investigate the orbital mechanics of the problem and develop control strategies which allow the Inspector Free-Flyer to manoeuvre safely from point to point around the ISS. The final step is now to combine these manoeuvres and skills into a global mission planning architecture and tool. This must encompass both a method of describing and choosing mission parameters, an interface to the skills available, and a means of optimising these skills and manoeuvres to achieve the mission goals. A common approach to high level mission planning for robots is to break the available skills down into basic tasks or objects reducing the planning problem to the selection and scheduling of these tasks [144]. This form of hierarchical architecture has been planned in a three-layered structure for NASA's AERCam project [145] [39], an alternative free-flying inspection robot designed for the ISS.

As previously mentioned, mission planning for the ISS-Inspector will be performed primarily from the ground. However, it is also necessary for planning and monitoring capabilities to be available onboard the ISS. This gives a greater degree of control to the astronauts who are closer to the tasks in hand, and also provides a backup for any unexpected break in communications that may occur during a mission. It does mean however that any mission planning software must be portable to the relatively modest computational capabilities available onboard the International Space Station.

The definition of a fixed set of available skills wrapped up within a single planning tool has the advantage of simplifying the task of mission planning, enabling at least preliminary planning to be performed within a very short time schedule. This ability to quickly plan and assess potential missions would greatly add to the flexibility and ultimate usefulness of the ISS-Inspector project. Inspection missions may even be planned on a fast track basis as they become needed, rather than requiring long lead-times to analyse and plan every mission. The accelerated planning of missions would also expand the range of missions to which the ISS-Inspector could be applied. Many potential inspection missions, such as the emergency inspection of accidental damage to the ISS, would typically arise unexpectedly and must be

performed in the shortest possible time. In situations such as this, rapid external inspections would allow ISS controllers to assess the situation and detect any serious danger to the station and its crew faster than might otherwise be possible. This brings obvious safety benefits to the International Space Station over its lifetime, and to the ISS crew.

With the individual skills and manoeuvres available to the ISS-Inspector vehicle having been previously defined in Chapter 3 and developed in Chapter 4 and 5, the task of mission planning is simplified to specifying mission goals and then using the available skills to complete these goals. In order to achieve this, a mission planner must make the best use of all these skills to complete each mission as efficiently and safely as possible within the constraints of the ISS environment and the Inspector's abilities. With the planning and execution of each manoeuvre effectively at a lower level within the overall planning structure, the planning sequence naturally breaks down into a quasi-hierarchical structure within the mission planning sequence. At the highest level is observation point selection, performed interactively by the operator to obtain suitable inspection opportunities of the target co-ordinates. This then defines each mission as a set of goal co-ordinates which subsequent planning stages must then attempt to reach. Secondary to goal specification in the planning hierarchy comes the planning and scheduling of the route to be taken between goal co-ordinates. This scheduling activity is closely related to the subordinate task of selection and planning of individual skills and manoeuvres, as it requires the results of manoeuvre planning to obtain the cost estimates necessary to optimise the mission sequence. The final level in the ISS-Inspector hierarchy is the actual low level execution of the planned manoeuvres, as described in Chapter 3 and Appendix IV, and the monitoring of the Inspector Free Flyer during its mission. The overall planning structure is therefore fairly compact, with an initial goal specification stage, followed by a 3-level skill selection, optimisation, and execution hierarchy:

- Observation point selection - Specification of mission goals.
- Scheduling and optimisation of complete mission.
- Planning and optimisation of individual mission elements.
- Low level execution and monitoring of planned manoeuvres.

Due to safety considerations however, the safety constraints and escape manoeuvres implemented in the low-level control system must take precedence over all higher level commands. In order to ensure the safety of the free-flyer, the availability of an autonomous CAM manoeuvre (defined earlier) must be maintained to permit a safe retreat from the ISS at

any time. The overall mission plan is therefore executed as a series of requests to the lower level command segments, rather than issuing direct commands to the system. This not only ensures the basic safety of the free-flyer, allowing reactive elements to be included if desired [146], but also permits flexibility in the low-level implementation of command requests and safety strategies in the Inspector Free-Flyer hardware.

New techniques are therefore required both to select the most suitable manoeuvres for any given transfer between goal points, and to optimise the sequence of manoeuvres to visit these points as safely and efficiently as possible.

7.2 The Vehicle Routing Problem (VRP)

The sequencing problem of finding the best path for a vehicle, or fleet of vehicles, to visit each node of a given set of co-ordinates, known as the Vehicle Routing Problem (VRP), is applicable to a large number of real world problems, associated not only with transportation. The simplest example of this problem, the Travelling Salesman Problem (TSP), is actually one of the oldest optimisation problems to be investigated by computational methods [147] [148], and together with the VRP it has received a great deal of attention in recent years [149]. The main reason for interest in the VRP is its applicability to such a large range of real world problems, coupled with the challenge involved in dealing with large instances of the problem. Applications range from relatively simple problems such as the TSP's namesake, a travelling salesman who must visit a number of customers in a single trip, to more complex problems such as the scheduling of a large fleet of vehicles to optimise deliveries. Some of the most complex problems arise from more diverse applications, such as the scheduling of drill head changes on a multi-headed CNC machine. With modern CNC machines having a hundred or more individual drill heads available, and the time taken to change heads a major percentage of machining time, making the best use of each head before requiring a switch has the potential to significantly increase machine efficiency.

For the ISS-Inspector mission, optimising the sequence in which the observation points are visited will be critical to the success of any series of inspections. As detailed in Chapter 3, the Inspector Free-Flyer will be subject to a number of constraints, defined both by the limitations of the hardware (i.e. power and propellant limits), and operational constraints such as crew work patterns and periodic orbital conditions (day-night cycle). All of these restrictions will limit the number of observations that may be performed within a

single mission, so it is imperative that the sequence be optimised to ensure that the ISS-Inspector is able to make the best use of its resources to maximise its capabilities.

7.2.1 The Travelling Salesman Problem

Despite its relatively narrow definition, the original Travelling Salesman Problem remains a crucial component to the solution of many higher level VRP's, which are in turn directly applicable to real world problems. In fact the solution to most VRP's lie in optimising a constituent set of smaller TSP's. To summarise the problem, the TSP describes the problem of optimising a tour through a set of nodes, which passes through each node in the set once, and returns to the start point. This definition is also known as the Hamiltonian cycle problem in graph theory [150]. Analysis of each tour (or cycle) is based on a given a set of costs associated with travel between each node in the set.

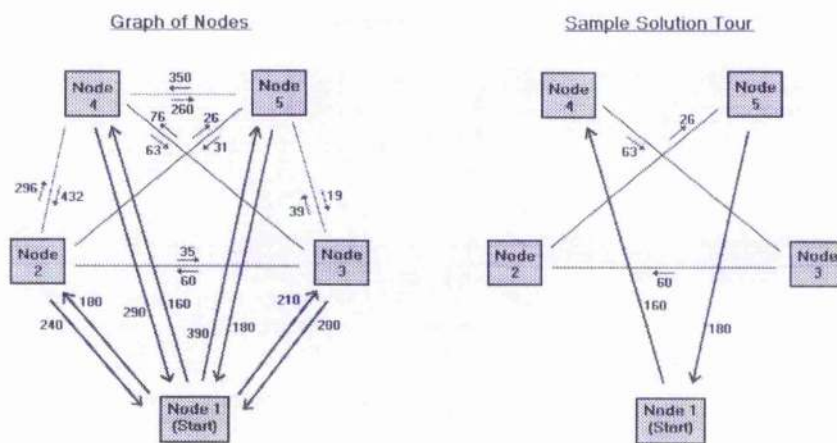


Figure 7-1 The Travelling Salesman Problem

Interestingly, as described in Figure 7-1, the TSP appears relatively similar to the path finding problem solved by Dijkstra's algorithm, as investigated in Chapter 5. The configuration space – a graph of nodes with transfer costs between each node – is identical. However rather than searching for the optimum route to a single goal node, the TSP is instead searching for the optimum path from the start node through each and every node in the graph before returning to the start node.

For the purposes of this investigation we shall limit ourselves to dealing with only very small sequencing problems of up to 10 nodes. This is sufficient for the planning of ISS-Inspector missions since operational constraints will preclude the selection of a large number of observation points, except where nodes are very close together, in which case a group of close co-ordinates may be treated as a single node for high level sequencing. Typically most of

the research effort in dealing with TSP problems has been targeted at solving ‘small’ problems of up to 30 nodes, and even in these cases only near optimal solutions are attainable within a reasonable computational limit. Larger problems are usually sub-divided into sets of smaller, more manageable problems [151]. Limiting ourselves to dealing with only 10 nodes greatly simplifies the problem, allowing fully optimal solutions to be obtained with moderate computational demands.

For such small instances of the TSP, a solution can be obtained by the brute force method of simply evaluating each possible complete sequence of the given set of nodes. This can be achieved by taking each possible sequence containing a single instance of each of the configuration nodes, excluding the start node, and evaluating the cost of transferring through the sequence. The cost of transferring from the start node to the initial node in the sequence, and from the final node back to the start, must of course be added to the total cost. Even the simplest solutions can however have their own drawbacks. In this case the problem is in finding all the valid sequences of the available nodes. A basic method that has been applied to the Inspector problem is to find possible sequences by stepping incrementally through a decimal numbering system, using each digit to represent a node in the sequence. So for example, in a 4 node problem, 4231 would represent the sequence 4, 2, 3, 1 where the given nodes are numbered 1 to 4. Each possible sequence must be evaluated to ensure that each digit, or node, only occurs once, but for small numbers of nodes this is relatively cheap to evaluate. The main advantage is the simplicity of the method, since for a 4 node problem we have simply to count through from 1234 to 4321, check for valid sequences, evaluate the cost of each sequence, and save the decimal sequence of the optimum result.

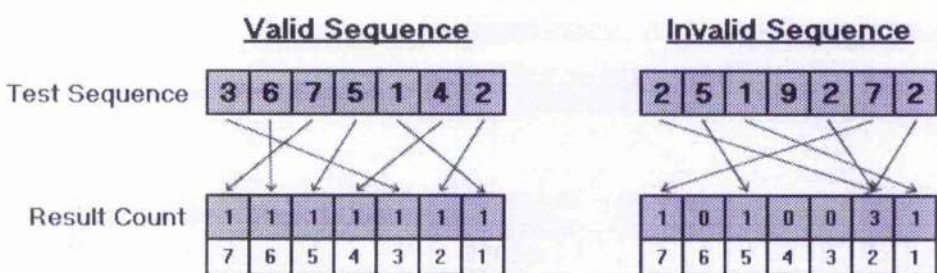


Figure 7-2 Decimal Sequence Checking

Of course, as described above this method can only deal with problems of up to 9 nodes (or correctly 10 nodes if we denote the nodes 0 to 9), or less depending on the size of integer variables available on the host hardware. For example a 16bit integer gives an upper limit of 65536 allowing 5 nodes, and a 32bit integer will allow just 9 nodes to be evaluated. This restriction could be easily overcome using an array to store the individual choices, but in

any case, past sets of 6 nodes the costs involved in evaluating large numbers of potential sequences quickly become prohibitive. From a computational perspective, the principal advantage of the method is the minimal memory storage requirements during evaluation, since the current and best sequences are stored compactly as integer variables.

7.2.2 A Dynamic Programming Solution to the TSP

A more elegant approach to optimising the small TSP can be accomplished by applying dynamic programming techniques to the problem. Invented by the American mathematician Richard Bellman [152], dynamic programming is a mathematical methodology that can be applied to many optimisation problems, amongst a range of other diverse applications [153]. The key to the method is in storing and sorting partial results to the problem in question, enabling otherwise expensive recursive function calls to be made quickly through reference to this previously calculated data. The technique of dynamic programming has already been employed in solving small TSP's, and the solution will be developed here for application to ISS-Inspector mission scheduling.

The first stage is to break down the problem into a series of smaller problems that may be determined through recursion. If we denote a set of nodes as S , then we can define the function call $f(S, x)$ to represent the optimum tour through all the nodes belonging to S to reach the node x , where x and S are exclusive. This function call can then be replaced by the recursion

$$\text{Eqn 7-1} \quad f(S, x) = \text{MIN}_{y \in S} \{f(S - y, y) + d(y, x)\}$$

where y belongs to S , and $d(y, x)$ represents the cost of transfer between node y and node x . By denoting the set of nodes S of the target TSP, including the start node, as nodes $x = 1$ to n , the solution to the TSP can be obtained by the function call $f(S, n+1)$ where node $n+1$ also represents the start position.

As it stands, it would be very expensive to evaluate the recursion described above to solve a TSP. Dynamic programming techniques, however, allow us to replace the full recursion by storing a history of partial results in an array. Evaluation of Eqn 7-1 then becomes a series of references to this array

$$\text{Eqn 7-2} \quad f(S, x) = \text{MIN}_{y \in S} \{F_{S-y, y} + d(y, x)\}$$

where the array F_{ij} contains the results of previous calls to Eqn 7-2, referenced by set (i) and node (j). Since the reference used for each set in this case is independent of the order of nodes stored, construction of each set index lends itself to binary representation. Each set or

subset of the TSP nodes can therefore be represented by a single variable, constructed so that each individual component ‘bit’ denotes the presence of the corresponding node in the set. So for example, if the 2nd bit is set to 1, then the 2nd node is contained within that particular set. Of course, as with the decimal representation used in the previous section, this is intrinsically limited by the storage afforded by an individual variable. In this case, however, the limit would be for 32 nodes in the case of a 32bit variable, by which time other constraints would have halted solution of the TSP.

Before this technique can be applied to the TSP, a methodology to fill the required history of results in the array F is required. Fortunately, this can be achieved by simply applying Eqn 7-2 sequentially to the lower entries of the array, after initialising the zero row with the cost of transferring to each node from the start node. Operationally, this process can be illustrated by the following pseudo code

For all x belonging to S : $F_{0,x} = d(0,x)$ (initialise zero row)

For $i = 1$ to binary representation of S : $F_{i,x} = f(i,x)$ (evaluate each subset of S)

{ *For all x in S : $F_{i,x} = f(i,x)$* }

The results stored in F are therefore incremental totals of the optimum cost incurred in reaching each node through each subset of S . This allows easy evaluation of the optimum cost to complete the TSP, but unfortunately does not include a reference to the sequence used to achieve that optimum cost. Finally then, the array F must be extended to store for each entry the intermediate node used to achieve the stored cost at that point in the calculations. This corresponds to the node y used in Eqn 7-2 that achieves the minimum cost for that step. Given this history stored in F , the optimum sequence can then be found by stepping backwards through the array once the optimum cost entry for the TSP has been found.

Performance of the dynamic programming solution to the TSP is impressive, especially in comparison to the results of the method described in the previous section. In illustration, on a base specification pc, pure evaluation of the TSP for an 8 node problem took 19.9 sec using the brute force method, while the time taken using the dynamic programming solution was too small to be measured using the standard windows timers. For a 9 node problem, time taken for the brute force method increased dramatically to 279.29sec, while the dynamic solution was still too quick to be measured by default timing routines. To get some point of reference, a 15 node problem was attempted using the dynamic programming solution, and took 0.83sec to complete.

The primary disadvantage of the dynamic programming solution is in the storage requirements necessary to maintain the intermediate results. As an example, a 9 node solution

would require an array of $2^{10} \times 10$ results, a storage requirement of at least 10 kilobytes, plus of course a calculation history array of the same size. For a 15 node TSP this would increase to a total storage requirement of at least 2 megabytes, an exponential increase in size.

It is also worth mentioning, since Genetic Algorithms have already been introduced for the problem of optimisation of multi-waypoint paths in Chapter 2, that GA's have also been applied to the travelling salesman problem [154]. However their use is unnecessary for the relatively small number of nodes required for the ISS-Inspector problem as the optimal solution to this TSP is possible.

7.2.3 Mission Scheduling Constraints and the VRP

Expanding on the relatively narrow definition of the TSP, the Vehicle Routing Problem refers to a more general description of the problem of visiting or transporting objects between nodes. In common with the TSP, specification of the problem deals with a graph of nodes, with given costs for transfer or transportation between connected nodes. In addition, the VRP also specifies a list of objects to be transported, located around the nodes of the graph. Associated with each object is also a destination node, to which the object requires transportation. The problem is therefore to optimise the transportation of the objects to their destinations with the minimum transport cost. A good example that demonstrates all the elements of the general VRP would be the scheduling of a lift in a tall building. Each floor that the lift stops at constitutes a node of the graph, with each node connected directly to each other node (since it is quicker to travel directly from one floor to another without stopping at intermediate floors). Objects (or passengers) may then be initially located at any available node, and may wish to be transported to any other available node in the fastest time possible. Of course a lift can only hold a finite number of passengers at any one time, and the capacity of the transportation vehicle is an additional variable that defines the general VRP. The simplest case is of a vehicle that can only carry a single object at any one time (unit capacity), compared to a vehicle that can carry a number of objects at once (multiple capacity) [155].

When dealing with actual physical transportation and distribution problems, a small constraint is frequently added to the general definition of the VRP in order to simplify the specification and solution of the problem. This simplification is to assume that either all the objects to be transported are initially located at a central depot and must be delivered to the nodes of the graph, or vice-versa that objects originally located at the nodes must be transported back to the depot. In practice this constrained definition matches a large number of real world problems, whilst greatly simplifying the problem. Comparing the general VRP to the TSP, we can see that the TSP is in fact a constrained instance of the VRP. For instance,

the TSP could be represented by a VRP with 1 virtual object at each node of the graph, each with a destination at the start node, to be collected by a vehicle of infinite capacity.

In addition to the standard definition of the VRP, an additional side constraint that is frequently applied to the problem is that of time windows, which may be applied to visits to specific nodes of the graph [156]. This constraint allows a time window to be applied to nodes, during which the node requires to be serviced. Effectively this is applied in the form of an additional cost to the tour for arriving at a node outside of the specified window, waiting costs for arriving early at a node, or by tightly constraining windows to exclude tours that do not meet the time constraints. Given the frequent application of the VRP to real transport and delivery problems, the problem of VRPs with time windows has been extensively investigated by the computing community. Although not currently implemented in the ISS Inspector scheduling tools developed here, the specification of time windows would be of interest in planning ISS inspections to meet potential time dependent mission constraints, such as the day-night cycle. As previously mentioned, the ability to plan inspection operations to be performed at particular times to take advantage of optimal lighting conditions, or to coincide with crew activities, would be useful. However, given the relatively short orbital period of the ISS and correspondingly rapid change of lighting orientation, artificial illumination of a target from the Inspector Free-Flyer would be required in any case. Furthermore, this is a separate issue from overall mission duration time constraints on the Inspector vehicle, which are essential mission constraints, and could be dealt with as an additional transfer cost in terms of the duration of manoeuvres.

7.2.4 The ISS-Inspector VRP

Concentrating on the ISS Inspector specific planning problem, there are a number of mission constraints that will narrow the applicable definition of the general VRP to the problem. Initially the Inspector problem appears very similar to the TSP, the Inspector Free-Flyer must visit each observation node once, starting from its docking port and returning to re-dock with the ISS. Additionally, the Inspector has no objects or cargo to transport between the nodes, merely requiring a visit to each node to perform its inspection. Nevertheless, the Inspector Free-Flyer is strictly constrained by both the physical limits of available electrical power and propulsive ΔV , and operational limits on mission duration. In addition, there is the complication of selecting between the fundamentally different transfer types available to manoeuvre the Inspector Free-Flyer between nodes. In other words, the greater propulsion and duration costs of EOS transfers compared to PFG manoeuvring must be balanced by the enhanced safety of the former.

In fact, the problem of costing transfers and missions based on factors other than the absolute distance between nodes is a typical one. In any real VRP or TSP problem the relevant cost of a transfer is more likely to be determined by the duration of the transfer, and perhaps fuel consumption, than distance. For surface transportation problems this should favour solutions that avoid areas of traffic congestion or resistance, to follow faster more efficient routes. In the case of the ISS-Inspector, transfer costs should be a weighted combination of transfer time and the ΔV required for the manoeuvre, allowing a balance to be found between satisfying these constraints on the mission. Absolute constraints on the total mission duration and propellant requirement can be implemented in the costing of transfers by incurring infinite cost to the route if the addition of the transfer would cause either limit to be exceeded.

The selection of suitable manoeuvres for each individual transfer can also be accomplished at the costing stage, where the graph of connected nodes with transfer costs is constructed from the defined mission observation points. At this stage the required manoeuvre type for a given transfer can be found independent of the mission as a whole by basing the selection criteria to optimise mission safety for each potential transfer individually. This means forcing EOS manoeuvres where necessary to maintain reasonable free-drift safety, and allowing PFG manoeuvring when safe to do so.

For an ISS-Inspector mission, the nodes of the TSP are allocated by observation point selection, rather than observation targets since these are the co-ordinates that the Inspector Free Flyer must actually visit to complete an inspection of the target. A complete inspection of one single target on the exterior of the ISS may require a number of individual inspections surrounding the inspection target to fully visualise the component. However, though the selected observation nodes would typically be grouped around the mission targets, in a mission with multiple targets it may not necessarily be efficient to perform all the individual inspections for each target in sequence. In addition, certain circumstances may demand the inspection of an area of the ISS structure as the Inspector Free-Flyer passes across it in order to assess the condition of large components of the station such as the solar panels. In this case, the start point of the inspection would be considered as the observation point, with an additional skill to be performed from there to complete the observation, adding an additional cost to any scheduled transfer to this node. The nodes of the observation point co-ordinates can therefore be optimised globally as an independent TSP, without any need for reference either to the target co-ordinates of each inspection or other skills to be executed at the observation point, other than to add the observation cost to the mission total.

These simplifications, primarily in off-loading mission duration and other global constraints into the pre-scheduling stage of graph cost calculations, allow the ISS-Inspector VRP to be considered as a simple TSP. For solution purposes this allows the dynamic programming techniques described in section 7.2.2 to be directly applied to the problem, with the proviso of incorporating infinite transfer costs to routes that exceed global duration or ΔV constraints. The advantages of this are twofold, both simplifying development of the mission scheduling tool, and constraining the computational requirements of the solution.

7.3 Mission Planning Tool

As previously mentioned, one of the primary objectives of this research has been to develop a rapid mission planning tool that is flexible enough to be used not only by operators on the ground, but also by the crew onboard the ISS. To this end, the software tool must not only be easy and intuitive to use, but also be portable to the computational facilities available on-orbit. To this end much effort has been made to ensure that all the techniques developed here make no great computational demands in terms of processor or memory requirements. In fact, none of the path-planning or guidance methods developed take any longer than a fraction of a second to execute on a relatively modest workstation, hopefully allowing the goal of rapid planning and analysis of ISS-Inspector missions to be realised.

Aside from the technical aspects of mission planning, the secondary challenge mentioned above is that of creating an interface to the Inspector Free-Flyer skills that is both flexible and intuitive to use [157] [158]. For even the simplest mission there is a wide range of information to be displayed to the operator, coupled with a large degree of freedom in the selection of parameters such as the selection of observation points from which to perform each inspection.

Given these goals, the most obvious choice of interface is to use an integrated multi-windowed view to allow various aspects of the planning process to be viewed simultaneously. The author's knowledge of pc based programming, and the ease of developing of Windows software through Microsoft's MFC libraries lead to the mission planning tool being developed for the Windows PC platform. However, the use of widely available OpenGL libraries for the graphics rendering, and ANSI standard C and C++ code for all the algorithms result in a program that would be easily portable to an alternate windowing platform by any programmer with knowledge of that system. Division of the user interface into distinct areas or views allows a combination of both numerical and graphical information to be displayed to the

operator, fulfilling the need for hard qualitative data, complimented by intuitive visual representations as shown in Figure 7-3.

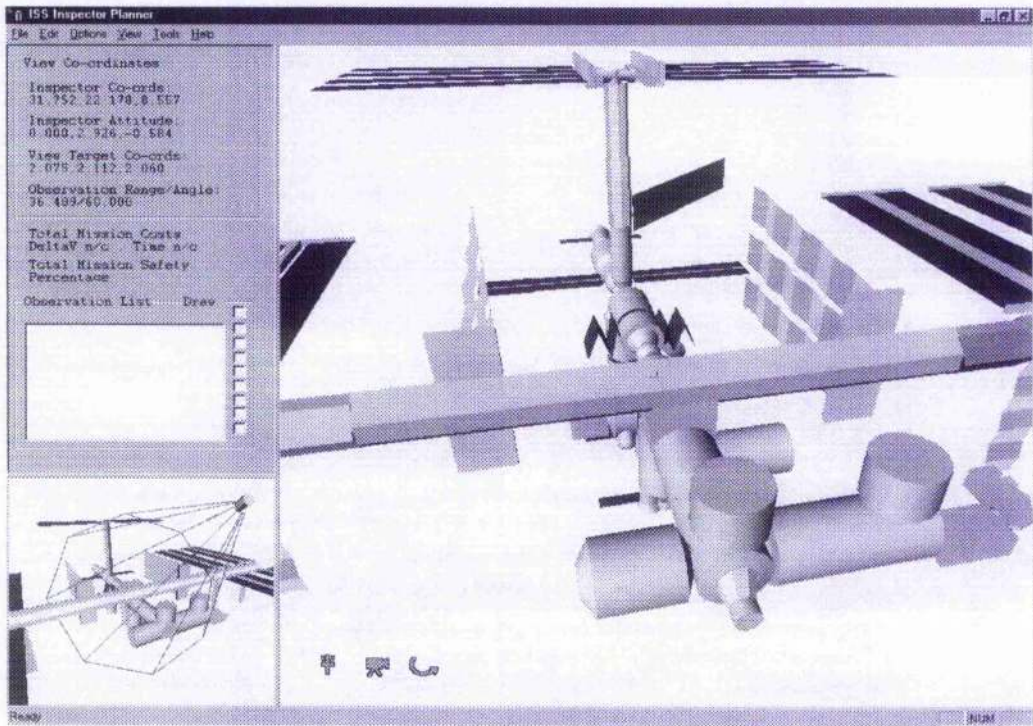


Figure 7-3 The Multi-Windows Interface

Even given the graphical interface of the tool, the use of a relatively simple (and scalable) rendering model of the ISS and the ability to temporarily suspend various optional features such as comms link integrity checking when not required, help maintain low computational hardware requirements.

7.3.1 Observation Point Selection Interface

The selection of suitable observation points from which to perform an inspection of the ISS is one of the most interactive and subjective aspects of mission planning, and is reliant almost exclusively on the input and skills of the operator. The interface used to choose observation points must therefore be intuitive, and supply as much useful information as possible to assist operators in their task. To accomplish these goals, the virtual Inspector camera simulation tool developed in Section 3.3 is incorporated into the mission planning tool, with the virtual view through the Inspector camera forming the primary window of the interface. This, along with a secondary external Inspector and ISS combined view and safety indicators to represent safety and radio comms constraints, form an easily accessible interface to the selection of observation points around the ISS. A third sub-window of the interface is then available to display numerical data, such as the current co-ordinates of the Inspector

Free-Flyer, its target, and previously selected observation points for the mission, as shown in Figure 7-4.

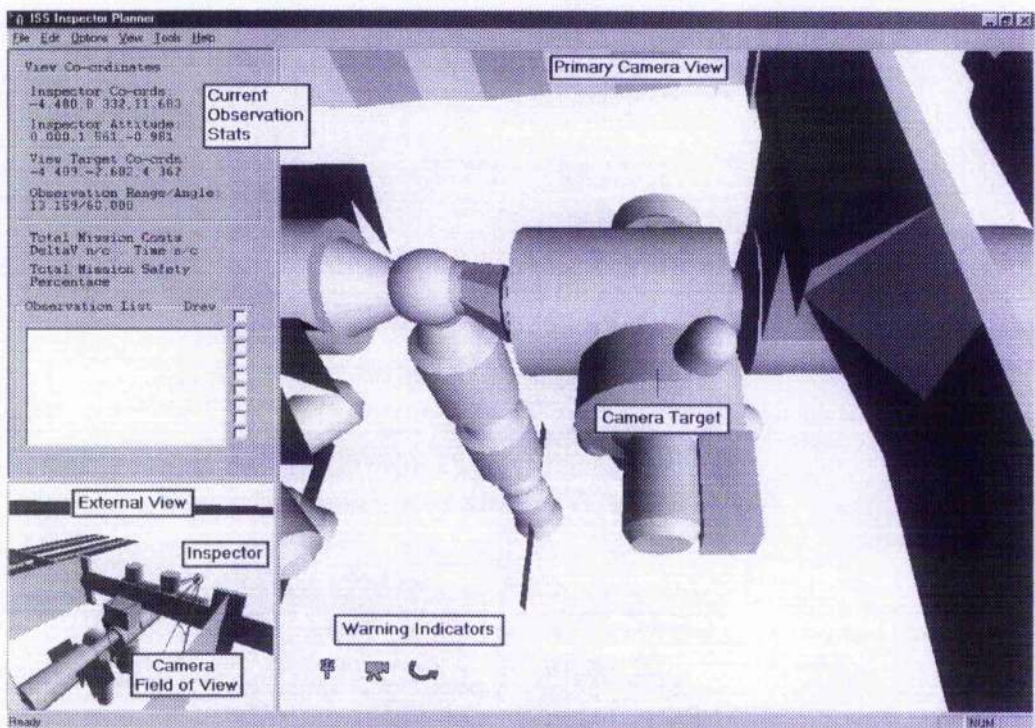


Figure 7-4 Observation Point Selection Interface

Extending the Inspector camera view to deal with multiple observation points, the graphical representation of previously selected points and inspection targets in both the primary camera view and secondary external view, further assists the operator in planning the observations required to fully inspect a given target. In the final step of the confirmation of an observation point and inspection target, a dialogue box permits the manual fine-tuning of co-ordinates, as shown in Figure 7-5.

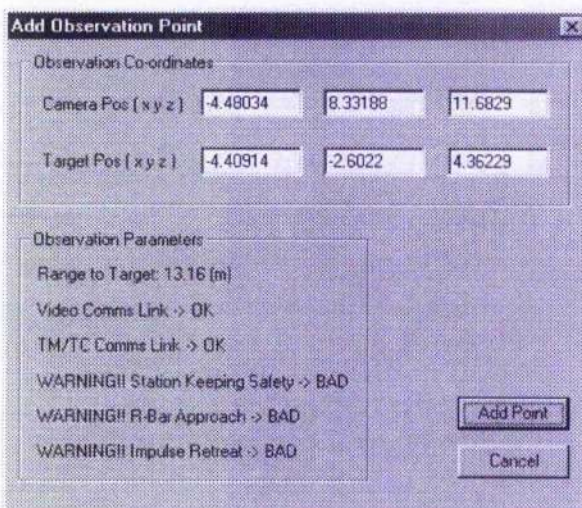


Figure 7-5 Observation Point Confirmation

At this point, additional warnings can be included to reinforce possible constraints such as the safety of the chosen co-ordinates, and the availability of R-bar approach and retreat manoeuvres to reach the position. The availability of such R-bar manoeuvres dictates the availability of EOS trajectories to and from each position, otherwise requiring the use of a PFG manoeuvre to reach the observation point, with the potential reduction in passive safety that entails. The correction of co-ordinates within the confirmation dialogue permits the manual rounding of values, as well as integrating the ability to specify externally planned mission elements or objectives.

7.3.2 Path Planning of Mission Elements

The initial goal of mission scheduling for the Inspector Free-Flyer is to optimise the cost of each Inspector mission within a set of constraints, such as vehicle ΔV and mission duration limits. The primary goal however, remains to maintain the safety of the mission and minimise the potential for mechanical failure to result in a collision with the ISS. Much effort has been made in previous chapters to develop manoeuvring techniques that make use of passively safe trajectories wherever possible. In addition, the basic control strategy for the ISS-Inspector requires the provision of a backup collision avoidance manoeuvre to be available at all times, allowing the Inspector vehicle to retreat safely from the ISS in the event of a problem. There remains however a marked difference between the absolute safety of a tightly defined manoeuvring strategy such as a EOS trajectory, which is specifically designed to be 100% passively safe, and more flexible but inherently less predictable trajectories such as those produced by PFG methods. Furthermore, it is possible to break down PFG transfers into distinct categories of manoeuvre, each with differing degrees of potential safety, both in terms of passive safety, and the ease of implementing a CAM. Hierarchical planning structures often try to make use at a high level of as much available prior information as possible in the selection of lower level tasks [159] [160]. Here, the aim in planning an Inspector mission must be to make the best use of economical PFG manoeuvres in cases where acceptable safety can be maintained, whilst employing EOS transfers when safety constraints make them either suitable or necessary. For example, the additional cost of employing an EOS transfer for an extended transfer along the length of the ISS would be small compared to the safety benefits of avoiding PFG manoeuvring. Similarly, for a transfer from above the ISS structure to below station, the lack of passive safety of PFG would prohibit its use despite the significant increased duration and ΔV cost of using an EOS transfer. On the other hand, for relatively short-range transfers, particularly if enclosed within open areas of space above or below the ISS, the minimal safety advantage of EOS trajectories would be negated by the high cost of the manoeuvre in comparison to the PFG alternative.

Given that the relative safety of PFG manoeuvring and the availability of EOS transfers between co-ordinates is dependent on the relative positions between the start point, the end point and the ISS structure, it follows that the selection of suitable manoeuvres can be made by referring to their position relative to the ISS. This is achieved by segmenting the space surrounding the ISS into zones based on the manoeuvres available within and between these areas, as shown in Figure 7-6. At the pre mission-sequencing cost calculation stage, the optimisation of overall mission safety can then be made by selecting the manoeuvre types available for each transfer between mission co-ordinates by referring to these zones within which the nodes are located.

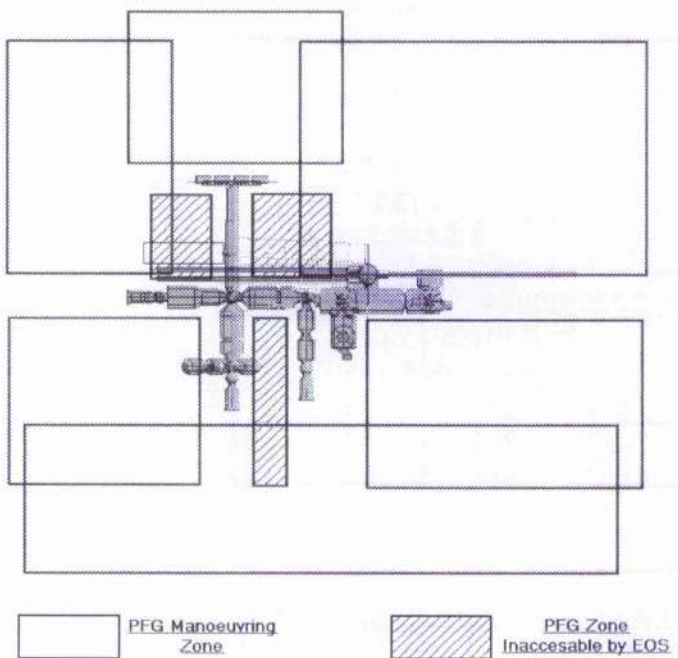


Figure 7-6 Manoeuvre Selection Segmentation Map

The criteria used to segment the space surrounding the ISS, as shown in Figure 7-6, has been to define areas within which PFG manoeuvring is permitted. Transfer between mutually exclusive areas can only be performed using EOS trajectories if available. Overlapping areas are used to afford access, by PFG manoeuvring, to regions that would otherwise be inaccessible as they cannot be reached using an R-bar approach from EOS transfer. The determination of those areas accessible by EOS transfer can be made by referring to the approach and retreat safety envelopes developed in Chapter 3. Meanwhile, a number of basic constraints on the use of PFG manoeuvres can be determined by observing the previously obtained results of the nature of PFG manoeuvring and referring to the orbital dynamics of the problem. Applying these constraints to the local configuration of the ISS

then allows the areas around the station within which PFG manoeuvring is safe to be identified. In general, point to point transfers using PFG can be broken down into five broad categories based on their position relative to the ISS structure, shown in Figure 7-7.

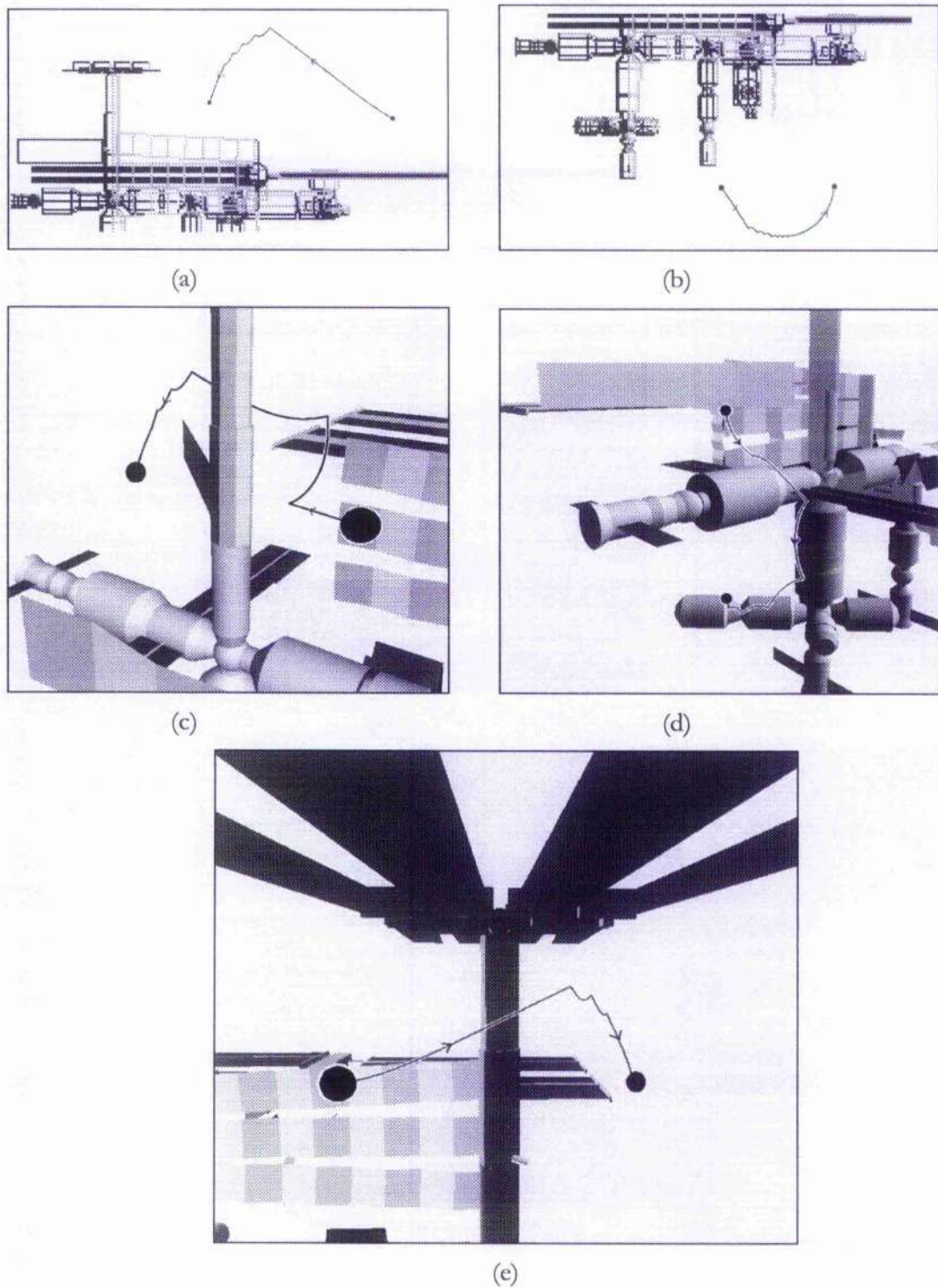


Figure 7-7 PFG Manoeuvre Categories

PFG manoeuvres performed entirely in the open space above or below the ISS structure, as shown in Figure 7-7(a) and Figure 7-7(b), form the primary zones available for safe PFG operations at the ISS. These zones are inherently safer due to their vertical offset from the V-bar, which ensures that the free drift trajectory from these points will tend to drift up and behind the ISS in the case of the zone above the V-bar, and down and ahead of the station when starting below the V-bar. Provided the manoeuvre velocities within these zones are controlled to limit the initial velocity along the R-bar toward the ISS structure, passive safety can be preserved in a similar manner to the R-bar approach manoeuvre demonstrated in Chapter 3. By contrast, PFG manoeuvres which must navigate away from the orbital plane in order to transfer past elements of the ISS structure, as shown in Figure 7-7(c) and Figure 7-7(d), cannot be executed in a passively safe manner. In these cases, the out-of-plane offset of the transfer path results in acceleration back toward the orbital plane, and towards the obstacle the manoeuvre is trying to avoid. This natural behaviour to accelerate toward the orbital plane can be easily observed in the out-of-plane component of the governing Clohessy-Wiltshire equations, given in Appendix III. This equation shows the out-of-plane acceleration at a point is directly proportional to its offset from the orbital plane.

$$\text{Eqn 7-3} \quad \ddot{z} = -\omega^2 z + f_z$$

During PFG manoeuvring, this undesirable motion requires frequent control impulses to maintain a collision free path around the obstacle, resulting in a relatively high ΔV cost on top of the safety disadvantages. The final category of PFG manoeuvring zones, shown in Figure 7-7(e), is in fact rather specific to one area of the ISS structure, located above the Russian portion to the rear of the station. In this area there is quite a sizeable volume that is shadowed by the PV-Arrays of the Science Power Platform, precluding an R-bar approach into this area. The presence of the PV-Arrays also limits the passive safe capabilities of PFG manoeuvring within this zone, since free-drift trajectories may drift upward into the arrays. If necessary, it may however be acceptable to permit limited PFG manoeuvring into this zone, relying on pre-determined CAM manoeuvres to ensure a safe retreat in emergencies.

The encompassing of the full range of PFG manoeuvres into these 5 broad categories is facilitated primarily by the configuration of the ISS structure. This places the bulk of the structure orientated either along the velocity vector (V-Bar) and orbital plane of ISS orbit (around $y \approx 0$), or in the plane perpendicular to the radial orbital vector (around $z \approx 0$). Of course, this configuration, represented in Figure 7-8, is a natural design since placing as much mass and volume as possible along the orbital velocity vector has the effect of minimising cross sectional area (and hence air drag) and gravity gradient torques.

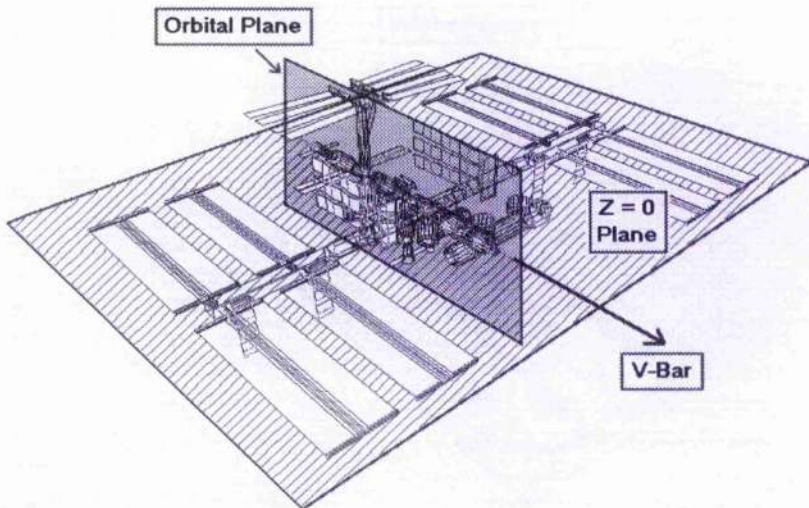


Figure 7-8 ISS Configuration Relative to Orbital Plane

As a final restriction on mission manoeuvre selection, each Inspector mission must start with an EOS retreat from docking and transfer to the first observation point, and finish with an EOS transfer to return from the final observation to berth at the docking port. In certain cases this may restrict the available initial and final observation nodes to co-ordinates accessible by EOS transfer.

7.3.3 Mission Sequencing

From the point of view of the user, the operation of the manoeuvre selection and mission scheduling strategies described in this chapter should be relatively transparent. There is little advantage to be gained at this stage in exposing a range of complex configuration options, but a significant risk of losing the intuitive interface of the mission-planning tool. For this reason, the mission-sequencing interface has been kept deliberately simple, with minimal user input required to generate an optimised mission sequence, as shown in Figure 7-9.

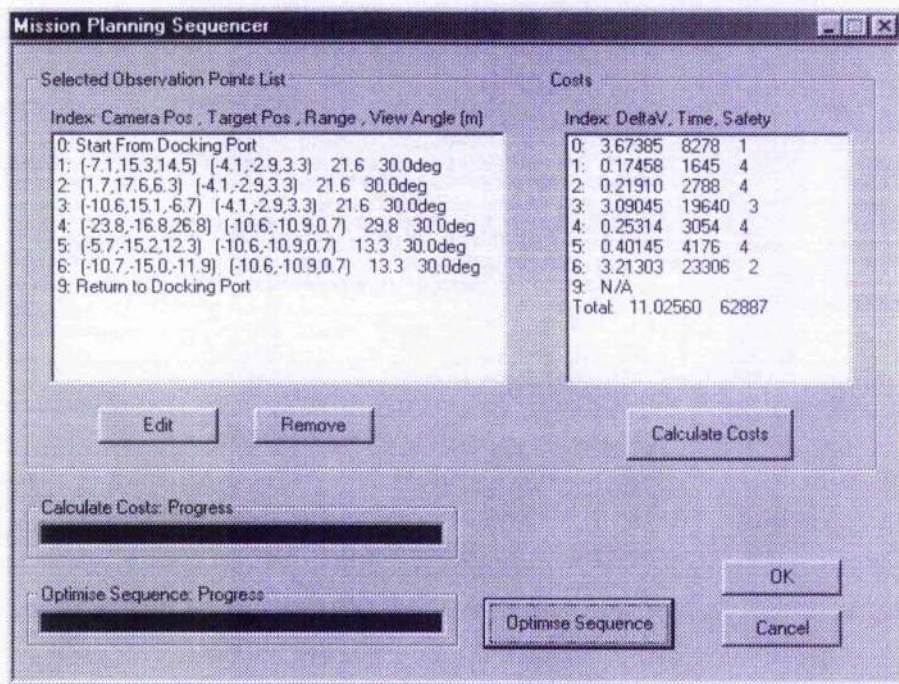


Figure 7-9 Mission Sequencing Interface

The first step of the sequencing operation is to select the manoeuvres to be used for each potential transfer between the defined observation points, and to calculate the graph of transfer costs between each node. The manoeuvre zones developed in the previous section are applied to each combination pair of observation points, determining whether PFG manoeuvring is available to transfer between the co-ordinates or an EOS transfer will be required. The cost for each transfer can then be estimated, either by simulating a PFG transfer between the points, or calculating the sequence of impulses required to execute the EOS trajectory. These manoeuvre costs, in terms of both duration and ΔV requirement, are then combined to give an overall weighted cost for the transfer which can be used to optimise the mission sequence. Invalid transfers, which cannot be performed due to the relative position of the two observation points, are represented in the graph by a connection with a prohibitively high (or essentially infinite) transfer cost.

The second sequencing stage is to optimise the mission sequence, as represented by the TSP graph calculated in the previous step, using the methods outlined in Section 7.2. This gives the sequence of manoeuvres required to visit each of the defined observation points, and an estimate of the total mission requirements in terms of ΔV and total mission duration, excluding the station keeping costs for whatever inspection is required at each observation point. At this stage the observation point list can be edited, if required, to constrain the scope of the observations to fit within overall mission limitations.

From a computational perspective, given the relatively small number of observation points available during a single mission, the limiting factor in the sequencing a mission comes down to the simulation of PFG transfers to obtain cost estimates for the TSP graph. The actual optimisation of the Inspector TSP requires a negligible amount of computational time, whilst on the development system the calculation of manoeuvre costs takes of the order of 30 – 60 sec for a 6 observation point mission, depending on the distribution of the individual observations points. Unfortunately the extended calculation required to simulate these PFG transfers is unavoidable if a reasonably accurate cost graph is to be determined. Nevertheless, within the original goal of a fast mission planning and evaluation tool, this order of time-scale is acceptable.

7.3.4 Mission Safety Analysis and Final Plan

Once the optimum sequence of transfers to visit the chosen observation points has been found for a given mission, and the manoeuvres required for each transfer planned, the results must be analysed to evaluate the suitability of the final mission plan. This evaluation is accomplished both by performing a brief safety analysis of the overall trajectory, and graphically displaying the mission plan to the operator in such a way that they can make their own informed analysis of the results. Referring to the collision impact velocity categories described in Chapter 6, for *Critical* and *Catastrophic* collision impacts, the safety of each element of the mission can be estimated by propagating the free-drift trajectory throughout each manoeuvre to locate the areas from which a collision could occur, and categorising each potential collision within these safety levels. Fortunately, the design of the EOS transfer methodology guarantees EOS manoeuvres to be 100% passively safe, and the safety of station-keeping at observation points is enforced at the observation point selection stage through the checking of free-drift safety. This leaves the PFG segments of the mission to be simulated, and the free-drift trajectories after each impulse propagated to estimate the fraction of the trajectory that is passively safe. During this simulation and propagation of the PFG path, the effect of errors in the ΔV impulses applied to the Inspector Free-Flyer are also incorporated into the paths and collision checking. This is achieved by propagating the initial velocity error range to obtain the resulting positional error throughout the trajectory, so that the area within which the path may drift is used to test for collisions with the ISS structure, as shown in Figure 7-10. The result is a more accurate check of potential collisions, but this will also skew the collision percentages toward higher values, since when collision tests are performed for each area within which the path will have drifted, no reference is made to the proportion of this area that results in collision. From a safety analysis perspective however, it

is better to err on the side of caution in this manner than to neglect ΔV errors and risk underestimating the risk of a given manoeuvre.

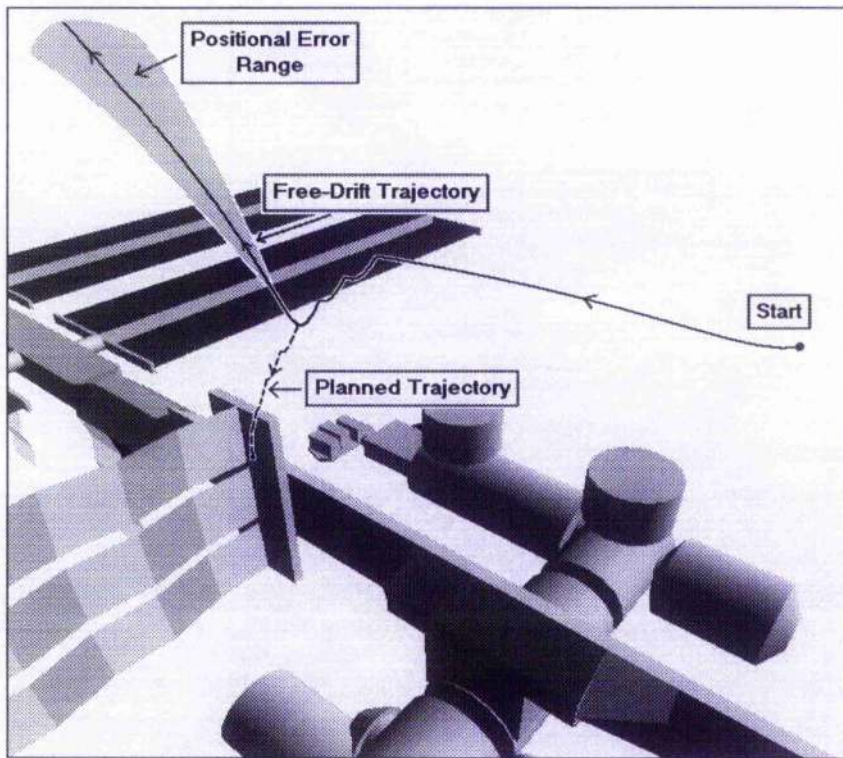


Figure 7-10 Free-Drift Path Propagation (With Errors)

The categorisation of potential collisions into graduated levels of risk greatly extends the feasibility of missions that can be performed by the Inspector Free-Flyer. The use of a 100% passively safe requirement for missions would virtually rule out PFG manoeuvring in a large number of cases, limiting manoeuvring to costly EOS transfers and seriously constraining the observations that could be performed in a single mission. However, the ISS structure is designed to absorb the impacts inflicted by astronauts manoeuvring along the hull during EVA missions, and the relative momentum of the Inspector Free-Flyer is comparable to a fully suited astronaut manoeuvring with a tool bag. By permitting manoeuvres that possess the potential for a *Critical* or sub-*Critical* collision along a fraction of the trajectory, the opportunities for utilising PFG manoeuvring to enhance inspection missions are greatly increased. The only downside of this will be a minimal reduction in absolute mission safety, given that the ISS structure is already designed to withstand a range of impacts from other sources.

Aside from the results of a safety analysis and numerical lists of manoeuvre types and costs, the best way to communicate the results of a mission plan to the operator is to provide a visual representation of the manoeuvre elements of the mission. This is especially true given the lack of exact data for the Inspector Free-Flyer systems and control structure, which make

any specific mission schedules or numeric data, including overall cost estimates, reasonable approximations at best. Thanks to the flexibility of the mission planning tool interface and primary camera view, the display of a mission through its individual elements is easily achieved by displaying path data for each selected transfer between nodes. This is in fact the manner in which the majority of figures in this chapter displaying PFG results have been produced. As we will see in the following results section, this method provides an easily accessible interface to the results of the mission planning process, giving an immediate correlation between the Inspector Free-Flyer's motion and position relative to the ISS structure.

7.4 Mission Test Cases

The only way to evaluate the use of an interactive tool such as the Inspector Mission Planner is to use it to achieve some goal. In order to demonstrate this, and to investigate the results obtained, this section will go in detail through the planning and analysis of a number example missions. Three test cases have been devised to represent as wide a range of mission objectives as possible, from a single target inspection mission requiring a set of observation points grouped around a the target, to the extreme scenario of a set of 6 observation targets distributed as widely as possible around the ISS structure. In each case, the goal is to investigate not only the use and capabilities of the mission planning tool, but also the resulting mission profiles and requirements with respect to their goals, since this will give an indication of the range of missions that will be achievable for the ISS-Inspector Free-Flyer.

7.4.1 Case A: A Single Target Inspection Mission

The first example is intended to demonstrate the objective *baseline* mission for the ISS-Inspector, the detailed inspection of a single target point on the ISS. To achieve this, the target must be viewed from a group of observation positions, designed to give a comprehensive overall view. The target point in this case is the top of the Pressurised Mating Adaptor (PMA1), which joins the Functional Cargo Block (FGB) to Resource Node 1 (Node 1), the first components of the ISS to be inserted into orbit, in 1998. The four observation points, shown in Figure 7-11, are grouped at different angles above the target to provide as complete a view of the top of PMA1 as possible within station-keeping safety and communications constraints.

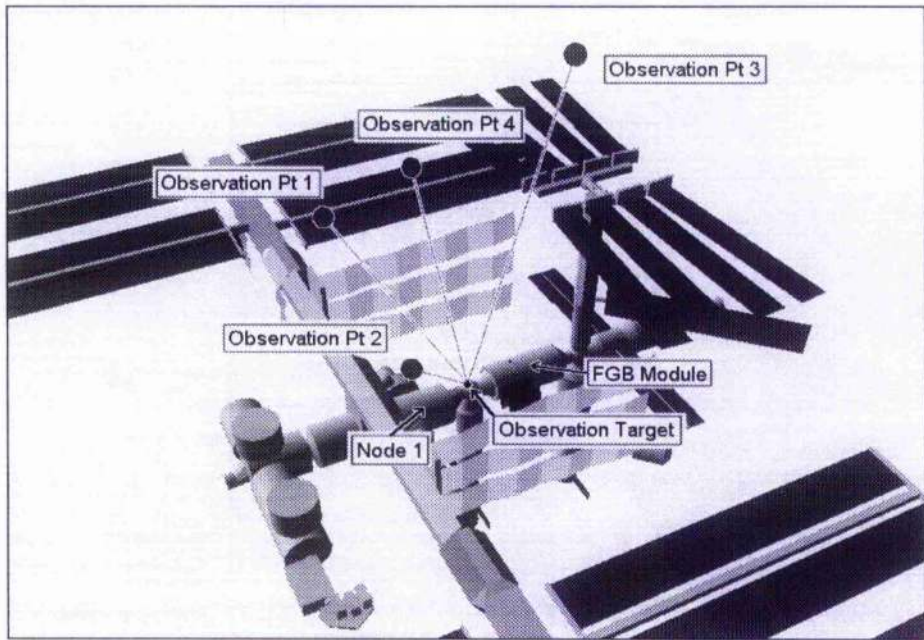
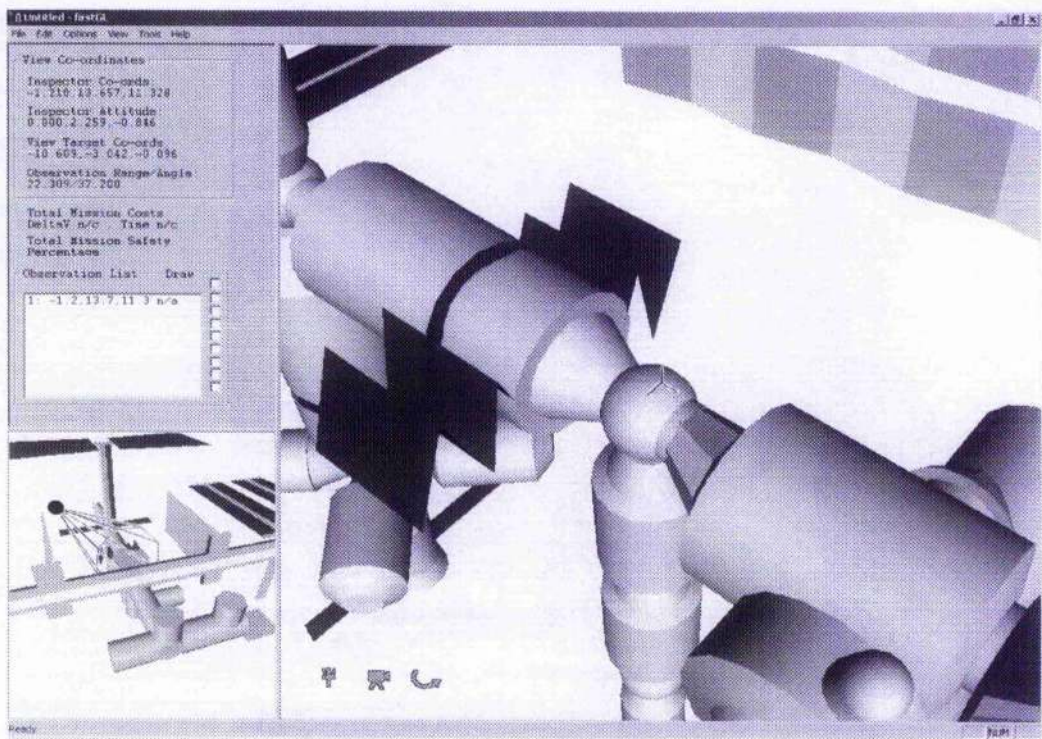


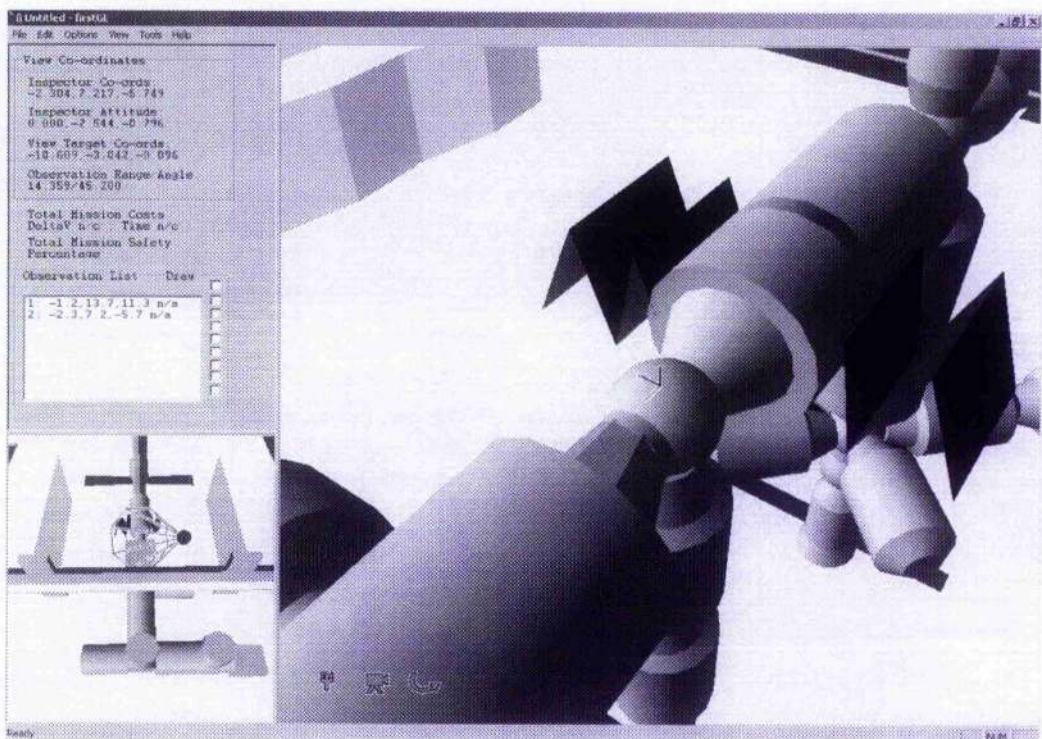
Figure 7-11 Case A: Inspection Target and Observation Points

In this test case the target co-ordinates are relatively exposed for visual inspection, with a relatively large area of free-space directly above the target. Available observation positions are however prevented from approaching the target too closely from above on the y-axis due to free-drift safety constraints. Combined with occlusion of the target from the side by the large vertically mounted radiators, the availability of low elevation views of the target are limited. Views from other angles above the ISS are available however, as demonstrated by Observation Pt. 3, though the camera position must be raised to maintain station-keeping and R-Bar approach safety. One subsequent advantage of these elevated observation positions is that video and comms radio links are maintained at all observation points. All the chosen observation positions are also easily accessible both to and from EOS trajectories, and furthermore all four points are within the same PFG manoeuvring zone, giving the maximum options for inter-observation point transfers.

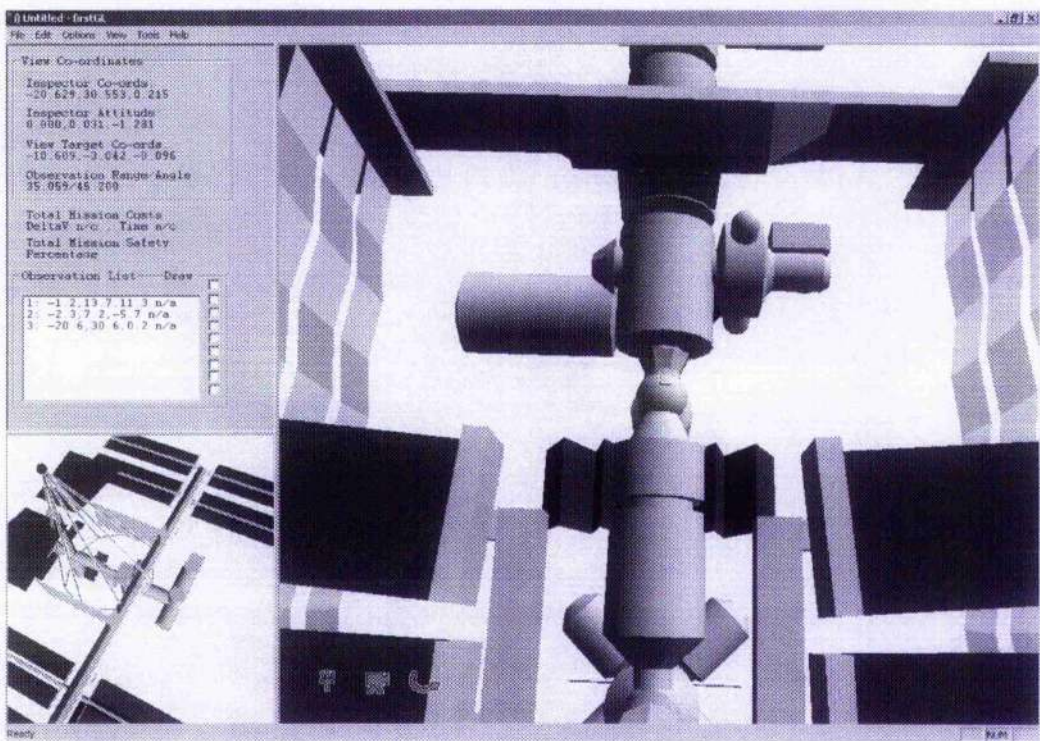
Views taken from the Inspector Mission Planner tool when defining each of the observation points are shown in Figure 7-12 (a-d), demonstrating the available camera position data and the external Inspector/ISS views which are used to assist in each selection.



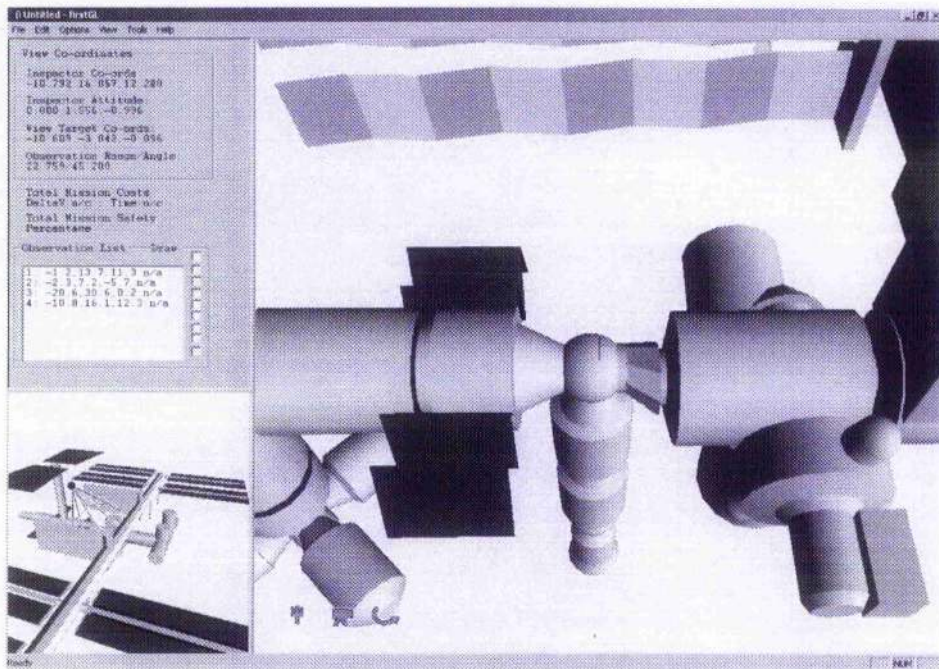
(a) Observation Pt 1



(b) Observation Pt 2



(b) Observation Pt 3



(d) Observation Pt 4

Figure 7-12 Case A: Observation Point Selection Procedure

The task of calculating and optimising the mission transfer sequence once the observation points have been defined is relatively straightforward within the Inspector

Mission Planner tool. The interface and numerical results of this optimisation for Case A, once the cost estimations and TPS solutions have been calculated, are shown in Figure 7-13.

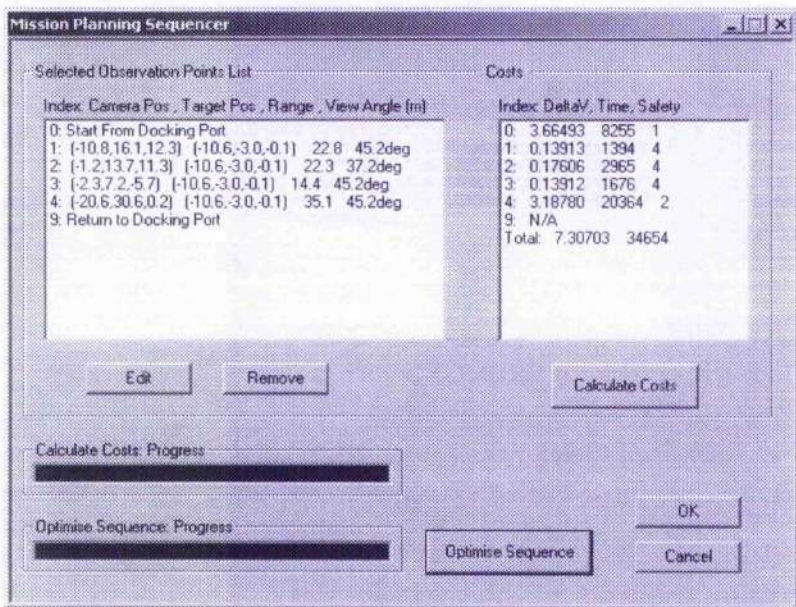


Figure 7-13 Case A: Transfer Optimisation Dialogue

The result of the optimisation is that the observation point transfers are sequenced in the order: 4, 1, 2, 3. PFG transfers are utilised between each observation points resulting in low transfer costs for this phase of the mission, with EOS trajectories used to transfer to and from docking at the ISS. Graphical representation of the resulting mission trajectory, given in Figure 7-14, shows clearly the suitability of the PFG manoeuvring strategy for the transfers between relatively closely grouped inspection positions, as characterised visually by the comparatively direct nature of the transfers. The EOS transfer to the first observation position from docking, and the return from the final observation position, show in comparison an extended trajectory retreating far from the ISS structure in order to assure long term passive-safety.

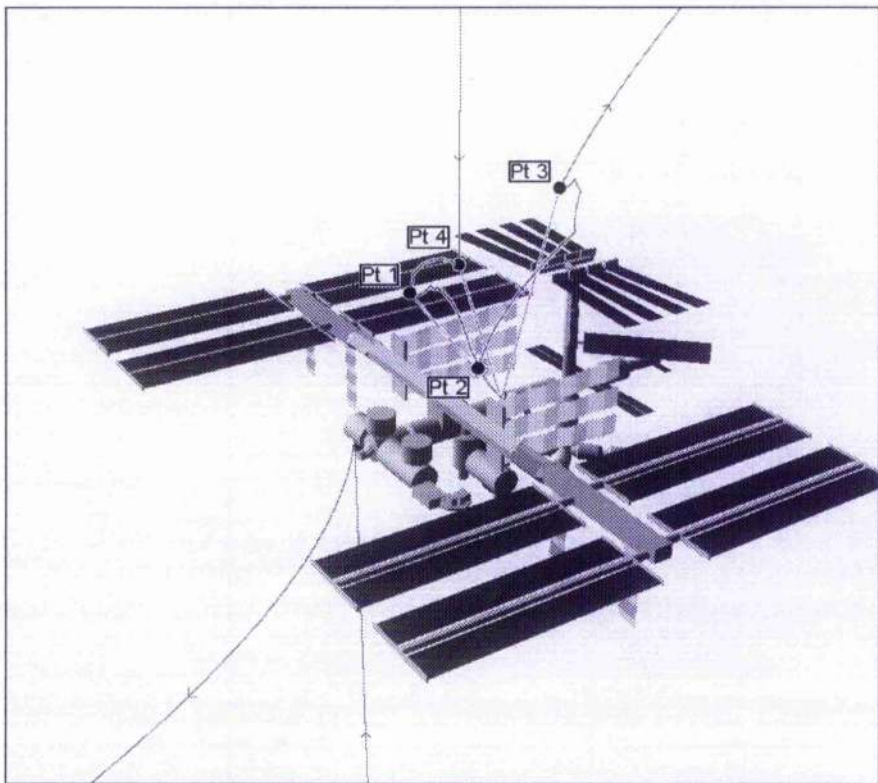
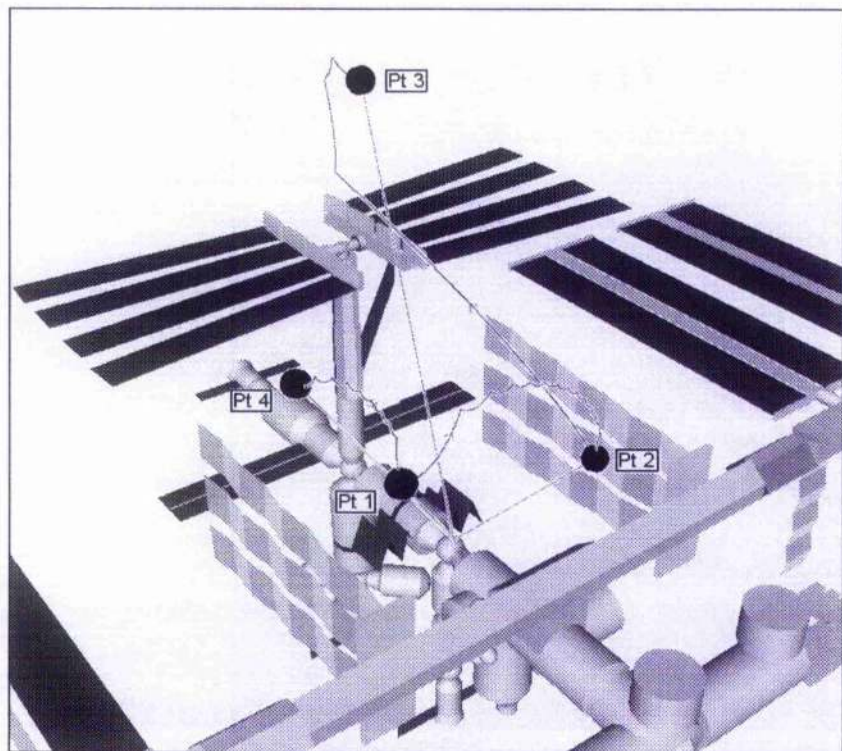
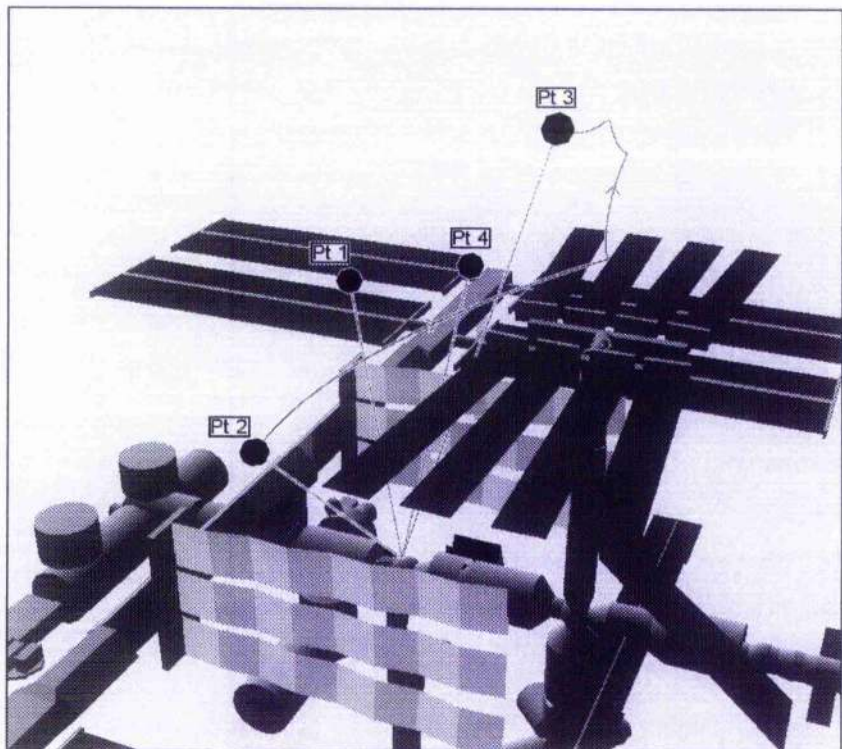


Figure 7-14 Case A: Overview of Mission Trajectory

Looking more closely at the PFG controlled portion of the mission, shown in Figure 7-15, it can be seen that for the first two transfers (Observation Pt 4 to 1 and Observation Pt 1 to 2) the looping trajectories are continually drifting safely away from the ISS structure requiring controller input every few metres to keep the path on course. This results in a safe free-drift trajectory in the short term along the transfer, whilst the control activations are still spaced widely enough to be relatively efficient in terms of ΔV . In the final PFG transfer, Observation Pt 2 to 3, the path has only a small number of control actions as the free-drift trajectory has a tendency to drift favourably towards the goal point. This does however lead to the path approaching closer to the Science Power Platform PV Array structure than might be desired. Of course this can be easily avoided by modifying the collision volume surrounding the PV Array to give a wider safety margin. In any case, since the free-drift trajectory at that point is actually moving safely away from the structure there is no real danger of contact.



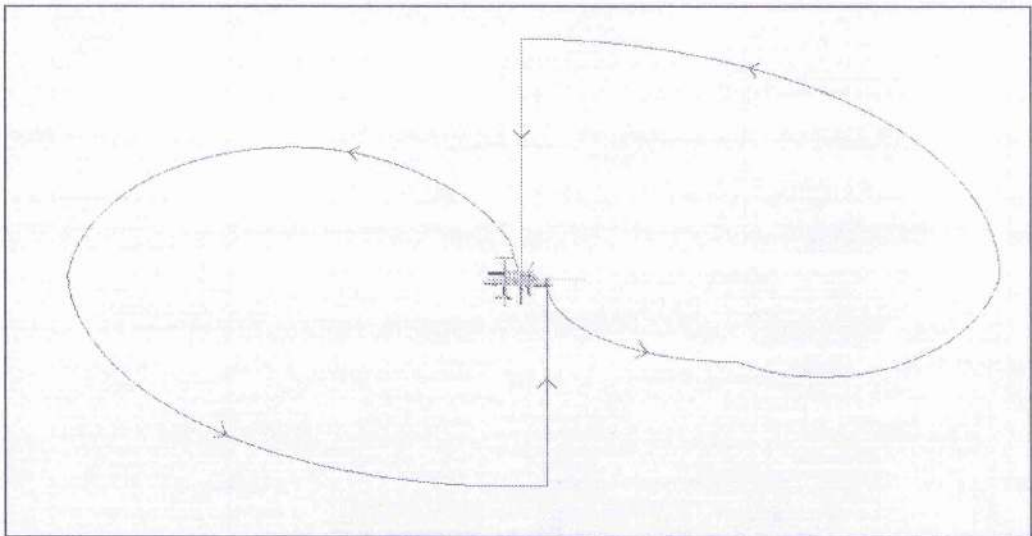
(a) Three PFG Trajectories



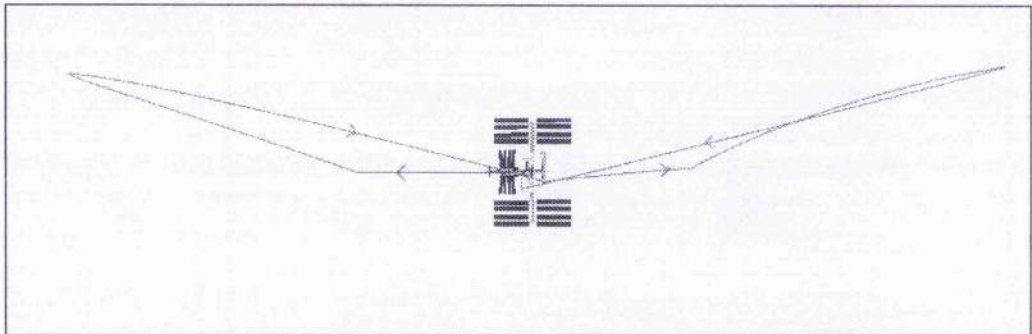
(b) PFG Trajectory between Pt 2 and Pt 3

Figure 7-15 Case A: PFG Trajectories

The profile of the EOS transfer sections of the mission, shown in Figure 7-16, describes a standard EOS retreat from docking with R-Bar transfer to the first observation point, and an equally standard EOS retreat and R-Bar return to docking from the final observation point. Aside from any additional out-of-plane motion that may be required to reach or retreat from observation points further from the orbital plane, this profile will remain broadly consistent for all EOS transfers to and from docking. The safety of the EOS strategy, built intrinsically into the definition of the trajectories, is reinforced by this graphical representation which emphasises the physically large safety margin while transferring around the ISS structure.



(a) EOS Trajectories in X-Y Plane



(b) EOS Trajectories in X-Z Plane

Figure 7-16 Case A: EOS Trajectories

The numerical results of the mission plan, given in Table 7-1, follow the same pattern as the graphical results. The PFG segments are relatively small and efficient, both in terms of ΔV requirements and duration, in comparison to the EOS segments which make up the majority of overall mission costs. Referring back to the original design capabilities for the

Inspector Free-Flyer outlined in Chapter 3, we can see that the calculated mission requirements fall just within maximum ΔV capabilities of 10 ms^{-1} and full power mission duration of 10.9hrs. From a mission duration perspective this should not be a problem, since the Inspector power requirements during the free-drift phases of EOS manoeuvring should be minimal. However, in terms of ΔV requirements this is rather close to the limit, given that station-keeping costs during the actual observation phase have not been taken into account.

Transfer	Type	$\Delta V (\text{ms}^{-1})$	Transfer Time (s)
Docking to Pt 4 (R-bar approach)	EOS	3.66493	8255
Pt 4 to Pt 1	R-bar	0.8	1300
Pt 1 to Pt 2	PFG	0.13913	1394
Pt 2 to Pt 3	PFG	0.17606	2965
Return to Docking (R-bar approach)	EOS	0.13912	1676
	R-bar	3.18780	20364
Total		8.90758	37254 ($\approx 10 \text{ hrs}$)

Table 7-1 Case A: Mission Transfer Costs

The final aspect of the mission plan to be considered is the safety of the resulting trajectories, specifically those of the PFG segments of the mission. The results of a safety analysis of each of the PFG segments, performed by propagating free-drift trajectories and testing for potential collisions over a period of 2 orbits of the ISS, are given in Table 7-2.

Transfer	Duration	Any Impact	Critical Impact	Catastrophic Impact
Pt 4 to Pt 1	1394 sec	0.00 %	0.00 %	0.00 %
Pt 1 to Pt 2	2965 sec	5.07 %	5.07 %	0.00 %
Pt 2 to Pt 3	1676 sec	57.45 %	57.45 %	57.45 %

Table 7-2 Case A: PFG Trajectory Safety Analysis

Of the three PFG manoeuvres performed it is only the final transfer, from Observation Pt 2 to 3, which has the potential to cause a catastrophic collision with the ISS. Examining this trajectory element closely in Figure 7-15 (b), it appears that this collision potential arises from the initial path taken as the Inspector Free-Flyer leaves Observation Pt 2 and drifts above the Science Power Platform before making a second control manoeuvre to correct its course toward the target at Observation Pt 3. During this relatively lengthy section (for a PFG manoeuvre at least), extrapolation of the free-drift trajectory would suggest that the extended path will drift around the rear of the ISS like an undersized EOS, before looping back up to collide with the lower ISS structure. The trajectory is safe however, for at least half an orbit

past the point where the second control action should occur, giving plenty time in the event of a problem to perform a Collision Avoidance Manoeuvre. The second PFG transfer, between Observation Pt 1 to 2, also has a small portion during which there is the potential for a collision with the ISS. The Velocity Selection strategy integrated into the PFG method has however managed to constrain the impact velocity, to reduce the level of possible damage to the ISS.

7.4.2 Case B: A Two Target Inspection Mission

The second test case is more ambitious, consisting of the multiple inspections of two distinct targets, with observation positions required both above and below the ISS structure. This scenario would be representative of the most challenging mission the ISS-Inspector would be likely to encounter or be expected to achieve.

The first target chosen is at the main Airlock, located below and to the rear of the main truss structure, as shown in Figure 7-17. The Airlock is positioned close to the ISS centre of mass, and is occluded from view in many directions by the surrounding structure of the core ISS modules, the main truss and the large truss-mounted thermal radiators, making it a challenging target to obtain a detailed view of.

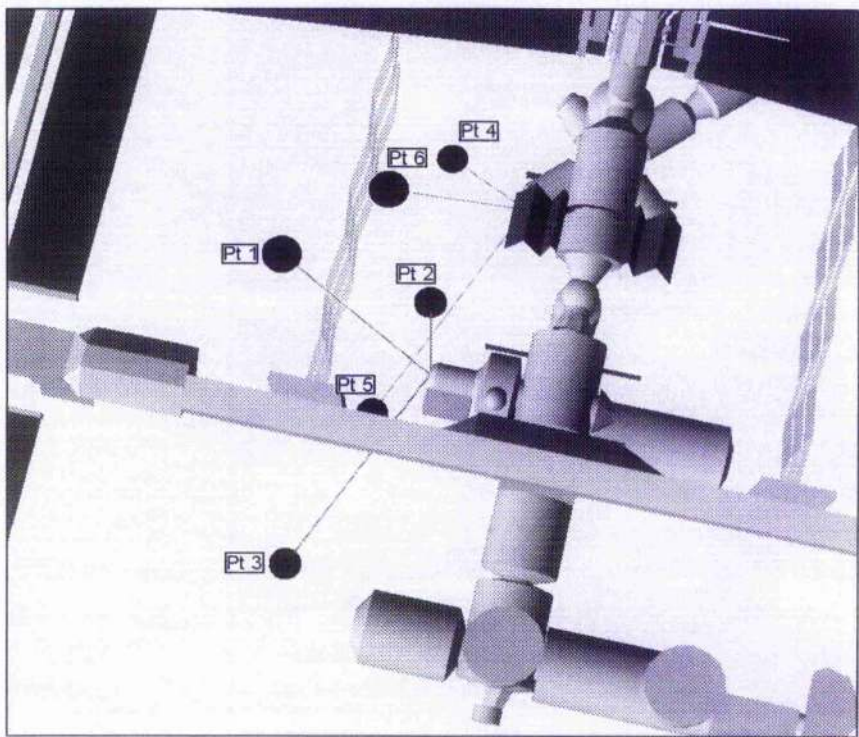


Figure 7-17 Case B: Inspection Target 1 and Observation Points

The positions available to observe Target 1 are constrained to view the Airlock at rather shallow angles by the obstruction caused by the right hand solar radiator which is

attached to the main truss. This obstruction prevents a head-on inspection of the airlock from a position close to the z-axis, and so to obtain a complete inspection of the Airlock, observations must be performed from positions surrounding the target in the orbital plane. The chosen observation positions therefore consist of a single point almost directly above the target, positioned high enough to safely avoid the radiator and main truss structure, and two additional points below the target. These lower observation points, positioned in the relatively clear space below the ISS structure, enable viewing angles from ahead and behind of the target along the x-axis to be obtained more easily than would be the case from above the target.

The second target is one of 3 Russian Research Modules (though on more recent ISS assembly plans the structure has been reduced to 2 Modules) attached to the Universal Docking Module below the Russian portion of the ISS, as shown in Figure 7-18. This target is primarily accessible for observation from below the ISS since it is obscured from above by the rest of the ISS structure, though overhead views are possible from certain angles. In addition, its location toward the rear of the ISS makes it an interesting study of accessibility and transfer costs using EOS manoeuvres.

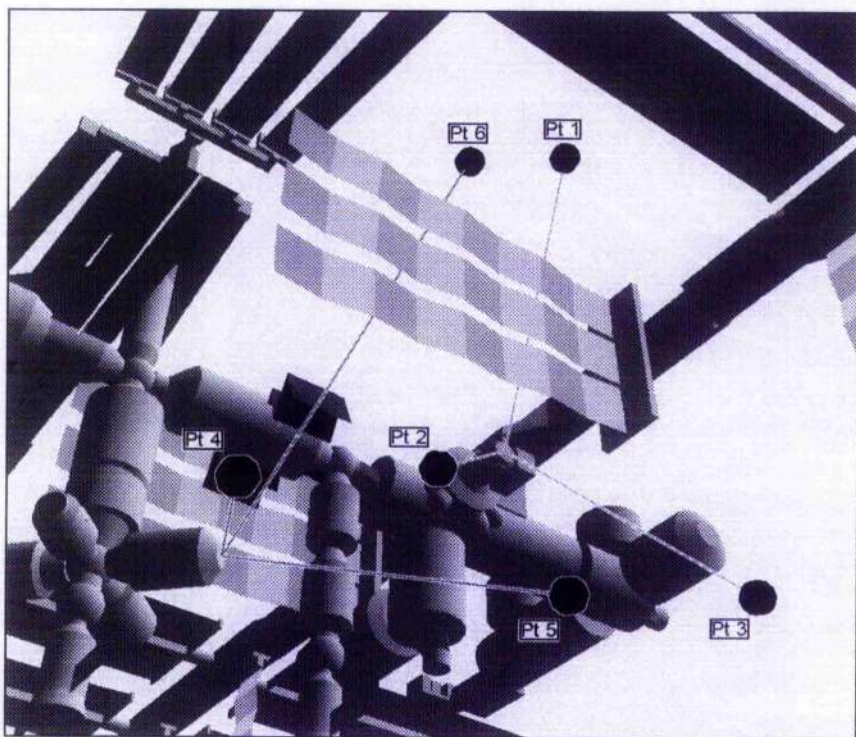
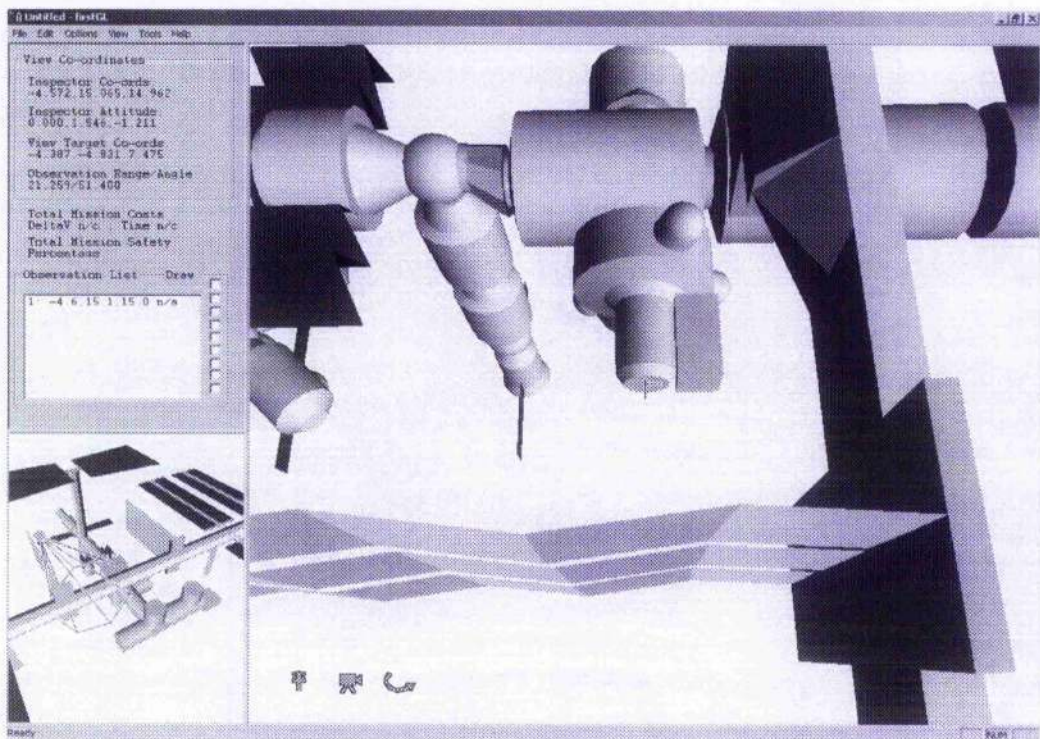


Figure 7-18 Case B: Inspection Target 2 and Observation Points

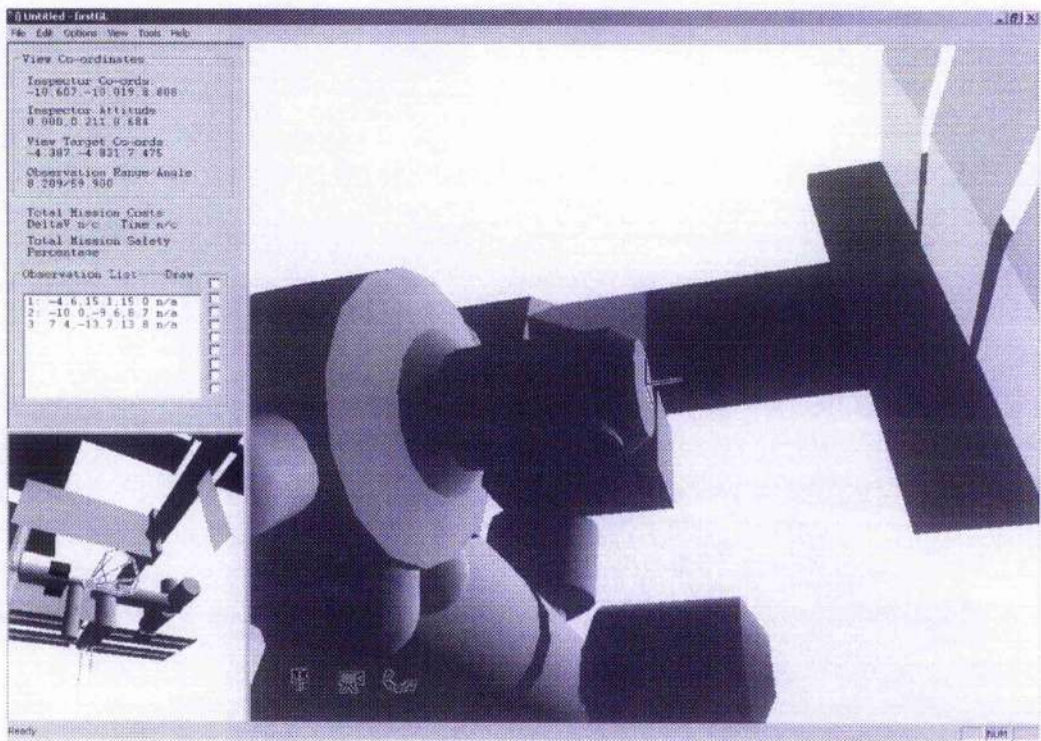
The selection of observation points to view Target 2 from angles below the ISS structure is relatively straightforward thanks to the target's position, clear of the main bulk of the main structure. The orientation of the module favours inspection from positions forward of the target along the x-axis, resulting in the positioning of Observation Pt 5, with

Observation Pt 4 producing a good end-on view of the module. Obtaining an inspection view from above the target is not so simple due to the obstruction caused by the rest of the ISS structure, however thanks to the Research Module's orientation angle away from the surrounding structure the target is visible through the structure from a point located above the main truss. Though the target is relatively far away from this observation position, this should be easily within the range of the Inspector's cameras.

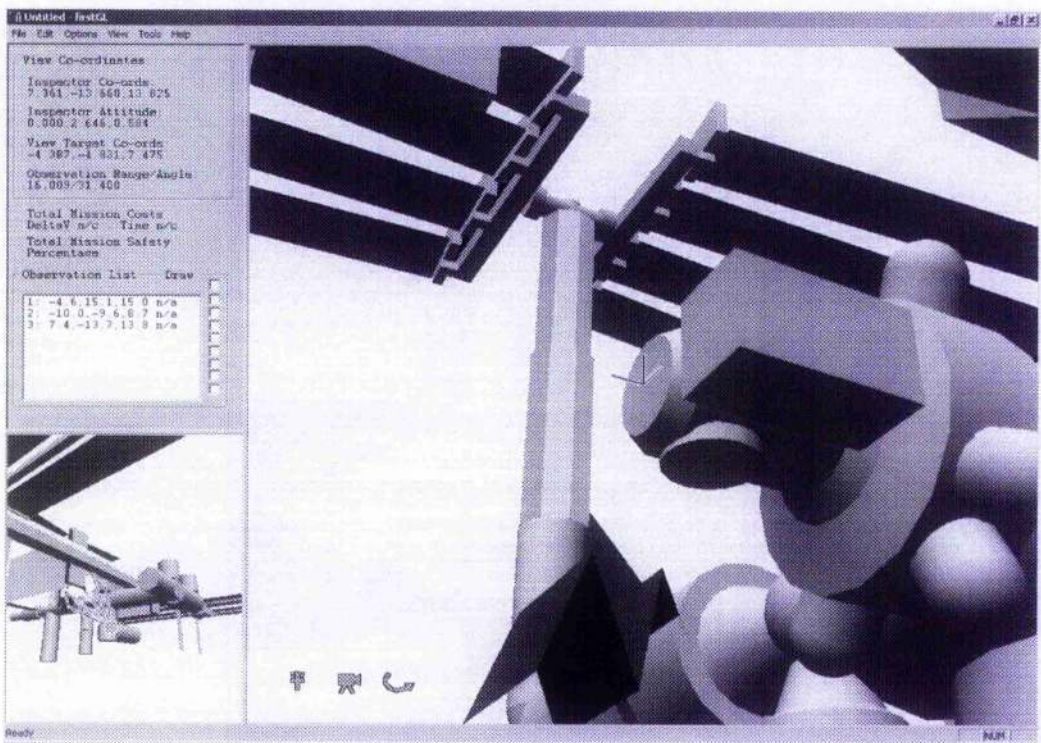
Interface screens from the Inspector Mission Planner tool used to define each of the observation points are shown in Figure 7-19 (a-c) and Figure 7-20 (a-c), detailing the views available of each target at their respective observation points and the information used to select each position.



(a) Observation Pt 1

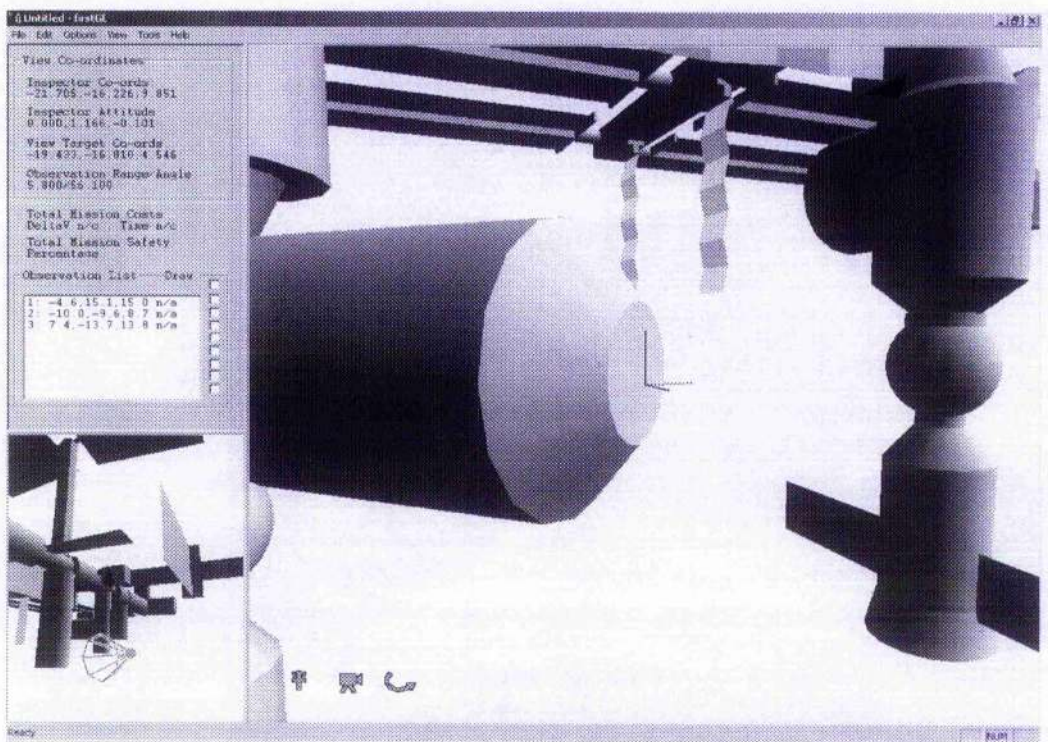


(b) Observation Pt 2

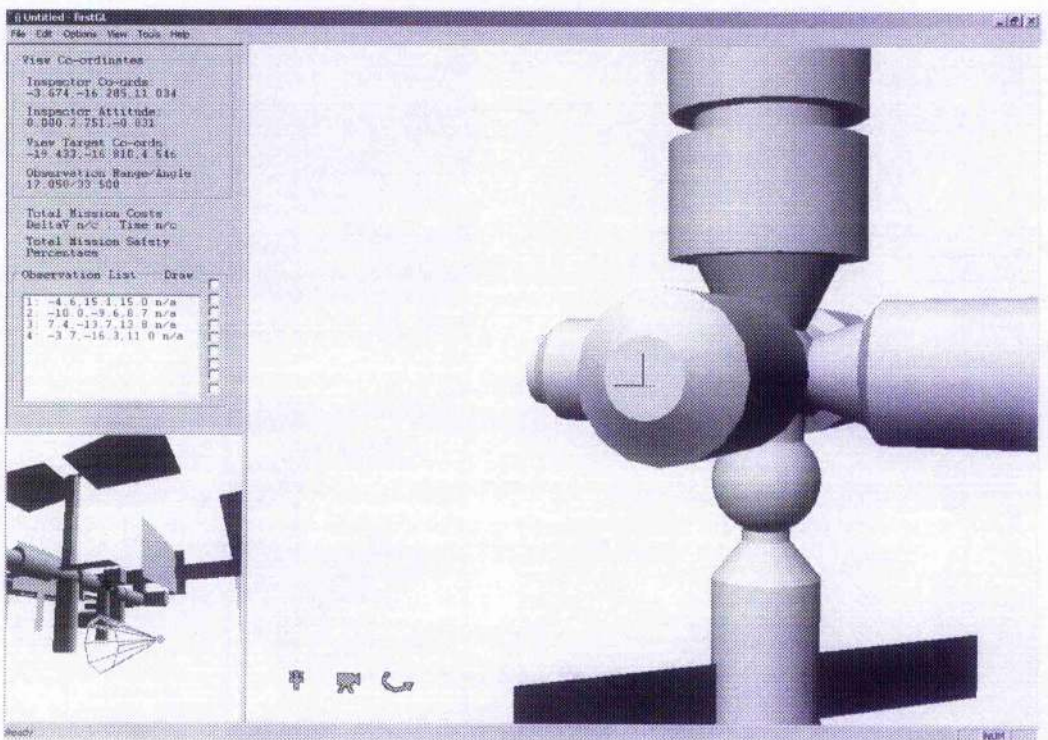


(c) Observation Pt 3

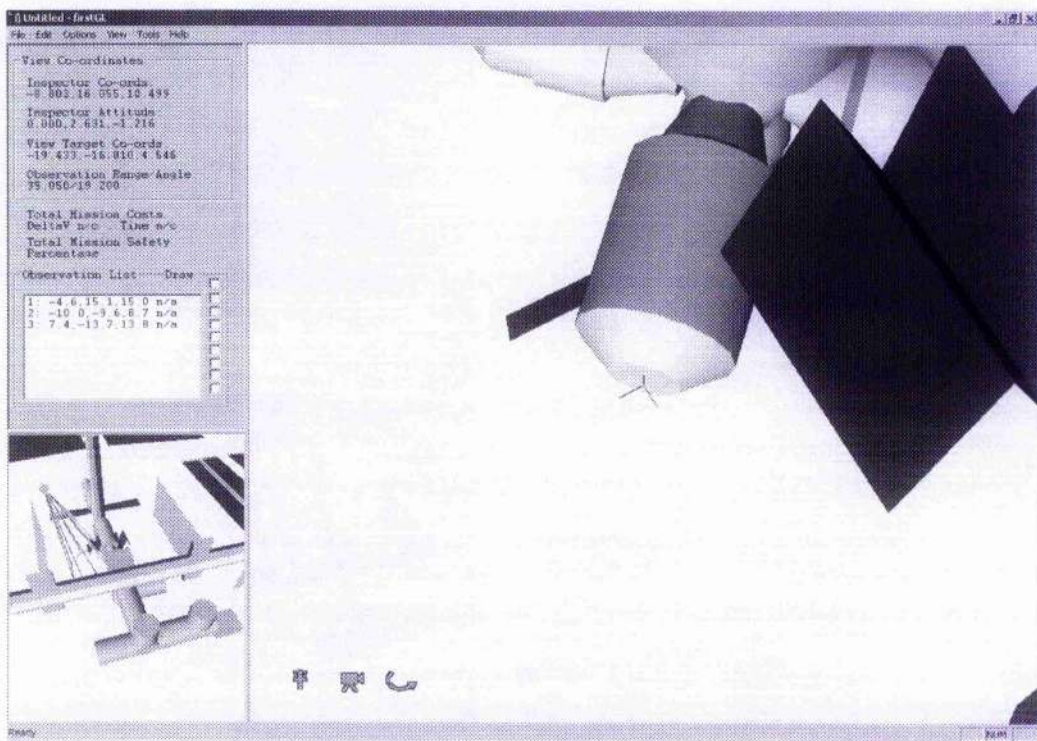
Figure 7-19 Case B: Target 1 Observation Points



(a) Observation Pt 4



(b) Observation Pt 5



(c) Observation Pt 6

Figure 7-20 Case B: Target 2 Observation Points

The sequencing and optimisation stage for this mission is slightly more computationally expensive than for Case A due to the spread of observation points above and below the V-bar, necessitating an additional EOS manoeuvre at some point to perform the required transfer from above to below the ISS. There are of course, a number of periods in the mission at which this transfer may occur, depending on the sequence of observation points visited. The numerical results of the sequencing optimisation task taken from the Mission Planner interface are shown in Figure 7-21 and a graphical overview of the resulting mission trajectory is given in Figure 7-22.

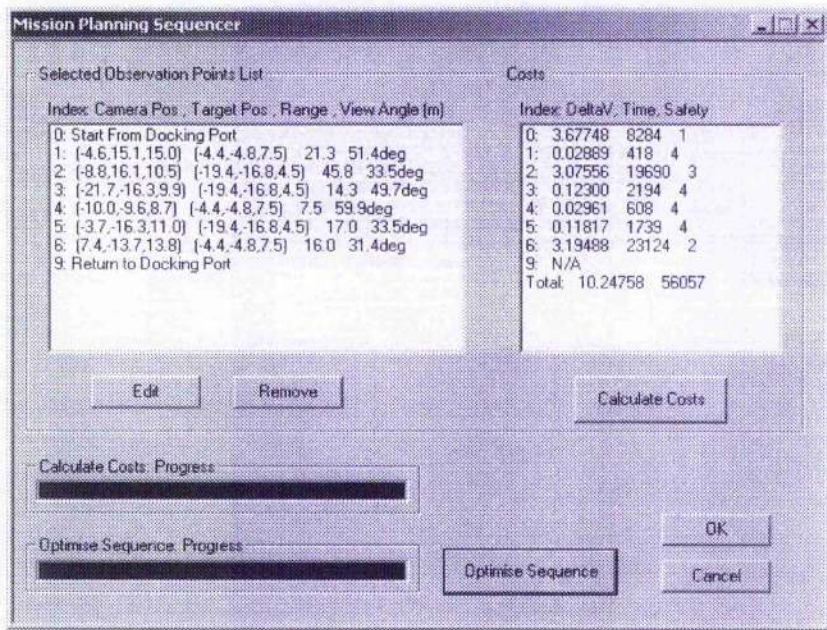


Figure 7-21 Case B: Transfer Optimisation Dialogue

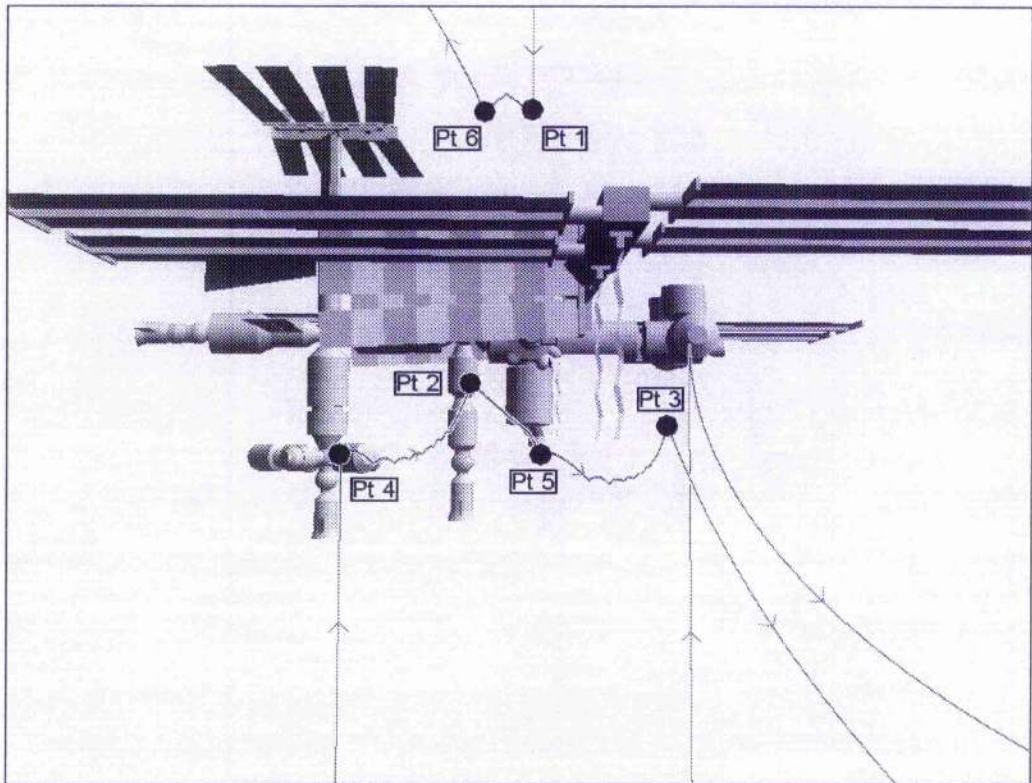


Figure 7-22 Case B: Mission Trajectory Overview

The result of this optimisation of mission transfers is that the observation points are to be visited in the sequence: 1, 6, 4, 2, 5, 3. After the initial retreat from docking and EOS transfer to Observation Pt 1, a PFG manoeuvre is used to transfer to the second point above the ISS, Observation Pt 6. A second EOS manoeuvre is then used to transfer to the first of

the observation points below the ISS structure. Further PFG manoeuvres are then employed to visit the remaining points, before a final EOS transfer is used to return to docking.

Concentrating on the PFG segments of the trajectory, it can be seen that the mission sequencer has automatically ordered the PFG transfers so that the direction of motion utilises the orbital dynamics of free-drift trajectories to enhance the safety of the PFG transfers. Below the ISS the transfers are ordered such that the broad direction of travel is always in a positive direction along the V-bar, resulting in a free-drift trajectory that naturally drifts away from the ISS structure. If this direction of travel were towards the rear of the ISS, the resulting trajectories would have a tendency to drift up towards the structure. This ordering of transfers is a natural consequence of the cost of PFG transfers used to optimise the mission sequence. The PFG strategy attempts to optimise path safety at the expense of ΔV and transfer time, resulting in increased transfer costs for transfer orientations that are less intrinsically safe. Given that the EOS cost of transferring to and from any given point is relatively independent of its position along the x-axis, it is natural that the free-drift characteristics of transfers above and below the V-bar will influence the optimal manoeuvre order for PFG transfers.

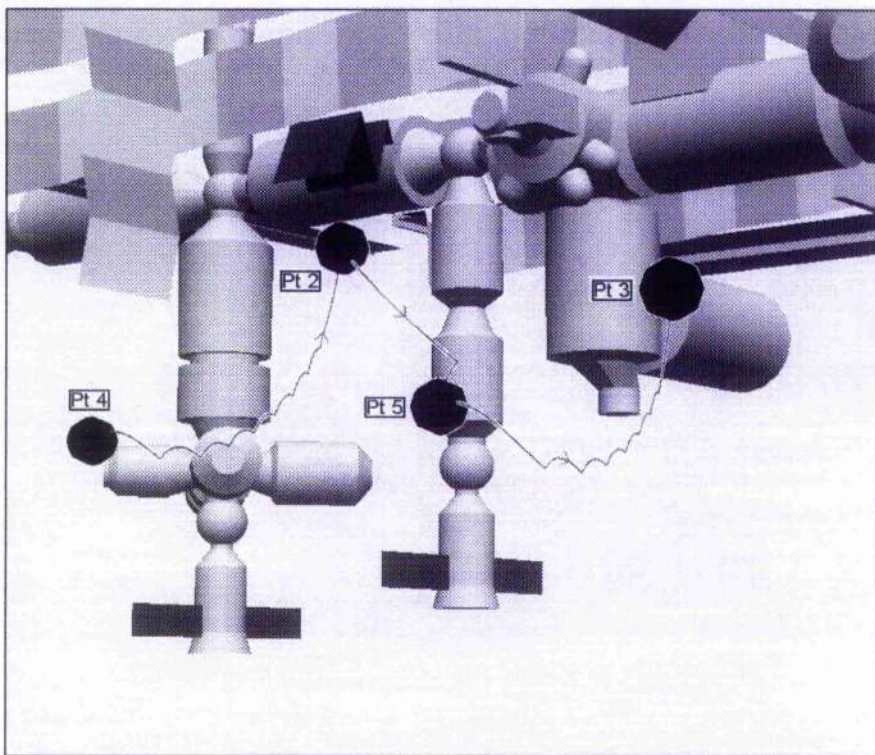
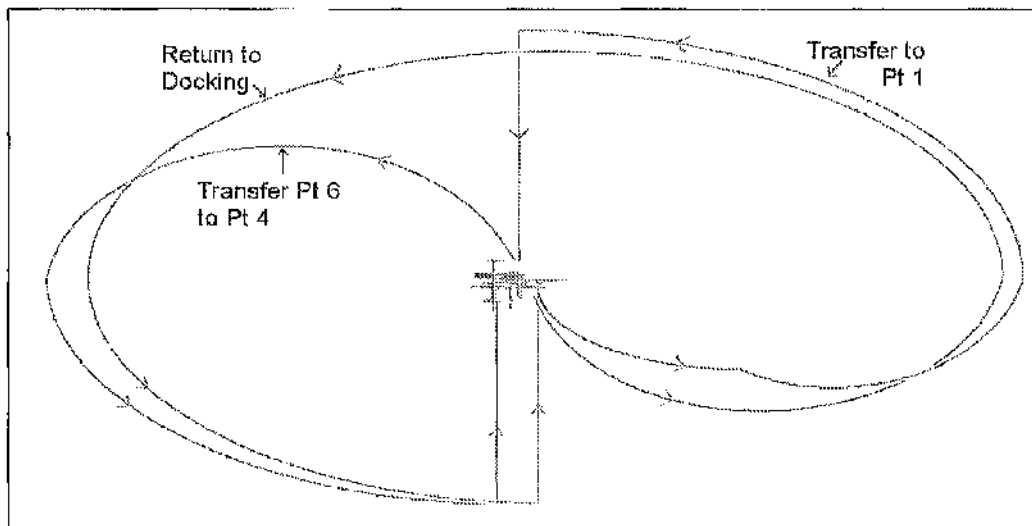


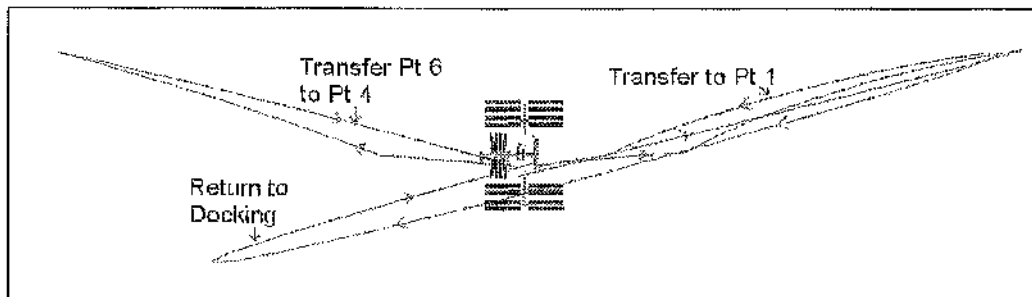
Figure 7-23 Case B: PFG Trajectories below the ISS

The EOS segments of the mission plan are relatively standard, consisting of a standard retreat and return to docking, with a single additional EOS manoeuvre performed to transfer between Observation Pt 6 above the ISS to Observation Pt 4 below. This EOS transfer from

above to below the V-bar closely resembles the standard return to docking manoeuvre from above the ISS as seen in the previous example. With the final observation point located below the V-bar, a complete orbit of the ISS is then required to perform the EOS transfer to the desired position below the docking port before the R-bar forced motion return to docking. Profiles of the planned EOS transfers are shown in Figure 7-24.



(a) EOS Trajectories in the X-Y Plane



(b) EOS Trajectories in the X-Z Plane

Figure 7-24 Case B: EOS Trajectories

The cost incurred by the additional EOS transfer can be clearly seen in the overall mission costs, shown in Table 7-3. In comparison to the results of test Case A, PFG transfer costs remain a small fraction of mission, whilst the extra EOS transfer has made a significant increase to the overall mission cost. In this case unfortunately, mission costs for Case B exceed the original ISS Inspector design capabilities, both in terms of ΔV requirements and mission duration. Of course these constraints are conservative minimum estimates and may be expanded as the Inspector Free-Flyer is developed and the capabilities it will require are realised. Without utilising an EOS transfer between Observation Pt 6 and Pt 4, the total cost would be within the Inspector's capabilities, even allowing for an additional PFG transfer between these points, however mission safety would be significantly reduced by the use of a

PFG transfer across the V-bar. One potential solution would be to replace the EOS return to docking from Observation Pt 3 with a direct PFG transfer to a point along the R-bar below the docking port. Given the proximity of Pt 3 to the docking port, this should be possible with a minimal impact on overall mission safety.

Transfer	Type	ΔV ($m s^{-1}$)	Transfer Time (s)
Docking to Pt 1 (with R-bar approach)	EOS	3.66748	8284
Pt 1 to Pt 6	R-bar	0.8	1300
Pt 6 to Pt 4 (with R-bar approach)	PFG	0.02889	418
Pt 4 to Pt 2	EOS	3.07556	19690
Pt 2 to Pt 5	R-bar	0.8	1300
Pt 5 to Pt 3	PFG	0.12300	2194
Pt 3 to Pt 2 (with R-bar approach)	EOS	0.02961	608
Pt 2 to Pt 3	PFG	0.11817	1739
Pt 3 Return to Docking (with R-bar approach)	EOS	3.19488	23124
Total		12.63759	59957 (≈ 17 hrs)

Table 7-3 Case B: Mission Transfer Costs

The results of a safety analysis of the PFG segments of the mission plan are given in Table 7-4. It can be seen that both the first and second PFG manoeuvres have a section of approximately 150 seconds during which their free-drift trajectory represents a potential threat to the ISS. In both cases however, velocities have been reduced to constrain the impact below that which would cause a catastrophic threat to the station. Given as a percentage of manoeuvring time, this critical damage threat represents just 6% of the PFG portion of the mission, a significantly better result than in Case A.

Transfer	Duration	Any Impact	Critical Impact	Catastrophic Impact
Pt 1 to Pt 6	418 sec	35.97 %	35.97 %	0.00 %
Pt 4 to Pt 2	2214 sec	6.78 %	6.78 %	0.00 %
Pt 2 to Pt 5	604 sec	0.00 %	0.00 %	0.00 %
Pt 5 to Pt 3	1750 sec	0.00 %	0.00 %	0.00 %

Table 7-4 Case B: PFG Trajectory Safety Analysis

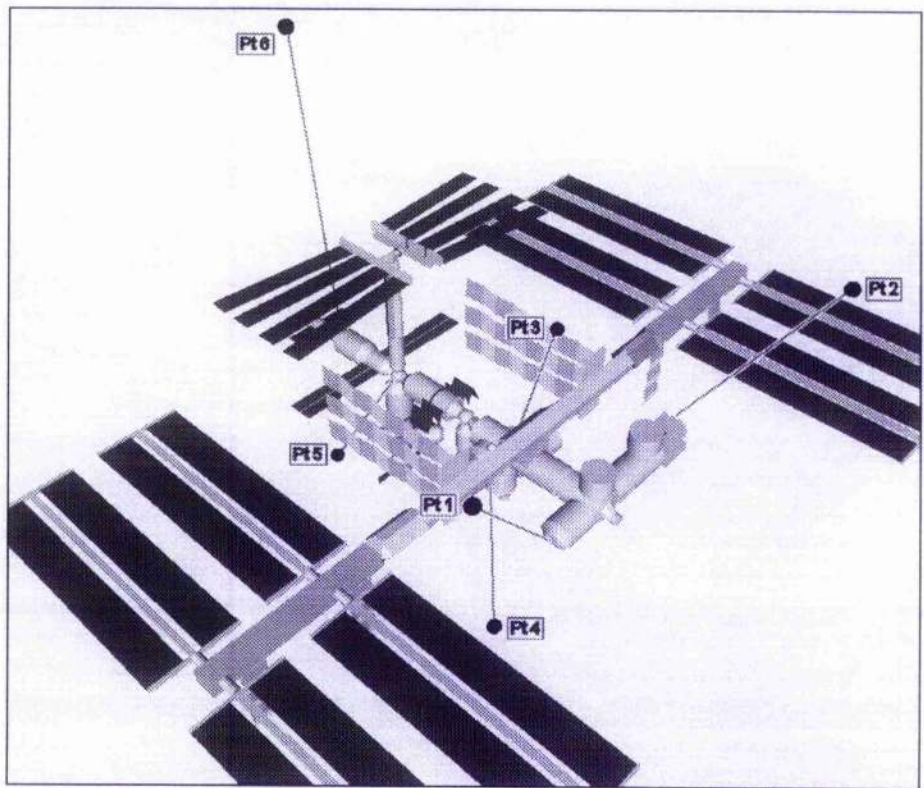
7.4.3 Case C: A 6 Target Inspection Mission

The final example is given as a test of the abilities of the ISS-Inspector and the Inspector Mission Planning Tool to perform the inspection of a wide range of targets

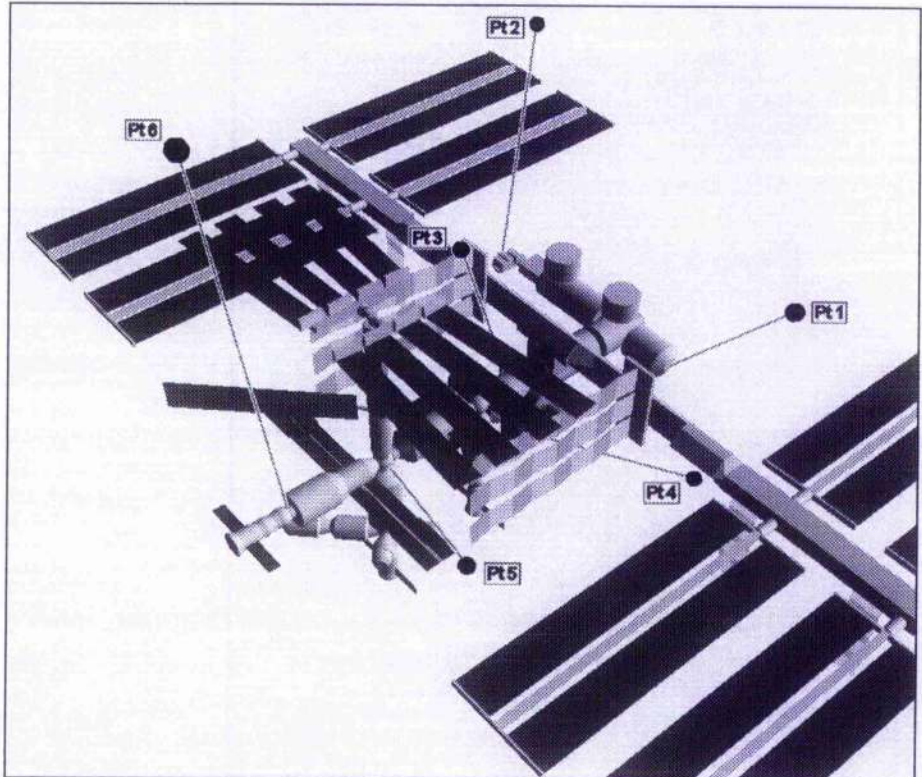
distributed extensively around the ISS structure. This is really intended to stretch the abilities both of the planning software and the Inspector Free-Flyer, rather than fulfilling a foreseeable mission requirement. However, it is useful to investigate how well observation positions towards the outskirts of the regular operating area are dealt with, and it also gives an opportunity to observe the PFG transfer between a number of widely separated observation positions. The inspection targets chosen are, from the front of the ISS to the rear:

- 1) The Inspector Free-Flyer docking point, located on the COF module.
- 2) The External Experiment Pallet, attached to the Japanese Experiment Module (JEM).
- 3) The Cupola viewing window.
- 4) The Crew Return Vehicle (CRV) docking point.
- 5) The connecting node between the Science Power Platform (SPP), the Russian research modules and the rest of the Russian ISS segment.
- 6) The rear Soyuz capsule and Progress supply vehicle docking point.

The observation positions required to view this range of targets are quite varied, both above and below the ISS structure, as shown in Figure 7-25. The orientation of targets 1 and 2 require inspection from opposite sides of the orbital plane (along the z-axis) resulting in a large out-of-plane separation between each of these observation points and all the others. Targets 5 and 6 meanwhile are located to the rear of the ISS, resulting in observation positions separated from the other points by a significant distance along the V-bar. The problem of radio frequency shadowing by the ISS structure, also forces Observation Pt 6 to be located high above the station in order to obtain a S-Band video connection during inspection.



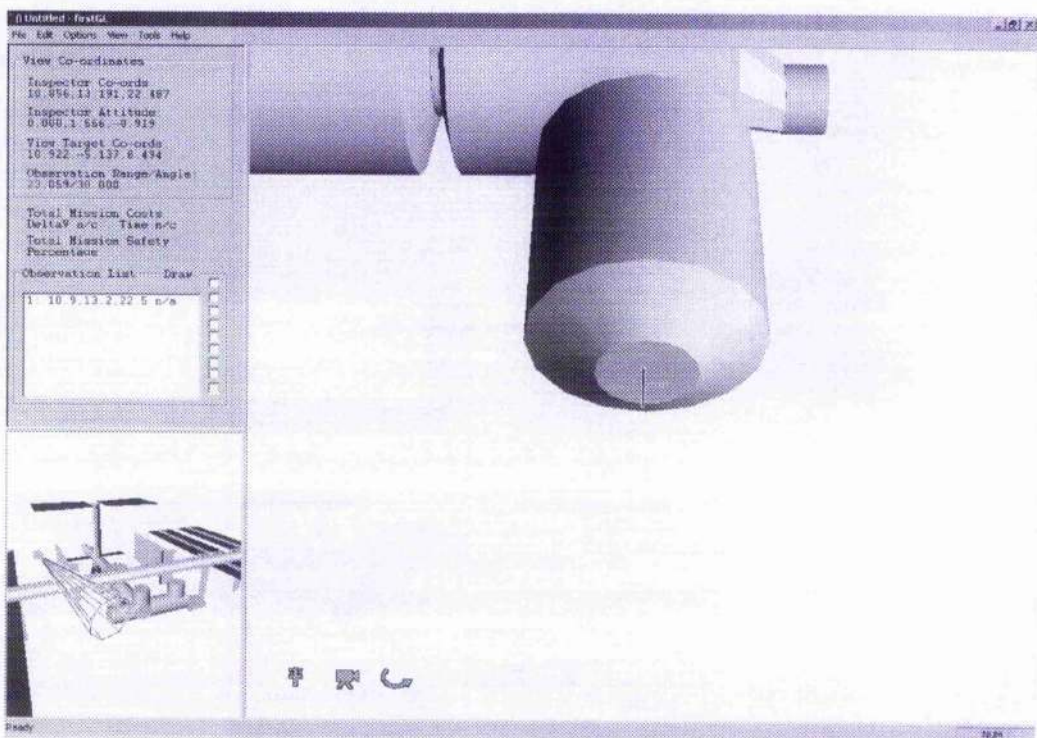
(a)



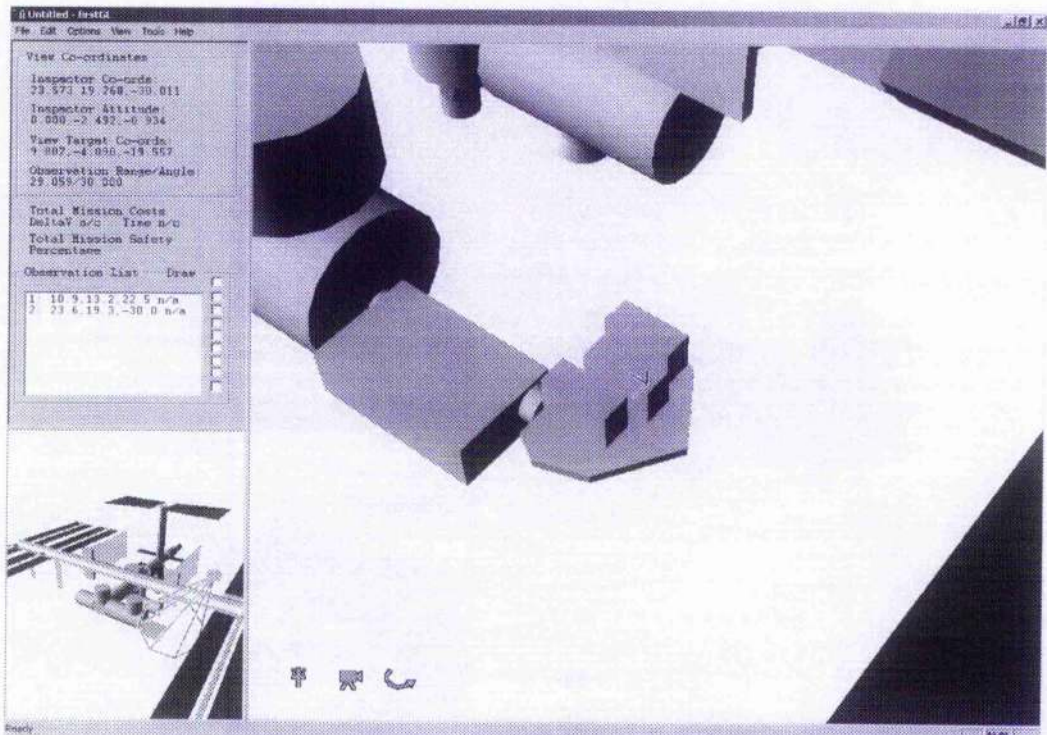
(b)

Figure 7-25 Case C: Observation Point Overview

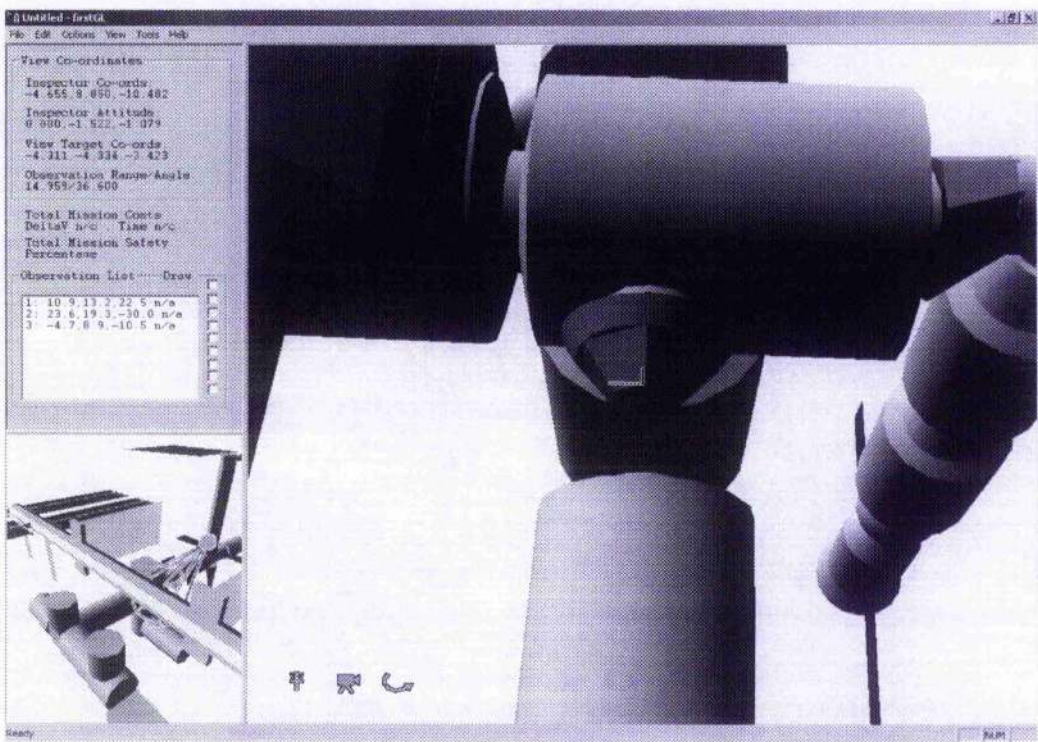
The interface screens from the Mission Planning Tool used to select each observation point are given in Figure 7-26.



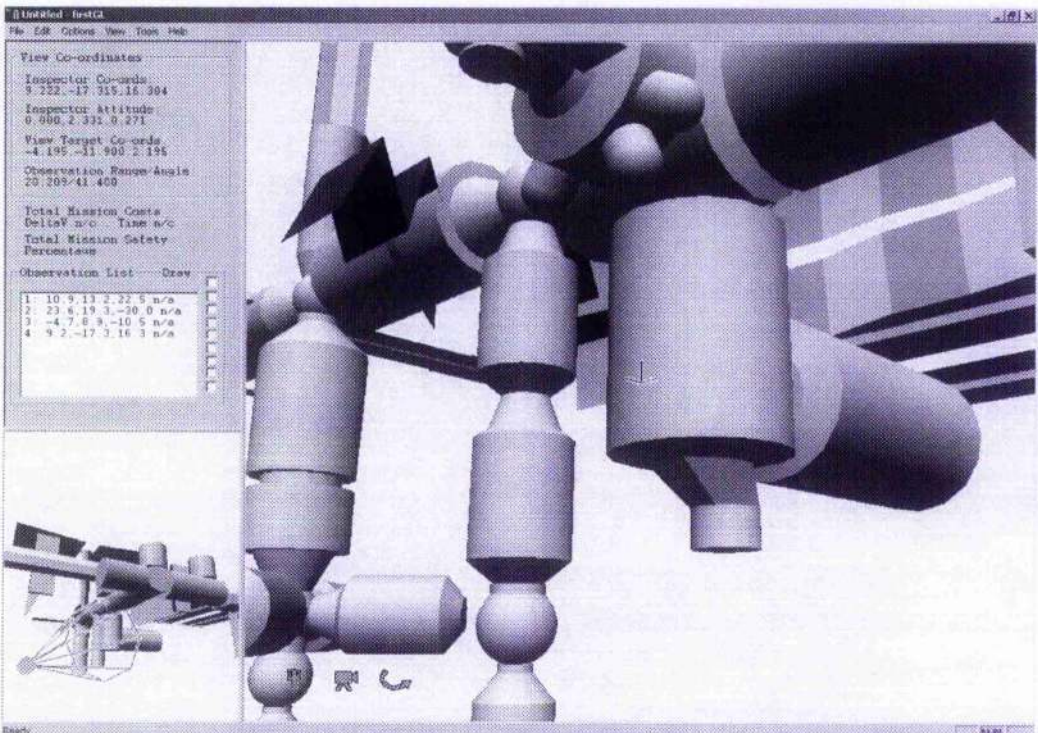
(a) Observation Pt 1 (COF Module)



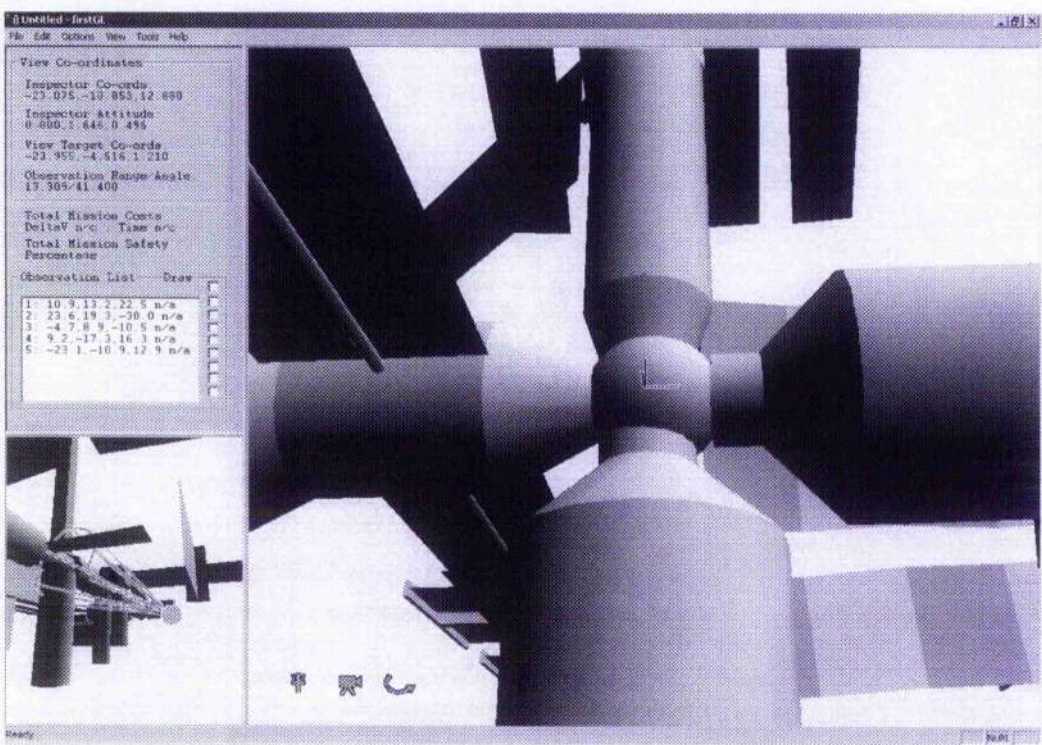
(b) Observation Pt 2 (JEM Pallet)



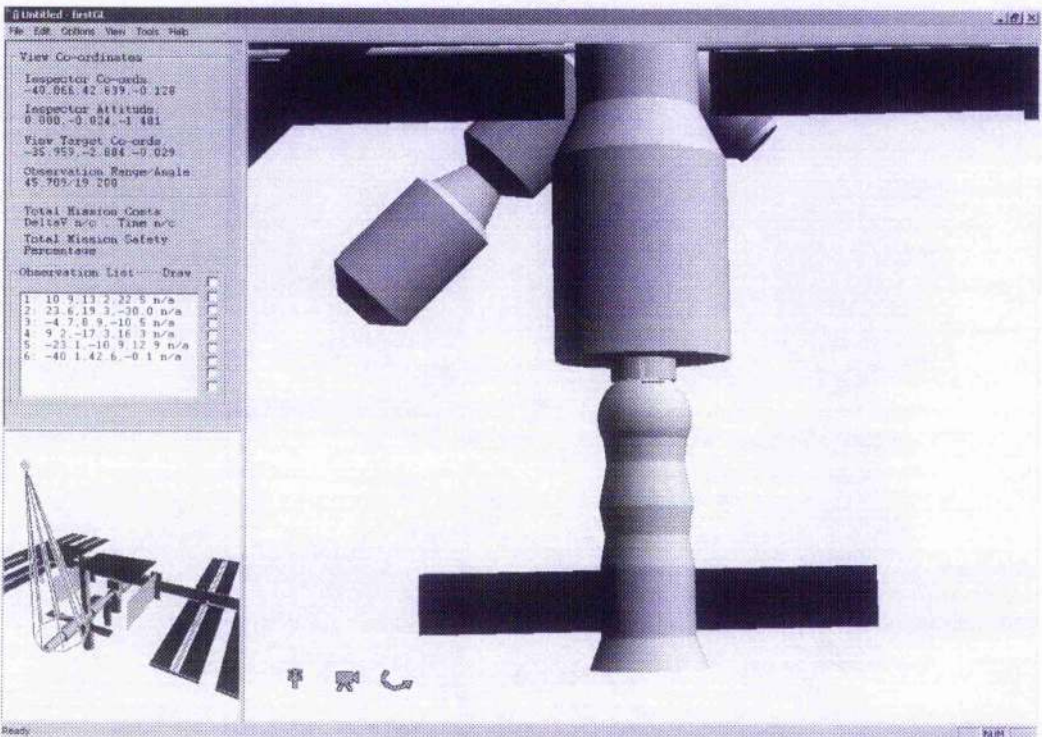
(c) Observation Pt 3 (Cupola Window)



(d) Observation Pt 4 (CRV Berth)



(e) Observation Pt 5 (Central Russian Node)



(f) Observation Pt 6 (Rear Soyuz Capsule)

Figure 7-26 Case C: Observation Point Selection Screens

Given the widely distributed nature of the observation points in this example, the results of the sequencing and optimisation stage of mission planning are particularly interesting. Visually studying the relative locations of the six observation points does not suggest any obvious sequence which they should be visited. The numerical results of this sequencing optimisation, given in Figure 7-27, show that using the Inspector Mission Planner results in visiting the observation points in the sequence 2, 3, 1, 6, 5, 4.

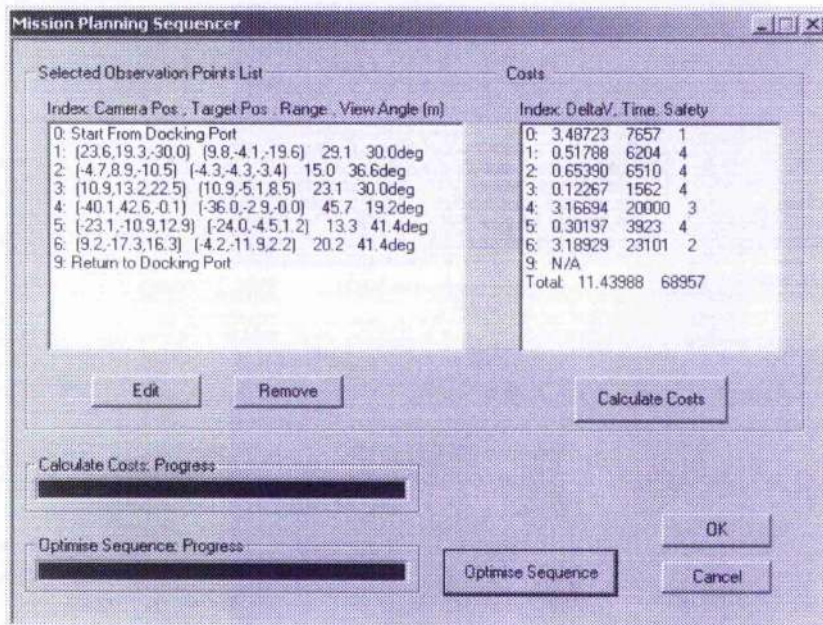
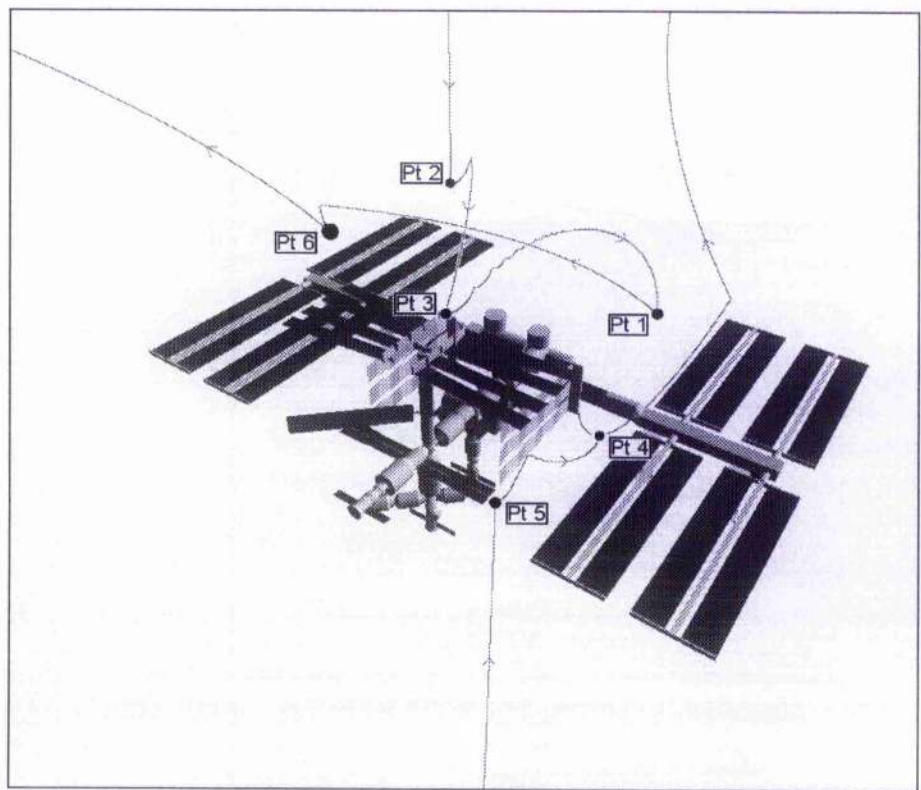
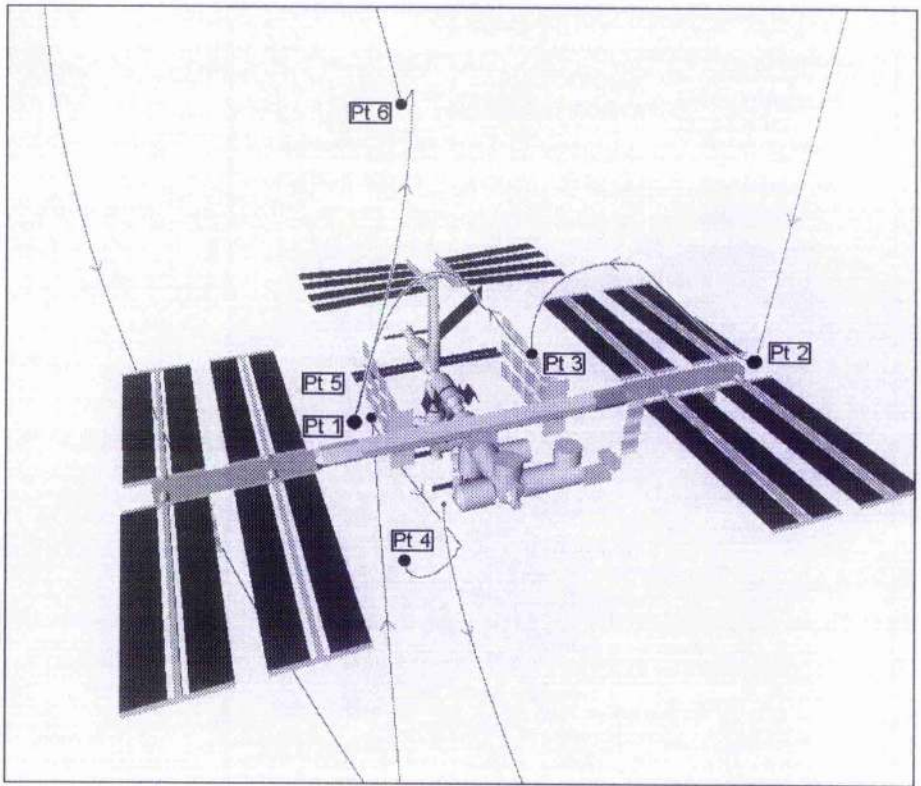


Figure 7-27 Case C: Transfer Optimisation Dialogue

The mission sequence comprises of two PFG manoeuvring segments, separated by and EOS transfer from above to below the V-bar. The initial retreat from docking is followed by an EOS transfer up Observation Pt 2 above the ISS. There is then a sequence of 3 PFG manoeuvres visiting Observation Pts 3, 1 and 6, before transferring to Observation Pt 5 below the ISS using an EOS. The final stage uses a PFG transfer to reach Observation Pt 4, before returning to docking on the standard return EOS. A visual overview of the resultant mission sequence and trajectory is given in Figure 7-28.



(a)

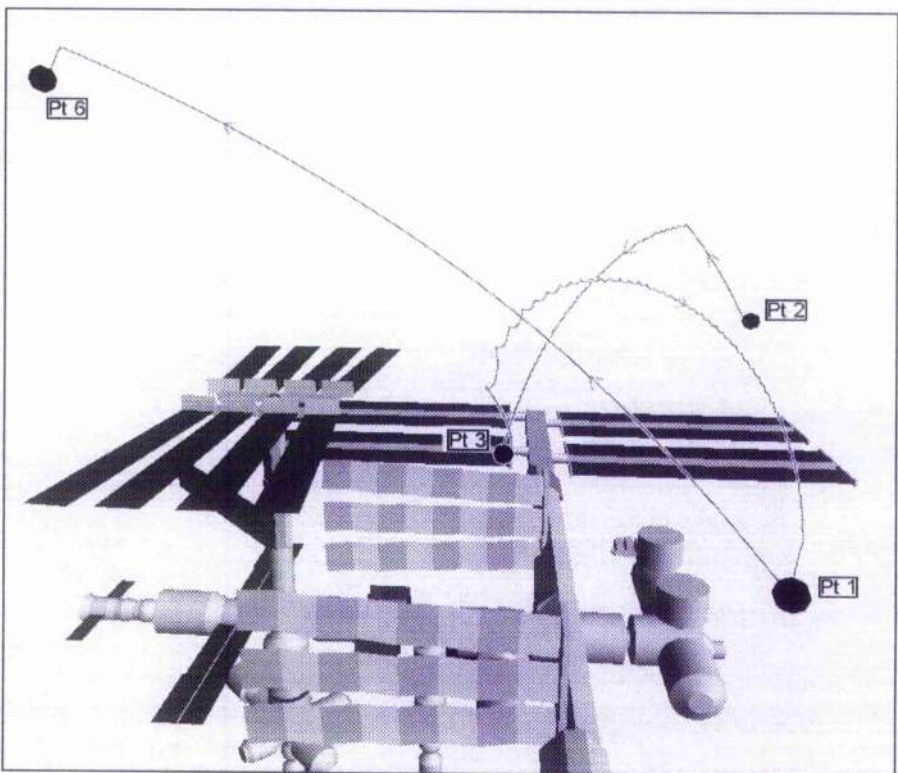


(b)

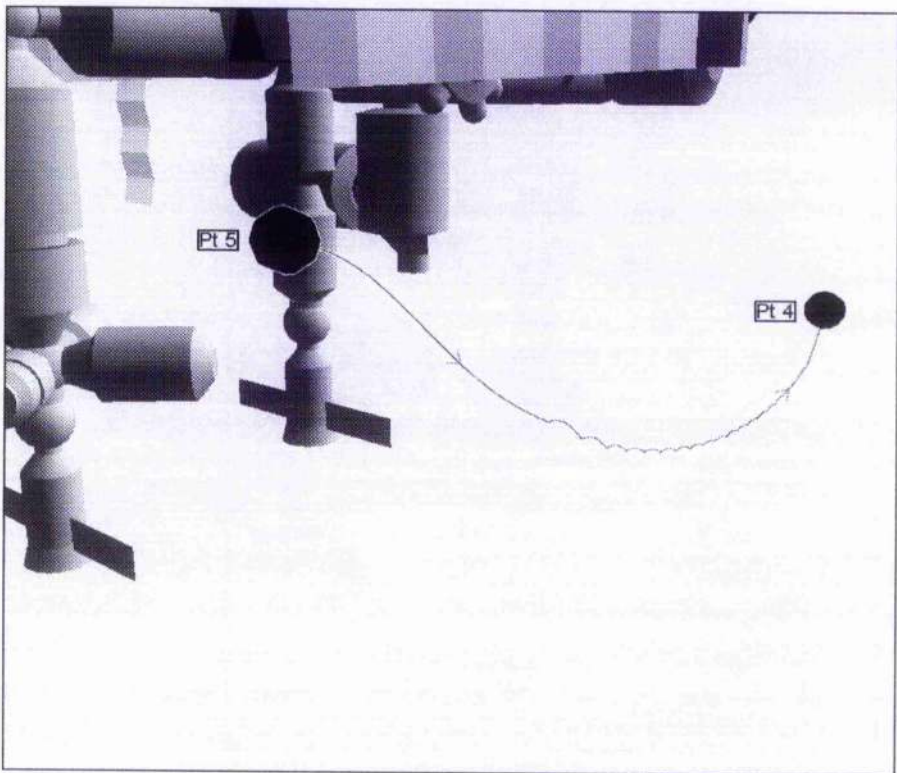
Figure 7-28 Case C: Mission Trajectory Overview

Concentrating initially on the first PFG segment between the observation points located above the ISS, shown in Figure 7-29(a), it appears that the manoeuvres have been sequenced in a slightly different manner than previous test cases. Other sets of observation points above the V-bar have arranged the sequence to traverse the points opposite to the V-bar direction starting with the point furthest ahead, but these results are quite different by making a transfet along the direction of the V-bar. This is most likely to be due to the additional cost of transferring across the orbital plane, significant here due to the relatively large out-of-plane offsets of Observation Pt 1 and Pt 2. By traversing the first three observation points in order along the z-axis this cost can be minimised despite the additional cost of translating back and forward along the V-bar. This sequencce also results in a favourable PFG trajectory from Observation Pt 1 to 6, which requires only one control action to drift for the majority of the transfer. This is in stark contrast to the other two PFG transfers (Pt 2 to 3 and Pt 3 to 1) which require a large number of control impulses to reach their goals, as shown in Figure 7-29(a) by the small looping arcs in the trajectories. Part of the reason for this feature in these trajectories is the Velocity Selection strategy of the PFG method, which will reduce the magnitude of control magnitudes to maintain the passive safety of the trajectories.

The second PFG segment consisting solely of the transfer between Observation Pt 5 and 4 below the ISS (shown in Figure 7-29(b)) is more typical of previous examples. Initially the trajectory takes advantage of the orbital dynamics, drifting for an extended period before being forced to make an increasing number of control impulses to maintain its final path to the goal.



(a) PFG Paths above the ISS



(b) PFG Paths below the ISS

Figure 7-29 Case C: PFG Trajectories

The EOS segments of the mission are once again similar to those seen on previous examples, though in this case the locations of the initial goal point (Pt 2) and second retreat point (Pt 6) are further away from the origin than before both in terms of in-plane and out-of-plane offset. This results in a noticeably cut-off ellipse in the initial trajectory to reach Pt 2, and a relatively elongated ellipse away from the rear of the ISS when retreating from Pt 6, shown in Figure 7-30.

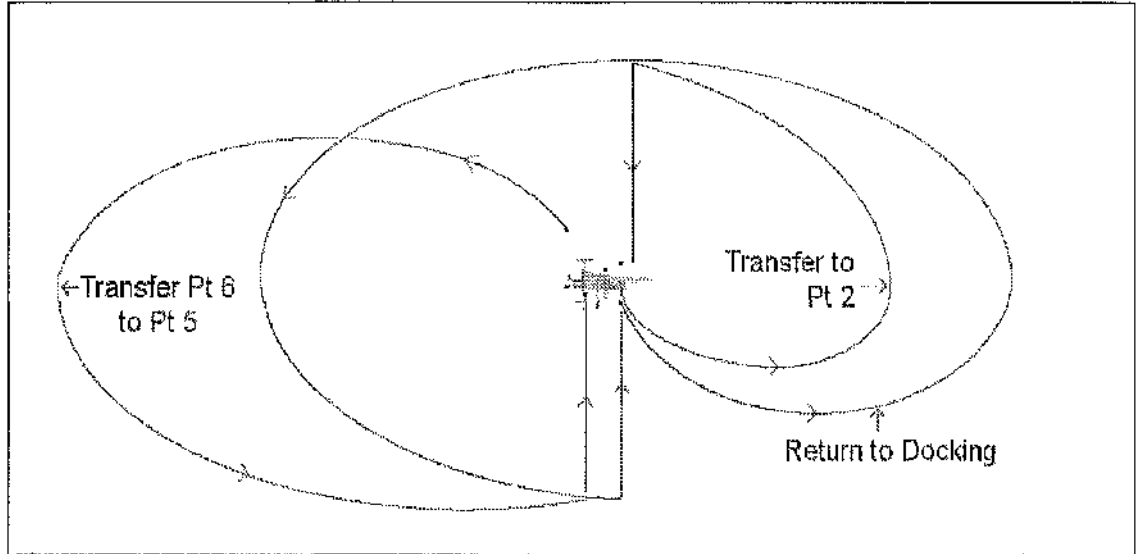


Figure 7-30 Case C: EOS Trajectory in X-Y Plane

Looking at the transfer costs for the mission, given in Table 7-5, the most immediate difference is that the PFG segments account for a significantly greater percentage of overall costs than in any previous examples. In Case B, the 4 PFG transfers account for less than 3% of total ΔV and 8% of transfer time costs, whereas in this case the 4 PFG transfer costs have risen to 11.5% of ΔV and 25% of transfer duration. This can be partly explained by the increased distance between observation points, however absolute distance has only increased by a factor of approximately 2, not sufficient to account for the 3-4 multiple increase in costs. However, as previously noted from the PFG trajectories, each of the more expensive PFG transfers (especially Pt 2 to 3 and Pt 3 to 1) require a relatively large number of small magnitude control impulses to achieve their goals whilst attempting to maintain passive safety. So it is this Velocity Selection strategy, along with the increased cost of transferring across the orbital plane that leads to the more costly PFG transfers seen here.

Transfer	Type	ΔV (m-s ⁻¹)	Transfer Time (s)
Docking to Pt 2 (R-bar approach)	EOS	3.48723	7657
Pt 2 to Pt 3	R-bar	0.8	1300
Pt 3 to Pt 1	PFG	0.51788	6204
Pt 1 to Pt 6	PFG	0.65390	6510
Pt 6 to Pt 5	PFG	0.12267	1562
(R-bar approach)	EOS	3.16694	20000
Pt 5 to Pt 4	R-bar	0.8	1300
Pt 4 Return to Docking (R-bar approach)	PFG	0.30197	3923
Total		13.83988	72857 (\approx 20 hrs)

Table 7-5 Case C: Mission Transfer Costs

Although the negative aspects for this mission of the PFG Velocity Selection strategy have been discussed in terms of increased PFG transfer costs, looking at the results of a safety analysis of these mission segments in Table 7-6 would indicate that the strategy was at least successful in that respect. The only transfer to possess any significant collision danger is from Pt 3 to Pt 1, during which the trajectory has the potential for a low velocity *Critical* impact for approximately two and a half minutes of a near two hour transfer. So, despite the extended length and duration of the PFG transfers in this example, overall mission safety has not been compromised.

Transfer	Duration	Any Impact	Critical Impact	Catastrophic Impact
Pt 2 to Pt 3	6204	0.00 %	0.00 %	0.00 %
Pt 3 to Pt 1	6510	2.42 %	2.42 %	0.00 %
Pt 1 to Pt 6	1562	0.72 %	0.72 %	0.72 %
Pt 5 to Pt 4	3923	0.00 %	0.00 %	0.00 %

Table 7-6 Case C: PFG Trajectory Safety Analysis

CHAPTER 8: CONCLUSIONS

8.1 Review

As a summary of the main results of this thesis, a review will be presented of what has been achieved through each chapter. To begin with the International Space Station was introduced, highlighting the increased size and complexity of this new space structure, and its associated maintenance and support requirements. The clear potential was seen to utilise a free-flying robotic agent to fulfil some of these support needs, especially given the high costs and risks involved in using astronaut EVA operations, and the limitations of the ISS robotic arm. From this, the primary problem of planning safe collision free paths and trajectories for a free-flying support robot such as the ISS-Inspector vehicle to facilitate manoeuvring around the exterior of the ISS was identified. The general problem of path planning for robots was then investigated, and an overall review of the available literature in the field of path planning made.

Of the available path planning techniques, two specific methods were chosen for application to the ISS-Inspector path planning problem, the discrete Laplace potential field, and a wave front cost method. These methods were chosen for their suitability to deal with a complex obstacle configuration such as the ISS structure, both in the straightforward representation of the obstacle shape using a discrete grid, and their avoidance of the formation of local minima in the potential field. This crucial result guarantees that the path planner will always be able to find a path to the goal, if one exists. The Laplace potential was chosen as the base method for its simple formulation, and the collision avoidance characteristics of the resulting paths which tend to avoid obstacles by a wide margin and follow a smooth path with no sudden changes in direction. The wave front method was chosen as an alternative for its ability to easily incorporate additional path constraints or costs, such as obstacle proximity or radio communications coverage, into the formulation of the basic cost function.

In Chapter 2, an existing solution to the orbital dynamics of the relative motion between a free flying vehicle and the ISS was introduced. This linearised solution to the relative motion of a free-flying body, in close proximity to a reference body in a constant circular orbit, is known as the Clohessy Wiltshire (CW) equations. The resulting relative motion, caused by the interaction of a constant circular orbit and a similar but slightly eccentric orbit, in a rotating reference frame attached to the circular orbit was then

investigated to provide a better understanding of the free-drift paths described by the CW equations. It was also shown that for the operating range of the Inspector vehicle, less than 1000m from the ISS, the errors introduced by the linearised equations of motion are negligible. Trajectory deviations caused by small thruster errors however were shown to be more significant, especially over extended free-drift trajectories, and must be taken into account when designing guidance and control strategies.

Through these simplified equations of motion the paths and trajectories of a free-flying vehicle operating close to the ISS to be planned and optimised. A brief investigation was then made into the basic optimisation of a two-impulse transfer between two points, highlighting the cost savings in terms of ΔV that can be obtained by manipulating the duration of a transfer. This was also extended to the optimisation of a transfer with a single waypoint positioned for obstacle avoidance. This showed a crucial conflict between the propulsive efficiency of extended looping trajectories and the need for relatively direct paths to maintain collision avoidance. A strategy was suggested and developed using the maximum deviation of the resulting trajectory from its desired route as a second criterion when optimising each transfer. This straightforward solution allowed routes to be followed using a series of waypoints, giving a simplistic method for adapting non-physics based path planning strategies to the orbital environment. However, this technique was too inefficient to be used for Inspector path planning due to large number of waypoints required to closely follow the desired path, and the control impulses required at each point.

The specific details and plans for the ISS-Inspector vehicle and mission, as developed by Daimler-Chrysler Aerospace (now EADS Astrium), were presented in Chapter 3. Although the ISS-Inspector project is at a relatively early stage, it was possible to obtain an approximation of the free-flyer's planned capabilities and control systems, as well as reviewing the operationally tested X-Mir Inspector vehicle. A number of potential problems and constraints on the operation of a free-flying vehicle operating from the ISS were identified, such as the flight rules imposed by NASA for visiting vehicles and the difficulties of maintaining radio communications with the ISS as the signals are shadowed by its structure. A range of pre-defined manoeuvring skills developed by EADS Astrium for the Inspector Free-Flyer were detailed. These included basic station-keeping and R-bar forced motion manoeuvres, as well as safety critical Collision Avoidance (CAM) manoeuvres which must be available at all times during Inspector operation to facilitate a safe retreat from the ISS in case of an emergency. An investigation was made into the safe approach of trajectories toward the ISS structure up and down the R-bar, resulting in the development by the author of approach safety envelopes, which can be used to define the areas of space surrounding the station which

are safely accessible through an R-bar approach. Finally, the concept of a graphical virtual camera view, incorporating observation point constraints such as approach and station-keeping safety, and command and video communications coverage, was developed to assist in selection of suitable observation points.

Following on from a simple elliptical trajectory known as an Ellipse of Safety (EOS) that was developed by EADS Astrium to provide passive safety during the fly-around phase of the X-Mit Inspector mission, a new point to point manoeuvring strategy making use of the EOS was developed in Chapter 4. The EOS utilises an ellipse trajectory around the ISS structure that is inclined in the out-of-plane direction, so that as the ellipse drifts along the V-bar due to a differential acceleration between the ISS and the free-flyer caused by aerodynamic drag effects, the ellipse trajectory will pass to the side of the station and avoid a collision. By controlling the initial position and inclination of the EOS, a method was developed here to force the resulting EOS to pass directly above or below a chosen target position. With the addition of a specifically designed passively safe free-drift retreat trajectory from the ISS to transfer onto the EOS, and a forced motion r-bar approach back toward the structure, the EOS strategy then facilitates fully passively safe manoeuvring from point to point around the ISS. The limitation is in both the ΔV cost of setting up and returning from the EOS, and the transfer times involved in orbiting around the ISS structure. This extended trajectory is useful in providing pre-mission overview observation and inspection opportunities, but the ΔV costs will limit the application of EOS transfers in any single mission. With this in mind two specific EOS applications were developed:

- A safe retreat from docking with EOS transfer to the first mission observation point.
- A return manoeuvre via an EOS and an R-Bar forced motion approach back to the docking point.

This enables the two most critical phases of each mission to be undertaken with the highest possible degree of passive safety, provided by the EOS transfer.

Moving on to the less stringently constrained manoeuvring permitted for close proximity transfers during the observation phase of the Inspector mission, the two alternate path planning methods chosen from the earlier review of path planning, were then applied to the ISS configuration space in Chapter 5. Previous work at the University of Glasgow had demonstrated the use of analytical potential functions for path planning and guidance. However, this method of potential specification was deemed unsuitable given the complex configuration of the ISS structure and the close proximity of ISS-Inspector manoeuvring

operations. The two alternatives applied for the ISS-Inspector were based on a potential field representation of Laplace's equation, and a numerical Wave-Front cost field.

Using these potential fields, guidance methods were then developed in Chapter 6 to manoeuvre the Inspector Free-Flyer safely around the structure of the ISS. The result of this was a guidance technique, Gradient Impulse – Potential Field Guidance (GI-PFG), which used the normalised potential gradient vector to trigger the control impulses required to maintain a path toward the goal and away from the ISS structure. This had the advantage of utilising the natural free-drift characteristics of the orbital dynamics where they suited the desired route, whilst not being directly linked to or limited by these constraints. The GI method was further developed by implementing velocity selection criteria at each control impulse. This performed collision checking on the predicted path for a range of impulse magnitudes in order to increase the safety of the resulting trajectory. Finally, to test the robustness of the GI-PFG method, the effect of errors both in the positional data supplied to the controller and in the supplied thruster impulses were investigated. It was found that the method naturally compensated for thrusters errors, whilst with the addition of a simple navigation smoothing stage, position and velocity errors could be successfully overcome.

The GI PFG method that has been developed is aimed primarily at real-time guidance of the Inspector Free-Flyer rather than off-line path planning prior to the mission. To this end, it has been shown how the technique can overcome the main obstacles to using such a potential field guidance system under error prone, real-world guidance and navigation conditions. For the mission planning element of the ISS-Inspector mission, the principal use of GI-PFG path finding is to assess the application of a PFG manoeuvre to a specific transfer, and to obtain an estimate of the costs and risks involved. The same potential fields calculated in the planning phase, can then be used later in the final execution of the PFG transfer.

It has also been shown that the GI guidance method is flexible enough to be used with a range of potential fields in addition to the potential functions it was originally designed for. The safety of the method comes partly from the potential fields used to generate the paths, but also using velocity selection at control points to choose the safest trajectory to follow at each step. The behaviour of the GI path in relation to the steepest descent path can also be controlled through the GI switching angle, permitting a degree of control over the path produced.

Finally, it may be possible to combine GI-PFG manoeuvring with alternative methods such as reactive control systems, to enhance the safety of the mission under off-nominal conditions such as an unexpected loss of navigation information. A combination of all these

safety elements of the GI method are, however, required to make PFG manoeuvring a viable option for Inspector Free-Flyer transfers at the ISS.

In Chapter 7, all the individual methods and techniques developed were brought together in order to meet the thesis goal of an overall ISS-Inspector mission planning tool. The observation camera visualisation tools developed in Chapter 3 were integrated to assist in the initial selection of suitable observation positions. The primary task was then to attempt to optimise the use of available manoeuvring techniques to accomplish each mission with minimum cost and maximum safety. This was achieved by combining conventional route scheduling techniques based on the Travelling Salesman Problem (TSP), with specifically developed cost graphs. These costs were based on segregated manoeuvring zones around the ISS structure, designed to choose PFG transfers wherever possible to reduce manoeuvre costs, whilst forcing EOS transfers where required to preserve mission safety. This strategy proved to be broadly successful, although small concessions were made to safety in certain circumstances. In addition, the use of multiple EOS transfers lead to ΔV costs close to or exceeding the Inspector Free-Flyer's original design capabilities. As a high level mission planning tool however, the Inspector tool fulfilled its goals in being both easy and quick to use, and accessible to a range of operators both on the ground and on orbit through its ability to execute on relatively low powered laptop computing systems such as those already installed onboard the ISS.

8.2 Summary

In summary, having identified the requirements for a free-flying vehicle such as the ISS Inspector, and the lack of the techniques necessary for safe and adaptable close proximity manoeuvring at the ISS, the key result of this thesis was the development of two complimentary manoeuvring methods for the Inspector Free-Flyer. These methods, namely Ellipse of Safety trajectories and Potential Field Guidance manoeuvring allow the Inspector vehicle to manoeuvre freely around the ISS with a high degree of passive safety in a manner not previously possible. The two distinct methods coexist by complimenting each others weaknesses. While the tightly constrained EOS method provides full passive safety for mission critical manoeuvring elements at the cost of ΔV and transfer time, PFG manoeuvring permits fast, efficient, and safety constrained manoeuvring within areas where it is safe to do so.

The primary purpose of the Inspector Mission Planning Tool was to investigate more closely the implementation and combination of EOS and PFG manoeuvring in complete missions, as well as to evaluate the rapid planning of missions through a simple user interface. From a manoeuvre implementation perspective the tool demonstrated that useful inspection missions could be realistically executed using the techniques developed. However, for more complex missions, cost estimations did exceed preliminary Inspector Free-Flyer design capabilities. Furthermore, these results were estimated to provide a high degree of passive safety throughout each mission, with only a small risk for reduced velocity impacts during certain stages of PFG manoeuvring. The three test cases were designed to represent a wide range of potential mission scenarios from a basic single target observation to an ambitious six target mission, so each should be considered individually.

- Test Case A: Three observation points, viewing a single target above the ISS.

On the whole the planning of mission A was successful, both in obtaining suitable inspection views and in planning the manoeuvres required to visit the observation points. The mission plan indicated that the chosen objectives are (excluding station keeping costs) within the predefined minimum capabilities of the ISS Inspector. Furthermore, aside from a single segment of one PFG manoeuvre (representing 16% of total PFG manoeuvring time, during which a CAM is still available) the mission planning tool managed to produce a mission that is passively safe.

- Test Case B: Six observation points, divided between two targets, above below the ISS.

Initially the mission plan and cost results for mission B would appear to represent a failure of the mission planner, with mission exceeding both ΔV and mission transfer duration constraints. However, the minor modification of using PFG manoeuvres to replace the EOS return to docking would transform this result into an achievable mission, whilst PFG safety analysis suggests that the overall mission would remain highly passively safe. This demonstrates how the results of the mission planning tool are not necessarily the final step. An experienced mission planner still has the potential to improve upon these results, and utilise options and strategies not currently integrated into the software to achieve mission goals.

- Test Case C: Six widely separated observation points, with six targets spread around the ISS.

Though (in common with mission B) the total mission costs for mission C exceeded the maximum design capabilities of the Inspector Free-Flyer, in this case the cause is not solely attributable to the planned intermediate EOS transfer. The suggested solution of

transferring directly from the final observation point to the docking port using PFG manoeuvres would again be applicable given the proximity of Observation Pt 4 to the docking position. However this would only bring total ΔV costs close to the prescribed 10 ms^{-1} maximum, and is stretching the limits of the Inspectors operational capabilities. Even so, it was not expected that this rather extreme example would be within the manoeuvring capacities of the Inspector Free-Flyer, and rather it was a test of the Mission Planning Tool, in which it has succeeded well.

From a planning and interface standpoint, the mission planning tool demonstrated the ability to rapidly plan or prototype inspection missions using a relatively simple operator interface. This was achieved by heavily utilising the graphical aspects of the mission representation and interface, to optimise the skills and input of the operator. The result was a relatively powerful mission planning tool, which is easy to use, and succeeds in presenting the results in an intuitive form for immediate operator evaluation.

8.3 Recommendations

Following on from the work detailed in this thesis, there are a number of directions in which further work would be recommended. Much of the specific mission designs developed for the ISS-Inspector mission planner are highly dependant on the physical design and capabilities of the Inspector vehicle, and it would be beneficial to update this tool to keep up with current and future advancements in free-flyer technologies. To further the development of PFG as a realistic solution to manoeuvring at the ISS however, it would be necessary to test these manoeuvring rules using a more realistic simulation and control model. This should include extending the guidance and control methods to include rotational controls both in manoeuvring and inspection phases, where development in this thesis has been limited to the pure translational problem.

The most important enhancement that could be made to either of the path planning methods from an operational point of view would be to be able to incorporate changing environments or obstacle configurations into the potential field. For the Laplace potential field a promising avenue of research has been presented by Zelek [62]. The paper proposes a method that allows a new potential field to be calculated mid-path by using an intermediate potential field, constructed by interpolating between the previous potential field and the incomplete new potential as it is calculated. Zelek demonstrates that this intermediate potential field is stable and suitable for safe path planning, so using this method the Laplace

potential could be updated at set sample intervals enabling the working potential field to account for any moving obstacles.

To achieve a similar result the wave-front method could be modified to use the D* algorithm [93] mentioned previously. As described in Chapter 1 this method allows the areas of the configuration space that are affected by changing obstacle configurations to be determined. Only these portions of the grid that are hidden from the goal by the changing obstacle then need to be recalculated. For movement of a small obstacle or component of the ISS this would mean that in many cases only minimal recalculation of the cost field would be required to account for this change. However the effectiveness of this optimisation would be reduced in the case of movement of a large obstacle, such as the PV arrays, positioned between the start and goal co-ordinates, as the majority of the cost field would require recalculation.

The wave-front cost field method also has further potential for improvement through manipulation of the movement cost function. This could be used to open up a form of direct configuration of the cost field, to allow the operator to shape paths around obstacles in a more favourable manner by manually modifying the local cost function.

For the Laplace potential field it would also be valuable to investigate methods of improving calculation and storage requirements. One possibility is to modify the iteration scheme used, which by default iterates each node in order of their position along the x, y, and z axes respectively, to use a wave front style calculation iterating each node in the order of their offset from the goal node. In theory this should propagate the low initial potential outwards from the goal far more quickly across the other nodes. However care must be taken not to compromise the avoidance of local minima during these iterations. The discrete formulation of the Laplace equation used here also relies upon regular grid spacing between the calculation nodes, both in the iteration equation and the subsequent interpolation methods. The use of variable node spacing, would allow more optimal grid representations such as a quadtree structure to be applied to the discrete Laplace equation in order to optimise storage requirements of the potential field, and provided increased detail in the potential field in complex areas of the configuration space. The use of alternative grid structures would have the same potential benefits for the wave-front method, however it would introduce problems in controlling the expansion of the wave-front in the cost calculation stage as open space areas encompassed by enlarged grid cells would jump the wave ahead and may cause the wave to become out of sync.

The area of the Gradient Impulse manoeuvring strategies that could be developed are the velocity selection routines developed to enhance mission safety. A more efficient path

propagation and collision detection method would permit improvements in the selection of velocity at each control impulse, either by allowing a wider range of potential velocity magnitudes to be tested, or by allowing the manipulation of impulse direction as well as magnitude. Efficient collision detection routines would have the additional benefit of speeding the calculation and improving the accuracy of overall mission safety estimates.

Finally, the mission planning tool could be enhanced in to reflect likely mission requirements. The introduction of time window constraints to the scheduling optimisation, would allow the planner to synchronise Inspector manoeuvring with external mission requirements such as astronaut EVA activities or optimal lighting conditions. It would also be beneficial to introduce more flexibility in the choice of manoeuvres available to the mission planner, such as allowing PFG return to docking, as proposed in Chapter 7 as a solution to the cost limitations of the EOS return to docking. The high cost of EOS manoeuvres, which given planned ISS-Inspector AV limits effectively constrain their use to two EOS transfers per mission, strongly favours the use of PFG manoeuvring for all short distance transfers. To do this however, would require a method of evaluating both the transfer cost and safety implications of alternate manoeuvres in a quantitative manner, enabling the selection of PFG manoeuvres to be incorporated into the overall mission optimisation.

APPENDIX I – SPACE STATION DEVELOPMENT

Space Station History (1971-1990's)

On the 19th April 1971, Salyut 1 was launched from Baikonur on a Soviet three-stage Proton rocket. For 6 months the first space station orbited the Earth before its orbit decayed and it re-entered the atmosphere on the 16th October. The first crew to visit Salyut 1 on 23rd April 1971 were unfortunately unable to gain access to the entry hatch, but the second crew successfully docked with the station on the 16th June, and made it their home for a total of 24 days, completing the primary mission to study the effects of long duration space flight on humans. Tragically an accident during re-entry caused their capsule to depressurise prematurely and the three cosmonauts were killed. This first generation of Salyut spacecraft were cylindrical structures approximately 12m long and 4m in diameter, equipped with fully integrated power and life-support subsystems to accommodate a crew of up to three cosmonauts. The Salyut series of space stations was then successfully developed through the 70's and 80's up to Salyut 7, which was launched on the 19th April 1982, remained in orbit for a record nine years and was home to a total of nine cosmonaut crews. Based on the second generation Salyut design, Salyut 7 was the first space station to support the docking of additional modules to enhance its capabilities, and with the docking of the Cosmos modules provided valuable experience to be used in the design of the subsequent Mir space station. One significant part of the Salyut program's success was the development of the Progress supply vehicle, an automated freighter with both pressurised and un-pressurised compartments. Progress greatly enhanced the capabilities of the station by enabling the delivery of supplies and new equipment to the interior of the station, as well as refuelling the station propellant tanks from the docked Progress vehicle's tanks.

Following the successes of the lunar Apollo program, the first American Space Station – Skylab was launched on the 14th May 1973 from the Kennedy Space Center by the last Saturn V rocket. Skylab, shown in Figure I-1, made extensive use of redundant Saturn and Apollo hardware. The station itself was in fact a 'dry' third stage of a Saturn V vehicle converted into a habitable structure, and astronauts were transported to and from the station by Apollo spacecraft. Once operational, Skylab was home to three crews who stayed for a total of 171 days. Nearly 400 man-hours of experiments were performed in such areas as Solar Astronomy, Earth Observation, Astrophysics, and Life Sciences. The work carried out through the life of Skylab demonstrated the ability of astronauts to perform repairs and EVA's in micro-gravity, with the EVA man-hours achieved on Skylab exceeding the sum total of all previous missions. Skylab was scheduled to remain in orbit for 8 to 10 years, however due to

greater than predicted solar activity its orbit deteriorated faster than anticipated and the station returned to earth during July 1979.

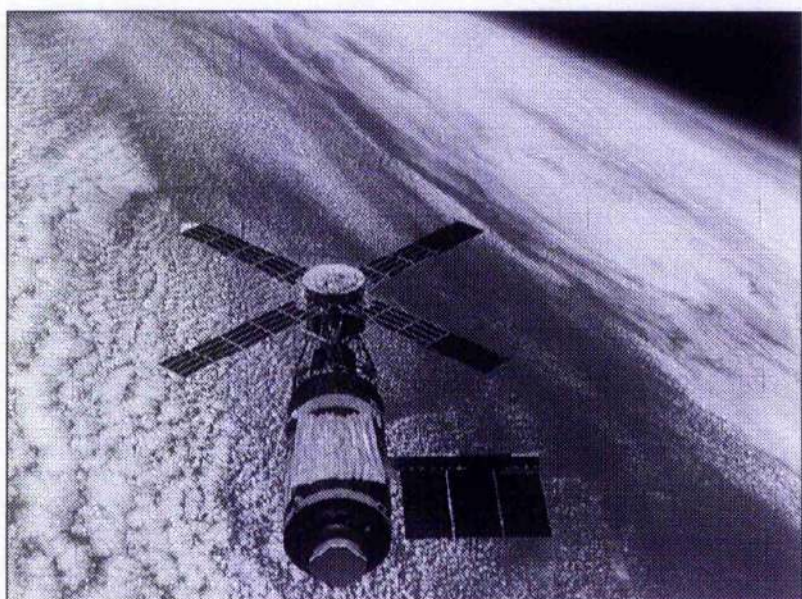


Figure I-1 Skylab from Orbit (source: NASA)

In the late 1970's and early 1980's NASA's manned space program focused on the development of the new reusable space vehicle, the Space Shuttle Orbiter. The first shuttle - *Columbia* was completed by contractors Rockwell International and launched from the Kennedy Space Center on April 12 1981. The Space Shuttle however was developed primarily as a transportation system, and possessed only limited facilities as a science platform within the Shuttle cabin. In order to enhance these capabilities and make use of the space in the Shuttle cargo bay for experimental purposes, the European space laboratory Spacelab was developed. The aim of Spacelab was to expand the Shuttle into a space laboratory that could support a crew of six for missions of up to nine days. Designed as a modular system consisting of pressurised modules of either one or two segments and external pallets, Spacelab provided a great deal of flexibility in the missions that could be undertaken. The first Spacelab flight launched in November 1983 aboard Space Shuttle Columbia and also carried the first European Space Agency astronaut Ulf Merbold. Since then Spacelab has become the most frequently flown payload on the Space Shuttle, having carried out a total of 33 missions, including 17 missions with the extended 2 segment 'long' module, and has performed a large number of science experiments.

The Mir Space Station

When the core module of the Mir space station was launched on 20th February 1986 it was initially estimated to have a five year life in orbit, but surprisingly the Mir station managed to survive nearly three times its design life. Developed from the preceding Salyut module, the Mir core made use of heavy docking ports to allow for multiple additional modules to be docked, expanding the size and volume of the station. Over its life 5 extra modules, along with an extra docking module, were attached to the Mir core as shown in Figure I-2:

Kvant I [1987] – Astrophysics telescopes, life support equipment and solar panels.

Kvant II [1989] – Earth observation, life support and EVA hardware and solar panels.

Kristall [1990] – Science and technology experiments, a special heavy docking port and solar panels.

Spektr [1995] – Astrophysical and geophysical observation experiments and solar panels.

Priroda [1996] – Remote sensing experiments and joint Russian - U.S. equipment.

An additional docking module was also attached to the special docking port on the Kristall module in 1995, enabling the U.S. space shuttle to dock with Mir.

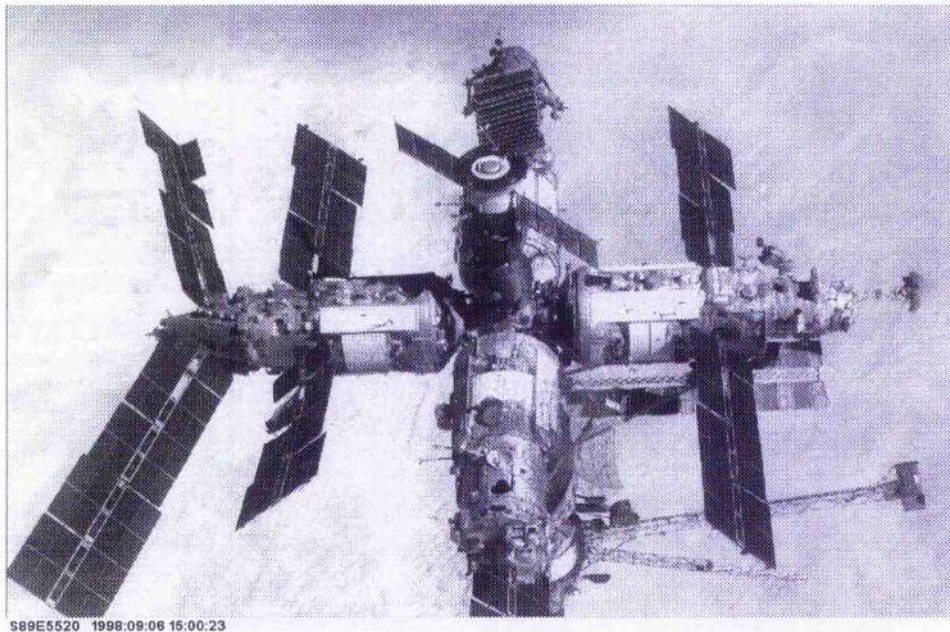


Figure I-2 The Mir Space Station (source: NASA)

The extended life span of the Mir station was made possible through the regular re-supply and re-boost by Progress supply vehicles and their successor, the Progress-M vehicle. This allowed a total of 43 cosmonauts and astronauts to make Mir their home for stays of

more than a month, and a further 59 had the opportunity to visit the station for short trips. The use of unmanned vehicles to dock with such a complex structure as Mir as not been without problems however. Docking with the station is normally an automated process, but on 24th June 1997 a Progress-M spacecraft was being controlled manually by the space station commander to test new remote control docking techniques developed to reduce reliance on the automated systems. Unfortunately, because of lighting from the remote camera, the Progress craft collided with the Mir station, damaging the Spektr module's solar panels and puncturing the module itself [1]. Luckily damage was restricted to a single module, however subsequent missions managed to reconnect electrical cables to the module restoring part of the lost power supply though the module remained fully depressurised. The last Soviet mission to Mir left the station in August 1999, with the future of the station in doubt as funds required to support Mir were being moved onto the International Space Station project, and MIR finally re-entered the earth's atmosphere on 23rd March 2001.

The International Space Station ISS (1998 - Future)

In 1984 the then U.S. President Ronald Reagan announced plans for an ambitious new space station to be launched within 10 years. Unfortunately this project, Space Station Freedom, did not advance beyond the planning stage due to escalating cost estimates and an ever decreasing NASA budget. Instead, the plans for an all American Space Station Freedom transformed over the years to incorporate co-operation between international partners in Canada, Europe and Japan. With the addition of Russia to the program in 1993 the program was streamlined, and with the co-operation of the member countries developed into the International Space Station as it stands today [161].

The first component of the International Space Station, the Russian built and launched Zarya control module, was launched into orbit on 20th November 1998, and was joined by the American Unity module on 10th December of the same year. Over the following 5 years the ISS structure has been expanded to approximately half its final size through a total of 37 assembly and re-supply missions utilising a range of launch vehicles including the Russian Proton and Soyuz Launchers and the U.S. Space Shuttle. The ISS became operational with the arrival of the Russian FGB (Functional Guidance Block) module in July 2000, and has been permanently crewed since 31st October 2000. Throughout its construction phase the ISS will also be capable of performing an increasing part of its science and research functions as modules and equipment are added, as shown in Figure I-3. However, it will not be able to support its full crew of 7 astronauts and cosmonauts until the addition of the final segment, the U.S. habitation module.

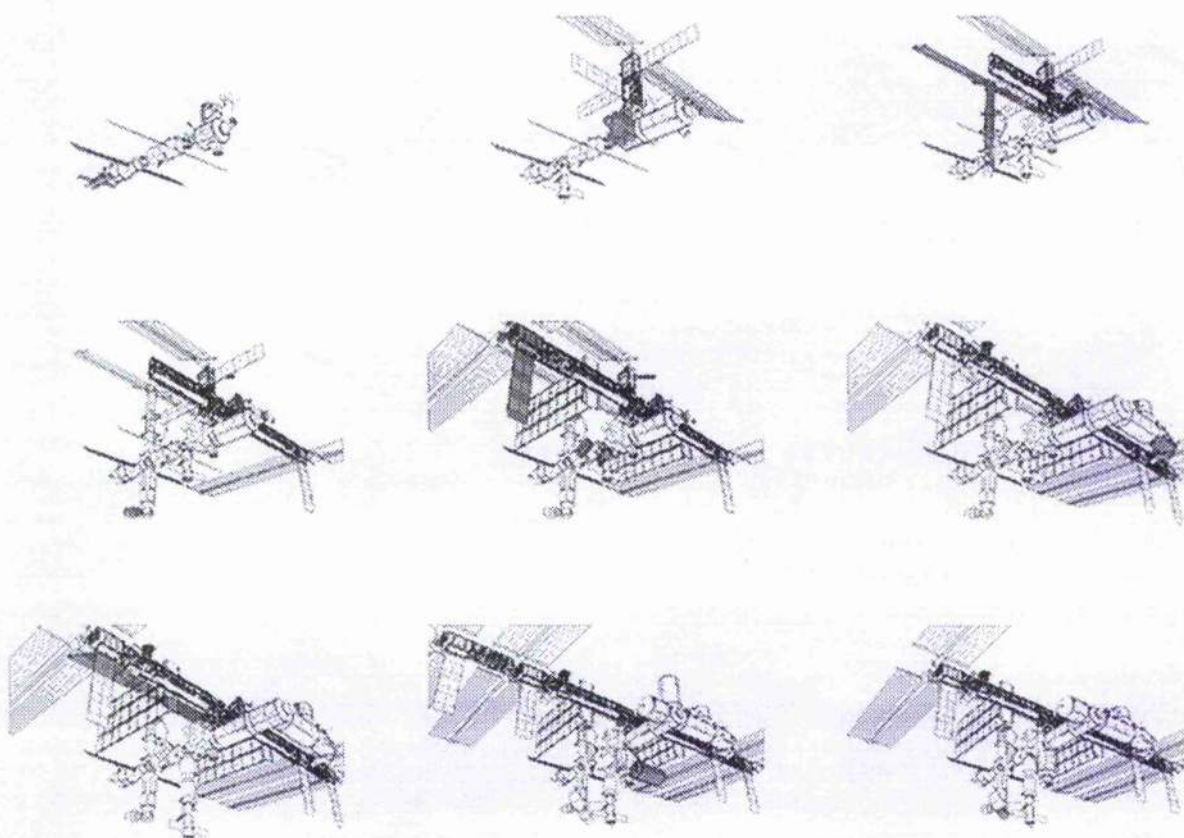


Figure I-3 ISS Construction Sequence (source: NASA)

The plentiful availability of research facilities, electrical power and manpower on the ISS, coupled with regular access for equipment change out and sample return, mean that the scope for science and research on the station are unmatched by any previous endeavour.

Research facilities will be provided by a total of 6 modules from 4 different space agencies:

- 2 U.S. modules – a Laboratory module and a Centrifuge.
- The European Space Agency (ESA) Columbus Orbital Facility (COF)
- The Japanese Experiment Module (JEM) including an external exposed palette
- 2 Russian Research Modules

These experiment modules are equipped with International Standard Payload Racks, which allow experiments to be designed to a standard format and easily transported between and installed in the ISS. In addition, there are a number of standard external platforms where instrumentation and experiments may be mounted on the outside of the station, for example to monitor the space environment or perform earth observation missions.

Finally, a number of options are available for transport to and from the ISS. Crew transfer to and from the station will normally be carried out by the U.S. Space Shuttle with the addition of Russian Soyuz capsules. Re-supply of materials and propellant will be provided by existing technology in the form of the Russian Progress-M autonomous vehicles, as well as the new ESA designed ATV (Automated Transfer Vehicle) launched by the Ariane-5 booster, and the Japanese H-II launched HTV vehicle.

Space Station Statistics

The International Space Station marks not only a leap in size and facilities over previous space stations, but also a vast increase in the resources required to assemble and support the station over its lifetime [3]. Since Salyut 1 was launched in 1971, space stations have evolved from one part structures transported into space by a single launch, into massive multi-part structures, constructed from a large number of separate modules and elements, launched over an extended period of time. Moreover, thanks to automated transfer and supply vehicles, the operational life-span of these stations in orbit has been dramatically extended. Table I-1 illustrates the evolution of space stations over the past 3 decades, and details the progression of both available size and power as well as assembly and support requirements.

Space Station [launched]	Mass (kg)	Pressurised Volume (m ³)	Modules	Power (kW)	Crew (max)	Life-span (years)
Salyut 1 [1971]	18,500	100	1 + Soyuz capsule	1	3	0.5
Skylab [1973]	74,783	361	1 + Apollo capsule	11	3	6
Salyut 7 (Core) [1982]	18,900	100	1 + Test modules	2	3	9
Mir [1986]	124,000	398	7 + capsules	35	>3	>14
ISS [1998]	454,000	1215	>18 + vehicles	110	7	Est >10

Table I-1 The Progress of Space Station Capability and Complexity

As can be seen in Table I-1, the ISS represents nearly a four fold increase in mass, pressurised volume, and power supply over the previous generation Mir Space Station. The International Space Station once fully assembled will have a span of over 70m across the solar arrays and total length of over 100m, and the internal pressurised volume available is equivalent or greater than that of a 300 seat passenger aircraft. As a result of the complex support

structure required such as the main truss, and the logistics of operating the station during assembly, the number of launches that will be required to completely assemble the ISS is a planned 46 assembly flights as opposed to the 7 flights necessary to assemble Mir in orbit, a six fold increase.

In addition to a simple increase in mass and volume, from an engineering perspective the most dramatic change in the last two generations of space stations has been the increase in the complexity of the completed structures. This has come about partly through the use of modular designs, which are assembled over an extended period of time, but must also be operational for a large part of the construction phase. Furthermore, these modules may not even have been designed at the same time (in the case of the Mir station) or even by similar design teams (as with the International Space Station), requiring designs that can be easily modified and adapted for changing conditions. Finally, a great deal of increased complexity is brought about by the power requirements of modern stations, necessitating large solar arrays as well as large thermal radiators to dissipate waste heat.

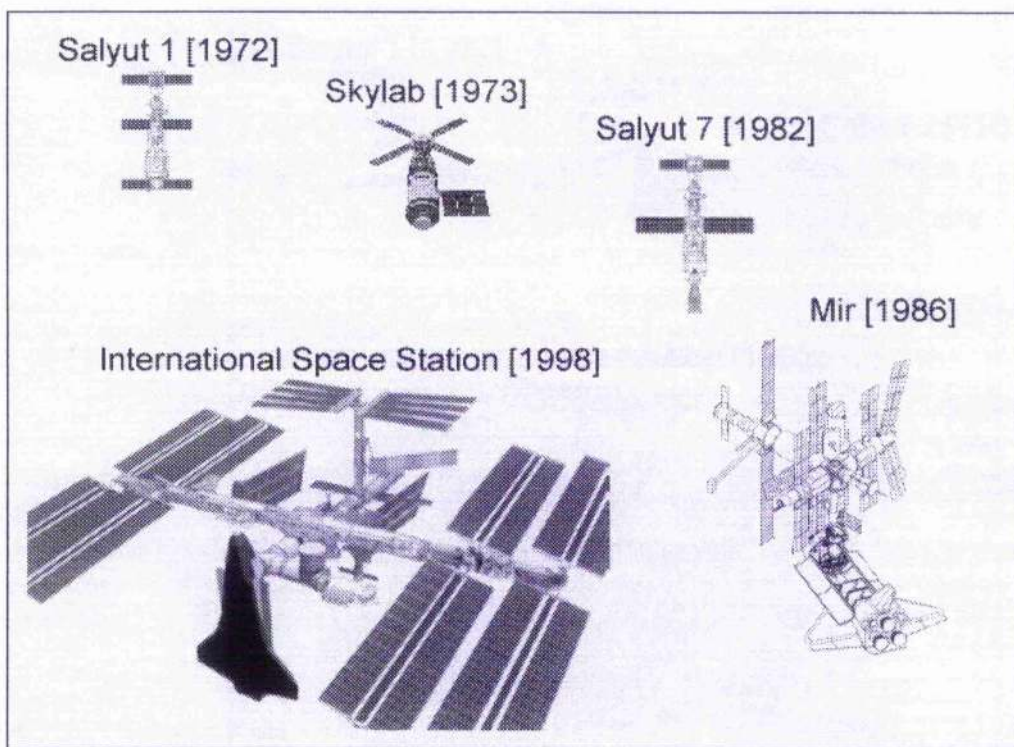


Figure I-4 The Evolution of Space Stations (source: NASA)

This increased complexity can easily be seen in images of the ISS and Mir compared to earlier space stations, as shown in Figure I-4. Early space stations such as the Salyut series and Skylab were simple cylindrical structures, fully constructed on the ground and fully integrated with all the station systems. Instead Mir and the ISS are far less one dimensional in their orientation with modules attached in various planes and additional support structure outside

the core modules further complicating the geometry. The consequence of such intricate structures is that operations on the exterior of the station become extremely difficult to plan, and more troublesome and hazardous to perform. In addition, the problem is compounded by the fact that it is these types of external missions that will be required more often because of the increased size and complexity of the systems.

APENDIX II: STATE OF THE ART ROBOTICS

The arrival of the U.S. Space Shuttle in the 1980's significantly increased the flight rate for crewed missions to Earth orbit. With a number of reusable shuttles regularly available, and human crews required to use the shuttle as a launch vehicle, human presence and availability in orbit has been greatly increased. This has enabled a range of new missions that were previously not possible, such as the launch and subsequent retrieval of satellites, and repair/upgrade missions to satellites such as the Hubble Space Telescope. Yet whilst the repair of Hubble was made possible by the skills of astronauts, without the Shuttle's robotic arm to capture the satellite and then provide a steady platform for the astronauts to work from, these missions would not have been possible at all.

To date the use of robotic arms has been primarily limited to crewed space vehicles, where they may be used to support human activities in space, and perform as a terrestrial crane to grasp and manoeuvre payloads. The completed ISS will have at least three robotic arms available to astronauts onboard the station, from the small manipulator on the JEM Exposed Facility for managing the external experiments on the platform, to the SSRMS developed from the Shuttle manipulator which will be used to manoeuvre complete ISS modules during the construction of the station. This 17 metre long manipulator, with a total of 7 motorised joints and a choice of actuator heads, will be able to handle very large payloads, and assist in docking/berthing operations. In addition the SSRMS will be mounted on a mobile base system which can travel on rails along the main truss structure and is self re-locatable, enabling it to be moved to other attachment points on the station.

The robotic assistance of the Shuttle SRMS, and the space station SSRMS will be invaluable during the construction of the ISS, yet the new space station will still require up to 40 EVA's or 300 to 400 hours *per year* over its lifetime. This is a full order of magnitude increase over previous Russian and American operations, which over the construction phase of the ISS will amount to more astronaut EVA time than all previous experience combined. In addition to the high cost in astronaut time for the construction of the station, another important limiting factor in human activities comes from the space environment. Unlike the Earth's surface, space lacks the shielding effect of the atmosphere which blocks most high energy solar and galactic radiation, and whilst space structures such as the ISS can be designed to protect their crew, EVA operations are inherently more risky as the crew must leave the relatively safe refuge of the station with only a pressure suit for protection. Each individual astronaut may therefore only perform a limited duration of EVA activities, limited by a safe

radiation dose. Therefore, every effort must be made to reduce the necessity for human presence outside the station wherever possible, through the use of robotics.

As well as the use of robotics in orbit, there are also possibilities for enabling completely new missions using robotic spacecraft, such as the on-orbit inspection, servicing and repair of commercial satellites [8]. With the high development and launch costs of large commercial communications satellites, there may be a future market for servicing vehicles in orbit, capable of rescuing satellites which have failures during their deployment or during their operational life, or even solely to make inspections to assess satellite failures. Another possible application of such orbital robots is for de-orbiting redundant satellites at the end of their lifetime to reduce orbital debris in geo-stationary orbit. Interestingly, there are many similarities between such satellite rendezvous and servicing/repair missions and the ISS inspection missions developed in this thesis, presenting a future alternative application for the tools and techniques developed.

As previously mentioned, the Progress automated supply vehicle has been a key factor in the success of the Soviet space station program since the 1980's. First used in 1978, Progress was eventually replaced by the enhanced Progress-M vehicle in 1989. Importantly, both spacecraft made use of an automated docking system, Igla on Progress and Kurs on Progress-M, allowing reliable re-supply of the Salyut and Mir space station. Although Progress-M will also be used to supply the International Space Station, the Automated Transfer Vehicle (ATV) is currently in development by the European Space Agency, utilising the latest in robotic technology to provide supply and re-boost services to the ISS [45].

A number of robotic missions have already been completed which demonstrate the possibilities for the future use of robots in Earth orbit and deep space. These missions have successfully shown the potential of robotics both to support human space flight, and to explore the solar system. In addition, the advantageous combination of human and robotic activities, as well as the use of spacecraft autonomy, have been tested and flight proven.

X - Mir Inspector

Launched onboard the Progress M-36 supply shuttle to the Mir space station on 5th October 1997, the German X-Mir Inspector [162] was the first step in the development of the Inspector product family of free-flying vehicles. Developed by DASA-RI (a division of Daimler-Chrysler Aerospace, now EADS Astrium) in Bremen, Germany, the X-Mir Inspector was designed to verify the concept of using a small free-flying vehicle to make observations of a space structure and to test the use of a custom monitoring and control station (MCS) onboard the Mir station to control the Inspector mission. The Inspector free-flyer was stored

in the pressurised compartment of the Progress vehicle so that the MCS hardware could be installed in the Mir station prior to the Inspector mission. Inspector was then transferred by cosmonauts on Mir onto a special separation mechanism in Progress allowing the free-flyer to be ejected from the supply vehicle once it had undocked and retreated from the space station.

X-Mir Inspector itself was a relatively simple spacecraft, with only two thrusters aligned along the longitudinal axis and reaction wheels to control attitude, as shown in Figure II-1. Due to this simplicity, and the lack of any back-up thruster systems, Inspector therefore required extensive safety rules in the flight software to prevent the possibility of a collision in the event of a thruster malfunction. For navigation a star camera along with laser rate gyros were used to determine attitude. Interestingly though, relative position measurements were made using a novel video navigation system that used the video data from the Inspector video camera, and reference points on the Mir station picked out by the operating cosmonaut, to determine the relative position to the station.

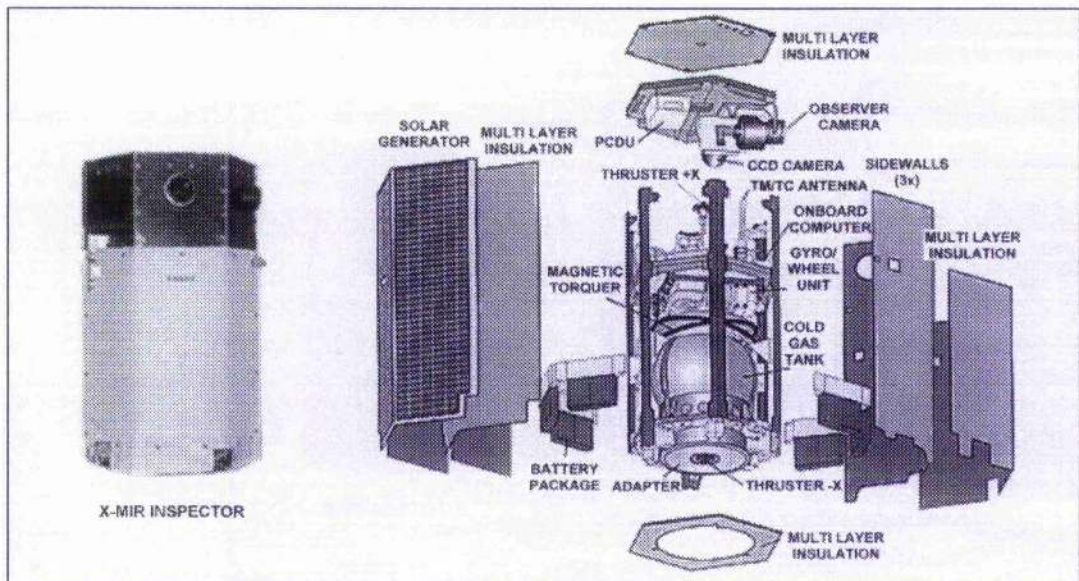


Figure II-1 The X-Mir Inspector Systems Diagram (source: EADS Astrium)

The mission profile, given in Figure II-2, was for Progress to undock and retreat to a safe distance from the Mir station before releasing the Inspector vehicle. Inspector would then make two complete fly-around inspections of Progress to verify its systems before moving to the Mir space station and completing three orbits to make a complete observation of the station with its onboard camera.

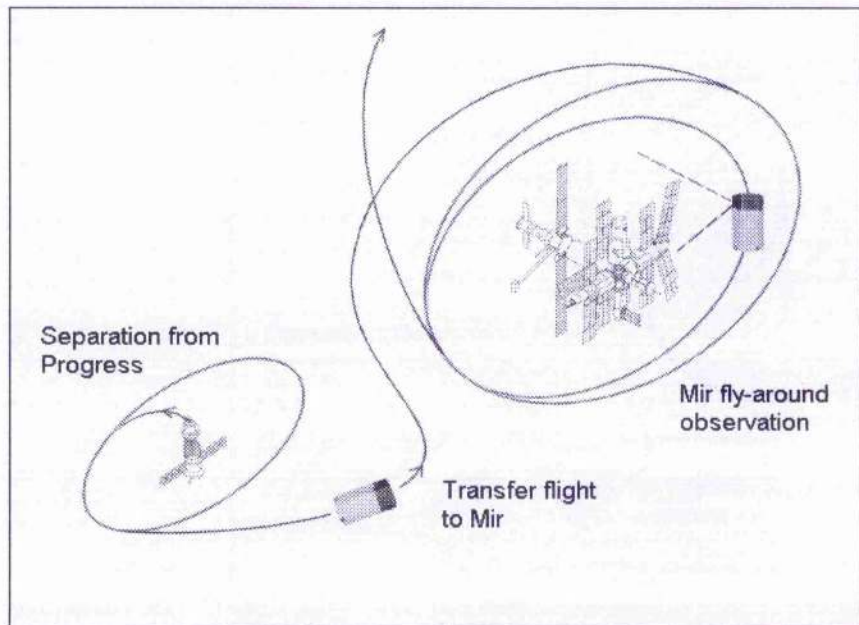


Figure II-2 The Mir – Progress – Inspector Mission Overview (source: EADS Astrium)

Unfortunately the Inspector Vehicle was unable to complete its first impulse manoeuvre as the star camera had been unsuccessful in acquiring enough stars to identify the initial attitude of the vehicle. This caused the safety rules embedded in the control software to inhibit the thruster firing, and as attitude could not be re-acquired, the active manoeuvring phases of the mission were cancelled leaving the Inspector drifting safely way from the Mir station. Nevertheless, manual attitude control via the MCS by cosmonauts onboard Mir allowed a number of observations of Progress and Mir to be made by the Inspector camera as it drifted away, fulfilling the majority of the primary mission goals. The lessons learned from the Mir Inspector mission are to be used in the design of subsequent, more sophisticated generations of the Inspector family operating in the complex International Space Station environment, such as the ISS Inspector.

Mars Pathfinder – The Sojourner Robot

The Mars Pathfinder spacecraft [163], launched on the 4th December 1996, and more specifically the Sojourner vehicle it carried to the Martian surface, are excellent examples of the application of robotics and autonomy to the control problems encountered in operating spacecraft at a significant distance from Earth. The Pathfinder project was the first project to be launched under the new NASA Discovery ‘‘Faster, Better, Cheaper’’ program, the most striking example of this philosophy being the Sojourner Rover [164] carried on the Pathfinder craft, shown in Figure II-3. While technically part of the mission payload, the Sojourner

vehicle was essentially a complete spacecraft in its own right, with all the necessary subsystems required for guidance and navigation, communications and data handling, and power and thermal control. Sojourner also carried a scientific payload of its own, including a colour imaging camera and an X-ray spectrometer. In addition, the rover was also highly automated, to the extent of being capable of fully autonomous operation in case of extended loss of radio contact. Yet despite this technology, the rover vehicle was designed and constructed in only 3 years to a budget of \$25M including mission support costs.

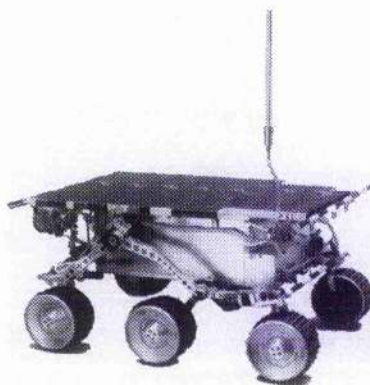


Figure II-3 The Mars Sojourner Rover (source: NASA)

The Sojourner micro-rover itself is a small 6 wheeled vehicle, $0.63 \times 0.48 \times 0.28$ m in size giving a ground clearance of 0.18 m. During the flight on the Lander however, the wheels can fold away, reducing the height from 0.28 m to 0.18 m. The 6 wheel rocker-bogie design of the rover, using 4 of the wheels for steering, makes the vehicle highly manoeuvrable enabling it to turn on the spot and traverse obstacles up to 1.5 wheel diameters in height. However the rover is not a high speed vehicle, due to power restrictions the electric drive motors are geared very low to provide the torque required to traverse the soft uneven terrain, resulting in an average speed of 0.7 cm/s. Communication with the rover is achieved by a radio modem connection to the Lander to relay the data back to Earth, though the rover itself is capable of backing up the data collected to transmit to the Lander at a later time in case communications are not possible.

The design of the control system for Sojourner was also dictated to a large extent by the requirement to satisfying the stringent power limits [165]. This effectively meant that no two pieces of major equipment onboard the rover could be operated at the same time, so for example the laser navigation system cannot operate at the same time as the wheel motors, and the radio modem cannot communicate with the Lander while the rover is taking measurements with the spectrometer. Consequently the control structure used is essentially sequential, with the added advantage of greatly simplifying the control software required.

Sojourner therefore operates in a step by step fashion to complete its goals. For example, in moving to a new waypoint the rover would move a small distance in the desired direction, stop and use its laser navigation system to detect any obstacles, and then make a communication check with the Lander before moving another step or turning to avoid any obstacles detected. Despite this relatively simple control structure and the very slow movement of the rover, it was in fact capable of demonstrating quite a sophisticated level of autonomous behaviour. Commands are given to Sojourner in the form of high level tasks such as take a spectrometer reading at a given point, and waypoints to be used to traverse the Martian surface. Due to the communications time-lag of approximately 10 minutes between Mars and the Earth, real time control by human operators was not possible, so the combination of human guidance via waypoints and autonomous hazard avoidance on the rover was used. These waypoints can be planned by controllers on the ground using terrain information gathered from the Lander and rover cameras to determine the preferred route to the goal point. In the event that communications with the Lander are temporarily lost, the rover will automatically retrace its steps to the last position where it successfully communicated and wait until it receives a response from the Lander. If however communications are lost for an extended length of time, the rover is then capable of undertaking a backup version of its mission fully autonomously, broadcasting the results in the hope that the Lander is still capable of receiving them.

Although a ground based exploratory vehicle, the Mars Sojourner Rover actually has a lot in common with a free-flying orbital inspection vehicle such as the ISS Inspector. Both vehicles are designed with the aim of gathering visual images of their environment. Both are designed to be as autonomous as possible, while at the same time making use of human decision making skills for mission planning and in case of emergencies. Finally, both vehicles have to be as small and efficient as possible, leading to some similar solutions to design problems. For example, the navigation system on Sojourner detects obstacles using a laser and a pair of video cameras, similar to the visual navigation system on the X-Mir Inspector which also used the vehicle's onboard camera. The lessons learned from Sojourner may therefore be highly applicable in the development of free-flying vehicles as well as future planetary rovers.

Space Shuttle Robotic Arm

The robotic arm on the Space Shuttle, known as the Shuttle Remote Manipulator System (SRMS) was developed by the Canadian company SPAR as part of the Canadian contribution to the NASA Shuttle program. Comprised of an upper and lower boom and an end effector

giving a wide range of motion, the SRMS was designed for capturing and manipulating payloads in orbit. Controlled by the Shuttle crew from the flight deck via 2 joysticks, the robotic arm is capable of manipulating payloads of up to 30 metric tonnes. To date a total of five SRMS have been built since 1983 and have proven to be an essential part of the Shuttle systems for a range of missions, demonstrating the reliability and usefulness of robotics as a long term solution in space. More recently the Shuttle manipulator has been used to perform the first phase in the assembly of the International Space Station, assisting in docking the Unity module carried aboard the Shuttle, to the orbiting Zarya module. Figure II-4 shows the SRMS being used to support two of the shuttle astronauts as they complete this stage of the assembly sequence.

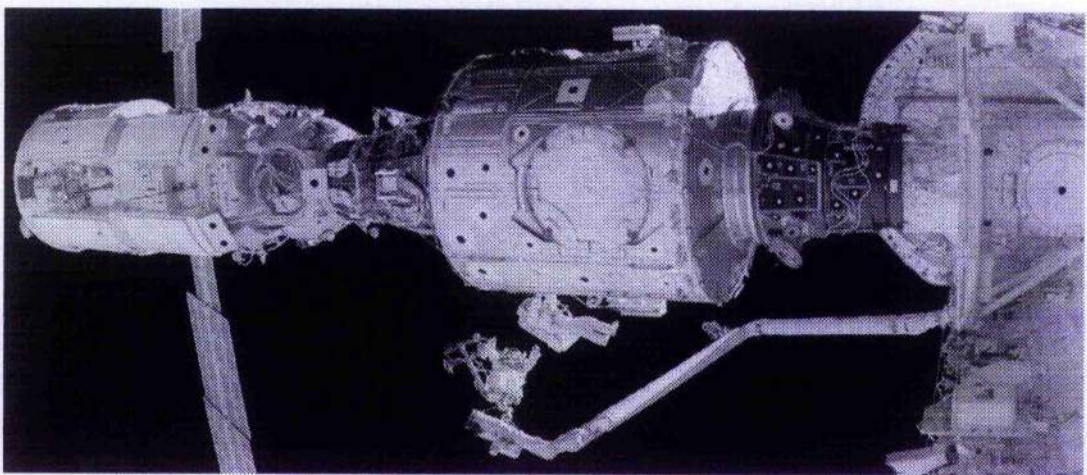


Figure II-4 SRMS Assists in the Assembly of the ISS (source: NASA)

In the future, as well as supporting the further assembly of the ISS, the SRMS design will form the basis for the enhanced Space Station Remote Manipulator System (SSRMS) which was then installed on the ISS on 22nd April 2001.

Japanese Robotic Experiments

Although not as well known as most western efforts in the field of space robotics, the Japanese space agency NASDA has had success with its recent robotic test missions [166]. Amongst the missions that NASDA has flown are the Manipulator Flight Demonstration (MFD) which was flown on board the US Space Shuttle in August 1997, and the ETS-VII Flight Experiment which was launched by an H-II Rocket on 26th November 1997. A number of additional technologies have also been developed as part of the Japanese space program, such as the orbital capture of satellites, and new approaches to planetary rovers.

The Manipulator Flight Demonstration was flown as a payload mounted in the bay of shuttle mission STS-85, with the purpose of demonstrating the robotic manipulator

technologies developed for the Japanese Experiment Module – Remote Manipulator System (JEM-RMS) for the International Space Station. The MFD mission was also the first opportunity for the Japanese and American space agencies, NASDA and NASA, to gain experience in co-operating on a space mission in preparation for their participation in the ISS. For the MFD mission, the robotic arm mounted in the payload bay was controlled from the shuttle flight deck. The change-out of an Orbital Replacement Unit (ORU) was demonstrated, along with other tasks such as the opening and closing of a door with the manipulator. In addition, a successful test was made of tele-operation technologies to command the arm from the ground, consisting of a command sequence uploaded from the ground and executed by the manipulator.

Unlike the collaborative MFD mission the ETS-VII Flight Experiment was exclusively Japanese, and a fully robotic mission [167]. Designed to test technologies to be used in the development of the H-II Transfer Vehicle (HTV) for the ISS, the ETS-VII mission completed a number of demonstrations including the fully autonomous rendezvous and docking (RVD) with a secondary vehicle, and the use of a robotic manipulator system controlled from the ground. The RVD experiment was made by detaching a small target satellite (named Orihime) from the main chaser (Hikoboshi), which then rendezvoused and re-docked with Orihime. Remotely controlled docking from the ground was also performed in order to compare the performance of autonomous RVD techniques. The ground controlled tests carried out on the Shuttle during the MFD mission were then extended for the robotics phase of the ETS-VII experiment, allowing the remotely controlled manipulator to carry out the intricate equipment exchange tests previously controlled by the astronauts onboard the Shuttle. Similarly the robot arm was also used to successfully demonstrate the remote assembly of an antenna and a truss structure.

Other projects that have been developed through the Japanese space agency include a planetary surface rover designed and manufactured at the Tokyo Institute of Technology. Based on an unusual symmetric 3 wheeled collapsible design, the rover offers improved ground clearance to traverse rocky terrain while still giving a compact stored footprint for transportation. Software has also been developed to assist in the tele-operation of such an explorer, to overcome the problems of human control with a time delay (~6 sec) for example in the exploration of the lunar surface. The final area of focus has been in research into the technologies required for on-orbit servicing of satellites, such as techniques for the capture of a non co-operative satellite and dexterous manipulators to carry out maintenance tasks.

Terrestrial Robots

Away from the space based projects and experiments of orbital robotics and planetary exploration, a number of terrestrial free-flying (and free-floating) autonomous vehicles have been developed which have a distinct similarity to orbital free-flying inspection vehicles. The similarities are not just in the goal applications of such vehicles to make visual inspections of a target, but significantly in the technologies required such as visual and GPS navigation systems, path planning and route following, obstacle avoidance, and autonomous vehicle control. One of the major drivers for the development of such vehicles has been from robotics competitions aimed to stimulate advances in the field. In particular, as a result of the Association for Unmanned Vehicle Systems - Aerial Robotics Competition, a large number of autonomous free-flying helicopter type vehicles have been developed to fulfil the competition objectives of autonomously mapping an area of terrain, and finding and retrieving a small target disk from the area. The winner of the 1997 competition was the Autonomous Helicopter from the Carnegie-Mellon University which will be discussed in detail later in this section. In the commercial arena, a great deal of development has gone into the field of autonomous subsea vehicles, both in the lucrative and hazardous oil industry, as well as underwater exploration. With an underwater environment as dangerous for humans as space resulting in high costs of exploration, subsea robots are driven by similar economics to the development of robotics in space.

C.M.U. Autonomous Helicopter Project

The development of the Autonomous Helicopter Project at Carnegie-Mellon University began in 1991 with the construction of an indoor test bed to examine the attitude control system that would be required for an autonomous helicopter. From this first electric helicopter experiment mounted on a swivelling platform, the project has grown into a fully autonomous free-flying helicopter [168]. The goal of the project was to develop a vision guided helicopter capable of fully autonomous operation, using only sensors and capabilities available onboard. To achieve this, the helicopter should be able to autonomously perform such tasks as takeoff and landing, flying a prescribed path, systematic search and location of a target, target tracking and following, and autonomous return to base.

In order to fulfil the goal capabilities for the project, a number of key technologies have been developed by the Autonomous Helicopter group at Carnegie-Mellon University, which have applications for space robots. To be able to accurately pilot and control a free-flying vehicle such as a helicopter, accurate measurements of the vehicle state in terms of accelerations and rates as well as position and attitude must be available. In the case of the

Autonomous Helicopter this has been achieved using conventional solid state inertial sensors to measure accelerations and angular rates, coupled with GPS data for the position and translational velocities. In addition, positional and translational rate information can also be obtained from visual tracking sensors below the helicopter, which track features on the terrain below providing, with the addition of a magnetic compass, a self reliant backup in the event of loss of GPS information. This visual tracking technology could be useful for orbital inspection applications if it can be extended to work with three dimensional solid targets. Three dimensional visual tracking may enable accurate position information to be obtained for a free-flying inspection vehicle, with respect to the ISS for example. Another key technology for the Autonomous Helicopter Project is pattern recognition and target tracking software developed to enable the helicopter to search for specific objects and track objects, enabling the helicopter to maintain its heading towards a target and follow moving targets. This kind of capability would have useful applications for a space-based robot for guiding the vehicle to a docking port, or pointing an inspection camera in the direction of a specific target point for example. Target tracking could also enable additional applications such as the slaving of an inspection robot to follow an astronaut's movement. The main application of the Autonomous Helicopter so far has been for aerial mapping missions using another new sensor, a scanning laser rangefinder linked to the control system state estimator to provide accurate detail of the terrain below as the helicopter flies above [169]. The accuracy of the results is only made possible by the high accuracy of the state information synchronised to the laser range results, and the relatively low altitude that the helicopter is capable of flying.

Subsea Robots

While the primary impetus for the development of aeronautical autonomous vehicles has been from robotics competitions and academic research, subsea robotic research has been driven to a large extent by the range of possible applications of such vehicles. One example of this is the range of Autonomous Underwater Vehicles (AUV's) developed by the Canadian company International Submarine Engineering Ltd. Their products range from the 6.5 meter underwater hydrographic survey vehicle ARCS, which was completed in 1986 and operated by the Department of National Defence - Canada for AUV research, to the huge 10.7 m long Theseus AUV, developed to autonomously lay fibre optic cables underneath the Arctic ice pack. Capable of supporting a configurable payload of nearly 2000 kg (wet) to a depth of 1000 m and a range of 750 km, Theseus successfully demonstrated its abilities by laying 190 km of cable under the ice during trials in 1996 [170].

A number of robotic underwater vehicles are also operated by the Woods Hole Oceanographic Institute in Massachusetts, to support their research ships, towed instruments, and manned submersible. Amongst these is the Remotely Operated Vehicle (ROV) Jason [171] which is operated, similarly to many space robots, by a pilot on the surface. Equipped with multiple CCD video cameras and a still camera, Jason is able to provide imaging capabilities down to a depth of 6000 m. Jason however requires continuous human control and is physically linked by a tether to the operating ship on the surface, making it unsuitable for long term underwater monitoring. For this purpose the Autonomous Benthic Explorer (ABE) was developed [172]. This fully autonomous vehicle is capable of following a set of commands without any contact from the surface, and by entering a sleep mode at a docking station in between excursions can remain underwater on a mission for up to a year.

As well as these commercial and scientific developments of AUV's, competitions such as the Annual International Autonomous Underwater Vehicle Contest are also beginning to be held following the aerospace example. The winner of the first year of this competition in 1998 was ORCA-1 developed by a team at the Massachusetts Institute of Technology (MIT) [173]. This 1.4 m long, 48 kg underwater vehicle was built for only \$5000 using many 'off the shelf' components to accomplish its goal of negotiating the competition gates of the course at the US Naval Coastal Systems Station in Florida. The systems used were similar in many ways to those that might be utilised in a space inspector type vehicle, such as accelerometers and gyroscopes for navigation, backed up by additional instruments to reset sensor drift. ORCA-1 also included two arrays of sonar transducers for obstacle/landmark detection, which could then also be used for navigation and obstacle avoidance. During the course of the competition, the AUV managed to successfully navigate its way through two of the control gates to win the competition.

Current Development Projects

With the assembly of the International Space Station already in progress, a number of vehicles are currently in development with the aim of providing free-flying robotic services to the completed station. These range from the competing free-flying external inspection vehicles of the ISS Inspector and AERCam II, to the Personal Satellite Assistant designed to support astronauts inside the space station. In 1998 collaborative work was undertaken between the University of Glasgow and the developers of the Inspector project EADS Astrium in Bremen, Germany, which resulted in the development of a number of mission planning tools for the Inspector project which are the subject of this thesis. We will therefore concentrate mainly on the Inspector mission, although these tools and techniques are also

applicable to other vehicles, in particular the NASA developed AERCam which bears many similarities to Inspector.

ISS – Inspector

Following the success of the X-Mir Inspector demonstration mission in 1997 discussed in section 0, the next step in the Inspector project was to design a new generation of Inspector vehicle to operate at the International Space Station - the ISS Inspector [174]. This new Inspector was to be greatly enhanced from the original X-Mir Inspector, possessing increased manoeuvrability and payload capacity along with the fault tolerance required to operate at the new manned space station. In addition, the ISS Inspector will be based at a docking station on the ISS itself, allowing it to be recharged and refuelled between missions.

In 1996 the original concept for the ISS Inspector project was submitted by a partnership of RSC-Energia (Russia), Dasa (Germany), and Boeing (USA) as a proposal to the NASA Advanced Engineering and Technology Demonstration (AETD) program, for which it was selected to provide observation and inspection capabilities for the ISS. The AETD program was later cancelled, becoming the Pre-Planned Program Improvement (P³I) of which Inspector was still a part, though the future of this is also now in doubt. Phase A of the ISS Inspector project, defining the mission and system requirements and initial system design, was however completed under funding from the German space agency DLR. It was during this phase that a number of the tools presented in this thesis were developed in conjunction with Dasa, and it is the mission concepts developed in this phase on which a large part of the work presented is based. In 1998 it was proposed by DLR to join the Inspector project with the DLR funded Experimental Servicing Satellite (ESS) study. The objective of the ESS study was to demonstrate the servicing and repair of satellites in geostationary (GEO) orbits. Consequently the fusion of the two projects would enable the baseline requirements of the Inspector mission for a free-flying inspection vehicle, to become the foundation for enhanced robotic manipulation capabilities in later phases of the project.

The ISS Inspector project development can be broken down into 3 distinct stages, shown in Figure II-5. The first step is essentially the original Inspector, a free-flying vehicle based at the ISS with onboard inspection capabilities from video cameras and other sensors. Following on from that is the Visitor vehicle, an extension of Inspector with the capability to support additional payloads loaded at the ISS, and retreat away from the interference and disturbances of the space station. Finally there is the Operator vehicle, equipped with robotic manipulators enabling repair and servicing tasks. The final two stages are however only at the initial concept stage, so we will concentrate on the original ISS Inspector.

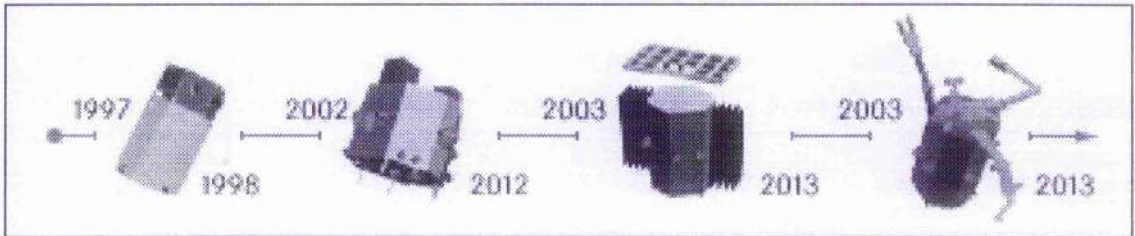


Figure II-5 The Inspector Product Family (source: EADS Astrium)

Unlike the X-Mir Inspector which was launched from the unmanned expendable Progress-M vehicle, and never manoeuvred close to the Mir space station, the ISS Inspector will be based at the International Space Station and will perform the majority of its operations within the 200m safety zone of the station. The project must therefore comply with all the NASA safety standards for manned space flight, which are far more stringent than for missions where human lives are not involved, as well as additional safety restrictions specific to the ISS. Furthermore, Inspector will also require RVD capabilities, similar to those of unmanned supply vehicles such as Progress-M and the ATV, to dock with its service port on the ISS. And finally, the vehicle must also be able to support a range of inspection payloads such as visual and infrared cameras, thermal imaging equipment, and possibly spotlights to extend inspection opportunities and support astronaut EVA's.

In order to satisfy the safety requirements for a free-flying vehicle operating at the ISS, the Inspector safety concept must rely on a number of layers of protection. At a hardware level the Inspector systems must be designed so that all critical systems, such as the propulsion system and the guidance, navigation and control (GNC) system are 2-fault tolerant. Then no combination of 2 failures in either system can result in hazardous consequences to the station. Also, the mission planning software must ensure that at all times the vehicle is travelling on the safest possible trajectory to reach its goals. This can be achieved by ensuring that the free-flyer is on passive safe trajectories where ever possible. The techniques used to ensure mission safety will be discussed extensively later in this thesis. However, Figure II-6 shows an early mission plan using EOS trajectories and forced motion transfers to perform an inspection of the ISS.

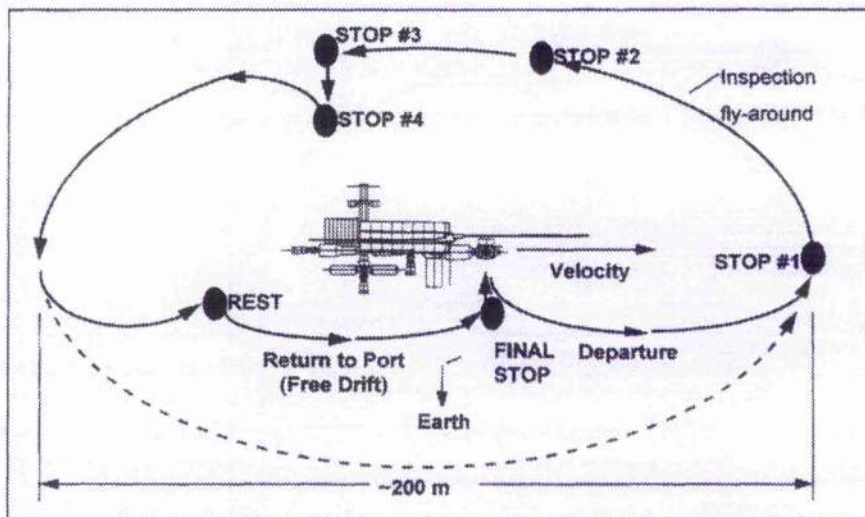


Figure II-6 ISS Inspector Preliminary Mission Concept (source: EADS Astrium)

NASA AERCam

The Autonomous Extra-vehicular Robotic Camera (AERCam) [175] developed by NASA has been a competitor to the ISS Inspector since both projects began. Also designed to provide camera views of the International Space Station and the Space Shuttle to the astronauts on board and controllers on the ground, the second generation of both vehicles look mechanically rather similar.

The first generation of AERCam was demonstrated by AERCam Sprint on a Shuttle mission in December 1997. Sprint was a small 14" diameter sphere, covered in a layer of felt to cushion any accidental impacts, as shown in Figure II-7. The free flying vehicle was controlled directly by an astronaut from the aft flight deck of the Shuttle using two PC's and a joystick in a similar way to the SRMS, and possessed only minimal autonomy. In fact many of the Sprint systems, including the thrusters, basic avionics, and hand controller, were adapted from the EVA rescue backpack used by astronauts for free-floating space walks. Sprint successfully demonstrated its control from the Shuttle, and the use of its two onboard micro-cameras to make inspections of the Shuttle during its 30 minute flight in the Shuttle cargo bay.

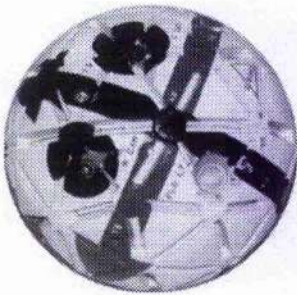


Figure II-7 AERCam Sprint (source: NASA)

The next generation vehicle, AERCam II, is now under development at the NASA Johnson Space Center. AERCam II will provide a much greater degree of autonomy than Sprint through the use of a three tiered control software architecture known as 3T. This divides software tasks to control AERCam into three levels;

Hardware skills enabling the software to directly perform task elements, such as moving to a specific position or tracking an object.

Sequencing abilities to build complex tasks from individual skills, for example to plan a path using multiple manoeuvres and obstacle avoidance skills.

High level planning capabilities to organise tasks and plan missions within constraints such as time and resources.

One of the most important hardware skills is the ability for the free-flyer to control its movement in the ISS environment. This is handled by the Motion Control System (MCS) which encapsulates navigation and control functions to support basic manoeuvres such as moving to a specific co-ordinate location, and station keeping at a point. In addition, the use of stereo vision has also been developed for the AERCam project, using stereo imaging cameras to provide tracking skills for the vehicle. This allows AERCam to track an object and determine its location relative to the camera, enabling the free-flyer to maintain a fixed distance and heading relative to, for example, a moving astronaut on EVA outside the station. Path planning software is also under development for the AERCam project [39], using a technique known as the Generalised Voronoi Diagram (GVD) and 3-dimensional Generalised Voronoi Graph, to construct a geometric roadmap to travel between any two points. These path planning techniques will be looked at in detail later in Chapter 3. The 3T control architecture will be deployed via a user interface running on a PC either onboard the ISS or on the ground. The user interface displays both the status and results from AERCam, and allows the user to both directly control and issue commands to the free-flyer with a joystick and keyboard, or to plan missions and tasks to be executed autonomously by the vehicle.

NASA Personal Satellite Assistant

In contrast to the relatively large external space vehicles Inspector and AERCam, the Personal Satellite Assistant (PSA) [176] is designed to be a highly miniaturised helper inside the space station. Using the atmosphere inside the station to propel itself with tiny ducted fans, the small ball shaped robot could rove around the ISS interior supporting astronauts by responding to voice commands, or be commanded by observers on the ground to monitor operations onboard the station. Furthermore, the PSA, wirelessly connected to the ISS network, is planned to house a small video screen to display information for the astronauts, along with a camera, microphone and speaker enabling two way video communications with the ground. In the event of an accident the PSA could be sent into damaged or dangerous parts of the station to check for damage and detect hazards such as smoke or gas with its onboard sensors. While only in the first stages of development, the PSA project gives an impression of what may be possible in the future of robotics and human spaceflight.

APPENDIX III: THE CLOHESSEY WILTSHERE EQUATIONS

Non-linear Equations of Motion

The first step in developing the equations of motion for the free-flyer in a co-ordinate system attached to the International Space Station is to transform all the relevant forces and position vectors into the ISS reference frame, as shown in Figure III-1.

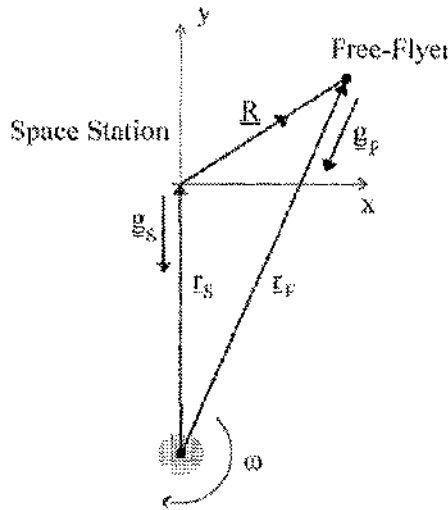


Figure III-1 Frames of reference for relative motion

We can write down all the vector quantities shown in the rotating ISS reference frame

$$\begin{aligned}
 \underline{r}_s &= [0 \quad |r_s| \quad 0]^T \\
 \underline{R} &= [x \quad y \quad z]^T \\
 \text{Eqn III-1} \quad \underline{\omega} &= [0 \quad 0 \quad -|\underline{\omega}|]^T \\
 \underline{g}_s &= [0 \quad -|\underline{g}_s| \quad 0]^T \\
 \underline{g}_F &= [|\underline{g}_F| l_1 \quad |\underline{g}_F| l_2 \quad |\underline{g}_F| l_3]^T
 \end{aligned}$$

where \underline{r}_s is the orbit radius vector of the station, \underline{R} is the relative position of the free-flyer, $\underline{\omega}$ is the orbital angular velocity vector of the station, and \underline{g}_s and \underline{g}_F are the gravitational force vectors of the station and free-flyer respectively.

The orbit radius vector of the free-flyer \underline{r}_F is given by

$$\text{Eqn III-2} \quad \underline{r}_F = \underline{r}_s + \underline{R}$$

and l_1 , l_2 , and l_3 are the components of \underline{g}_F along the ISS frame x, y, z axes, given by

$$\text{Eqn III-3} \quad l_1 = -\frac{x}{|\underline{r}_F|}$$

$$l_2 = -\frac{|\underline{r}_s| + y}{|\underline{r}_F|}$$

$$l_3 = -\frac{z}{|\underline{r}_F|}$$

Newton's Second Law can now be applied to the free-flyer, in the ISS frame to obtain

$$\text{Eqn III-4} \quad m_F \frac{d^2 \underline{r}_F}{dt^2} \Big|_{xyz} = m_F \underline{g}_F + \sum_i \underline{f}_{F_i}$$

where the summation term $\sum_i \underline{f}_{F_i}$ represents all the external forces, with the exception of gravity, acting on the respective vehicles. This includes all disturbance forces such as atmospheric drag, as well as applied manoeuvring forces in the case of the free-flyer.

Similarly, Newton's second law can be written for the ISS

$$\text{Eqn III-5} \quad m_s \frac{d^2 \underline{r}_s}{dt^2} \Big|_{xyz} = m_s \underline{g}_s + \sum_i \underline{f}_{s_i}$$

Using the rules of differentiation of vectors, in a rotation frame of reference, the left hand side of Eqn III-4 and Eqn III-5 can be expanded as

$$\text{Eqn III-6} \quad \frac{d^2 \underline{r}_F}{dt^2} \Big|_{xyz} = \ddot{\underline{r}}_F + 2(\underline{\omega} \times \dot{\underline{r}}_F) + \dot{\underline{\omega}} \times \underline{r}_F + \underline{\omega} \times (\underline{\omega} \times \underline{r}_F)$$

and

$$\text{Eqn III-7} \quad \frac{d^2 \underline{r}_s}{dt^2} \Big|_{xyz} = \ddot{\underline{r}}_s + 2(\underline{\omega} \times \dot{\underline{r}}_s) + \dot{\underline{\omega}} \times \underline{r}_s + \underline{\omega} \times (\underline{\omega} \times \underline{r}_s)$$

Substituting Eqn III-2 for \underline{g}_P in Eqn III-6 then gives

$$\text{Eqn III-8} \quad \frac{d^2 \underline{r}_F}{dt^2} \Big|_{xyz} = \ddot{\underline{r}}_s + \ddot{\underline{R}} + 2(\underline{\omega} \times \dot{\underline{r}}_s + \underline{\omega} \times \ddot{\underline{R}}) + \dot{\underline{\omega}} \times \underline{r}_s + \dot{\underline{\omega}} \times \ddot{\underline{R}}$$

$$+ \underline{\omega} \times (\underline{\omega} \times \underline{r}_s) + \underline{\omega} \times (\underline{\omega} \times \ddot{\underline{R}})$$

Now, from Eqn III-2 we have $\underline{R} = \underline{r}_F - \underline{r}_s$, so that

$$\text{Eqn III-9} \quad \frac{d^2 \underline{R}}{dt^2} \Big|_{XYZ} = \frac{d^2 \underline{L}_F}{dt^2} \Big|_{XYZ} - \frac{d^2 \underline{r}_S}{dt^2} \Big|_{XYZ}$$

And from Eqn III-4 and Eqn III-5

$$\text{Eqn III-10} \quad \frac{d^2 \underline{r}_F}{dt^2} \Big|_{XYZ} - \frac{d^2 \underline{r}_S}{dt^2} \Big|_{XYZ} = \underline{g}_F - \underline{g}_S + \frac{1}{m_F} \sum_i \underline{f}_{F_i} - \frac{1}{m_S} \sum_j \underline{f}_{S_j}$$

Finally, substituting Eqn III-7 and Eqn III-8 into Eqn III-10, gives the vector form of the equations of relative motion for the free-flyer

$$\text{Eqn III-11} \quad \ddot{\underline{R}} + 2(\underline{\omega} \times \dot{\underline{R}}) + (\dot{\underline{\omega}} \times \underline{R}) + \underline{\omega} \times (\underline{\omega} \times \underline{R}) \\ = \underline{g}_F - \underline{g}_S + \frac{1}{m_F} \sum_i \underline{f}_{F_i} - \frac{1}{m_S} \sum_j \underline{f}_{S_j}$$

The vector cross product terms can be expanded as

$$\text{Eqn III-12} \quad \begin{aligned} \dot{\underline{\omega}} \times \underline{R} &= [\underline{\omega} y, -\underline{\omega} x, 0]^T \\ \underline{\omega} \times \dot{\underline{R}} &= [\underline{\omega} \dot{y}, -\underline{\omega} \dot{x}, 0]^T \\ \underline{\omega} \times (\underline{\omega} \times \underline{R}) &= [-\underline{\omega}^2 x, -\underline{\omega}^2 y, 0]^T \end{aligned}$$

and the two summations of disturbance forces can be represented by the total difference in applied force to the free-flyer $\underline{f}_F = \frac{1}{m_F} \sum_i \underline{f}_{F_i} - \frac{1}{m_S} \sum_j \underline{f}_{S_j}$, given in component form by

$$\text{Eqn III-13} \quad \underline{f}_F = [f_x \quad f_y \quad f_z]^T$$

Substituting Eqn III-12 and Eqn III-13 into Eqn III-11, and writing the result in component form gives

$$\text{Eqn III-14} \quad \begin{aligned} \ddot{x} + 2\omega\dot{y} - \dot{\omega}y - \omega^2 x &= |\underline{g}_F| l_1 + f_x \\ \ddot{y} - 2\omega\dot{x} - \dot{\omega}x - \omega^2 y &= |\underline{g}_F| l_2 + |\underline{g}_S| + f_y \\ \ddot{z} &= |\underline{g}_F| l_3 + f_z \end{aligned}$$

Finally, Eqn III-14 may be rearranged to give the more common form of the equations

$$\text{Eqn III-15} \quad \begin{aligned} \ddot{x} &= -2\omega\dot{y} - \dot{\omega}y + \omega^2 x + |\underline{g}_F| l_1 + f_x \\ \ddot{y} &= 2\omega\dot{x} + \dot{\omega}x + \omega^2 y + |\underline{g}_F| l_2 + |\underline{g}_S| + f_y \\ \ddot{z} &= |\underline{g}_F| l_3 + f_z \end{aligned}$$

These equations represent the inertial acceleration of the free-flyer, resolved along the axes of the ISS co-ordinate system. However the equations are non-linear, and can only be used to solve for the free-flyer motion by numerical methods. They cannot be easily manipulated further to derive equations to predict and plan trajectories in this orbital co-ordinate frame.

Linearised Equations of Motion – The Clohessy Wiltshire Equations

To make the equations of motion easier to use, they may be simplified based on the assumption that the space station is on a circular orbit, and approximated since the distance between it and the free-flyer is relatively small compared to its orbital radius.

From the laws of gravitation it is clear that

$$\underline{g}_F \|\underline{r}_F\|^2 = \underline{g}_S \|\underline{r}_S\|^2$$

Eqn III-16

$$\Rightarrow |\underline{g}_F| = \frac{|\underline{g}_S| \|\underline{r}_S\|^2}{\|\underline{r}_F\|^2}$$

In addition, from Eqn III-2 it can be seen that

$$\begin{aligned} \underline{r}_F &= \underline{r}_S + \underline{R} = [x - (y + |\underline{r}_S|) \quad z]^T \\ \Rightarrow |\underline{r}_F| &= (x^2 + y^2 + 2y|\underline{r}_S| + |\underline{r}_S|^2 + z^2)^{\frac{1}{2}} \\ \text{Eqn III-17} \quad |\underline{r}_F| &\approx (2y|\underline{r}_S| + |\underline{r}_S|^2)^{\frac{1}{2}} \\ \Rightarrow |\underline{r}_F| &\approx |\underline{r}_S| \left(1 + \frac{2y}{|\underline{r}_S|}\right)^{\frac{1}{2}} \end{aligned}$$

which through a binomial expansion may be reduced to

$$\text{Eqn III-18} \quad |\underline{r}_F| \approx |\underline{r}_S| \left(1 + \frac{y}{|\underline{r}_S|}\right)$$

Substituting Eqn III-17 into Eqn III-16 gives

$$\text{Eqn III-19} \quad |\underline{g}_F| = \frac{|\underline{g}_S| \|\underline{r}_S\|^2}{|\underline{r}_S|^2 \left(1 + \frac{2y}{|\underline{r}_S|}\right)}$$

and by another binomial expansion

$$\text{Eqn III-20} \quad |\underline{g}_F| \approx |\underline{g}_S| \left(1 - \frac{2y}{|\underline{r}_S|}\right)$$

Now, using the definition of l_2 given in Eqn III-3 the y component of the gravitational force may be written as

$$\text{Eqn III-21} \quad |\underline{g}_F| l_2 + |\underline{g}_S| = -|\underline{g}_S| \frac{|\underline{r}_S| + y}{|\underline{r}_F|} + |\underline{g}_S|$$

which by substituting Eqn III-18 and Eqn III-20 becomes

$$\begin{aligned} \text{Eqn III-22} \quad |\underline{g}_F| l_2 + |\underline{g}_S| &\approx -|\underline{g}_S| \left(1 - \frac{2y}{|\underline{r}_S|} \right) \left(\frac{|\underline{r}_S| + y}{|\underline{r}_S| \left(1 + \frac{y}{|\underline{r}_S|} \right)} \right) + |\underline{g}_S| \\ &\approx -|\underline{g}_S| \left(1 - \frac{2y}{|\underline{r}_S|} \right) \left(\frac{\left(1 + \frac{y}{|\underline{r}_S|} \right)}{\left(1 + \frac{y}{|\underline{r}_S|} \right)} \right) + |\underline{g}_S| \\ \Rightarrow \quad |\underline{g}_F| l_2 + |\underline{g}_S| &\approx |\underline{g}_S| \frac{2y}{|\underline{r}_S|} \end{aligned}$$

Since the deviation in the x-z plane is small for proximity operations, the x and y components of gravitational force can be approximated by

$$\begin{aligned} \text{Eqn III-23} \quad |\underline{g}_F| l_1 &= -|\underline{g}_F| \frac{x}{|\underline{r}_F|} \approx -|\underline{g}_S| \frac{x}{|\underline{r}_S|} \\ |\underline{g}_F| l_2 &= -|\underline{g}_F| \frac{z}{|\underline{r}_F|} \approx -|\underline{g}_S| \frac{z}{|\underline{r}_S|} \end{aligned}$$

Finally, substituting Eqn III-22 and Eqn III-23 into the non-linear equations (Eqn III-15), and

noting that for a circular orbit $|\dot{\omega}| = 0$ and $|\omega|^2 = \frac{|\underline{g}_S|}{|\underline{r}_S|}$ produces

$$\begin{aligned} \ddot{x} &= -2\omega\dot{y} + f_x \\ \text{Eqn III-24} \quad \ddot{y} &= 2\omega\dot{x} + 3\omega^2 y + f_y \\ \ddot{z} &= -\omega^2 z + f_z \end{aligned}$$

These equations are known as the Clohessy Wiltshire (CW) Equations [103], regardless of the frame of reference in which they have been obtained.

APPENDIX IV: THE ISS INSPECTOR HARDWARE SYSTEM

The Inspector Free-Flyer, with its associated support systems, is planned to be launched by the Shuttle STS to the ISS during the latter construction phase of the space station. From then it will be permanently based at the ISS to fulfil an inspection and EVA support role in addition to documenting the later stages of station assembly. This role, defined under the NASA Pre-Planned Program Improvement (P³I), outlines the primary capabilities of Inspector for the visual and non-visual inspection of the ISS and its associated structures, using both visual video and stills cameras, and optional environmental monitoring payloads such as infra-red cameras and radiation detectors. In addition, the Inspector Free-Flyer must be capable of providing visual support and monitoring for a full astronaut EVA mission, which is clearly vital for the assembly of the space station.

As a free-flying payload platform, future Inspector vehicles should also be capable of supporting modular payloads, exchangeable by the space station remote manipulator system (SSRMS) while the free-flyer is docked at the station. Third party scientific payloads could then be flown on the Inspector Free-Flyer, away from the ISS to provide a disturbance free micro-gravity environment, coupled with easy access to space and return capabilities provided by docking with the space station. Finally, though outside of the scope of this thesis, Inspector must support future robotic payloads for the demonstration of robotic missions such as remote on-orbit maintenance and repair operations, to open up future markets for robotic satellite servicing [5].

Vehicle Capabilities

The physical design of the Inspector Free-Flyer to satisfy all the mission requirements has resulted in an octagonal shape with the inspection cameras and payload mounted on the upper face. The propulsion system consists of 16 cold-gas thrusters mounted in 4 clusters on 4 of the 8 faces of the vehicle, as shown in Figure IV-1. This design provides full six-degree-of-freedom manoeuvrability, whilst retaining failsafe control over the vehicle in case of any two thruster failures. Also, due to this layout the available thrust direction can be assumed to be independent of the vehicle attitude allowing, for the purposes of path planning, translational control to be separated from attitude control.

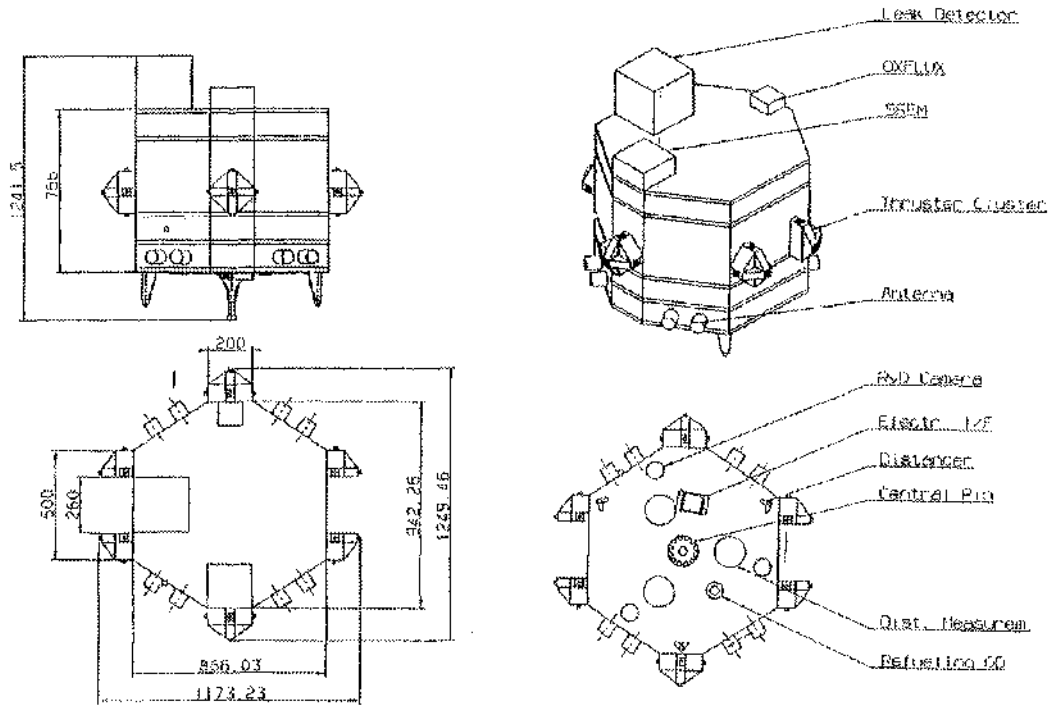


Figure IV-1 Inspector Free-Flyer Configuration (source: EADS Astrium)

The planned duration of an Inspector mission is up to 10 hrs of continuous operation, enabling the support of a maximum 7 hr astronaut EVA mission plus transfer to and from the observation position. Retreat to a safe holding point away from the ISS for several weeks is also a requirement in the event that the Inspector Free-Flyer is prevented from returning to docking. Whilst at this safe hold point, the free-flyer will operate in a power-saving hibernation mode until it can return to the station. To fulfil these requirements the Inspector Free-Flyer must therefore have sufficient electrical power and ΔV capacity to transfer between any point on the ISS and station-keep for the duration of a 7 hr observation phase, plus additional capacity to safely retreat from the station and hibernate before returning to docking.

For the baseline Inspector configuration shown in Figure IV-1, with a mass of approximately 210 kg, a fuel tank holding 4 kg of nitrogen provides a minimum overall ΔV capability of 10 ms^{-1} for each mission. Power is provided by rechargeable NiH_2 batteries giving an available capacity of 2300 Wh, and solar cells which can power Inspector indefinitely whilst in low-power hibernation mode. The batteries and solar cells provide a combined 10.9 hrs operating time during observation. Given these limitations, the planning of each individual mission must therefore be constrained within the available time, ΔV , and power budget, with the aim of providing the maximum level of safety and observation time within these limits.

Docking and Berthing

Rather than docking directly with the ISS, Inspector will have its own docking port mounted on the station, both to provide a base for Inspector operations, and to re-supply the vehicle with power and propellant between missions. The docking port is designed to fit onto two standard Express Pallet adapters, allowing mounting at a range of locations on the main ISS hull and truss structure, and also providing standard mechanical, data, and power connections with the space station. Also, the docking port will provide a communications node for the Inspector Free-Flyer, reducing dependency on the available ISS systems. For the initial ISS-Inspector the baseline location for the docking port is on the European Columbus Orbital Facility (COF) module, and it is this location that is used to drive the planned docking release and return strategies. The COF docking location utilises the planned ‘flower-box’ mounting platform on the end of the module, simplifying the integration of the European Inspector project into the multinational space station through the use of European module systems.

Between missions, Inspector will remain attached to the docking port, where it can be refuelled from the port propellant tanks shown in Figure IV-2. Also, the vehicle batteries can be charged from the space station power supply, and any required servicing or payload replacement can be carried out via the station robotic arm. Once serviced, the Inspector Free-Flyer is then de-activated and lowered into its storage position inside the docking port, shown below, where it remains protected from the space environment until required for the next mission.

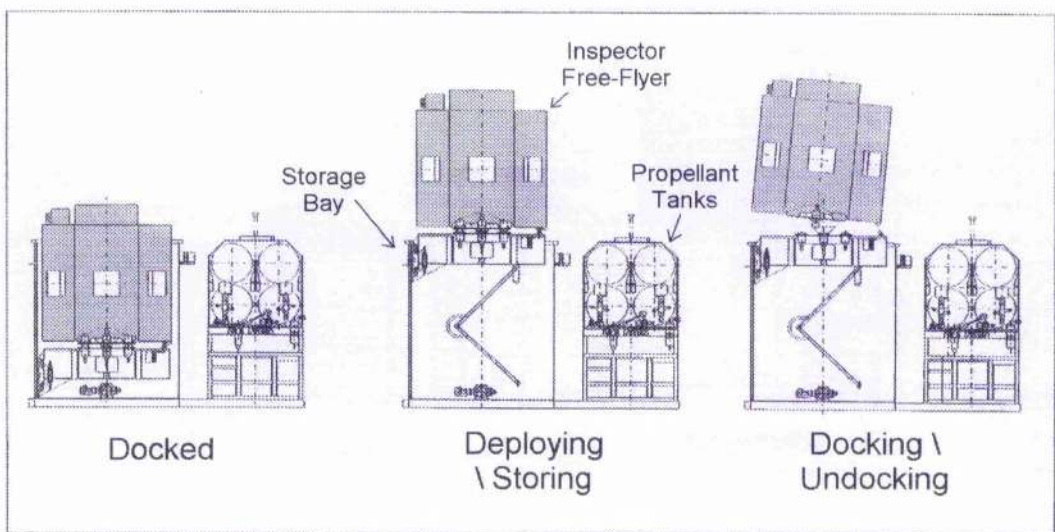


Figure IV-2 The Inspector Docking Port (source: EADS Astrium)

The free-flyer approach to the docking port is carried out using a forced motion manoeuvre along the R-bar, detailed in section 3.1.2. The main distinction between the approach to an observation point and the docking manoeuvre is the increased navigation accuracy required for the final stage of the rendezvous with the docking adapter. To overcome this, and to simplify automation of the docking approach, a docking specific navigation system is used. This consists of a laser range-finder and two black and white optical video cameras mounted on Inspector, and a custom target pattern on the docking port. The video cameras are used to track the target pattern, enabling the free-flyer to stay on path along the R-bar, while the laser provides accurate range and range-rate data.

Alternatively, it may be necessary for Inspector to berth with the ISS via the SSRMS rather than performing a hard dock with the station. This strategy requires that the free-flyer approach the station as normal, into a defined berthing box, and then remain within the pre-defined inner capture box for a period of time to allow capture by the SSRMS. Berthing simplifies the Inspector design, since the free-flyer plays an essentially passive role in the capture. However, the procedure is not automated, requiring an operator onboard the ISS to control the robotic arm and increasing the operational cost of Inspector to the ISS. Moreover, in the absence of the target pattern on the docking port, navigation accuracy in the berthing box may be problematic, making docking to the Inspector port the preferred option.

Navigation

Further away from the space station structure, navigation data is available to Inspector from the ISS Relative GPS (RGPS) system [125]. This system, developed for visiting vehicles such as ATV and the Shuttle, will provide positional data with an expected accuracy of 0.025m at 100 m from the ISS. Closer to the space station however, RGPS data will become corrupted due to signal interference and shadowing caused by the ISS structure. For Inspector therefore, an alternative method of navigation is required for the observation phase of the mission since this is planned to take place close (10~40 m) to the station.

The X-Mir Inspector made use of a visual navigation system through its observation cameras, which may be enhanced for use at the ISS. However, currently this system requires the station reference points to be manually selected from the visual data, resulting in a very high workload for the operator onboard the ISS, combined with a slow update interval of the order 1-2 minutes which is too long for close proximity manoeuvring. Furthermore, the additional use of inspection video cameras for navigation will limit inspection camera pointing and zoom by the need to keep a sufficient viewing angle of the station in frame for navigation. The future of automated visual navigation is still under development in many fields where

navigation availability is limited, such as for autonomous underwater vehicles [177]. The possibilities offered by high quality visual navigation have already been demonstrated operationally by such projects as the CMU Autonomous Helicopter discussed in Chapter 1. The prior knowledge available of the ISS structure about which the Inspector Free-Flyer operates, coupled with good visibility, unobscured by liquid, gas or constant vibration should make Inspector an ideal future application for these emerging technologies.

The current baseline navigation concept developed for the Inspector Free-Flyer, requires the use of more proven technologies, using a single laser range-finder pointed at specific target points marked on the ISS surface to derive navigation data. Given attitude data for Inspector obtained independently, and the ISS attitude, the Inspector position and velocity can be determined from the laser range and range-rate data. ISS attitude data is available at all times through the station navigation systems, while the Inspector attitude system consists of laser rate gyros, updated periodically with a star camera. The technologies required for this laser navigation system, including the visual tracking of the target points to enable the laser to point at fixed position, have already been well developed, resulting in a less ambitious, more proven concept than a completely visual navigation system. The main limitation is in requiring the Inspector vehicle to point in a fixed direction toward the target points, though this can be solved by an independently mounted laser and tracking camera.

Communications and Data Links

The communications links between the Inspector Free-Flyer and the ISS are vital not only for the telemetry and telecommand (TM/TC) link required to monitor and control Inspector, but also to receive data from the inspection cameras and other instruments. Since Inspector will be controlled primarily from the ground with backup control on the ISS, and has only limited onboard control software, the two-way TM/TC connection will be utilised continuously throughout a mission though the data rates required will be relatively small for the telemetric data. Conversely, the video and camera data link will only be required during the observation phase of a mission, but requires a high bandwidth connection to transmit data intensive imaging to the ISS. Two separate radio connections are therefore planned for Inspector communications:

UHF-Band TM/TC connection	- 20 kbps, bi-directional
S-Band Video/Imaging connection	- 2 Mbps, uni-directional

The UHF-Band supplies a low data rate, but its relatively long wavelength is capable of passing through most of the ISS structure with minimal interference, supplying a continuous link. The S-Band transmission, whilst providing a high data rate is easily masked by the ISS

structure, restricting coverage to areas with a direct line-of-sight link to the S-Band antenna mounted on the station. The placement of the Inspector communications antennae will therefore have an impact on the planning of a mission, since the S-Band link is necessary at the observation point to complete the inspection objectives.

Communications with the ground station are supplied through the ISS via the Tracking and Data Relay Satellite System (TDRSS), along with all ISS ground communications. With a total available data rate of 50 Mbps shared with a range of other applications, and an estimated 70% minimum ground coverage, the ground control strategy must take into account the limited bandwidth and plan for possible breaks in transmissions during a mission. In addition, a transmission delay of up to 5 seconds between the station and ground is expected, though the whole ISS communications system is under review, in view of the increasing data requirements for recent station utilisation proposals [178].

Control Architecture

Unlike the X-Mir Inspector which was controlled by a cosmonaut onboard the Mir space station, the primary control method for the ISS-Inspector will be from the ground, to reduce the workload on the ISS astronauts. For the X-Mir Inspector, on-orbit control was necessitated by infrequent ground communications coverage, and the required cosmonaut time was justified for the one-off demonstration mission. However, for ISS-Inspector the additional mission frequency favours increased automation and the off-loading of as many control tasks as possible to the ground, making use of the reliable ISS communications down-link. However, as a backup there will also be a monitoring and control station (MCS) onboard the station to provide secondary on-orbit control capabilities when required. These systems are linked by the Central Data Handling System based at the ISS, which essentially acts as a server between the Inspector Free-Flyer and the control stations on the ground and on the ISS. The proposed configuration of these control and data handling systems is shown in Figure IV-3.

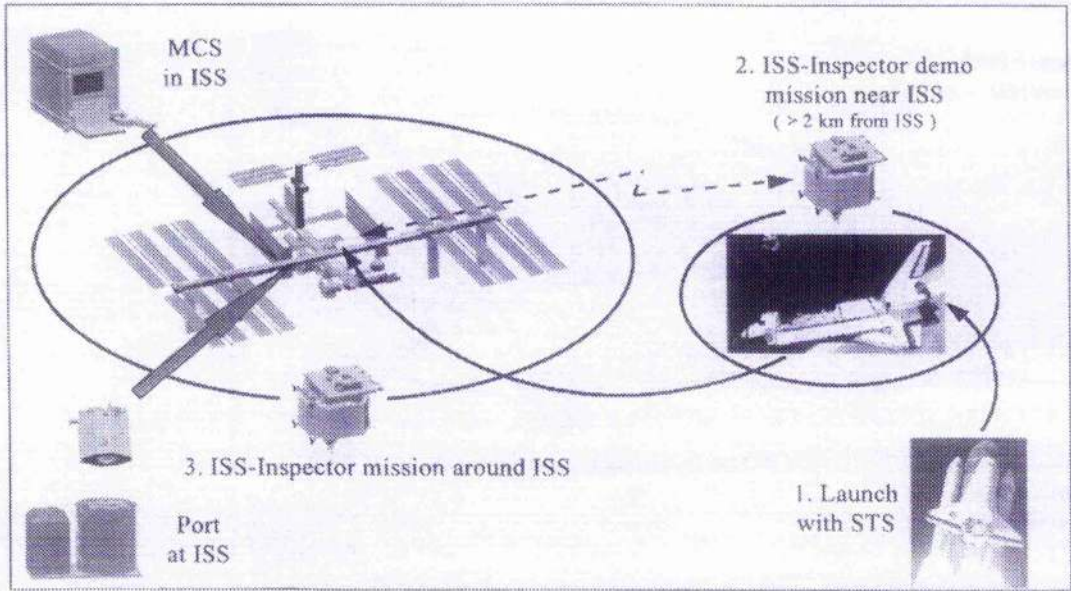


Figure IV-3 Inspector Control Systems Configuration (source: EADS Astrium)

Though the ISS communications link is much improved over the Mir system, there will still be constraints on the available bandwidth, and occasional breaks in coverage. While the control strategy is developed for increased direct involvement to ease the load on astronauts, an alternative control option on-orbit must also be available to compensate for any such breaks in the ground link. This problem can also be reduced through the timing of critical manoeuvres, such as docking/undocking, to ensure ground coverage, so that astronaut monitoring is only necessary during passive mission phases. Initially, the tasks most easily delegated to ground control systems are all the mission planning and verification tasks that must be performed prior to each mission. This leads to a hierarchical control concept, where missions can be planned at a high level as a sequence of manoeuvres and tasks, each of which can be broken down and verified on the ground before execution. The final sequence of manoeuvres can then be uploaded to the free-flyer for execution, with supervisor monitoring from the ground or via the MCS onboard the ISS in case of a communications break. This gives a high level control strategy making use of human planning capabilities and strengths and the increased computing power available on the ground, followed by the automated execution of simple commands by the Inspector Free-Flyer. The use of standard manoeuvres helps compensate for the difficulties involved in mission planning under the complex free-flyer dynamics and safety constraints, while the execution of a pre-planned sequence helps overcome any control delay between Inspector and the ground.

An exception to the ground control strategy occurs during the actual inspection phase of a mission, where the quick assessment of imaging is better performed onboard the ISS to

limit the down-link bandwidth of high-resolution imaging. In this phase, Inspector will make use of automated station-keeping to act as a stationary remote controlled camera, enabling the operator onboard the ISS to manually make inspections and obtain the best available imaging. Selected final results can then be forwarded to the ground by the operator for further analysis and archiving.

REFERENCES

- [1] S.R. Ellis, *Collision in Space, Human Factor Elements of the Mir Progress Collision*, Ergonomics in Design, Winter 2000. Advanced Displays and Spatial Perception Laboratory, Human Information Processing Research Branch, NASA Ames Research Center, Moffett Field, CA, USA.
- [2] S.R. Ellis, *The Elements of Human Factors: Illustrations from the Collision at the Mir Space Station*, IEEE Virtual Reality 2000 Conference, New Brunswick, NJ, USA, March 2000, IEEE Computer Society, pp.185-188
- [3] E. Messerschmid and R. Bertrand, *Space Stations - Systems and Utilization*, 1999, Springer-Verlag, New York, USA. ISBN 3-540-65464-X
- [4] E. St. John-Olcayto and C.R. McInnes, *Applicability of Potential Function Method to Path Constrained Manoeuvre*, Nov 1997, European Space and Technology Research Centre ESTEC Contract 11478/95/NL/JQ/SC, 2200 AG Noordwijk, The Netherlands.
- [5] *ISS-Inspector Design Definition Document*, IINS-RIBRE-RP-0001, Issue 1, 30/06/1998, EADS Astrium, Space Infrastructure, 28059 Bremen, Germany.
- [6] N.J. Nilsson, *Problem Solving Methods in Artificial Intelligence*, June 1971. Pub: McGraw-Hill, ASIN: 0070465738
- [7] J.T. Schwartz and M. Sharir, *On the Piano Movers' Problem: 1. The Case of a Two-Dimensional Rigid Polygonal Body Moving Amidst Polygonal Barriers*, Communications in Pure Applied Mathematics, vol.34, pp.345-398, 1983. Pub. Wiley, Indianapolis, USA.
- [8] A. Ellery, *An introduction To Space Robotics*, August 2000, Praxis Publishing, Chichester, UK. ISBN: 1-85233-164-X
- [9] V. Braatenberg, *Vehicles: Experiments in Synthetic Psychology*, 1984. Pub: MIT Press, Cambridge, MA, USA.
- [10] V.C. Lumelsky, *Continuous Robot Motion Planning in an Unknown Environment*, Adaptive Learning Systems, pp.339-358, 1986. Pub: Plenum, New York, USA.
- [11] E. Pellegrini, *Spacecraft Proximity Control using Sensor-Based Navigation*, Masters Thesis, August 1998, Dept of Aerospace Engineering, University of Glasgow, UK.
- [12] A. Roger, T. Welsh and C.R. McInnes, *Tunable Autonomy and Human Interfaces for Free Flying Servicing Vehicles*, STAIF 2001, AIP Conference Proceedings vol.552(1), pp.103-108. February 2, 2001.
- [13] T. Lozano-Perez, *Spatial Planning: A Configuration Space Approach*, IEEE Trans. on Computers, vol.C-32, No.2, 1983.
- [14] R.A. Brooks, *Solving the Find-Path Problem by Representing Free Space as Generalized Cones*, Technical Report No.AIM-674, MIT Artificial Intelligence Laboratory, May 1982.
- [15] R.A. Brooks, *Solving the Find-Path Problem by Good Representation of Free Space*, IEEE Transactions on Systems, Man, and Cybernetics, Vol.13, No.3, pp.190-197, Mar 1983.

- [16] E. Dijkstra, *A Note on Two Problems in Connection with Graphs*, Numerische Math., vol.1, pp 269-271, 1959.
- [17] B. Faverjon and P. Tournassoud, *A Local Approach for Path Planning of Manipulators with a High Number of Degrees of Freedom*, Proc. IEEE International Conference on Robotics and Automation, 1987, pp.1152-1159.
- [18] Y.K. Hwang and N. Ahuja, *A Potential Field Approach to Path Planning*, IEEE Transactions on Robotics and Automation, Vol.8, No.1, February 1992, pp.23-32.
- [19] J.H. Reif, *Complexity of the Mover's Problem and Generalizations*, Proc. 20th IEEE Symposium on Foundations of Computer Science, San Juan, Puerto Rico, Oct 1979. IEEE Computer Society Press, pp.421-427.
- [20] Y.K. Hwang and N. Ahuja, *Gross Motion Planning - A Survey*, ACM Computing Surveys, Vol.24, No.3, pp. 219-291, Sept 1992. ISSN: 0360-0300
- [21] B.R. Donald, *Motion planning with Six Degrees of Freedom*, MIT Intelligence Lab, Report No. AI-TR-791, 1984. Pub: MIT Press, Cambridge, MA, USA.
- [22] J.F. Canny, *The Complexity of Robot Motion Planning*, 1988, Pub: MIT Press, Cambridge, MA, USA.
- [23] B. Paden, A. Mees and M. Fisher, *Path Planning Using a Jacobian-Based FreeSpace Generation Algorithm*, Proc. IEEE International Conference on Robotics and Automation, 1989, pp.1732-1737.
- [24] L. Dorst, I. Mandhyan and K. Trovato, *The Geometrical Representation of Path Planning Problems*, Robotics and Autonomous Systems, vol.7, 1991, pp.181-195. Pub. Elsevier.
- [25] F. Avnaim, J.D. Boissonnat and B. Faverjon, *A Practical Exact Motion Planning Algorithm for Polygonal Objects Amidst Polygonal Obstacles*, Technical Report, RR-890, 1988. INRIA Documentation, Rocquencourt, FRANCE.
- [26] C. O'Dunlaing, M. Sharir and C.K. Yap, *Retraction: A New Approach to Motion-Planning*, Proc. 15th Annual (ACM) Symposium on Theory of Computing, Boston MA, 1983. pp. 207-220
- [27] T. Lozano-Perez, M.A. Wesley, *An Algorithm for Planning Collision-Free Paths Among Polyhedral Obstacles*, Commun. ACM, vol.22, no.10, pp. 560-570, 1979.
- [28] D.T. Lee, *Proximity and Reachability in the Plane*, Ph.D. thesis, Dept. of Electrical Engineering, University of Illinois at Urbana-Champaign, 1979.
- [29] M. Sharir and A. Schorr, *On Shortest Paths in Polyhedral Spaces*, Proc. 16th ACM Symposium on Theory of Computing, 1984, pp. 144-153. Pub. ACM Press, ISBN:0-89791-133-4
- [30] E. Welzl, *Constructing the Visibility Graph For n Line Segments in $O(n^2)$ Time*, Information Processing Letters, Vol.20, No.4, May 1985, pp.167-171. ISSN:0020-0190. Pub. Elsevier, 6277 Sea Harbor Drive, Orlando, FL 32887-4800 USA.

- [31] T. Asano, L. Guibas, J. Hershberger and H. Imai, *Visibility of Disjoint Polygons*, Algorithmica 1 (1986) pp. 49-63. Pub. Springer, NY, USA.
- [32] C.A. Klein, *Use of Redundancy in the Design of Robotic Systems*, Robotics Research, The Second International Symposium, ed. H. Hanafusa and H. Inoue, MIT Press, 1985. (Proc. Symposium on Robotics Research, Kyoto, Japan, August, 1984.) pp.207-214
- [33] L.C. Fu and D.Y. Liu, *An Efficient Algorithm for Finding a Collision free Path Among Polyhedral Obstacles*, Journal of Robotic Systems, Vol.7, No.1, 1990, pp.129-137.
- [34] M.H. Overmars and E. Welzl, *New Methods for Computing Visibility Graphs*, Proc. Fourth Annual Symposium on Computational Geometry, Urbana-Champaign IL, June 1988, ACM Press New York, pp.164-171.
- [35] D.T. Lee and R.L. Drysdale, *Generalisation of Voronoi Diagrams in the Plane*, SIAM Journal Computing, Vol. 10: pp.73-87, 1981.
- [36] H. Choset and J.W. Burdick, *Sensor Based Planning, Part I: The Generalized Voronoi Graph*, Proceedings of the IEEE International Conference on Robotics and Automation, 1995.
- [37] H. Choset, *Sensor Based Motion Planning: The Hierarchical Generalized Voronoi Diagram*, PhD Thesis, 1996. California Institute of Technology, Pasadena, CA 91125. USA.
- [38] J. Barraquand and J.C. Latombe, *Robot Motion Planning: A Distributed Approach*, The International Journal of Robotics Research, December 1991, Vol.10, No.6, pp.628-649, Pub MIT
- [39] H. Choset and D. Kortenkamp, *Path Planning and Control for AERCam, A Free-flying Inspection Robot*, Proc. 1999 IEEE International Conference on Space Robotics and Automation (ICRA '99), Vol.2, pp.1396-1403, Pub. IEEE.
- [40] F. Miyazaki and S. Arimoto, *Sensory Feedback based on the Artificial Potential for Robots*, Proc. 9th IFAC Congress, 1984, Budapest. Pub. Elsevier.
- [41] V.V. Pavlov and A.N. Voronin, *The Method of Potential Functions for Coding Constraints of the External Space in an Intelligent Mobile Robot*, Soviet Automation and Control, Vol.6, 1984.
- [42] O. Khatib and L.M. Mampey, *Fonction Decision-Commande d'un Robot Manipulateur*, (in French) DERA/CERT Report 2/7156, 1978, Toulouse France.
- [43] O. Khatib, *Real-Time Obstacle Avoidance for Manipulators and Mobile Robots*, Proc. IEEE International Conference on Robotics and Automation, St. Louis, Missouri, 1985. Pub IEEE, New York, pp.500-505.
- [44] C.R. McInnes, *Non-Linear Control for Large Angle Attitude Slew Manoeuvres*, Proc. 3rd ESA Symposium on Spacecraft Guidance, Navigation and Control, ESTEC, Noordwijk, The Netherlands, November 1996.
- [45] E. St. John-Olcayto, C.R. McInnes, F. Ankersen and J. Binder, *Control Design and Simulation of the Automated Transfer Vehicle within the MATLAB/Simulink Environment*, Advances in the Astronautical Sciences, Vol.102, pp.569-580, 1999.

- [46] C.R. McInnes, *Potential Function Methods for Autonomous Spacecraft Guidance and Control*, Paper AAS 95-447, AAS/AIAA Astrodynamics Specialist Conference, Halifax, Nova Scotia, 14-17th August 1995.
- [47] F. Csaki, *Modern Control Theories: Non-Linear, Optimal and Adaptive Systems*, 1972, pp. 449-500. Pub: Akademiai Kiado, Budapest, ISBN: 056907237
- [48] E. Rimon and D.E. Koditschek, *Exact Robot Navigation Using Artificial Potential Functions*, IEEE Transactions on Robotics and Automation, October 1992, Vol.8, No.5, pp.501-518.
- [49] S. Akishita, S. Kawamura and T. Hisanobu, *Velocity Potential Approach to Path Planning for Avoiding Moving Obstacles*, Journal of Advanced Robotics, Vol.7, No.5, 1993, pp.463-478, Pub. IEEE Computer Society Press
- [50] J. Barraquand, B. Langlois and J. Latombe, *Robot Motion Planning with Many Degrees of Freedom and Dynamic Constraints*, Preprint of the 5th Annual Symposium of Robotics Research, 1989, Tokyo, Japan, pp.74-83
- [51] P. Khcsia and R. Volpe, *Superguaradratic Potential for Obstacle Avoidance and Approach*, Proc. IEEE Conference on Robotics and Automation, pp. 1779-1784, Philadelphia, 1988.
- [52] D.E. Koditschek, *The Control of Natural Motion in a Mechanical System*, Trans. ASME Journal of Dynamic Systems, Measurement and Control, vol.113, pp.547-551, 1991.
- [53] D.E. Koditschek, *Some applications of Natural Motion Control*, Trans. ASME Journal of Dynamic Systems, Measurement and Control, vol.113, pp.552-557, 1991.
- [54] R. Weinstock, *Calculus of Variations with Applications to Physics and Engineering*, Dover Publications Inc. June 1974. ISBN: 0486630692
- [55] K. Sato, *Collision Avoidance in Multi-Dimensional Space using Laplace Potential*, (in Japanese) Proc. 5th Annual Conference of the Robotics Society of Japan, pp. 155-156, 1987.
- [56] S. Akishita, S. Kawamura and K. Hayashi, *Laplace Potential for Moving Obstacle Avoidance and Approach of a Mobile Robot*, Proc. 1990 Japan - USA Symposium on Flexible Automation, A Pacific Rim Conference, TSCIE, Kyoto, Japan, 1990, pp.139-142.
- [57] C.I. Connolly, J.B. Burns, R. Weiss, *Path Planning Using Laplace's Equation*, Proc. IEEE Int. Conf. on Robotics and Automation, 1990, pp.2102-2106
- [58] J. Decuyper and D. Keymeulen, *A Reactive Robot Navigation System Based on a Fluid Dynamics Metaphor*, Lecture Notes in Computer Science, vol.496, 1991, pp.348-355. Pub. Springer-Verlag, New York, USA.
- [59] K. Sato, *Deadlock-Free Motion Planning using the Laplace Potential Field*, Advanced Robotics, Vol. 7, No. 5, pp 449-461, 1993, Pub. VSP and Robotics Society of Japan.
- [60] H.P. Moravec and A. Elfes, *High Resolution Maps from Wide Angle Sonar*, Proc. IEEE International Conference on Robotics and Automation, March 1985, pp.166-171.

- [61] C.I. Connolly, R.A. Grupen and K.X. Souccar, *A Hamiltonian Approach to Kinodynamic Planning*, Proc. 1995 IEEE International Conference on Robotics and Automation, Silver Spring MD. Pub: IEEE.
- [62] J.S. Zelek, *Dynamic Path Planning*, IEEE International Conference on Systems, Man, and Cybernetics, Vancouver, British Columbia, Canada, October 1995, Vol.2, pp.1285-1290
- [63] C.I. Connolly, *Harmonic Functions and Collision Probabilities*, International Journal of Robotics Research, Vol. 16, No. 4, August 1997. pp 497-507.
- [64] P. Doyle and J.L. Snell, *Random Walks and Electric Networks*, Carus Monographs in Mathematics, 1984. American Mathematical Society, Washington DC.
- [65] L.M. Milne-Thomson, *Theoretical Hydrodynamics*, 5th edn. 1976. Pub. MacMillan Press, New York, USA.
- [66] S. Akishita, S. Kawamura and K. Hayashi, *New Navigation Function Utilizing Hydrodynamic Potential for a Mobile Robot*, Proc. IEEE Int. Workshop on Intelligent Motion Control, Bogazici University, Istanbul, Turkey, 1990, pp.413.
- [67] S. Akishita and S. Kawamura, *Obstacle Avoidance of an Autonomous Mobile Robot: Theory and Experiment*, Proc. Japan/USA Symposium Flexible Automation, ASME, 1992, vol.2, pp.1357
- [68] J.O. Kim, P.K. Khosla, *Real-Time Obstacle Avoidance Using Harmonic Potential Functions*, IEEE Transactions on Robotics and Automation, vol.8, no.3, June 1992, pp.338-349.
- [69] G.K. Schmidt and K. Azarm, *Mobile Robot Navigation in a Dynamic World Using an Unsteady Diffusion Equation Strategy*, Proc. 1992 IEEE/RSJ International Conference on Intelligent Robots and Systems, Raleigh, NC, USA, July 1992, pp.642-647.
- [70] S. Kirkpatrick, C.D. Gelatt and M.P. Vecchi, *Optimization by Simulated Annealing*, Science, vol.220, pp.671-680, 1983. Pub. AAAS, Washington DC, USA.
- [71] V. Cerny, *Thermodynamical Approach to the Traveling Salesman Problem: An Efficient Simulation Algorithm*, Journal of Optimization Theory Applications, vol.45 no.1, pp.41-51, 1985.
- [72] G.D. MacCann and C.H. Wilts, *Application of Electric-Analog Computers to Heat-Transfer and Fluid-Flow Problems*, Journal of Applied Mechanics, vol.16, no.2, pp.247-258, September 1949.
- [73] I. Tarassenko and A. Blake, *Analogue Computation of Collision-Free Paths*, Proc. IEEE Int. Conf. Robotics Automat., Sacramento, CA, Apr. 1991, pp.540-545.
- [74] J.R. Andrews and N. Hogan, *Impedance Control as a Framework for Implementing Obstacle Avoidance in a Manipulator*, Control of Manufacturing Processes and Robotic Systems, Eds. Hardt, D. E. 1983, pp. 243-251. ASME Winter Conf., Boston Nov 1983, (Reprinted in: Control of Manufacturing Processes and Robotic Systems, ed. D.E. Hardt

- [75] N.J. Nilsson, *A Mobile Automation: An Application of Artificial Intelligence Techniques*, Proceedings of the 1st International Joint Conference on Artificial Intelligence, Washington, D. C., May, 1969, pp. 509-520, ISBN: 0-86576-053-5, Pub William Kaufmann.
- [76] N.J. Nilsson, *Principles of Artificial Intelligence*, Tioga Publishing Company, Palo Alto CA. 1980.
- [77] B. Stout, *Smart Moves: Intelligent Pathfinding*, Game Developer, July 1997. Pub: CMP Media LLC, 600 Harrison Street, 3rd Floor, San Francisco, CA 94107
- [78] B.R. Donald, *A Search Algorithm for Motion Planning with Six Degrees of Freedom*, *Artificial Intelligence*, vol.31, 1987, pp.186-197, Pub. Elsevier.
- [79] L. Dorst and K. Trovato, *Optimal Path Planning by Cost Wave Propagation in Metric Configuration Space*, Proc. SPIE - The International Society for Optical Engineering. *Mobile Robots III*, Vol. 1007 (1988), pp. 188-197.
- [80] T. Pavlidis, *Contour Filling in Raster Graphics*, Proc. SIGGRAPH '81, Dallas TX, August 1981. pp. 29-36.
- [81] J. Lengyel, M. Reichert, B.R. Donald and D.P. Greenberg, *Real-Time Robot Motion Planning Using Rasterizing Computer Graphics Hardware*, *Mobile Robots III*, SPIE proceedings vol.1007, November 1988, pp.186-197.
- [82] C. Thorpe, *Path Relaxation: Path Planning for a Mobile Robot*, AAAI - Proceedings of the National Conference on Artificial Intelligence, 1984. pp.318-321
- [83] S. Kambhampati and L.S. Davis, *Multi-Resolution Path Planning for Mobile Robots*, IEEE Journal of Robotics and Automation, Vol. RA-2, No.3, September 1986
- [84] R.A. Jarvis, *Collision-Free Trajectory Planning Using the Distance Transforms*, Mechanical Engineering, Trans. of the Institution of Engineers, ME10(3), September 1985.
- [85] E.G. Gilbert, and D.W. Johnson, *Distance Functions and Their Applications to Path Planning in the Presence of Obstacles*, IEEE Trans. Robotics Automation, vol.RA-1, pp.21-30, March 1985
- [86] R.A. Jarvis and J.C. Byrne, *Robot Navigation: Touching, Seeing and Knowing*, Proc. 1st Australian Conference on Artificial Intelligence, Nov 1986. Pub. Springer-Verlag, NY, USA.
- [87] S. Suh and K. Shin, *A Variational Dynamic Programming Approach to Robot-Path Planning with a Distance-Safety Criterion*, IEEE Journal on Robotics and Automation, vol.4, no.3, pp.334-349, 1988.
- [88] A.M. Thompson, *The Navigation System of the JPL Robot*, Proc. 5th International Joint Conference on Artificial Intelligence, Aug. 1977, pp. 749-757. Pub. Morgan Kaufmann.
- [89] R. Chatila, *Path Planning and Environment Learning*, Proc. European Congress on Artificial Intelligence, July 1982, Orsay, France, pp.211-215.

- [90] V.J. Lumelsky and A.A. Stepanov, *Path Planning Strategies for a Point Mobile Automation Moving Amidst Unknown Obstacles of Arbitrary Shape*, Algorithmica, vol.2, no.4, pp.403-430, 1987, Pub. Springer, NY, USA.
- [91] T. Boult, *Updating Distance Maps When Objects Move*, Proc. SPIE Symposium on Mobile Robots II, pages 232-238, 1987.
- [92] K.I. Trovato, *Differential A*: An Adaptive Search Method Illustrated with Robot Path Planning for Moving Obstacles and Goals, and an Uncertain Environment*, Journal of Pattern Recognition and Artificial Intelligence, vol.4, no.2, 1990, pp.245-268.
- [93] A. Stentz, *The Focussed D* Algorithm for Real-Time Replanning*, Proc. International Joint Conference on Artificial Intelligence, August 1995, pp.1652-1659
- [94] A. Zelinsky, *A Mobile Robot Exploration Algorithm*, IEEE Transactions on Robotics and Automation, vol.8, no.6, December 1992, pp.707-717.
- [95] N.C. Rowe and R.S. Ross, *Optimal Grid-Free Path Planning Across Arbitrarily Contoured Terrain with Anisotropic Friction and Gravity Effects*, IEEE Transactions on Robotics and Automation, vol.6, no.5, 1990, pp.540-553
- [96] Z. Shiller and Y.R. Gwo, *Dynamic Motion Planning of Autonomous Vehicles*, IEEE Transactions on Robotics and Automation, vol.7, no.2, April 1991, pp.241-249.
- [97] A. Yahja, S. Singh and A. Stentz, *Recent Results in Path Planning for Mobile Robots Operating in Vast Outdoor Environments*, Proc. 1998 Symposium on Image, Speech, Signal Processing and Robotics, September 1998.
- [98] A.B. Roger and C.R. McInnes, *Safety Constrained Free-Flyer Path Planning at the International Space Station*, AIAA Journal of Guidance, Control, and Dynamics, November 2000, vol.23, no.6, pp.971-979.
- [99] C.S. Sallaberger and G.M.T. D'Eleuterio, *Optimal Motion Planning for Space Robots*, Proc. 43rd Congress of the IAF, Aug-Sept 1992, Washington DC, Pub. AIAA, IAF-92-0040.
- [100] A.R. Brody and S.R. Ellis, *A Comparison of Acceleration Control and Pulse Control in Simulated Spacecraft Docking Maneuvers*, Proc. 29th Aerospace Sciences Meeting, Reno, NV. January, 1991. AIAA Paper 91-0787
- [101] W.T. Thomson, *Introduction to Space Dynamics*, Dover Publications Inc. New York, 1986. ISBN: 0-486-65113-4
- [102] W.E. Wiesel, *Spaceflight Dynamics*, McGraw-Hill series in Aeronautical and Aerospace Engineering. McGraw-Hill Book Company, 1989. ISBN: 0-07-070106-7
- [103] W.H. Clohessy and R.S. Wiltshire, *Terminal Guidance System for Satellite Rendezvous*, Journal of the Aerospace Sciences, vol.27, 1960, pp.653-658.
- [104] O.W. Olszewski, *Automated Terminal Guidance for a Shuttle Rendezvous to Space Station Freedom*, AIAA-90-3356 CP, 1990.

- [105] G. Porcelli and D. Tabak, *Fuel-Time-Optimal Orbital Rendezvous by Nonlinear Programming*, Astronautica Acta, vol.16, 1971. pp.167-172, Pergamon Press 1971, UK.
- [106] S.A. Stern, *A Rectilinear Guidance Strategy for Short Orbital Transfers*, AIAA Journal of Spacecraft and Rockets, Nov-Dec 1984, pp.542-545.
- [107] J.A. Nelder and R. Mead, *A Simplex Method for Function Minimization*, Computer Journal, vol.7, pp.308-313, 1965. Oxford University Press.
- [108] J.C. Lagarias, J.A. Reeds, M.H. Wright and P.E. Wright, *Convergence Properties of the Nelder-Mead Simplex Algorithm in Low Dimensions*, SIAM Journal on Optimization, vol.9, pp.112-147, 1998.
- [109] J.H. Holland, *Adaptation in Natural and Artificial Systems: An Introductory Analysis with Applications to Biology, Control and Artificial Intelligence*, December 1975, Pub. University of Michigan Press, ISBN: 0472084607
- [110] K.A. DeJong, *Analysis of the Behavior of a Class of Genetic Adaptive Systems*, Phd. Thesis, Department of Computer and Communications Sciences, University of Michigan, Ann Arbor, 1975.
- [111] M. Vose, *Modeling Simple Genetic Algorithms*, in Foundations of Genetic Algorithms, Chap.2, Pub. Morgan Kaufmann, October 1997, ISBN: 155860460X
- [112] J.J. Grefenstette, *A User's Guide to GENESIS*, 1987, Navy Center for Applied Research in Artificial Intelligence, Naval Research Laboratory, Washington DC, USA.
- [113] G. Janin and M.A. Gomez-Tierno, *The Genetic Algorithm for Trajectory Optimization*, Proc. 36th International Astronautical Congress, Stockholm, Sweden, 1985. Pub: AIAA, IAF Paper.85-244
- [114] A.R. Brody, *Significance of Logistics in Spacecraft Docking (Berthing) Manoeuvres*, Engineering Notes, AIAA Journal of Spacecraft and Robotics, vol.30, no.4, July 1993, pp.519-520.
- [115] H.S. London, *Second Approximation to the Solution of the Rendezvous Equations*, AIAA Journal, vol.1, no.7, 1963, pp.1691-1693.
- [116] E.A. Euler and Y. Shulman, *Second-Order Solution to the Elliptical Rendezvous Problem*, AIAA Journal, vol.5, no.5, 1967, pp.1033-1035.
- [117] M. Baune, D. Wilde, F. Steinsiek, *ISS - Inspector. Inspector at the International Space Station*, ESA report. CR (P) 4050 vol.1, Pub. RADS Astrium, Space Infrastructure, 28059 Bremen, Germany, 1996. ESA contract number. 11531/95/NL/VK.
- [118] L. Kerstein, F. Steinsiek, G. Degtyarenko, D. Brockschmidt and E. Graf, *Inspector and the International Space Station*, Space Technology, vol.16, issue.2, March, 1996, pp.83-96, Pub. Elsevier Science, ISSN: 0892-9270.
- [119] *Interface Definition Document for ISS Visiting Vehicles*, SPP 50235, 10 February 2000, ISS Program Office, NASA.

- [120] J. Artol and D.E. Headley, *The International Space Station as a Free Flyer Servicing Node*, Space Technology and Applications International Forum (STAIF '99), Albuquerque, New Mexico, January 31 - February 4, 1999, p.389, AIP Conference Proceedings.
- [121] W. Wohlke, *Rendezvous and Berthing Between Columbus Free-Flying Laboratory and Space Station Freedom*, IFAC Automatic Control in Aerospace, Ottobrunn, Germany, 1992. IFAC Publications Office, Elsevier Ltd. Oxford, UK.
- [122] J. Magne, R. Canu and A. Joulot, *Optimization of Manoeuvres and Resources for the Rendezvous of a Servicing Vehicle to a Space Station*, Advances in the Astronautical Sciences, Spaceflight Dynamics, 1993, vol.84, part.2, Pub. American Astronautical Society (AAS 93-343)
- [123] S.H. Yu, *Range-Rate Control Algorithms and Space Rendezvous Schemes*, AIAA Journal of Guidance, Control and Dynamics, vol.20, no.1, 1997.
- [124] R.N. Lea, *Automated Space Vehicle Control for Rendezvous Proximity Operations*, Telematics and Informatics, vol.5, no.3, pp 179-185, 1988, Pergamon Press plc, USA.
- [125] J.M. Hanson and A.W. Deaton, *Guidance Schemes for Automated Terminal Rendezvous*, Advances in the Astronautical Sciences, Space Flight Mechanics, 1994, vol.87, part.2, pp.765-784, Pub. American Astronautical Society (AAS 94-163)
- [126] K.N. Leabourne, S.M. Rock and S.D. Fleischer, *Station Keeping of an ROV using Vision Technology*, Proc. OCEAN 97 Conference, pp.634-640, Halifax, Nova Scotia, October 1997. Pub. MTS/IEEE
- [127] A.R. Brody and S.R. Ellis, *Effect of an Anomalous Thruster Input During a Simulated Docking Maneuver*, AIAA Journal of Spacecraft and Rockets, vol.27, no.6, 1990, pp.630-633.
- [128] B. Stroustrup, *The C++ Programming Language*, 2nd Edition, June 1994, Addison-Wesley Pub Co., ISBN: 0-201-53992-6
- [129] D. Shreiner, M. Woo, J. Neider, T. Davis, *OpenGL Programming Guide: The Official Guide to Learning OpenGL*, Version 1.4, 4th Edition, November 14, 2003, Addison-Wesley Pub Co., ISBN: 0321173481.
- [130] D.D. Mueller, *Relative Motion in the Docking Phase of Orbital Rendezvous*, Technical Documentary Report No. AMRL-TDR-62-124, December 1962, Project No. 7184, Task No. 718405, Behavioural Sciences Laboratory, Aerospace Medical Division, Air Force Systems Command, Wright-Patterson Air Force Base, Ohio, USA.
- [131] X-Mir Inspector Design Definition Document, INS-RIBRE-SPE-0009, Issue 3, 08/11/1996, EADS Astraum, Space Infrastructure, 28059 Bremen, Germany.
- [132] G. Janin, *Relative Motion*, M.A.D Working Paper 3, March 1976, European Space Operations Centre (ESOC), Information Handling Department, Mission Analysis Division, 5 Robert-Bosch Strasse, 64293 Darmstadt, Germany.
- [133] L.D. Mullins, *The Motion of Throw Away Detectors Relative to the Space Shuttle*, 1975, G.C. Marshall Space Flight Center, NASA TM-X-64948

- [134] C.L. Leonard, W.M. Hollister, E.V. Bergmann, *Orbital Formation-Keeping with Differential Drag*, AIAA Journal of Guidance, Control and Dynamics, vol.12, no.1, Jan 1989.
- [135] W.H. Press, S.A. Teukolsky, W.T. Vetterling and B.P. Flannery, *Interpolation in Two or More Dimensions*, Numerical Recipes in C: The Art of Scientific Computing, 2nd ed., pp. 123-125, Cambridge University Press, May 19, 1988, ISBN 052135465X
- [136] M. Abramowitz and I.A. Stegun, *Handbook of Mathematical Functions*, June 1974, Dover Publications, New York. ISBN: 0486612724
- [137] A.B. Roger, *Autonomous Free-Flyer Path Planning at International Space Station Alpha*, Proc. 48th International Astronautical Federation Congress, Turin, Italy, October, 1997, Pub. AIAA.
- [138] C.R. McInnes and I. Lopez, *Autonomous Rendezvous using Artificial Potential Function Guidance*, AIAA Journal of Guidance, Control and Dynamics, vol.18, no.2, pp.237-237, 1995.
- [139] J.W. Dichalm and S.A. Heise, *Optimal In-Plane Orbital Evasive Manoeuvres Using Continuous Low Thrust Propulsion*, AIAA Journal of Guidance, Control and Dynamics, vol.14, no.6, pp.1323-1326, 1991.
- [140] B.W. Brown, J. Lovato, K. Russell and J. Venier, *Randlib.c: Library of C Routines for Random Number Generation*, Version 1.3 August 1997, available from: StatLib, Department of Statistics, Carnegie Mellon University. [<http://lib.stat.cmu.edu/general/>]
- [141] H. Sorenson, *Kalman Filtering: Theory and Application*, June 1985, IEEE Press, ISBN: 0879421916
- [142] E.S. Gardner Jr., *Exponential Smoothing: The State of the Art*, *Journal of Forecasting*, vol.4, 1985, pp.1-38. Pub. John Wiley & Sons, Hoboken, NJ 07030, U.S.A.
- [143] C. Chatfield, *The Holt-Winters Forecasting Procedure*, Applied Statistics, vol.27, no.3, 1978, pp.264-279, Blackwell Publishing for the Royal Statistical Society.
- [144] S.G. Wakefield, *Task Path Planning, Scheduling and Learning for Free-Ranging Robot Systems*, NASA Marshall Space Center, Third Conference on Artificial Intelligence for Space Applications, Nov 1987, part.1, pp.137-141. Pub: NASA Technical Reports.
- [145] R.P. Bonasso, R.J. Firby, E. Gat, D. Kortenkamp, D.P. Miller and M.G. Slack, *Experiences with an Architecture for Intelligent Reactive Agents*, Special Issue: Software Architectures for Hardware Agents, *Journal of Experimental and Theoretical Artificial Intelligence*, vol.9(2/3), pp.237-256, 1997. Pub. Taylor & Francis Ltd
- [146] C. Elsaesser and M.G. Slack, *Integrating Deliberative Planning in a Robot Architecture*, Proc AIAA/NASA Conference on Intelligent Robots in Field, Factory, Service and Space, March 1994. pp.782-787. Pub: AIAA.
- [147] K. Menger, *Das Botenproblem*, (in German) Ergebnisse eines Mathematischen Kolloquiums 2 (K. Menger, editor), 1932, pp.11-12, Pub: Teubner, Leipzig, Germany.

- [148] G. Dantzig, R. Fulkerson, and S. Johnson, *Solution of a Large-Scale Traveling-Salesman Problem*, Journal of the Operations Research Society of America, vol.2, 1954, pp.393-410.
- [149] Y. Caseau and F. Laburthe, Solving Small TSPs with Constraints, Proc. International Conference on Logic Programming, 1997, pp.316-330. Pub. Springer.
- [150] V. Chvatal, *Hamiltonian Cycles*, in E.L. Lawler, J.K. Lenstra, A.H.G. Rinnooy Kan, D.B. Shmoys, *The Travelling Salesman Problem - A guided tour of combinatorial optimization*, Wiley & Sons, Chichester, 1985, pp.403-429.
- [151] M. Desrochers, C.V. Jones, J.K. Lenstra, M.W.P. Savelsbergh and L. Stougie, *Towards a Model and Algorithm Management System for Vehicle Routing and Scheduling Problems*, Journal of Decision Support Systems, vol.25, pp.109-133. Mar 1999. Pub. Elsevier
- [152] R. Bellman, *Dynamic Programming*, 1957, Pub. Princeton University Press, Princeton NJ, USA. ISBN: B0000CJYFH
- [153] D.P. Bertsekas, *Dynamic Programming and Optimal Control*, June 1, 1995. Pub. Athena Scientific, ISBN: 1886529116
- [154] J. Grefenstette, R. Gopal, B. Rosmaita and D. Van Gucht, *Genetic Algorithms for the TSP*, Proc. First International Conference on Genetic Algorithms and Their Applications, 1985, Lawrence Erlbaum, Hillsdale, New Jersey, pp.160-165. Pub. Morgan Kaufmann, San Mateo CA, USA.
- [155] D.J. Guan and X. Zhu, *Multiple Capacity Vehicle Routing on Paths*, SIAM Journal of Discrete Mathematics, vol.11, no.4, pp.590-602, November 1998. Society for Industrial and Applied Mathematics.
- [156] J. Bramel and D. Simchi-Levi, *Probabilistic Analyses and Practical Algorithms for the Vehicle Routing Problem with Time Windows*, Journal of Operations Research, vol.44, pp.501-509, September 1992.
- [157] A.R. Brody, *EivaN, A Forward-Looking Interactive Orbital Trajectory Plotting Tool for use with proximity Operations and Other Maneuvers : Description and User's Manual*, June 1988, NASA CR 1.26:177490, National Aeronautics and Space Administration, Ames Research Center National Technical Information Service, ASIN: B00010TVHK
- [158] A.J. Grunwald, and S.R. Ellis, *A Visual Display Aid for Orbital Maneuvering: Design Considerations*, AIAA Journal of Guidance, Control and Dynamics, vol.16, no.1, 1993.
- [159] R.A. Brooks, *A Layered Intelligent Control System for a Mobile Robot*, IEEE Journal of Robotics and Automation, vol.RA-2, no.1, pp.14-23, Apr 1986.
- [160] J.S.B Mitchell, D.W. Payton and D.M. Keirsey, *Planning and Reasoning for Autonomous Vehicle Control*, International Journal of Intelligent Systems, 1987, vol.2, pp.129-198. Pub: John Wiley & Sons.
- [161] *The International Space Station, A Guide For European Users*, BR-137 February 1999, ESA Publications Division, ESTEC, PO Box 299, 2200 AG Noordwijk, The Netherlands.

- [162] D. Wilde and O. Sytin, *The Mir-Progress-Inspector Mission*, MS95/020, International Symposium Space Dynamics, June 19-23, 1995, Toulouse, France. Pub. ESOC, 5 Robert-Bosch Strasse, 64293 Darmstadt, Germany.
- [163] R.A. Cook and A.J. Spear, *Back to Mars: The Mars Pathfinder Mission*, IAF-97-O.3.01, Proc. 48th IAF Congress, Turin, Italy, October 1997. AIAA Publications.
- [164] H.W. Stone, *Mars Pathfinder Microrover: A Small, Low-Cost, Low-Power Spacecraft*, Proc. 1996 AIAA Forum on Advanced Developments in Space Robotics, Aug. 1996. Pub. AIAA
- [165] *Sojourner's 'Smarts' Reflect Latest in Automation*, Press Release August 8th, 1997, Public Information Office, Jet Propulsion Laboratory, California Institute of Technology, National Aeronautics and Space Administration, Pasadena, Calif. 91109.
- [166] Y. Wakabayashi, *Advances in Space Robotics of NASDA*, IAF-97-U.4.04, Proc. 48th IAF Congress, Turin, Italy, October 1997. Pub. AIAA.
- [167] I. Kawano, M. Mokuno, T. Kasai, *Relative GPS Navigation for an Automated Rendezvous Docking Test Satellite ETS-VII*, Proc. 10th International Technical Meeting of the Satellite Division of the Institute of Navigation, September 16-19, 1997, Kansas City, Missouri, pp.707-716. Pub. ION Publications, Fairfax, VA, USA.
- [168] J.R. Miller, O. Amidi and M. Delouis, *Arctic Tests of the CMU Autonomous Helicopter*, Proc. Association for Unmanned Vehicle Systems International 1999, 26th Annual Symposium, July 1999. Pub. Association for Unmanned Vehicle Systems International, Arlington, VA 22204, USA.
- [169] J.R. Miller and O. Amidi, *3-D Site Mapping with the CMU Autonomous Helicopter*, Proc. International Conference on Intelligent Autonomous Systems (IAS-5), June 1998. Pub. Elsevier, Orlando FL, USA.
- [170] B. Butler and M. Black, *The Theseus Autonomous Underwater Vehicle - Two Successful Missions*, Proc. 10th International Symposium on Unmanned Untethered Submersible Technology, Autonomous Undersea Systems Institute, pp.12-22, 1997. Pub. Storming Media, Washington DC, USA.
- [171] L.L. Whitcomb, D.R. Yoerger, H. Singh and D.A. Mindell, *Towards Precision Robotic Maneuvering, Survey, and Manipulation in Unstructured Undersea Environments*, Robotics Research - The Eighth International Symposium, London, 1998, pp.45-54, Pub. Springer-Verlag,
- [172] D.R. Yoerger, A.M. Bradley and B. Walden, *System Testing of the Autonomous Benthic Explorer*, IARP International Advanced Robotics Program, Workshop on Mobile Robots in Subsea Environments, Monterey, CA May 3-6, 1994, Pub. IARP. LAAS-CNRS, Toulouse, France.
- [173] P. Ramakrishnan and R. Turner, *Integrating Partial-Order Planning into the Orca Schema-Based Mission Controller*, Proc. 10th International Symposium on Unmanned Untethered Submersible Technology, 1997, Pub. Autonomous Undersea Systems Institute, 6 Old Concord Turnpike Lee, 03824 NH, USA.

- [174] D. Wildc, L. Korstoin, Y. Frumkin and O. Sytin, *The Inspector Family*, TAF-98 T.3.03, Proc. 49th International Astronautical Congress, September/Ocotober 1998, Melbourne, Australilia. Pub. AIAA.
- [175] J. Powell, *AERCam Sprint*, Spaceflight, vol.40, no.5, May 1998. Pub. The British Interplanetary Society, 27/29 South Lambeth Road, London SW8 1SZ, England, UK.
- [176] C. Zandonella, *Space Balls*, New Scientist, 17 July 1999, pp.7, New Scientist, 151 Wardour St, London, UK.
- [177] A. Huster, S.D. Fleischer and S.M. Rock, *Demonstration of a Vision-Based Dead-Reckoning System for Navigation of an Underwater Vehicle*, Proc. 1998 IEEE Symposium on Autonomous Underwater Technology, pp.185-189, Cambridge MA, August 20-21 1998.
- [178] F.H. Stillwagen, *Communications and Tracking of Visiting Vehicles near ISS: The design of the Reusable Launch Vehicle Communications*, AAS 99-103, AIAA International Space Station Service Vehicles Conference, Houston TX, April 25-28 1999.